

Thin Film Polymer Photonics: Spin Cast Distributed Bragg Reflectors

James Bailey, MPhys

Thesis submitted to The University of Nottingham
for the degree of Doctor of Philosophy

July 2014

Abstract

Polymer distributed Bragg reflectors (DBRs) were prepared by spin-casting alternating layers of polystyrene (PS) and poly(vinylpyrrolidone) (PVP) from mutually exclusive (orthogonal) solvents. These all polymer photonic structures were prepared using a purpose built automated spin-coater system. Samples were prepared with targeted optical properties such as the wavelength position, intensity and bandwidth of reflection peaks. The wavelength position of the reflection peaks was controlled by the deposition spin-speed used during sample preparation. Reflectance was controlled by the number of layers deposited onto the sample. The bandwidth was increased by chirping the layers in the photonic structure.

Reflection bands were measured in the UV/visible region of the spectrum using two different (transmission and reflection mode) purpose built spectrometer set-ups. Measured reflection bands had narrow bandwidths between $10nm$ and $20nm$. Chirping these photonic structures broadened the peaks to bandwidths of $\sim 50nm$. A 100 layer PVP/PS DBR had a total reflectance of $93 \pm 1\%$. The wavelength of the reflection peaks from flat DBR samples blue-shifted when measured away from normal incidence. This was reduced when corrugating a DBR by wrinkling the films with mechanical strain. The wavelength of the reflection band from a corrugated DBR remained constant when the sample was rotated. Thus improving the angular dependence of the structures.

Fourier transform infra-red spectroscopy was used to measure reflection bands which were between wavelengths of $1600nm$ and $2700nm$. These reflection bands had narrow bandwidths between $\sim 40nm$ and $60nm$. The largest reflectance measured within the infra-red spectra was $80 \pm 1\%$ from a 50 layer PVP/PS DBR.

A modified optical transfer matrix method was used to model the optical properties of the DBRs. Changes in the refractive index contrast (between 0.020 and 0.028 for 30 layer PVP/PS DBRs) were needed to fit the model to

the measured UV/visible spectra. It was concluded that trapped solvent (from sample preparation) was lowering the refractive indices of the layers.

The polymer-polymer interface widths of spin-cast polymer multi-layers were measured using neutron reflectivity. Each polymer-polymer interface width was less than $1nm$ throughout the DBR samples.

The polymer multi-layer samples were measured using time of flight secondary ion mass spectrometry (TOF-SIMS). An Ar_{2000}^+ sputtering source was used to etch through the multi-layer samples. It was concluded that the thickness of spin-cast films did not change when preparing a multi-layer structure. However, other techniques, such as ellipsometry, are more suitable for measuring the thickness of films. The TOF-SIMS technique was unable to measure polymer-polymer interface widths in multi-layer samples. This was due to the sputtering beam roughening/mixing the polymers at the interfaces.

It was concluded that PVP/PS DBRs could be used as inexpensive narrowband reflectors/filters. However, alternative polymer systems may be more useful for other applications which require a greater reflectance. This includes creating resonant cavities to improve the efficiency of optical devices (such as LEDS and solar cells). The results and techniques from these experiments are useful for further development in polymer photonic structures and polymer multi-layer devices.

Acknowledgements

I am glad that I did a PhD because I enjoyed the experience as a whole. Although there were a few low moments along this journey and I was frequently challenged by the work. I couldn't have done this alone and there are many people that I would like to sincerely thank.

I would like to thank Dr James Sharp. He has never said that he was 'too busy' or 'wouldn't help' whenever I knocked on his door. I believe that James offers more advice and guidance than what is expected of him. His passion for soft matter physics is inspirational. It is no secret that he is the best PhD supervisor in the department. Thank you James for all the challenges and turning me into a scientist.

I have been very lucky to have worked with some excellent people within the soft matter group. This includes students past and present; Zoe Langham, Kevin Langley, David Farmer, Rob Temperton and Richard Taylor. Special thanks should go to Dr Mike Smith. Mike has been like a second supervisor to me. He was always on hand to help and was too nice to tell me to 'shut up' when I was blabbering on too much. Thanks should also go to the Nano science group for being a great bunch of people. I wish them all the best.

The fantastic workshop team deserve my thanks for turning bits of plastic and metal into functioning laboratory equipment. They are true master craftsmen. Thanks should also go to the Nano-center technicians for letting me use their fancy pieces of equipment when needed.

I have been fortunate to have collaborated with many people during my PhD. Working with experts from different disciplines has been interesting because I always learn something new. I would like to thank Dr David Scurr, Dr Rasmus Havelund, Dr Anthony Higgins, Dr Ashley Cadby and all of the other people who have shown interest in my work.

I would like to thank my family for their continuing support. It has made my life a lot easier and I feel fortunate to be able to pursue my dreams. I would

also like to thank Tonya and Mark for helping me out when I needed a place to stay during the first few weeks of my PhD.

Finally, I would like to thank Bella. Our relationship started a few weeks before my PhD. She has been there for me during the whole experience. This included every time I was stressing about work, too busy to spend time with her and being boring whenever I had a geek moment. She is the love of my life. I hope our lives have many more chapters together as this 'PhD chapter' becomes closed.

Publications list

1. James Bailey and James S. Sharp, “Thin Film Polymer Photonics: Spin Cast Distributed Bragg Reflectors and Chirped Polymer Structures”, European Physical Journal E, 33:41-49, 2010.
2. James Bailey and James S. Sharp, “Infrared Dielectric Mirrors Based on Thin Film Multilayers of Polystyrene and Polyvinylpyrrolidone”, Journal of Polymer Science Part B: Polymer Physics, 49:732-739, 2011.
3. Rasmus Havelund, Antonino Licciardello, James Bailey, Nunzio Tuccitto, Davide Sapuppo, Ian S Gilmore, James S Sharp, Joanna LS Lee, Taoufiq Mouhib and A Delcorte, “Improving secondary ion mass spectrometry C_{60}^{n+} sputter depth profiling of challenging polymers with nitric oxide gas dosing”, American Chemical Society”, vol.85, no.10, 5064-5070, 2013.

Contents

1	Motivation	10
2	Literature review	13
2.1	Introduction	13
2.2	Structural colour and Bragg reflection	13
2.3	Structural colour in nature	19
2.4	Man-made photonic structures	21
2.5	Optical devices which make use of photonic structure	23
2.6	Polymer multi-layer devices	25
3	The physics of reflection from films and multi-layers	27
3.1	Introduction	27
3.2	Fresnel reflection and transmission coefficients	27
3.3	Boundary matrix	30
3.4	Transmission matrix	33
3.5	The optical matrix method	35
3.6	Application to multi-layers	37
3.7	Modelling diffuse interfaces	39
3.8	Summary	39
4	Experimental techniques	41
4.1	Introduction	41
4.2	Spin-coating thin films	41
4.2.1	Polymer and solvent selection	43
4.3	Multi-layer sample preparation	47
4.3.1	Automated sample preparation	49
4.3.2	Multi-layer film thickness	53
4.3.3	Annealing DBR samples	53

4.4	Ellipsometry	55
4.4.1	Film thickness calibration	62
4.4.2	Spectroscopic ellipsometry	66
4.5	UV/visible spectrometry	71
4.5.1	UV/visible spectra measured in transmission	71
4.5.2	UV/visible spectra measured in reflection	73
4.6	Fourier transform infra-red spectroscopy	74
4.7	Neutron reflectivity	77
4.7.1	Preparation of neutron reflectivity samples	85
4.8	Time of flight secondary ion mass spectrometry	88
4.8.1	Chemical analysis of mass spectra	91
4.8.2	Selecting regions of interest	93
4.8.3	Depth profiling and calibration of sputter rate	94
5	UV/visible properties of PVP/PS DBRs	99
5.1	Introduction	99
5.2	Controlling the wavelength of the reflection bands	99
5.3	Inefficiencies and defects which reduce DBR peak reflectance	105
5.3.1	Polymer-polymer interfaces	106
5.3.2	Reduction of refractive index contrast	109
5.3.3	Effects of disorder in layer thickness	113
5.3.4	Asymmetry in the layer thickness	115
5.4	Controlling the reflectance	117
5.5	Angular dependence of DBR spectra	120
5.6	Chirping the photonic structure	128
5.7	Summary	131
6	Improving the preparation and reflectance of PVP/PS DBRs	133
6.1	Introduction	133
6.2	DBR samples after ageing	133
6.3	Asymmetry and symmetry of film thickness	139
6.4	Periodically annealing during sample preparation	144
6.5	Summary	146
7	Infra-red measurements and properties of polymer DBRs	148
7.1	Introduction	148
7.2	Measuring the effects of HCl swelling	149

7.3	DBR reflection bands in FTIR spectra	152
7.3.1	Position of the reflection bands	152
7.3.2	Controlling the reflectance of infra-red DBRs	156
7.4	Modelling infra-red DBR spectra	158
7.4.1	Wavelength dependence of refractive index	158
7.5	Summary	160
8	Neutron reflectivity measurements of polymer multi-layers	161
8.1	Introduction	161
8.2	Measuring and modelling polymer samples	162
8.2.1	Deuterated PS	162
8.2.2	PVP (top) → dPS (bottom) bi-layer	165
8.2.3	10 layer PVP/dPS structure	168
8.3	Comparison with UV/visible spectra	172
8.4	Summary	176
9	Using polymer multi-layers to calibrate TOF-SIMS experiments	177
9.1	Introduction	177
9.2	Bi-layers	178
9.3	Asymmetric multi-layers	184
9.3.1	Non-chirped samples	186
9.3.2	Chirped	191
9.4	Multi-layers of thicker films	195
9.5	Analysis of errors in TOF-SIMS measurements	199
9.6	Summary	200
10	Improving the angular dependence by corrugating DBR films	201
10.1	Introduction	201
10.2	Optical properties of curved DBRs	202
10.3	Corrugating thin films	204
10.3.1	Preparing the elastomer substrate	205
10.3.2	Preparing the CA/PVK DBR	205
10.3.3	Corrugating the CA/PVK DBR	211
10.4	Physical properties of the corrugated DBR	211
10.5	UV/visible properties of corrugated DBRs	214
10.5.1	Specular reflection measurements	215
10.5.2	Changing measured angle of reflection θ_r	218

10.5.3	Changing angle of incidence θ_i	220
10.5.4	Rotating the corrugated sample	226
10.6	Reflectance of the corrugated DBR	230
10.7	Summary	232
11	Conclusion and future work	234

Chapter 1

Motivation

Optical devices are becoming increasingly important as they are being used in a growing number of applications. Improving our control of light could lead towards better optical filters [1, 2], sensors [3], displays [4, 5], lasers [6, 7] and solar cells [8, 9]. Making these devices is often challenging as optical devices require thoughtful design and are often difficult to make. The following properties should be considered when building a photonic structure;

- *Choice of materials:* The pigmentation, refractive index and structural arrangement of materials will change the optical properties of a device [10, 11, 12]. For this research, the materials were required to be optically transparent and have a sufficient refractive index contrast between layers (this is discussed further in chapters 2 and 3). Also, the materials must be capable of being processed into a defect-free photonic structure. Depositing layers with poor homogeneity (non-uniform throughout the layer) and topography (surface roughness) reduces the efficiency of a photonic structure by scattering light [10, 11].
- *Design of the structure:* Thoughtful design is needed to create an efficient optical device. The spatial separation between materials (because of differences in refractive indices) will change the optical properties of a photonic device (this is discussed further in chapters 2 and 3) [10, 13, 14].
- *High precision fabrication:* UV/visible wavelength optical devices are sensitive to changes on the *nm* scale. Fabrication techniques must be able to prepare samples which have defect free and nano-scale features. Any discrepancies in the structural arrangement and/or defects in the sample will reduce the efficiency of the device [5, 7].

Materials and techniques from the semi-conductor industry have contributed significantly towards the development of man-made photonic devices. For example, 1D photonic structures are frequently made using ultra high vacuum (UHV) deposition of semiconductor materials, such as heavily doped Silicon and/or Gallium [4, 15, 16]. However, this techniques is expensive and the materials used are environmentally unfriendly.

Polymers are significantly cheaper than the specialised inorganic materials/techniques needed to make inorganic optical devices. Polymer processing techniques do not require UHV deposition or high temperatures. Instead, they can be solution processed at room temperature [17, 18]. However, the thickness of films, which are used to make multi-layer UV/visible photonic devices, need to be within the $\mu m \rightarrow nm$ length scale [12]. Processing polymer structures within these length scales is difficult, as using the wrong techniques will damage a sample (discussed in section 4.3). Overcoming these challenges would significantly reduce the cost of optical devices.

There have been previous attempts to make all polymer and composite polymer/in-organic material devices [19, 20, 21]. However, the motivation for this research was to prepare functioning optical mirrors which were ‘all polymer’. These samples were prepared from cheap, readily available polymers, which could be easily processed.

Distributed Bragg reflectors (DBRs) were prepared with reflection bands in the UV/visible wavelength (between $450nm$ and $650nm$) which are useful for optical filters [1, 2] (discussed in section 4.3 and chapters 5 and 6). Samples were also prepared with reflection bands in the infra-red wavelength range which is useful for telecommunications [10] (discussed in chapter 7). For example, optical fibre telecommunication cables operate between wavelengths of $1.3\mu m$ and $1.6\mu m$ [22]. The polymers used to prepare these samples (which is discussed in section 4.3) were non-absorbing and did not degrade in either the UV/visible or infra-red wavelengths tested. Although not yet tested, these DBRs could be used to make new sensors by adding ‘functional’ components which change the refractive indices and/or structure of the sample [3]. DBRs can also be used to make resonant cavities which will improve the efficiency of displays [4, 5], lasers [6, 7] and solar cells [8, 9] etc.

Applications would benefit from the ability to control the optical properties of a device. The following are examples of optical properties which could be controlled;

- Magnitude of the reflectance (discussed in sections 5.4 and 7.3.2 and chapter 6).
- Position of the reflection bands with respect to wave-length (discussed in sections 5.2 and 7.3.1).
- Bandwidth of the reflection bands (discussed in section 5.6).
- Angular dependence of the reflection band wavelength (Discussed in section 5.5 and chapter 10)

Analysis of nano-scale polymer structures is not limited to research for optical devices. Complex polymer nano-structures are currently being investigated for making drug delivery systems [23, 24], chemical sensors [25] and polymer electronics [5, 26, 27]. Hence, any investigation into measuring the properties of polymer multi-layer structures is beneficial to these other emerging research areas. The polymer-polymer interface widths between deposited polymer layers (using solution processing) were measured using neutron reflectivity (discussed in chapter 8). Also, the multi-layer structure was investigated using time of flight secondary ion mass spectrometry (TOF-SIMS) (discussed in chapter 9). These results enabled the properties of the polymer samples to be measured, discussed and compared with optical spectra which were measured from polymer multi-layers.

Chapter 2

Literature review

2.1 Introduction

A brief history, theory, examples and application of photonic structures are discussed in this chapter. Photonic structures are being researched due to their interesting optical properties, which could be used in applications such as optical filters [1, 2], sensors [3], displays [4, 5], lasers [6, 7] and solar cells [8, 9]. The research in this thesis focused specifically on distributed Bragg reflectors (DBRs) which are a type of photonic structure [10, 12, 13].

2.2 Structural colour and Bragg reflection

Interesting optical properties (for light of wavelength λ) occur when the refractive index of a material spatially varies on length scales which are of the order of the wavelength of light λ . This is known as a photonic structure, as the optical response of the sample is due to spatial variations of the refractive index and not pigmentation [10, 12, 13]. There are many different types of structures which produce different optical effects. These include [12];

- Reflection.
- Refraction.
- Light scattering.
- Diffraction.
- Thin film interference.



Figure 2.1: The wide range of reflected colours in soap bubbles are due to thin film interference [10, 12]. Patches of white are due to light being scattered by the ‘foamy’ regions of the soap bubbles [10, 12].

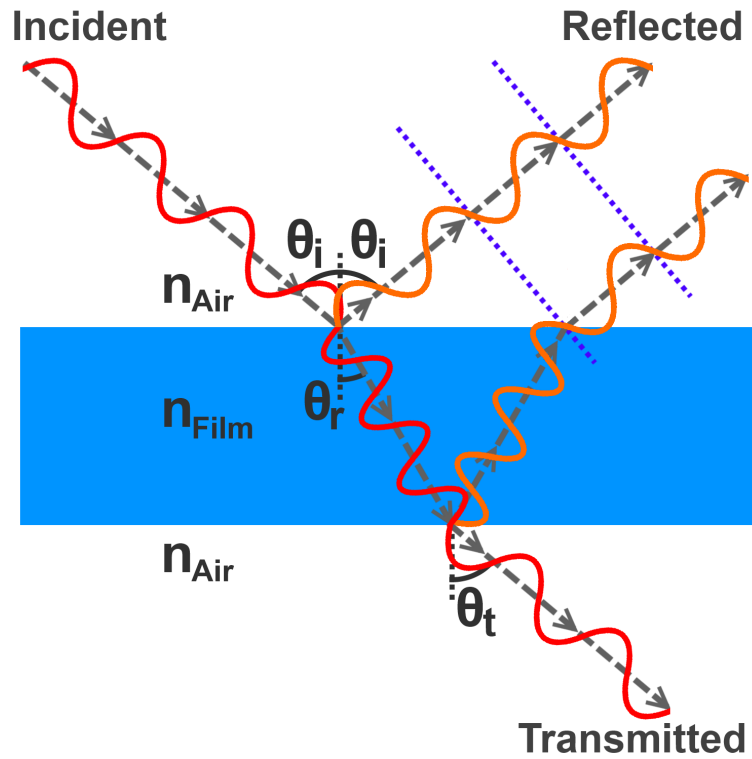


Figure 2.2: A diagram of thin film interference where n_{Air} = refractive index of air, n_{Film} = refractive index of film (in this case $n_{\text{Film}} > n_{\text{Air}}$), θ_i = angle of incidence and reflection, θ_r = angle of refraction and θ_t = angle of transmission (which in this case is equal to θ_i). The incident light is reflected off both the top and bottom interfaces, which then undergo interference [28].

- Photonic crystals.

This research focused mostly on photonic crystals (specifically DBRs). The optical properties of these samples are best introduced by considering the simplest example of structural colour, thin film interference. Some of the most common examples of thin film interference are soap bubbles (shown in figure 2.1) and a oil film spread across water. Both examples are from materials which have weak or no pigmentation, but display a variety of colours when reduced to thin films [10,12]. Figure 2.2 is a diagram of reflected light undergoing thin film interference. Incident light is reflected from both the top (air→film) and bottom (film→air) interfaces of the thin film. The film preferentially reflects wavelengths of light which constructively interfere. This is controlled by the separation of the interfaces in the film [10,11]. The speed a light wave travelling through a material is controlled by the refractive index of the material. Light transmits slower through media with a higher refractive index [10],

$$v_i = c/n_i, \tag{2.1}$$

Where v = velocity of light in medium i , c = speed of light in a vacuum and n_i = refractive index of medium i

The frequency of the light is unchanged, but the wavelength decreases if the refractive index is greater [10],

$$\lambda_i = \lambda_0/n_i, \tag{2.2}$$

Where λ_i = wavelength in medium i and λ_0 = wavelength in a vacuum.

The optical path length of light travelling through a film is calculated by [10],

$$\text{OPL} = d_{\text{Film}}n_{\text{Film}}/\cos(\theta_{\text{Film}}) \tag{2.3}$$

Where, d_{Film} = film thickness, n_{Film} = refractive index of the film, θ_{Film} = angle of transmission through the film.

Decreasing the film thickness d_{Film} , or the refractive index n_{Film} will decrease the optical path length. Doing this to a thin film will *blue-shift* the reflected spectra, since smaller wavelengths are required for the reflected waves to constructively interfere. The wavelength of light reflected by a Bragg reflector, when measured at normal incidence, is calculated by [12];

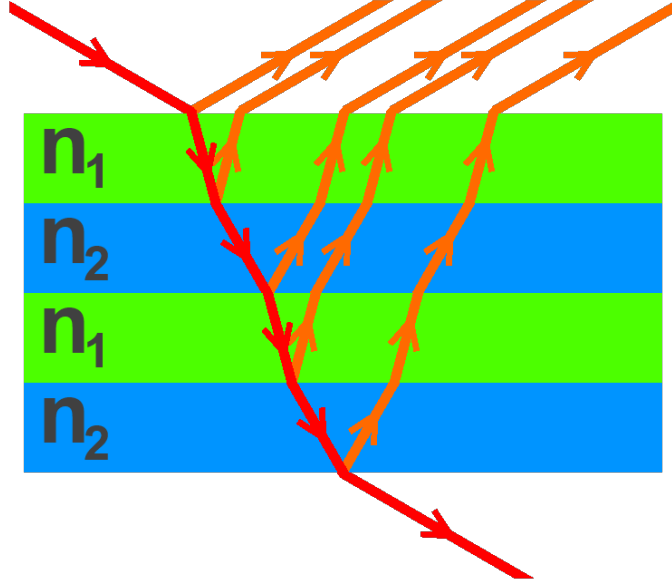


Figure 2.3: A ray diagram of a multi-layer structure with alternating refractive indices n_1 and n_2 (where $n_1 > n_2$). An incident wave transmits through the material and partially reflects off each interface where the refractive index changes. Each interface always causes the light to partially reflect and transmit. This includes any rays which have previously been partially transmitted/reflected by a interface.

$$\lambda_M = \frac{2}{M} [d_1 n_1(\lambda) + d_2 n_2(\lambda)], \quad (2.4)$$

Where n_1 and n_2 are the refractive indices of media ‘1’ and ‘2’ respectively, d_1 and d_2 are thickness of alternating polymer layers ‘1’ and ‘2’ respectively and $M = 1, 2, 3, \dots$, etc.

Multiple reflection peaks may be reflected by the same sample. Reflection peaks which correspond to the longest wavelength are calculated when $M = 1$. Increasing M decreases the wavelength of the reflection peak being measured.

If the optical path length of the two alternating layers are the same ($d_1 n_1 = d_2 n_2$), then some reflection peaks disappear because of de-constructive interference (which is discussed further in section 6.3). The wavelengths of the reflection bands, when $d_1 n_1 = d_2 n_2$, are calculated by,

$$\lambda_M = \frac{2}{2M - 1} [d_1 n_1(\lambda) + d_2 n_2(\lambda)], \quad (2.5)$$

Where $M = 1, 2, 3, \dots$, etc.

Equations 2.4 and 2.5 cannot calculate the wavelength of a reflection peak when the incident light is not normal to the sample surface ($\theta_i \neq 0$). Instead, the wavelength of the reflection peaks are calculated using a modified optical transfer matrix method (see chapter 3).

Moving the incident beam away from the surface normal ($\theta_i \neq 0$) results in the wavelength of the reflected beam blue-shifting. This initially appears to be counter-intuitive, as the optical path length of the beam within the sample is increased when $\theta_i > 0$. However, only wavelengths which constructively interfere are reflected by the sample [10] (shown in figure 2.2). This is discussed further in section 5.5. Both the variation in film thickness and the different angles of incidence are why, examples such as, soap bubbles show a variety of colours [11, 13].

The properties of light can be controlled further by using more complex photonic structures than single layer films. This includes distributed Bragg reflectors (DBRs), which were the main focus of the research in this thesis. DBRs are prepared by depositing an alternating stack of thin films with differing refractive indices to make a multi-layer (shown in figure 2.3). This type of structure leads to optical confinement in one dimension, which results in the sample having interesting optical properties [10, 12] (discussed further in chapter 3). There are many applications which would benefit from the use and integration of DBRs (which is discussed in section 2.5).

Distributed Bragg reflectors inherited their name from Sir William Lawrence Bragg [10, 11]. He developed x-ray crystallography, which measures the properties of atomic lattices by their diffraction properties [11]. The 1D photonic structures in this thesis are similar to crystal lattices, but are made of alternating layers with differing refractive indices (shown in figure 2.3) instead of an atomic lattice. The separation between the interfaces is $\sim \lambda$. This is comparable to when x-rays are used to measure atomic lattice spacings [29].

There is an interface at the point where the refractive index changes between two layers, which causes incident light to partially reflect or transmit [10, 11]. Figure 2.3 is a diagram of a DBR which is a multi-layer sample made by routinely stacking two alternating materials of differing refractive indices. The diagram shows an incident wave as it passes through the sample. At each interface there is a partial reflection and transmission (which transmits through to the next interface). Light which has previously transmitted or reflected will also undergo the same process if it encounters another interface. This continues

to occurs, at each interface, until it is reflected or transmitted out from the entire sample [10, 11, 12, 13, 14]. Layers are deposited so the spacing between interfaces is of the order the wavelength of the reflected light λ . However, the photonic structure only reflects rays which constructively interfere. The other wavelengths are not partially reflected, but instead transmit through the sample. This creates a *photonic band-gap*, where only wavelengths within the band-gap are reflected [10, 11, 12, 13, 14].

The magnitude of the partial reflection is greater when the contrast of the refractive index between the two materials is larger [10, 11, 12, 13]. Increasing/decreasing the optical contrast between layers respectively increases/decreases the total reflectance. This is because the total reflectance is due to the constructive interference of the partial reflections. Increasing the refractive index contrast increases the magnitude of the partial reflections.

2.3 Structural colour in nature

Photonic structures which occur in nature are discussed in this section to provide historical context and insight into the development of man-made equivalents. Nature has been using structural colour ever since the *Cambrian explosion*. This period of time (approximately 515 million years ago) was when life was at its most diverse [12]. Fish scales, peacock feathers, beetle shells and butterfly wings are all examples of photonic structures in nature [12, 31]. The bright colours from these examples are not due to pigmentation. Instead, they are due to the structural arrangement of materials on the surface [12, 31]. Photonic structures offer a wider range of capability to control light when compared to pigmentation. Nature uses structural colour (from photonic structures) to lure in prey, confuse predators, and/or attract a mate [12, 31].

Structural colour was first discovered during the investigation of a peacock feather by Hook [10, 31]. Another commonly studied and described examples of structural colour in nature, specifically Bragg reflection, are butterfly wings (shown in figure 2.4 caption [a]). Electron microscopy has enabled researchers to study these types of samples with greater detail (such as Anderson and Richards in 1942) [30, 31, 32]. The captions [b] and [c] in figure 2.4 respectively show cross section images of *Morpho rhetenor* and *Morpho didius* butterfly wings. These images were taken by Pete Vukusic and J. Roy Sambles at the School of Physics, University of Exeter, UK. Both of the cross-section images

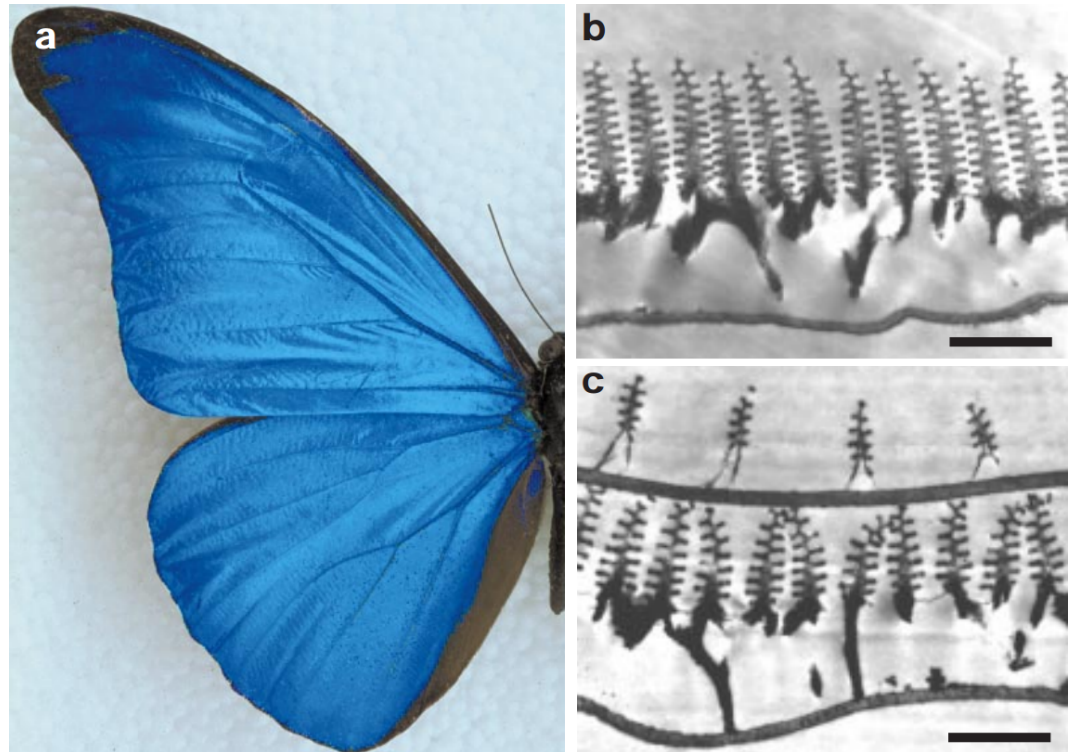


Figure 2.4: This image was captured by Pete Vukusic and J. Roy Sambles at the School of Physics, University of Exeter, UK [30]. It is reproduced in this thesis with permission from the Nature publishing group. [a] A photographic image of the intense blue colour reflected from a *Morpho rhetenor* butterfly wing. [b] A transmission electron microscope (TEM) image of a *Morpho rhetenor* butterfly wing cross section. The multi-layer 'ridge' features function as a distributed Bragg reflector [30]. [c] A (TEM) image of a *Morpho didius* butterfly wing cross section. The secondary layer of ridges diffract the light which diffuses the reflected light [30]. The scale bars in figures [b] and [c] are $1.8\mu\text{m}$ and $1.3\mu\text{m}$ respectively.

were measured using transmission electron microscopy (TEM). They reveal the multi-layer structures of the butterfly wings [30]. Both of the wings are covered in fibrous structures, which have well defined spatially separated scales along their length. The intense reflection of the butterfly wing is due to the separation of the scales being comparable to the wavelength of blue light [12, 30]. The multi-layer in figure 2.3 is an approximation of the butterfly wing structure. It would be difficult to fabricate the same structure that Morpho butterflies use for Bragg reflection in the UV/visible wavelengths. The closest attempt was by 3D printing the butterfly wing structure on the centimetre length scale. This was shown to function as a Bragg reflector at microwave wavelengths [33].

In the early 20th century, Lord Rayleigh successfully modelled the properties of multi-layer dielectric films using electromagnetic theory [12]. He supported his argument by observing the iridescence (variation in reflected colour with respect to angle of incidence) of natural examples of structural colour (beetle shells and butterfly wings). These optical effects do not occur when colour is caused by pigmentation. This clarified that the interesting optical properties of the biological samples were due to the structural arrangement of material (rather than pigmentation). Furthermore, the mathematical theory showed that these properties could be replicated by processing dielectric materials into similar multi-layer structures [12].

2.4 Man-made photonic structures

Photonic structures are usually made using inorganic materials (such as SiO_2 , TiO_2 and ZrO_2 [15]) as it is possible to prepare DBRs with a large refractive index contrast between layers (typically $\Delta n \approx 0.5$ [4]). A larger optical contrast means that fewer layers are required to make a sample with a high reflectance (this is discussed in chapter 3). Ultra high vacuum (UHV) deposition is commonly used to prepare multi-layer dielectric structures [4, 15]. These multi-layer structures are prepared by controlled deposition of each layer in sequence. This is a well understood technique since it is used in a variety of other applications such as micro-electronics [4, 15]. However, the inorganic materials used in these DBRs using UHV deposition are expensive. Furthermore, the materials need to be carefully selected since each layer is a thin dielectric crystal. Mismatches in the lattice spacing cause strain between the layers. The strain can be sufficient to overcome the stability of the sample and cause defects/cracks to appear in

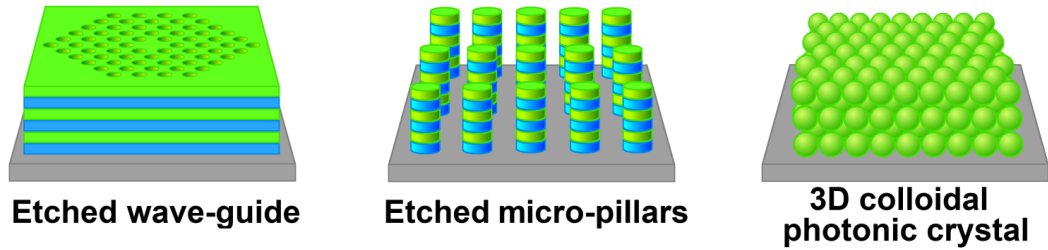


Figure 2.5: Diagram of more complex photonic structures which could be used for potential applications. The *etched optical trap* and *etched micro-pillars* are fabricated from a 1D photonic crystal. Etched wave-guides are made by milling a series of periodic holes into the multi-layer and/or nano-imprinting [16,36]. The central hole is left intact to confine photons within a small region of the structure. Etched wave-guides and micro-pillars are both examples of 2D photonic crystals. The *3D colloidal photonic crystal* is a self assembled structure which uses a high refractive index colloid and air as the alternating materials [37,38].

the structure [34].

Recently, there have been advancements in making hybrid devices which use a combination of both polymer and inorganic materials [35]. Using relatively cheap polymers can reduce the cost these mirrors/devices. However, the costs are not significantly reduced and the processing procedures are relatively complex [35]. Recently, all-polymer DBRs have been attempted [6, 20]. Polymer materials and thin film polymer processing techniques are significantly cheaper than their inorganic alternatives. However, processing polymer films into multi-layers presents its own challenges. For example, the solvent which is used to solution process one type of polymer may dissolve previously deposited polymer films. The optical contrast between polymers is also significantly less than what is available with in-organic materials. However, this can be compensated for by adding more layers to the photonic structure (discussed in section 5.4). These challenges are outweighed by their significant reduction in cost.

There has been significant research into patterning multi-layer photonic structures to create 2D photonic crystals, wave-guides and optical traps [16] (discussed further in section 2.5 and illustrated in figure 2.5). The multi-layer is etched using an ion beam and/or lithography [36]. Both techniques are well established since they are extensively used in the semi-conductor industry. The most common etching patterns used are micro-pillar or a lattice of holes, which have well defined spatial distributions [16]. Etching these structures is often time consuming and therefore expensive. These techniques are not suitable

for large scale optical devices because of the patterning areas needed. Instead, these techniques are only applied to small-scale integrated devices, such as optical ‘lab on a chip’ sensors [39] and small telecommunications devices [16].

Fabrication of 3D photonic structures is significantly more challenging than 1D and 2D structures. Early investigations used large scale models ($m \rightarrow cm$ length scales) which were analysed in the microwaves [40]. However, photonic structures which have UV/visible optical properties must have features which are tens of nano-metres in scale [12]. Research into these structures has been limited because of the challenges associated with preparing samples on such a small scale. The ‘*woodpile*’ array is one of the most common techniques previously used to prepare 3D optical structures. It uses stacks of equally spaced strips, which are prepared by etching each layer deposited onto the sample [41]. This is impractical because of the lengthy preparation time. The most promising technique is by using self-assembly to create ordered structures (illustrated in figure 2.5). Colloids are nano-scale particles which are suspended in a solution. These particles self assemble into 3D periodic structures when carefully dried [37, 38]. The spatial separation of the interfaces is dependent upon the size of the colloid particles. This offers limited control, as changing the optical properties of a sample requires different materials to be used [16, 37, 38].

Only 1D photonic structures were prepared in this thesis. However, it is worth keeping more complex photonic structures in mind for future developments and applications.

2.5 Optical devices which make use of photonic structure

Photonic structures have reflection peaks over a narrow range of wavelengths (bandwidth). This is also known as the *photonic band-gap* as reflected light is removed in the transmission spectra of the samples. The reflectance of the sample depends on the thickness and refractive index contrast between the layers. The materials used should be non-absorbing and non-scattering so that it is possible to attain a reflectance greater than 99% [42, 43]. It is possible to control the position of reflection bands and the bandwidth (with respect to wavelength) by changing the film thickness and/or the refractive index of the layers within the sample. These properties have enabled DBRs to be used as

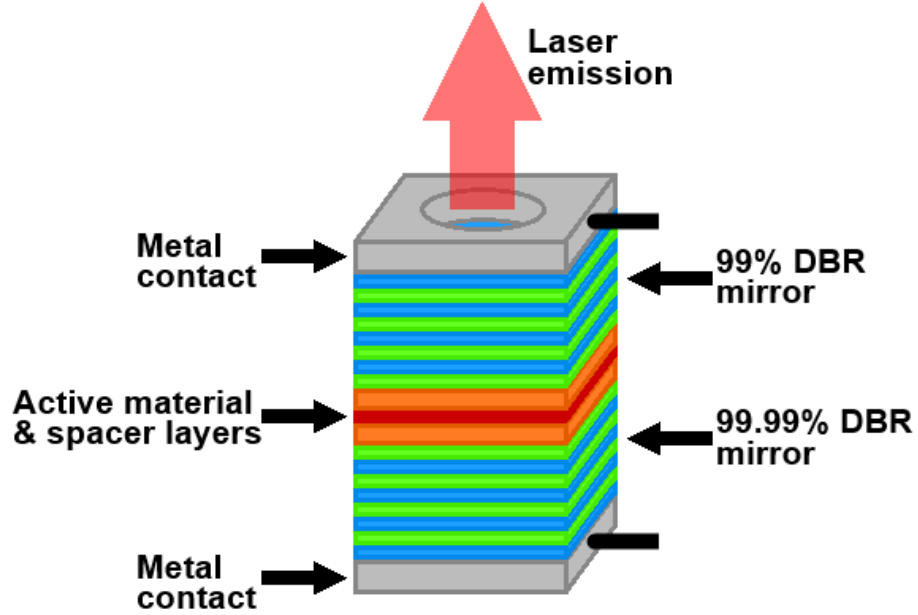


Figure 2.6: A diagram of a basic VCSEL laser design. An active/lasing material is placed between a optical cavity using two high reflecting DBR mirrors. The top mirror has a slightly lower reflectance for the laser light to emit through.

band-pass and band-stop filters for communication and sensors [1,2].

Encapsulating a medium between two high reflecting DBRs results in a photonic cavity [4]. Light within the cavity is continuously reflected in between the DBR mirrors. Constructive interference occurs when the spacing between the mirrors is multiples of $\lambda/2$. This creates a resonant cavity where the ‘active layer’ of a optical device can be placed. The DBR mirrors are tuned to the same wavelength which stimulates the active layer. This significantly reduces the density of states for the active layer. Vertical cavity surface emission lasers (VCSELs, which is shown in figure 2.6) depend on resonant cavities to function by optically pumping the lasing medium [11, 43, 44]. The efficiency of other optical devices can also be improved by placing them in a resonant cavity layer (such as LEDs [4, 45] and solar cells [8]).

Reducing the number of dimensions of a photonic structure further reduces the number of energy states. This is because the propagation of the photon is confined within a reduced number of dimensions. This can further improve the efficiency of optical devices (such as displays, solar cells) [46]. The optical properties of these devices are also more sensitive to changes in film thickness and/or refractive index. This has lead towards research into using 2D photonic crystals as chemical and biological sensors [39].

2.6 Polymer multi-layer devices

Polymers are long molecules which are made from smaller molecular subunits (monomers), which are linked together by covalent bonds. Biological structures such as proteins and DNA are examples of polymers which occur in nature [17, 18]. Polystyrene (PS) and Polyvinylpyrrolidone (PVP) are examples of synthetic polymers [18, 47, 48]. Most polymers are based on long chains of carbon. The simplest polymer structures have a main chain of carbon, which have two covalently bonded hydrogen atoms per carbon atom. However, other elements such as oxygen, nitrogen, fluorine and silicon can also be part of a polymer structure. Furthermore, the arrangement of atoms can also include smaller chains and/or loops of atoms which are side-groups to the backbone of the monomer chain. Differences in the composition and arrangement of atoms in a polymer will change its chemical properties [18, 47, 49]. Polymers can be dissolved using solvents to make a solution. However, this depends on the chemical properties of the polymer and the solvent [18, 47, 49]. For example, polystyrene is hydrophobic (repels water) and will not dissolve in water. On the other hand, polyvinylpyrrolidone is hydrophilic (attracted to water) and does dissolve in water.

The physical properties of a polymers should also be considered when using them in applications. There are many characteristics which are universal to the physical properties of polymers. This is due to them being long, ‘string-like’, molecular chains. For example, changes in the molecular length of a polymer will change the level of entanglement in the sample. Entanglement result in polymer solutions having viscoelastic properties (both viscous and elastic characteristics) [18, 47]. Cross-linking (physically interconnecting long polymer chains) a polymer melt (above its glass transition temperature T_g) gives it ‘rubbery’ properties. The polymer chains in the rubber will unbundle when the material is stretched. This lowers the entropy of the polymers in the sample. However, the polymer chains will fluctuate back into a bundle (a higher entropy state) if the force stretching the polymer is removed. This is known as *entropic elasticity*. This entropic elasticity returns the rubber sample back to its original shape [18, 47].

Polymer materials are readily available and are therefore cheap. Furthermore, polymers can be readily processed. For example, solution processing (handling solvents when they are suspended in a solvent) can be used to make

thin films at room temperature [17]. There are a broad range of diverse properties from different polymers. The specific properties of a certain polymer can be used to make useful materials and devices for applications [18,47]. Organic materials are also relatively cheap and specialised molecules can often be mass produced [27].

There is a growing demand to make devices which are easy to process, cheap and efficient. Devices made from polymer materials are an emerging technology and gaining research momentum [9,17,27]. This is because polymers are cheap and can be processed without the need for UHV deposition and/or high temperatures. Polymers can be processed using a variety of techniques such as solution processing (spin-coating and dip-coating), spraying and printing [9].

Nano-structures are utilised to manipulate light (for example) at the smallest length-scales possible. Interesting optical effects occur when you control the nano-structure of a material [6,20]. Nature has already demonstrated how efficient systems can be made from organic materials at the nano-scale [17,20]. There are many challenges which must be investigated and overcome to manufacture devices which are made from nano-scale polymer structures.

Polymers nano-structures are also being used in other applications such as;

- *Drug delivery systems*: The permeability, solubility and structure of polymer materials is being used for controlled drug release and prolong the products shelf-life [23].
- *Polymer electronics*: Functional polymer materials are currently being researched to create cheap, efficient and flexible devices. These devices are prepared by depositing layers of different organic materials on top of one another [26,27]. Polymer electronics and devices can also be stacked multiple devices onto the same substrate to save space [50].

These devices are relevant to the research in this thesis, as they all used layered deposition of polymer materials. Researching a relatively simple polymer multi-layer (like the polymer DBRs) may contribute towards the analysis of other devices which use structured polymer materials.

Chapter 3

The physics of reflection from films and multi-layers

3.1 Introduction

This chapter discusses the physics of reflection from films and multi-layers. The optical properties of single layer and multi-layer samples were measured throughout this thesis. A modified optical transfer matrix method was used to model the reflection spectra in the UV/visible and infra-red wavelengths. Ellipsometry data was also analysed using this technique (discussed in section 4.4). Measurements from neutron reflectivity were also modelled using transfer matrix methods (discussed in section 4.7). The model uses a series of boundary and transmission matrices, which describe the reflectance at interfaces and transmission through the individual layers of the DBR [11, 51, 52]. This technique uses a series of different steps/calculations which are discussed within this chapter.

3.2 Fresnel reflection and transmission coefficients

Figure 3.1 illustrates a light ray as it is incident on a sample with layers of differing refractive indices. There is an interface between each layer because of the changes in refractive index. This causes incident light to partially reflect and transmit. The angle of incidence θ_i is equal to the angle of reflection θ_r , as the reflection is specular. The angle of refraction is calculated according to Snell's

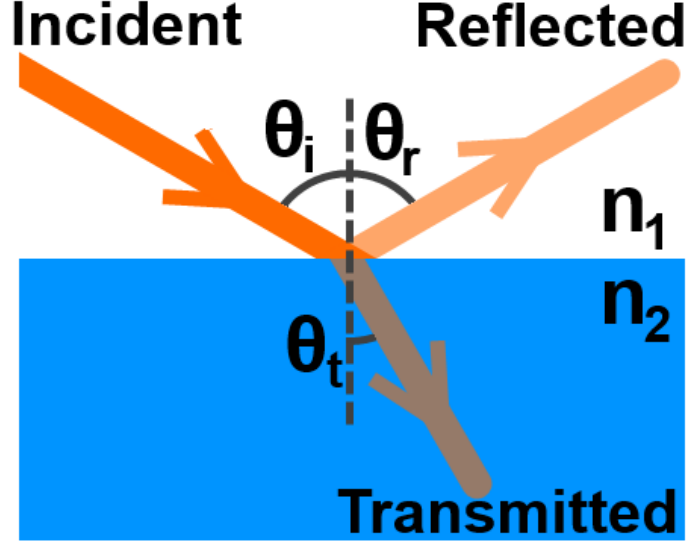


Figure 3.1: Light is partially reflected and transmitted by a dielectric interface, which is created by a change refractive index between one medium (n_1) and another (n_2). The angle of the reflected light θ_r is equal to the angle of incidence θ_i (specular reflection) [10]. Snell's law calculates the angle of refraction [10].

law of refraction [10].

The magnitude of the transmitted and reflected light is different for polarisations which are parallel to perpendicular (p and s respectively) to the plane of incidence [10]. The electric field of the two polarisations is calculated separately for both the partial reflection and transmission. The *Fresnel coefficients* give the p and s reflection coefficients as [10];

$$r_s = \frac{n_1 \cos(\theta_i) - n_2 \cos(\theta_t)}{n_1 \cos(\theta_i) + n_2 \cos(\theta_t)}, \quad (3.1)$$

$$r_p = \frac{n_2 \cos(\theta_i) - n_1 \cos(\theta_t)}{n_1 \cos(\theta_t) + n_2 \cos(\theta_i)}, \quad (3.2)$$

$$t_s = \frac{2n_1 \cos(\theta_i)}{n_1 \cos(\theta_i) + n_2 \cos(\theta_t)}, \quad (3.3)$$

$$t_p = \frac{2n_1 \cos(\theta_i)}{n_1 \cos(\theta_t) + n_2 \cos(\theta_i)}. \quad (3.4)$$

Where r_s and r_p are the reflection coefficients for the s and p polarisations respectively. Likewise, t_s and t_p are the transmission coefficients for the s and p polarisations respectively. n_1 and n_2 are the refractive indices of the first and second media respectively. θ_i = angle of incidence and θ_t = angle of refraction

which were illustrated in figure 3.1.

The reflectance R and transmittance T are calculated by the fraction of the beams reflected or transmitted power respectively. For a beam with polarisation s and passing through a single interface the reflectance and transmittance are calculated respectively by [10];

$$R_s = |r_s|^2, \quad (3.5)$$

and,

$$T_s = |t_s|^2 \frac{n_2 \cos(\theta_t)}{n_1 \cos(\theta_i)}. \quad (3.6)$$

Likewise, $R_p = |r_p|^2$ and $T_p = |t_p|^2 \frac{n_2 \cos(\theta_t)}{n_1 \cos(\theta_i)}$ calculate the reflectance and transmittance of a single interface for p polarisation. $n_2 \cos(\theta_t)/n_1 \cos(\theta_i)$ in equation 3.6 was used to correct for when $\theta_i \neq \theta_r \neq 0$. Also, n_2 changes the speed of the transmitted light with respect to the incident light in n_1 . Both change the flux [$Jm^{-2}s^{-1}$] of the transmitted beam and hence the transmittance [10, 11].

A DBR consists of many dielectric layers which are stacked to make multiple dielectric interfaces. A partial reflection and transmission occurs from the first interface as the beam passes through. The second interface partially reflects and transmits light which was transmitted by the first interface. This process repeats at each interface in the sample. All of the partially reflected light rays from each interface interfere and contribute towards the total reflectance of the sample. However, only light from select wavelengths are reflected by the sample, whilst the remaining wavelengths are transmitted through the sample. This is controlled by the spatial separation of the interfaces and the refractive indices of the materials [10, 11].

The optical properties of a multi-layer sample cannot be adequately modelled by using only the Fresnel equations. This is due to the spatial separation between the interfaces in the multi-layer. The medium and separation between each interface must be considered because the phase of the the light changes as it travels through the sample [11, 52].

A modified optical transfer matrix method was used to calculate the optical properties of DBR samples [11, 12, 52]. Each interface was characterised by a 2×2 *boundary matrix*. Likewise, changes in the phase of the travelling light between each interface was modelled by a 2×2 *transmission matrix*. Each

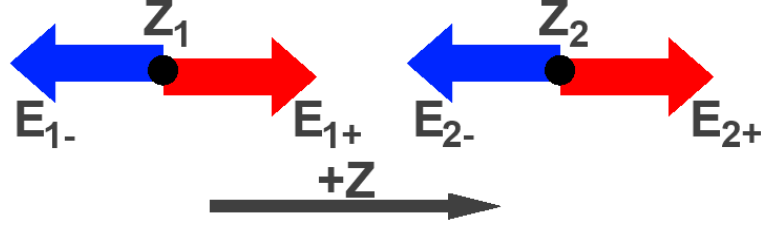


Figure 3.2: This diagram is as a visual aid for the notation used in the optical transfer matrix method.

matrix was multiplied together in a sequence to result in a final 2×2 matrix which characterises the entire sample [13, 51]. This is derived in the following sections.

3.3 Boundary matrix

Figure 3.2 is a visual aid to assist with the assumptions when modelling a travelling wave. We consider light at two points z_1 and z_2 . The properties of the wave are with respect to only one dimension z . This model considers the electric field of a wave when it is travelling in either positive $+z$ or negative $-z$ direction at points z_1 and z_2 [13, 52, 53]. The magnitudes of the electric fields E_{1+} and E_{2+} are for waves moving in the $+z$ direction at points z_1 and z_2 respectively. Likewise, E_{1-} and E_{2-} are the magnitudes of the electric fields of waves moving in the $-z$ direction at points z_1 and z_2 respectively [13, 51].

The electric field of the waves in the z_1 media with respect to the waves in the z_2 media are initially considered. E_{1-} and E_{1+} are calculated separately and it is assumed that their magnitudes are can be written in terms of E_{2+} and E_{2-} . Hence [13, 51],

$$E_{1+} = \alpha_{11}E_{2+} + \alpha_{12}E_{2-}, \quad (3.7)$$

and,

$$E_{1-} = \alpha_{21}E_{2+} + \alpha_{22}E_{2-}. \quad (3.8)$$

Where α_{11} , α_{12} , α_{21} and α_{22} are coefficients which are determined later.

Equations 3.7 and 3.8 can be written in the following [13, 51],

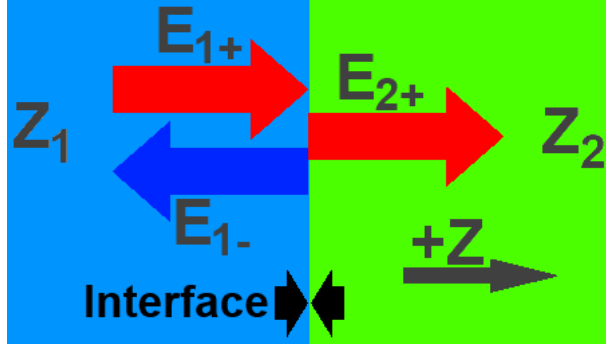


Figure 3.3: The wave (represented by the magnitude of its electric field E_{1-}) is partially reflected by the interface between the two media z_1 and z_2 . E_{2+} is the magnitude of the electric field for the transmitted wave. E_{2-} is not shown as there is no interface for the transmitted wave to be reflect back. No light travels in the $-z$ direction in the z_2 medium.

$$\begin{pmatrix} E_{1+} \\ E_{1-} \end{pmatrix} = \begin{pmatrix} \alpha_{11} & \alpha_{12} \\ \alpha_{21} & \alpha_{22} \end{pmatrix} \begin{pmatrix} E_{2+} \\ E_{2-} \end{pmatrix} = \mathbf{B}_{12} \begin{pmatrix} E_{2+} \\ E_{2-} \end{pmatrix}. \quad (3.9)$$

The boundary matrix \mathbf{B} is calculated by assuming there is a interface between z_1 and z_2 (shown in figure 3.3). This creates a boundary for the light to partially transmit and reflect. There are no other interfaces as both of the media are *semi-infinite*. Furthermore, both of the media are assumed to be homogeneous and non-absorbing, so light does not scatter or get absorbed [13,51].

The light was initially considered to be propagating from the z_1 medium into the positive z -direction only. E_{1+} is the electric field of a wave propagating towards medium z_2 . An electric field of a reflected wave E_{1-} is created by partially reflecting off the interface between z_1 and z_2 . The wave is also partially transmitted at the interface and has an electric field E_{2+} . There is no wave travelling in the $-z$ direction in region z_2 ($E_{2-} = 0$). This is due to the semi-infinite approximation which assumes there are no interfaces to reflect the light from E_{2+} back. Equations 3.7 and 3.8 are reduced to [13, 51];

$$E_{1+} = \alpha_{11}E_{2+}, \quad (3.10)$$

and,

$$E_{1-} = \alpha_{21}E_{2+}. \quad (3.11)$$

The transmission and reflection coefficients of light respectively are [10];

$$t = \frac{E_t}{E_i}, \quad (3.12)$$

and,

$$r = \frac{E_r}{E_i}. \quad (3.13)$$

Where E_i = electric field in the incident wave, E_r = electric field in the reflected wave and E_t = electric field in the transmitted wave.

Equation 3.10 is compared with equation 3.12 to determine the coefficient α_{11} ,

$$\begin{aligned} t_{12} &= \frac{E_{2+}}{E_{1+}} = \frac{1}{\alpha_{11}}, \\ \alpha_{11} &= \frac{1}{t_{12}}. \end{aligned} \quad (3.14)$$

Where t_{12} = transmission coefficient for a boundary from medium 1 \rightarrow 2.

The α_{21} coefficient is calculated by dividing 3.11 by 3.10 such that,

$$\begin{aligned} r_{21} = \frac{E_{1-}}{E_{1+}} &= \alpha_{21} \frac{E_{2+}}{E_{1+}} = \frac{\alpha_{21}}{\alpha_{11}} = \alpha_{21} t_{21}, \\ \alpha_{21} &= \frac{r_{12}}{t_{12}}. \end{aligned} \quad (3.15)$$

Where r_{12} = reflection coefficient for a boundary from medium 1 \rightarrow 2.

The α_{12} and α_{22} coefficients were calculated by reversing the problem. Whereby, the incident light is from region z_2 and propagates into the $-z$ direction. Hence, via a lengthy calculation;

$$\alpha_{12} = \frac{r_{12}}{t_{12}}, \quad (3.16)$$

and,

$$\alpha_{22} = \frac{1}{t_{12}}, \quad (3.17)$$

Substituting these coefficients back into equation 3.9 results in the *boundary matrix*. This 2×2 matrix calculates the reflection/refraction properties of the boundary at each interface [13, 51, 52]. The boundary matrix for the interface

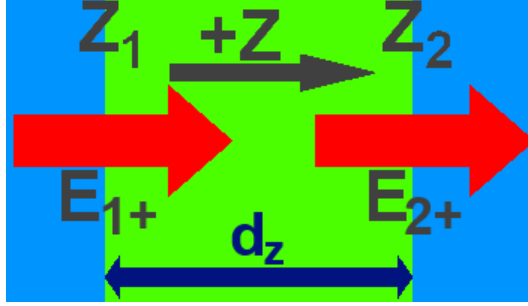


Figure 3.4: A light wave passes through the medium between z_1 and z_2 in the positive $+z$ direction. The wave is not passing through interfaces at z_1 or z_2 as this simplifies the calculation. The separation between the interfaces is d_z .

12 is written as;

$$B_{12} = \begin{pmatrix} 1/t_{12} & r_{12}/t_{12} \\ r_{12}/t_{12} & 1/t_{12} \end{pmatrix}. \quad (3.18)$$

3.4 Transmission matrix

The speed and phase of the wave changes when it is transmitted in a medium of differing refractive indices. Changing the thickness of the layer also changes the phase difference introduced between interfaces [10, 13, 51]. The diagram in figure 3.4 and the following steps are used to calculate the *transmission matrix* for each layer.

A wave is considered as it propagates through space in the $+z$ direction [10, 51],

$$E_+(z) = E_0 e^{i(\omega t - k_z z)}. \quad (3.19)$$

Where k_z is the magnitude of the wave-vector $|\underline{k}_z|$ which is expanded as, [51],

$$k_z = 2\pi n \cos(\theta_t) / \lambda. \quad (3.20)$$

Where E_0 = the maximum of the amplitude, n = refractive index of the material, θ_t angle of refracted light as it is transmitted through the material and λ = wavelength of the light.

It was assumed that the wave is only travelling in the $+z$ direction. Furthermore, z_1 is considered to be the beginning of the material and the wave is initially described by E_{1+} . The thickness of the material is defined as d_z

which is where the medium ends at z_2 . The resulting wave at the end of the material is described by E_{2+} . This is illustrated in figure 3.4. This model only considers the medium between the interfaces. The interaction between the wave and the interfaces is not considered. No waves are reflected into the negative z direction. Hence, $E_{1-} = E_{2-} = 0$ [13, 51, 52]. The wave-equation shown in 3.19 is re-written for the medium between z_1 and z_2 as;

$$E_{1+}(0) = E_0 e^{i\omega t}, \quad (3.21)$$

and

$$E_{2+}(d_z) = E_0 e^{i\omega t} e^{-ik_z d_z}. \quad (3.22)$$

Equation 3.22 is re-written as,

$$E_{2+}(d_z) = E_{1+} e^{-ik_z d_z}. \quad (3.23)$$

Like the boundary matrix problem, the transmission of the wave is considered as a 2×2 matrix [13, 51, 52]. Hence,

$$\begin{pmatrix} E_{1+} \\ E_{1-} \end{pmatrix} = \begin{pmatrix} \beta_{11} & \beta_{12} \\ \beta_{21} & \beta_{22} \end{pmatrix} \begin{pmatrix} E_{2+} \\ E_{2-} \end{pmatrix}. \quad (3.24)$$

However, $E_{1-} = E_{2-} = 0$ as the light does not travel in the $-z$ direction [13, 51]. Solving equation 3.24 results in;

$$E_{1+} = \beta_{11} E_{2+} \quad (3.25)$$

The coefficient β_{11} is re-written as,

$$\beta_{11} = \frac{E_{1+}}{E_{2+}} = e^{+ik_z d_z}. \quad (3.26)$$

The coefficient β_{21} is solved by;

$$\begin{aligned} 0 &= \beta_{21} E_{2+}, \\ \beta_{21} &= 0. \end{aligned} \quad (3.27)$$

Like the boundary matrix problem, this method was calculated for when the wave is moving in the $-z$ direction. This results in;

$$\beta_{12} = 0, \quad (3.28)$$

and,

$$\beta_{22} = e^{-ik_z d_z}. \quad (3.29)$$

The coefficients are substituted back into equation 3.24, which results in the transmission matrix,

$$\mathbb{T}(d_z) = \begin{pmatrix} e^{i\delta} & 0 \\ 0 & e^{-i\delta} \end{pmatrix}. \quad (3.30)$$

where $\delta = 2\pi n d_z \cos(\theta)/\lambda$.

Changing the thickness of a layer (d_z) will change the phase of the light at the end of the medium (d_2) [13, 51, 52]. Only reflections which are in phase will constructively interfere. Therefore, the transmission matrix contributes towards calculating the wavelength which is reflected by the DBR.

3.5 The optical matrix method

The simplicity of a single film is considered before extending this approach to model a multi-layer. Figure 3.5 illustrates a free standing thin film which has 2 interfaces (which are air-polymer and polymer-air) and a single medium for transmission (which is the film). The free standing film ‘sample’ is modelled by multiplying the boundary and transmission matrices in sequential order [13, 51, 52]. This is from left to right in the diagram. For a single free standing film [51],

$$\mathbb{M} = \mathbb{B}_{12} \mathbb{T}_2(d_z) \mathbb{B}_{23} \quad (3.31)$$

Which is expanded to;

$$\begin{aligned} \mathbb{M} &= \begin{pmatrix} 1/t_{12} & r_{12}/t_{12} \\ r_{12}/t_{12} & 1/t_{12} \end{pmatrix} \begin{pmatrix} e^{i\delta} & 0 \\ 0 & e^{-i\delta} \end{pmatrix} \begin{pmatrix} 1/t_{23} & r_{23}/t_{23} \\ r_{23}/t_{23} & 1/t_{23} \end{pmatrix} \begin{pmatrix} E_{1+} \\ E_{1-} \end{pmatrix} \\ &= \begin{pmatrix} m_{11} & m_{12} \\ m_{21} & m_{22} \end{pmatrix} \begin{pmatrix} E_{3+} \\ E_{3-} \end{pmatrix} \end{aligned} \quad (3.32)$$

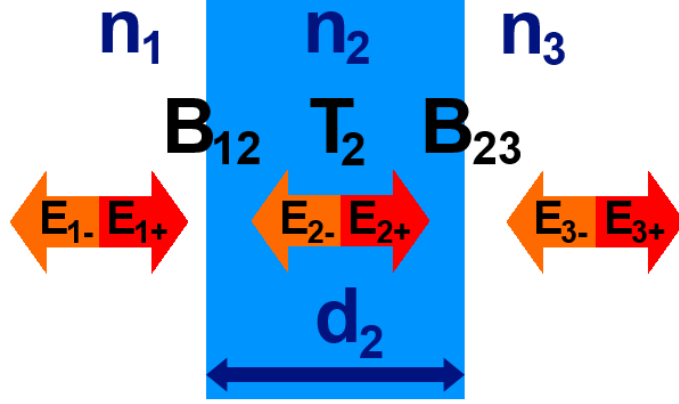


Figure 3.5: A visual interpretation of the modified optical transfer matrix method being used to model a free standing film. There are three mediums (n_1 , n_2 and n_3), two interfaces (B_{12} and B_{23}) and a transmission medium (T_2) which spans over layer thickness d_2 . The magnitude of the electric field for a wave is considered for each medium.

Where M = the matrix which represents the optical properties of the sample, B_{nm} = the boundary matrix for the appropriate interface and T_m = the transmission matrix for the appropriate medium.

Multiplying the matrices together results in a 2×2 matrix which has the corresponding elements;

$$m_{11} = \frac{r_{12}r_{23}e^{-2i\delta} + 1}{t_{12}t_{23}e^{-i\delta}}, \quad (3.33)$$

$$m_{12} = \frac{r_{12}e^{-2i\delta} + r_{23}}{t_{12}t_{23}e^{-i\delta}}, \quad (3.34)$$

$$m_{21} = \frac{r_{23}e^{-2i\delta} + r_{12}}{t_{12}t_{23}e^{-i\delta}}, \quad (3.35)$$

and,

$$m_{22} = \frac{e^{-2i\delta} + r_{12}r_{23}}{t_{12}t_{23}e^{-i\delta}}. \quad (3.36)$$

The total reflection and transmission coefficients of the whole sample are calculated by considering the magnitude of the electric fields in the first and final region after passing through the tri-layer [13, 51, 52]. B_{23} is the final interface of the tri-layer and no light travels in the negative direction in the final medium ($E_{3-} = 0$). E_{1+} and E_{1-} are solved using equation 3.31;

$$E_{1+} = m_{11}E_{3+}, \quad (3.37)$$

and,

$$E_{1-} = m_{21}E_{3+}, \quad (3.38)$$

The total reflection for the sample is calculated by substituting these two equations into the reflection coefficient [10, 13, 51, 52],

$$r_{Total} = \frac{E_{1-}}{E_{1+}} = \frac{m_{21}}{m_{11}}. \quad (3.39)$$

Substituting in the coefficients from equations 3.33 and 3.35 results in,

$$r_{Total} = \frac{r_{12} + r_{23}e^{-2i\delta}}{1 + r_{12}r_{23}e^{-2i\delta}}. \quad (3.40)$$

This is also a well known formula for the reflection coefficient of a free standing thin film [10, 13]. The total transmission coefficient t_{Total} of the sample is calculated by considering it as the ratio of transmitted light with respect to the incident light (E_{3+}/E_{1+}) [10, 13, 51, 52]. Comparing this with equation 3.37 and substituting in the coefficient from equation 3.33 results in;

$$\begin{aligned} t_{Total} &= \frac{E_{3+}}{E_{1+}} \\ &= \frac{1}{m_{11}} \\ &= \frac{t_{12}t_{23}e^{-i\delta}}{1 + r_{12}r_{23}e^{-2i\delta}}. \end{aligned} \quad (3.41)$$

3.6 Application to multi-layers

The modified matrix method technique can calculate the optical properties of multi-layers, since the 2×2 matrix with ‘ m ’ coefficients in equation 3.31 can be extended [13, 51, 52]. More layers are included by multiplying more boundary and transmission matrices in sequence. Hence, a sample of N layers is calculated by;

$$\mathbf{M}_{Total} = \mathbf{M}_{1,2}\mathbf{T}_2(d_2)\mathbf{M}_{2,3}\dots\mathbf{T}_N(d_{[N+1]})\mathbf{M}_{[N+1],[N+2]} = \begin{pmatrix} m_{11} & m_{12} \\ m_{21} & m_{22} \end{pmatrix}. \quad (3.42)$$

\mathbf{M}_{Total} is a 2×2 matrix for any number of N layers [13, 51, 52]. Furthermore, the total reflection and total transmission are still calculated by $r_{Total} = m_{21}/m_{11}$ and $t_{Total} = 1/m_{11}$ respectively [13, 51, 52].

The reflectance of the sample is calculated by [10, 13, 51],

$$R = |r_{Total}|^2 = r_{Total}r_{Total}^*. \quad (3.43)$$

Where r_{Total}^* is the complex conjugate of the total reflection coefficient r_{Total} .

Likewise, the transmittance is calculated by [10, 13, 51],

$$T = |t_{Total}|^2 = t_{Total}t_{Total}^* \frac{n_2 \cos(\theta_t)}{n_1 \cos(\theta_i)}. \quad (3.44)$$

Where $n_2 \cos(\theta_t)/n_1 \cos(\theta_i)$ corrects for the change in flux of transmitted light when not at normal incidence. This was also shown in equation 3.6.

It is important to note that the matrix method should be calculated for both s and p polarisations separately [13, 51]. The total reflectance R_s and total transmittance T_s for s polarisation should be calculated using the reflection r_s and transmission t_s Fresnel coefficients (shown in equations 3.1 and 3.3 respectively). Likewise, the total reflectance R_p and total transmittance T_p for p polarisation should be calculated using the reflection r_p and transmission t_p Fresnel coefficients (shown in equations 3.2 and 3.4 respectively). This is because the magnitude of the electric field will be different for the two polarisations when they are partially transmitted and reflected from the interfaces if the angle of incidence $\theta_i \neq 0$ [10, 13, 51]. The total reflectance of the sample is the average of the total reflectance for the s and p waves [10, 13, 51],

$$R = \frac{R_s + R_p}{2}. \quad (3.45)$$

This is also the case when calculating the transmittance [10].

$$T = \frac{T_s + T_p}{2}. \quad (3.46)$$

3.7 Modelling diffuse interfaces

UV/visible spectroscopic measurements (discussed in chapter 5) showed that the reflectance of polymer DBR samples were not as large as those predicted by the optical matrix method model. Broad polymer-polymer interface widths were considered as an explanation for the loss in reflectance. Previously, the model inaccurately assumed that the interfaces were *sharp* (the transition from one medium to another is instantaneous) and broad interfacial widths were not considered. However, polymer-polymer interfaces are likely to have intrinsic roughness due to the interfacial mixing. The interface widths become diffuse and broaden by polymer-polymer intermixing [18]. Each reflection coefficient (shown in equation 3.18) was modified by a factor such that [11, 52, 54],

$$r_{int} = r \exp \left[-8 \left(\frac{\pi \sigma n_{N+1}}{\lambda} \right)^2 \right]. \quad (3.47)$$

Where σ = width of polymer-polymer interface [m], n_{N+1} = refractive index of the medium the light is passing in to.

Increasing the widths of the interfaces σ , decreases the magnitude of the reflection coefficient r for the relevant interface [54]. This is discussed in greater detail in section 5.3.1. Neutron reflectivity was later used to measure the polymer-polymer interface widths σ (discussed in chapter 8). All of the polymer-polymer interfaces were less than $1nm$.

3.8 Summary

The modified optical transfer matrix method is able to calculate the reflection properties of DBRs. Each interface is assigned a boundary matrix and the medium in each layer is assigned a transmission matrix. Diffuse polymer-polymer interface widths were also considered in these calculations. The reflection spectra of DBRs measured later in this thesis were modelled using this technique.

Ellipsometry measurements were modelled using the total reflection coefficients of the s and p polarisations (see section 4.4). These results were used to extract the refractive index and thickness of spin-cast films.

A similar transfer matrix method was also used to model the specular reflection of a neutron beam from multi-layer samples (see section 4.7). The internal structure of a sample is measured by the interference between partially reflected

neutron beams. This ‘optical method’ can be applied to neutron reflectivity due to the particle-wave duality of neutrons [55].

Chapter 4

Experimental techniques

4.1 Introduction

A brief overview of the most common experimental techniques used in this research are discussed in this chapter. This includes preparation of single layer and multi-layer samples. It also includes techniques used to measure the properties of the samples.

4.2 Spin-coating thin films

Spin-coating is a technique commonly used to cast polymer solutions into uniform thin films. The polymer solution is deposited onto a substrate which is then quickly rotated to spread and dry the solution to make a thin film. This technique is capable of producing uniform films which are $\sim 10nm$ to a few microns in thickness [56, 57, 58]. Spin-coating was used to cast single layer and also multi-layer polymer films during this research. The technique is relatively quick, does not require a ultra-high vacuum environment and sample preparation is also at room temperature.

Polymer solutions were deposited and then spin-cast onto substrates of either freshly cleaved silicon wafers or glass slides. The glass slides were cleaned prior to use by sonicating them in methanol for several hours. The spin-coating process is illustrated in figure 4.1).

Spin-cast films may require annealing to remove any residual solvent. Films are annealed by heating them above their glass transition temperature (T_g). The solvent more readily leaves the polymer film during this rubber-like state when it is heated above it's T_g [18].

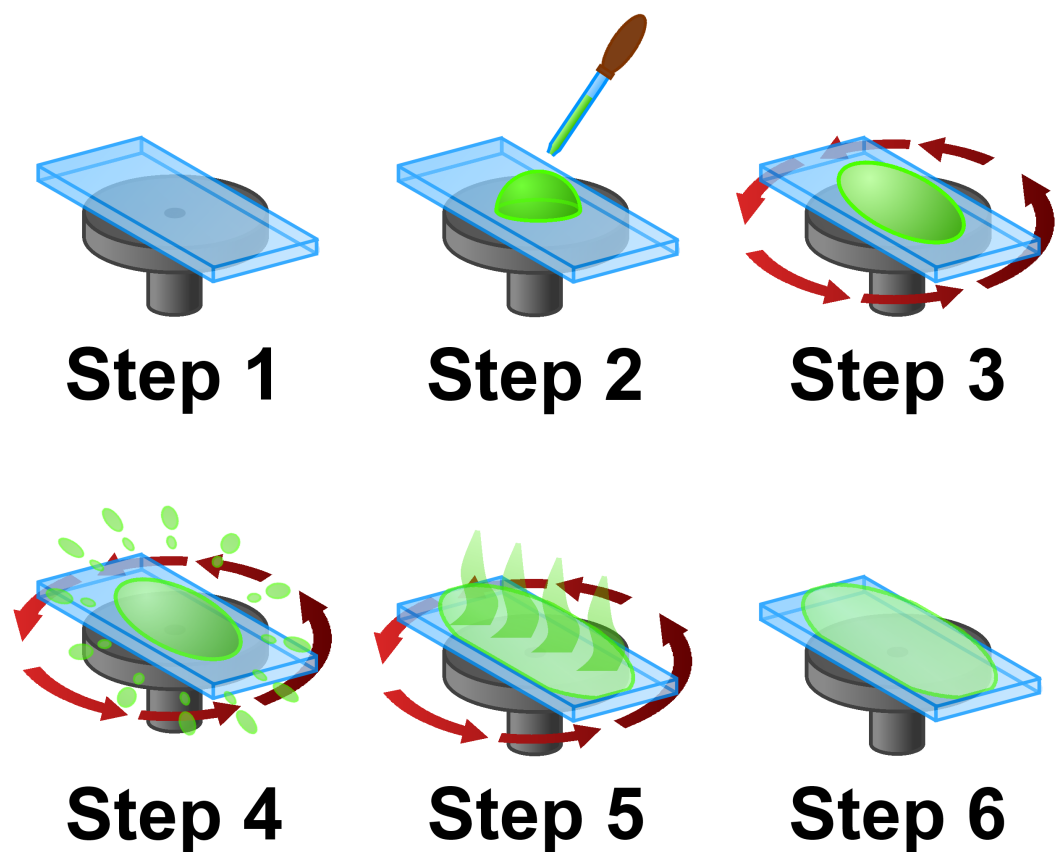


Figure 4.1: The spin-coating process is illustrated in a series of steps; *Step 1* - secure a substrate to the spin-coater using a vacuum seal. *Step 2* - thoroughly wet the center of the substrate with deposited solution. *Step 3* - wet the sample with the polymer solution by rotating the substrate at a constant spin-speed. *Step 4* - excess solution is ejected off the substrate. *Step 5* - the film thins as the remaining solvent from the remaining solution is evaporated. *Step 6* - spinning is stopped when the film is dry and stable. The sample may require annealing to remove any residual solvent in the film.

There are several parameters which change the features and quality of a spin-cast film. The following parameters were considered when casting polymer films during this research;

- *Spin speed*: A faster spin-speed ejects more polymer solution off the substrate during spin-casting. Less solution is left in contact with the substrate, which results in less polymer remaining on the surface of the substrate. Thinner films are prepared by rotating the sample at a faster spin-speed [57, 59].
- *Viscosity*: Solutions with a higher polymer concentration are usually more viscous. This results in less solution being ejected off the substrate during spin-coating. Depositing a solution with a higher polymer concentration will result in a thicker spin-cast film [57, 59].
- *Solvent selection*: A solvent which evaporates too readily will result in a rough film. The solvent on the surface of the liquid film evaporates too quickly. This results in a solid ‘skin’ above a liquid film. The whole of the film is prevented from drying uniformly and results in the surface becoming roughened [60]. On the other hand, a non-volatile solvent may take too long to dry. This results in a film which needs a longer spin-coating duration and/or annealing to stabilise and dry.
- *Interfaces*: The solvent and/or polymer may not be able to sufficiently bond to the substrate. A low adhesion energy between the substrate and the polymer solution results in a film which has ‘streaks’ on its surface (the *Marangoni effect* [61, 62]).

4.2.1 Polymer and solvent selection

Polymers were dissolved into solvents to prepare solutions for spin-coating. Homogeneous films were needed to make efficient 1D Bragg reflectors as defects will scatter reflected and transmitted light. These solutions must be capable of being cast into homogeneous films of an appropriate thickness onto silicon, glass and polymer substrates (to make multi-layers).

The solvent used to spin-cast a film must not dissolve and/or damage any previously deposited polymer by swelling the film. Swelling previously deposited layers can cause them to strain and crack the sample. If a solvent was

Polymer	Molecular weight M_w	Polymer chemical formula	refractive index at $\lambda = 633nm$	Solvent	Solvent chemical formula	Polar or non-polar
Polyvinylpyrrolidone (PVP)	1300k	$(C_6H_9NO)_n$	1.516 ± 0.001	50:50 ethanol: acetonitrile mixture	C_2H_6O (ethanol) and C_2H_3N (acetonitrile)	Polar
Cellulose acetate (CA)	50k	$C_6H_7O_2(OH)_3$	1.474 ± 0.001	Diacetone alcohol	$C_6H_{12}O_2$	Polar
Polystyrene (PS)	192k	$(C_8H_8)_n$	1.586 ± 0.001	Toluene	C_7H_8	Non-polar
Poly(9-vinylcarbazole) (PVK)	1100k	$C_{14}H_{11}N$	1.675 ± 0.001	Chlorobenzene	C_6H_5Cl	Non-polar

Table 4.1: Properties of the polymers and solvents used to make solutions for spin-casting thin film multi-layers. *Polar* and *non-polar* chemicals were used so that the multi-layer could be prepared using an orthogonal solvent system. The chemical structure of the chemicals are shown in figure 4.2

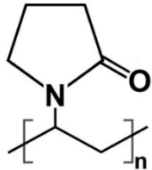
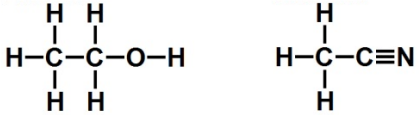
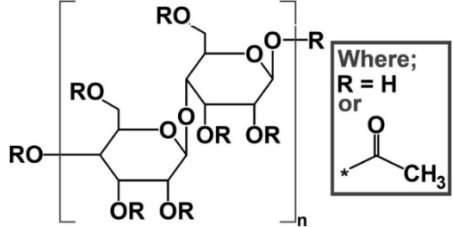
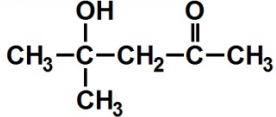
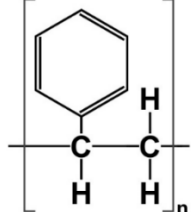
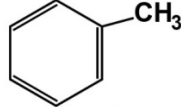
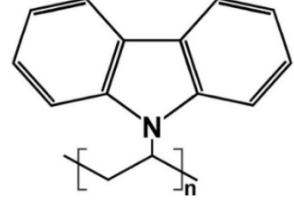
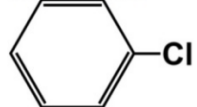
	Polymer	Solvent
Polar	Polyvinylpyrrolidone (PVP) 	Ethanol & Acetonitrile 
	Cellulose acetate (CA) 	Diacetone alcohol 
Non-polar	Polystyrene (PS) 	Toluene 
	Poly(9-vinylcarbazole) (PVK) 	Chlorobenzene 

Figure 4.2: The chemical structures of the polymers and solvents used to make spin-cast polymer multi-layer films. Each polymer is shown alongside the appropriate solvent which was used to make the solutions. *Polar* and *non-polar* chemicals were used so that the multi-layer could be prepared using an orthogonal solvent system. More detailed information about the polymers are shown in table 4.1

used to dissolve polymer ‘A’, it must not be allowed to dissolve the alternate polymer ‘B’ and vice-versa. This is known as a orthogonal solvent system and was used to prepare polymer multi-layers. Previously deposited layers would be damaged by depositing new layers if an orthogonal solvent system was not used [15].

Using an orthogonal system significantly reduces the selection of polymers and solvents which can be used for sample preparation. This problem was solved by initially considering solvents which are orthogonal with respect to one another. It is well known that polar and non-polar solvents do not mix [63,64]. A molecule is polar when the distribution of electric charge is not evenly distributed. This occurs when there is unequal sharing of electron pairs in covalent bonds. The atoms in the molecule are in a non-symmetric arrangement and the charge distribution is equivalent to a pair of separate and opposite charges [49].

Polar and non-polar polymer materials were also considered and paired with their appropriate solvents. Four different polymers and four different solvents/mixtures were used to make solutions for sample preparation. The polymers and their solvents which they were dissolved in are shown in table 4.1. The chemical structure of the polymers and solvents are illustrated in figure 4.2.

Two different polymer/solvent systems were tested when making the multi-layer samples. Most of the experiments were made by depositing alternating layers of polyvinylpyrrolidone (PVP) and polystyrene (PS). These materials are cheap, readily available and easy to process into solutions and spin-coated. The contrast in refractive between the two polymers ($\Delta n = 0.07$) was sufficient for reflection bands to be measured (which is discussed in chapter 5). The other multi-layer technique used cellulose acetate (CA) and poly(9-vinylcarbazole) (PVK), which is discussed in chapter 10.

Experiments showed that spin-casting PVP from either ethanol or acetonitrile solution resulted in poor quality films. However, solutions using a 50:50 mixture of both solvents were known to produce good quality spin-cast films [61]. PS was dissolved into toluene which spin-coated into homogeneous films. Tests showed that each polymer was immiscible in the solvent used for the alternate polymer layer.

4.3 Multi-layer sample preparation

The polymer distributed Bragg reflectors were prepared by spin-coating alternate polymer films on top of one another. This section discusses the techniques used to prepare PVP/PS multi-layers. Preparation of multi-layers made from CA and PVK are discussed in section 10.3.2.

Initial attempts to make PVP/PS multi-layers resulted in poor quality/cracked samples. Defects such as cracks would cause the samples to scatter light and reduce their efficiency as DBRs. Cracking occurred when a PVP layer was sandwiched between two PS films. Specifically, it is when a PS layer is deposited on top of a PVP(top)→PS(bottom) bilayer. The toluene solvent in the PS solution attempted to penetrate through the intermediate PVP layer. This swells the underlying PS film which creates a strain and cracks the rigid PVP film. The PVP layers were protected by swelling them with hydrochloric acid (HCl) vapour. This prevented the toluene (from a freshly deposited PS layer) penetrating through the PVP layer and damaging the sample. Using this protective step enabled multi-layers of PVP/PS to be prepared without cracks. Fourier transform infra-red (FTIR) spectroscopy was used to measure any chemical changes when swelling the polymers with HCl vapour (this is discussed in chapter 7). The results indicated that neither PVP or PS films chemically reacted with HCl vapour. Furthermore, all of the HCl vapour was removed from the multi-layers during annealing.

Preparation of the PVP/PS multi-layers is shown in the flow diagram in figure 4.3. All of the polymer solutions were deposited at spin-speeds between $1.0krpm$ and $4.5krpm$. Spin-speed which were slower than $1.0krpm$ resulted in poor film uniformity. The vacuum pump was unable to keep the substrate secured the sample were spun faster than $4.0krpm$.

These samples were finished by annealing them for 5 hours at $110^{\circ}C$ under a $\sim 1mtorr$ vacuum. This is above the glass transition T_g temperature of PS, but not PVP. The glass transition temperature of PS and PVP are $97^{\circ}C$ and $170^{\circ}C$ respectively [65]. A polymer below its T_g is relatively rigid and brittle. Whilst above the T_g , the polymer is more malleable and rubber-like [18]. Annealing releases residual spin-coating stresses and enables residual solvent to more readily escape the polymer films [18, 47]. Unfortunately, not all of the solvent would have been released from the multi-layer samples due to annealing below the T_g of PVP. The solvent from underlying PS layers may have also

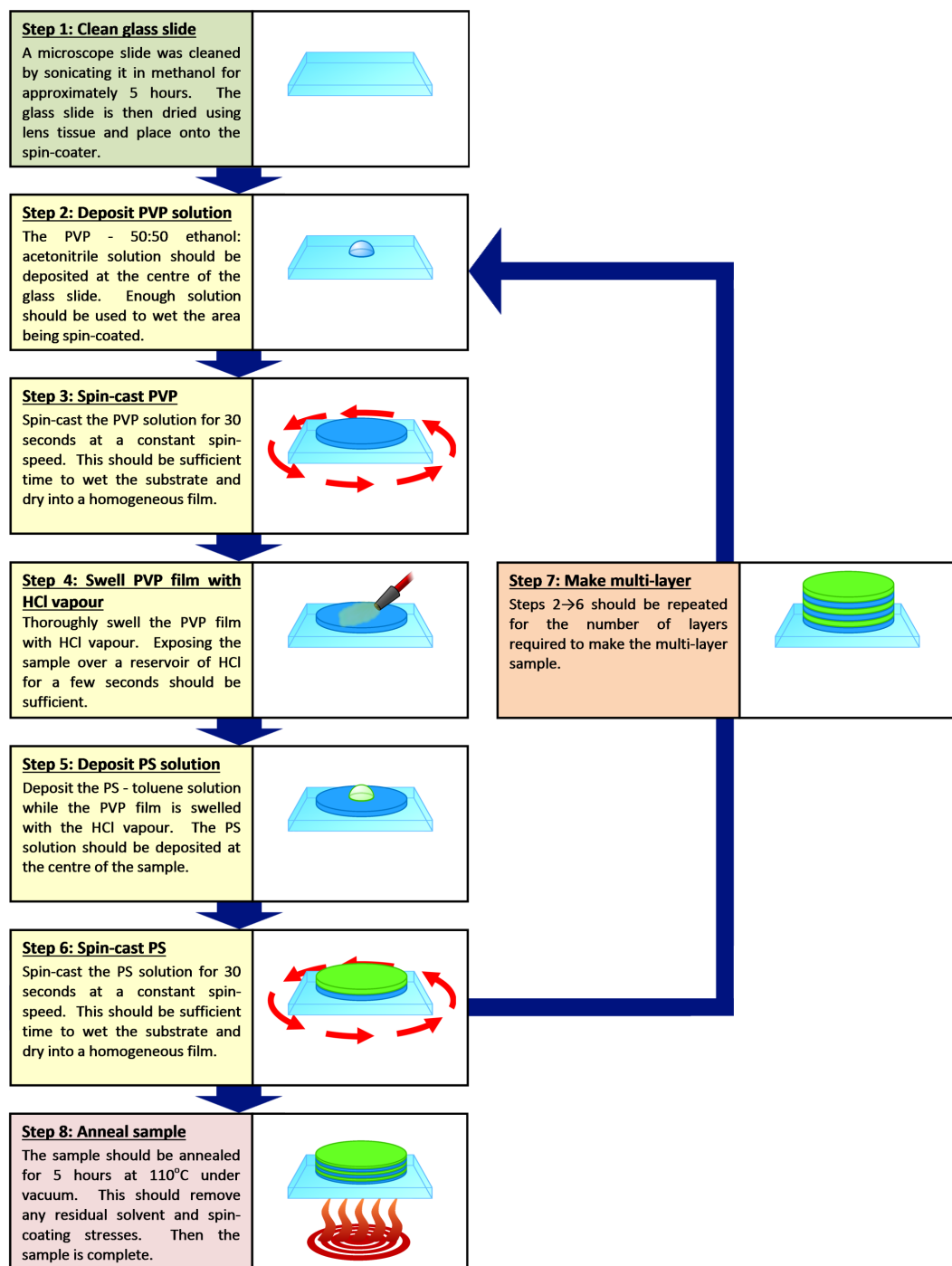


Figure 4.3: Flow diagram illustrating the preparation procedure for making PVP/PS multilayer samples. The wavelength of the reflection peak was controlled by changing the spin-speed. Adding or removing the number of layers deposited changed the reflectance of the reflection peak. This process was later automated using a computer control system.

struggled to penetrate through the un-annealed PVP layers [66]. The possible effects of trapped solvent discussed in chapter 5 as it was a likely cause for reductions in the reflectance of the DBRs.

4.3.1 Automated sample preparation

Samples were initially prepared by hand and it typically took approximately one hour to make a 50 layer sample. An automated system was developed so samples could be prepared without the need for continuous attention. The computer control system was later used to make chirped DBR samples (discussed in section 5.6). Figure 4.4 shows a diagram of the automated spin-coater design. A photograph of the system is shown in figure 4.5 and how the pre-existing spin-coater (Dr James Sharp had built the spin-coater before this research had begun) was modified. The automated system was designed and built by myself for controlled multi-layer sample preparation. Credit should also be given to the University of Nottingham School of Physics and Astronomy workshop team for manufacturing bespoke components for these modifications. The automated set-up consisted of many components which are listed below. Each number in the list corresponds to the labelling numbers in figure 4.4;

1. *Reservoirs of solutions and HCl*: Large quantities of polymer solutions were prepared so samples could be made without interruption. The solution bottles were sufficiently sealed to prevent evaporation. This would otherwise lead to the concentration of the solutions changing during sample preparation. A bottle of HCl solution was used to syphon HCl vapour onto the sample and swell PVP layers when needed.
2. *Peristaltic pumps*: The polymer solutions and HCl vapour were delivered onto the sample by using peristaltic pumps and Viton tubing (both were supplied by Williamson manufacturing company UK). The peristaltic pumps enabled a controlled the flow of solution/vapour by applying a voltage using a computer control card (National instruments USB DAQ control card). The Viton tubing did not chemically react with any of the solvents or vapour. Viton does swell in toluene, but this did not hinder the preparation of samples.
3. *Hypodermic needles*: Both polymer solutions were deposited onto the center of the substrate by using hypodermic needles. Capillary action/surface

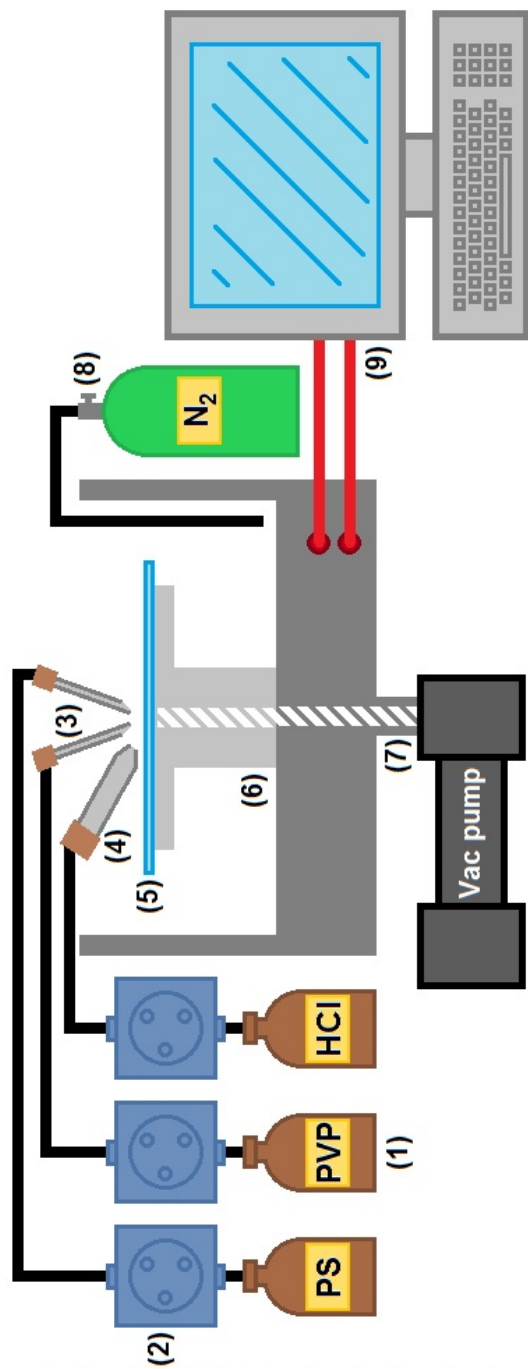


Figure 4.4: Schematic diagram of automated spin-coater; (1) Reservoir of polymer solutions and HCl vapour, (2) Peristaltic pumps, (3) Syringe needles, (4) Delivery tube for HCl vapour, (5) Glass slide substrate, (6) Spin-coater, (7) Vacuum pump, (8) Nitrogen gas reservoir, (9) Computer control system. A photograph of the automated spin-coater set up is shown in figure 4.5.

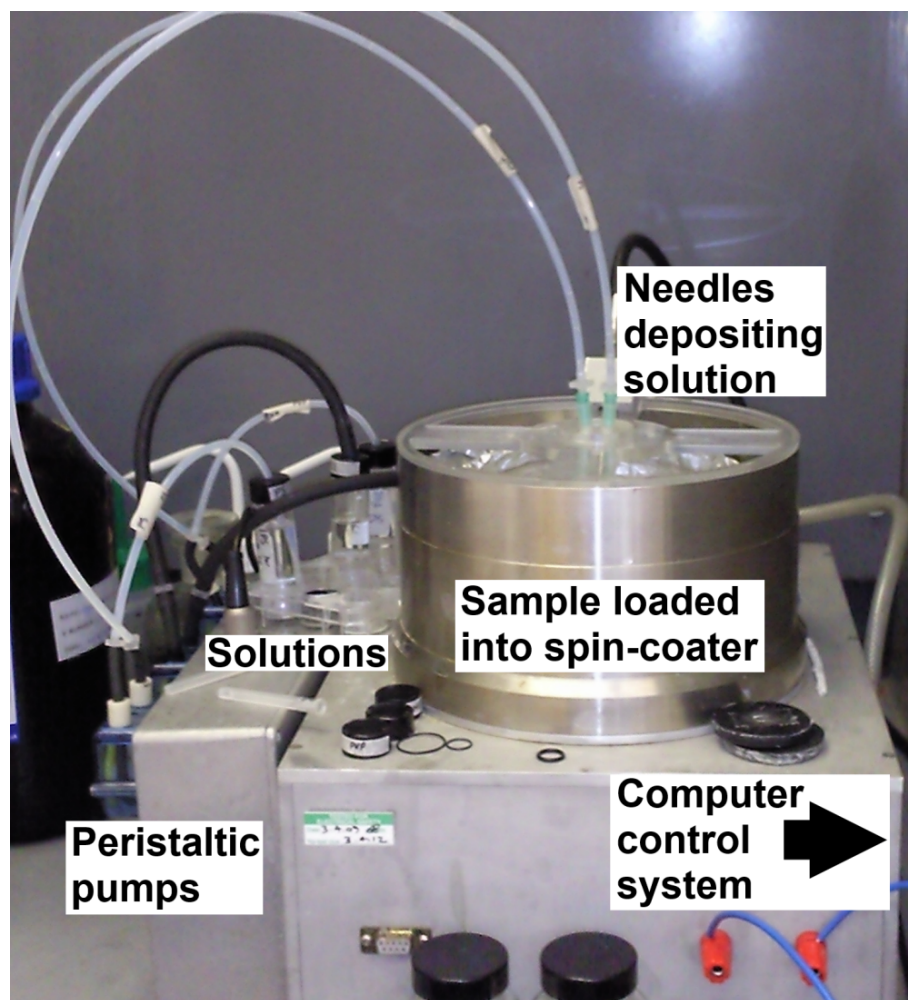


Figure 4.5: Photograph of the modified spin-coater for automated sample preparation. The automated spin-coater modifications were designed and built by myself and the workshop team at the School of Physics and Astronomy at the University of Nottingham. The home-built spin-coater was made by Dr James Sharp before my research in this thesis had begun. All of the modifications were easily removed so the spin-coater could be used for other experiments. The automated spin-coater was used to prepare samples without the need for continuous user input. A computer control card and a self written Matlab program were used to prepare multi-layer samples with specific film thickness values. A schematic of the automated spin-coater was shown in figure 4.4.

tension was sufficiently high to prevent the solutions from depositing onto the samples when the peristaltic pumps were not in motion.

4. *HCl delivery tube*: A large metal tube was used to deliver and spray HCl vapour onto the sample. This was positioned as close to the substrate as possible to reduce the quantities of HCl needed to swell the PVP films.
5. *Glass slide*: A cleaned glass slide was placed into the spin-coater where it remained until all of the layer depositions were complete. The system was designed so the sample would not have to be removed out of the spin-coating chamber during sample preparation. This also includes when swelling each PVP film with HCl vapour.
6. *Spin-coater*: The home-built spin-coater was made by Dr James Sharp and was used throughout this research. Spin-speed was increased/decreased by raising/lowering the applied voltage respectively. The computer control card was able to change the voltage applied to the spin-coater to control the spin-speed. Modifications used to automate sample preparation could be readily removed so the spin-coater could be used for other experiments.
7. *Vacuum pump*: Substrates were secured to the rotation stage of the spin-coater using a vacuum seal.
8. *Nitrogen feed*: A continuous flow of nitrogen gas was fed into the sample chamber to purge the atmosphere of residual organic solvent and HCl vapour. Too much residual vapour would reduce sample quality. This was due to the films not adequately drying when surrounded by a solvent atmosphere.
9. *Computer control system*: A Matlab program was written by myself to control the sample preparation. The program allowed samples to be prepared with tailored optical properties. This was achieved by controlling the spin-speed (which changes the layer thickness and the wavelength of the reflection peak) and number of layers deposited (which changes the reflectance of the reflection peaks). Chirped samples were also prepared by programming the spin-coater to incrementally change the layer thickness during sample preparation (discussed in section 5.6).

4.3.2 Multi-layer film thickness

DBR samples were prepared using the techniques discussed in sections 4.3. The most efficient DBR structure is when the optical thickness of each layer is $\lambda/4$ [12] (this is discussed further in chapters 6 and 7). However, attempts to make PVP/PS DBRs with layers as thin as $d \simeq \lambda/4n$, resulted in cracked and inhomogeneous samples. This occurred despite attempting various methods to reduce cracking which included;

- *Swelling deposited films using various solvents (including HCl vapour):* Swelling the PVP layer helps prevent the toluene in the PS solution from penetrating through the PVP film. This would occur when depositing a PS solution on top of a PVP film which had an underlying PS layer.
- *Intermediate annealing to remove residual solvent and spin-coating stresses:* Lingering solvent is removed by annealing past the glassing temperature T_g of polymer films. Residual stresses which occurred due to spin-coating would have also been reduced during annealing.
- *Depositing solutions while spinning the substrate:* This reduces the contact time of solvents onto the pre-deposited multi-layers.

Unfortunately, these experiments did not result in any significant improvements in $\lambda/4$ sample preparation. Therefore, it was not possible to make $\lambda/4$ multi-layer PVP/PS samples. Hence, thicker films were used to make multi-layer samples. However, it is worth noting that the PVP films still needed protecting by swelling them with HCl vapour swelling (which was discussed in section 4.3).

4.3.3 Annealing DBR samples

Figure 4.6 shows the UV/visible spectra of an early attempt at making a polymer DBR. The reflection spectra was measured before and after annealing using a UV/visible spectrometer. This sample was 40 layers of alternative $423 \pm 1nm$ PVP and $426 \pm 1nm$ PS (measured using comparable single layer films using ellipsometry) and annealed for 5 hours at $110^\circ C$ under $\sim 1mtorr$ atmosphere after the initial measurement. Reflection spectra was remeasured after the sample was annealed. The plot (in figure 4.6) indicates that the position of the reflection band blue-shifted after annealing.

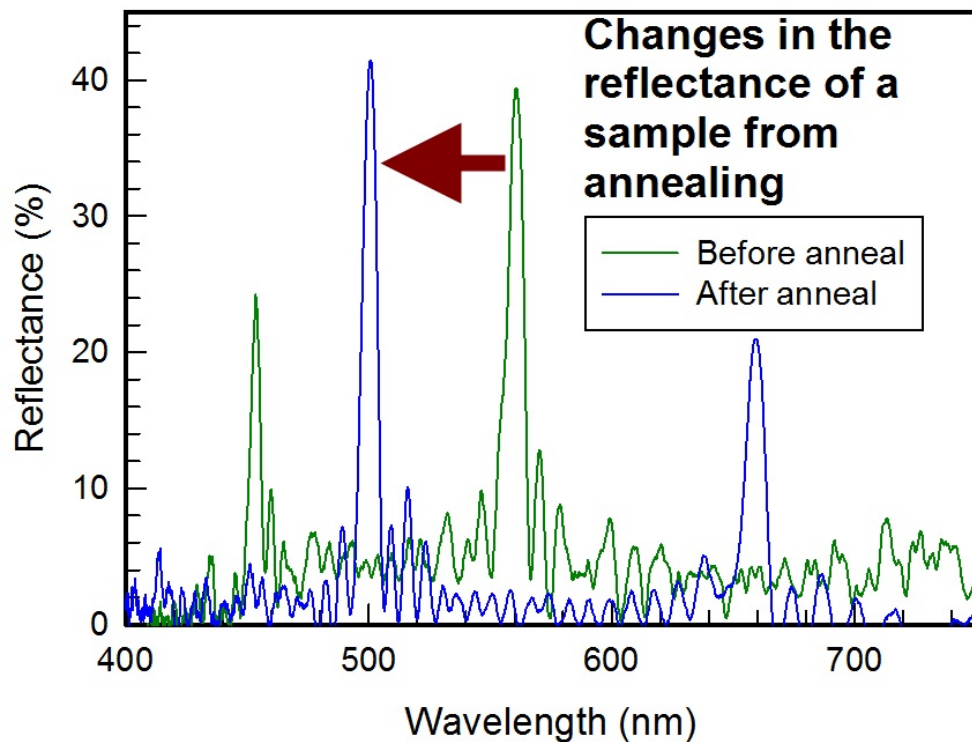


Figure 4.6: UV/visible reflection spectra of a 40 layer DBR with $d_{PVP} = 423 \pm 1\text{nm}$ and $d_{PS} = 426 \pm 1\text{nm}$. The green and blue curves are the reflection spectra measured before and after the sample was annealed respectively. The blue curve is the reflection spectra measured after the sample was annealed for 5 hours at 110°C under a 1mtorr vacuum. Annealing the sample de-swelled the layers within the sample which blue-shifted the reflection peak.

Solvent	Refractive index
Toluene	1.496
Ethanol	1.362
Acetonitrile	1.344

Table 4.2: Refractive indices of the different solvents used to dissolve the polymers for spin-casting. All values for the refractive indices were from the product specification sheets from Sigma-Aldrich for the appropriate solvents.

A large proportion of the residual solvent was removed during annealing. Residual solvent causes the layers to swell and increase their thickness. Solvents within the polymer would also lower the refractive index of the film. This is because the solvents have a much lower refractive index than the polymer (refractive indices of the polymers are $n_{PVP} = 1.516$ and $n_{PS} = 1.586$). Table 4.2 shows the refractive indices of the solvents. The refractive index contrast of the polymer layers in a DBR are reduced when swollen with solvent. Residual solvent changes the wavelength and intensity of the reflection band because of the following;

- *Film thickness*: The optical path length between each interface in the sample changes with respect to layer thickness. Increasing the layer thickness will also increase the optical path length ($OPL = d_{film}n_{film} / \cos(\theta_{film})$ [10]). Interference between the partially reflected waves is changed when the separation between the interfaces is shifted. This changes the optical properties of the sample, which includes reflectance (which is discussed in section 5.3).
- *Refractive index*: The partial reflections within the photonic structure are due to the optical contrast between the layers. Increasing/decreasing the optical contrast increases/decreases the reflectance of the sample respectively. Changing the refractive index of a layer also changes its optical path length. The optical path length of a film will increase/decrease if its refractive index is larger/smaller respectively [10].

4.4 Ellipsometry

The film thickness and refractive index of the polymer films were measured using ellipsometry throughout this research. Ellipsometry is able to measure the thickness of homogeneous films with a resolution of $\sim 1\text{\AA}$ [51]. Samples were

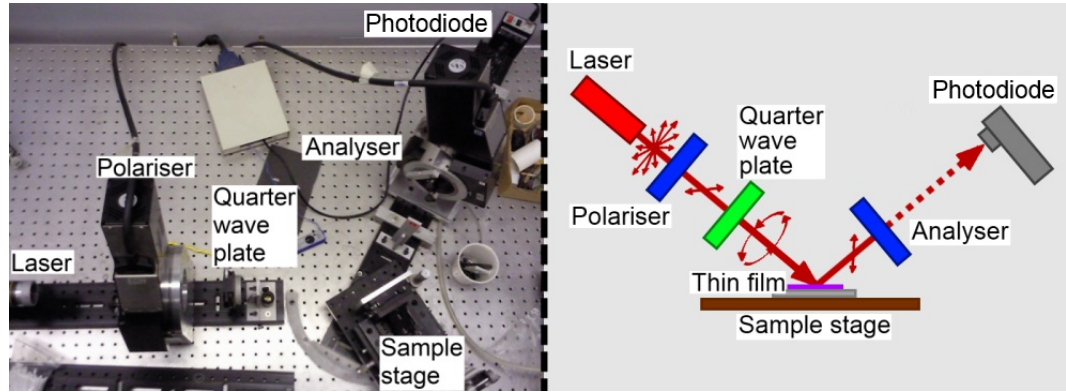


Figure 4.7: [Left panel] Photograph of the ellipsometer set-up. [Right panel] Schematic of the consisting parts of the ellipsometer.

prepared by spin-coating polymer solutions onto freshly cleaved silicon wafers. The ellipsometer was used to measure film thickness changes with respect to spin-speed and also solution concentration (discussed later in this section). Measurements of film thickness and refractive index were used to model the optical properties of DBRs using a modified optical transfer matrix method (discussed in chapter 3). These results were used to refine the preparation of the polymer photonic structures by controlling the thickness of deposited layers.

Figure 4.7 shows an image of the home-built ellipsometer and an illustration of its constituent parts and function. The Ellipsometer was built by Dr James Sharp before I joined the Polymer Physics group. A light source (which was a 632.8nm HeNe laser) emits a collimated beam through a linear *polariser*. The linearly polarised light then passes through quarter wave-plate which elliptically polarises the laser light. Rotating the polariser also changes the orientation of the elliptically polarised light. This falls incident onto a pre-prepared sample at a fixed angle of incidence θ_i . The sample was a polymer film which was spin-cast onto a freshly cleaved silicon (100) substrate. An *Analyser* (a linear polariser which is rotated to change its orientation) was used to test the polarisation of light reflected from the sample. A photodiode was used to measure the intensity of light which has passed through the analyser [51,67].

The polarisation of the reflected light is changed by the optical properties of the sample. This is illustrated in figure 4.8, which shows how incident light is partially reflected from the top and bottom interfaces of a single layer film. Interference between the partially reflected rays contribute towards the reflectance of the sample. The polarisation of the partially reflected waves

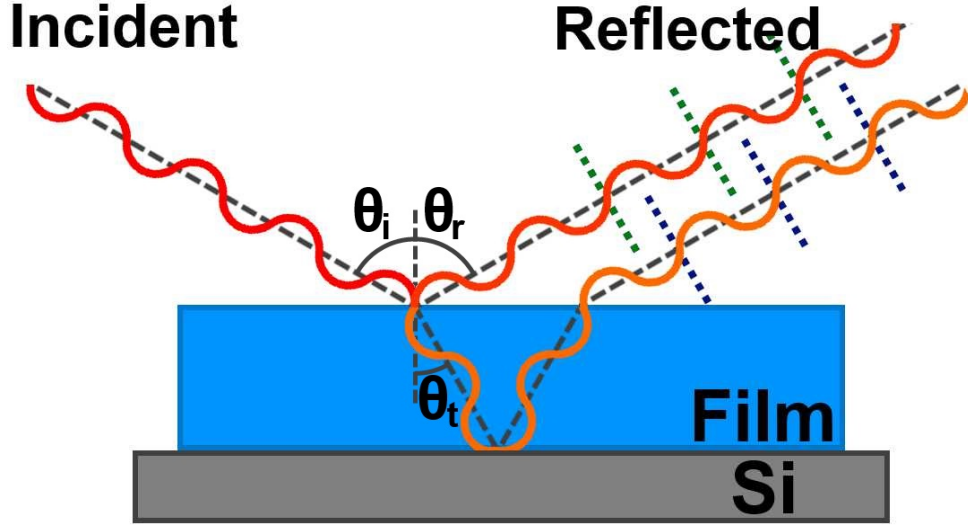


Figure 4.8: Thin film interference is utilised by an ellipsometer to measure the thickness of the films. The incident light is reflected by interfaces at the top and the bottom of the film. Interference between the two rays changes the amplitude of the reflectance. The interface changes the magnitude of the rays electric field components which are parallel and perpendicular (p and s respectively) to the surface. Reflected light from a thin film can have a different polarisation (when compared to the incident light) because changes in the p and s electric field magnitudes.

electric fields should also be considered, as their magnitudes change when light is not perpendicular to the sample surface ($\theta_i \neq 0$) [51,67]. Component waves which have electric fields polarised normal and parallel the sample surface are represented by the s and p notations respectively. The total reflectance of the s and p polarisations (R_s and R_p) is calculated by the square of their corresponding Fresnel reflection coefficients (r_s and r_p). This is shown in the following equations [10,51,67];

$$R_s = r_s^2 = \left[\frac{n_1 \cos(\theta_i) - n_2 \cos(\theta_t)}{n_1 \cos(\theta_i) + n_2 \cos(\theta_t)} \right]^2, \quad (4.1)$$

and

$$R_p = r_p^2 = \left[\frac{n_2 \cos(\theta_i) - n_1 \cos(\theta_t)}{n_1 \cos(\theta_i) + n_2 \cos(\theta_t)} \right]^2. \quad (4.2)$$

Where R_s = reflectance of the wave with respect to the s polarisation, R_p = reflectance of the wave with respect to the p polarisation, r_s = reflection coefficient for the s polarisation, r_p = reflection coefficient for the p polarisation,

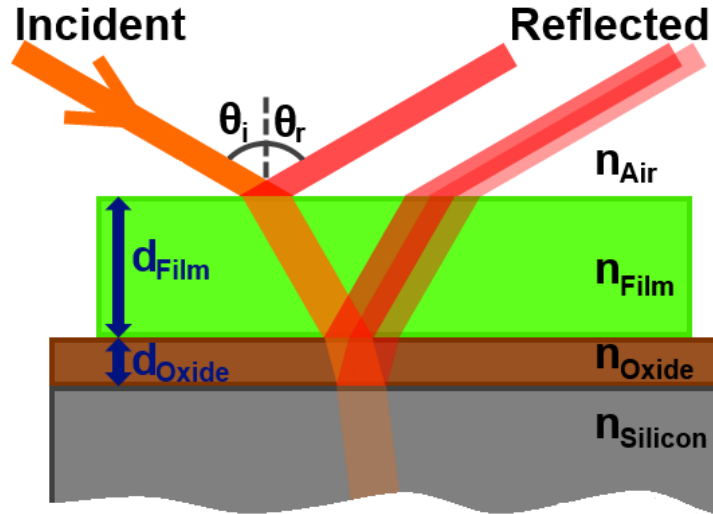


Figure 4.9: Incident light is reflected by a sample which consists of a polymer film on top of a silicon substrate. The oxide layer on top of the silicon substrate should be considered in modelling calculations as it contributes towards the optical properties of the sample. Changing the angle of incidence, refractive index of the layers and/or thickness of the films will change the properties of the light reflected by the sample.

n_1 = refractive index of the incident and reflected medium, n_2 = refractive index of the medium for the transmitted wave, θ_i = angle of incidence [*degrees*] and θ_r = angle of reflectance [*degrees*].

The quarter wave plate combination (shown in figure 4.7) elliptically polarises the light before it is incident on the sample. The orientation of the elliptically polarised light is controlled by the angle of the polariser. Under specific conditions, the sample can change the polarisation state of the elliptically polarised light into linearly polarised light [51,67]. The photodiode does not detect any light when the analyser is orientated perpendicular to the polarisation of the linearly polarised light reflected from the sample. This is known as ‘nulling’ and it only occurs when the polariser P and analyser A accurately aligned for each sample [51,67]. The optical properties of the samples are calculated by measuring P , A and θ_i . A model of samples optical properties is used to extract the film thickness and refractive index of the polymer film from the measurements of P , A and θ_i .

It is not possible to calculate the optical properties of these samples using only the Fresnel equations. This is due to the spatial separation of the interfaces and the refractive index of each layer. Changing these variables will change the optical path length of each layer and how the partial reflections interfere.

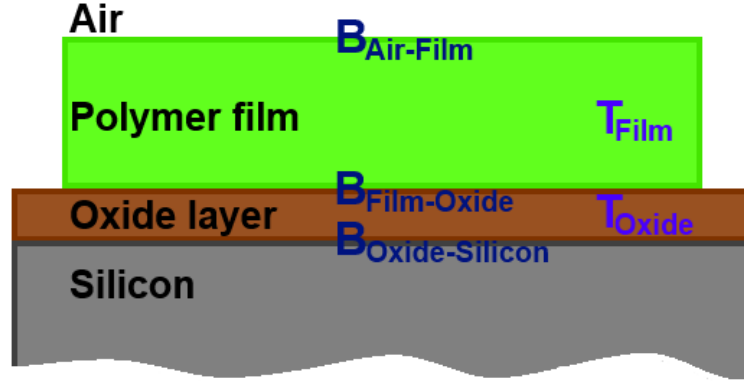


Figure 4.10: This diagram illustrates the structure used to model the optical properties of samples measured using ellipsometry. The reflection from each interface are characterised by a 2×2 boundary matrix. The effects of the spatial separation and media between interfaces are characterised by a 2×2 transmission matrix. These matrices are used to calculate the optical properties of the entire sample.

This is illustrated in figure 4.9 where the angle of incidence, film thickness and refractive index of the layers can vary the interference of the partially reflected waves. The optical path length is calculated by [10],

$$\text{OPL} = \frac{nd}{\cos(\theta)}, \quad (4.3)$$

Where OPL = optical path length [m], n = refractive index, d = thickness of film [m] and θ = angle with respect to the surface normal [$degrees$].

A modified optical transfer matrix model was used to calculate the optical properties of the sample (this was more thoroughly discussed in chapter 3). Each interface is represented by a 2×2 *boundary matrix* and each medium is represented by a 2×2 *transmission matrix* (illustrated in figure 4.10). The boundary (B) and transmission (T) matrices are multiplied in sequence and results in a 2×2 matrix which represents the optical properties of the whole sample [10, 13, 51]. Hence;

$$M_{Total} = B_{Air-Film} T_{Film} B_{Film-Oxide} \cdot T_{Oxide} B_{Oxide-Silicon}. \quad (4.4)$$

Where B = boundary matrix and $T_{[N+1]}$ = transmission matrix.

Reflection coefficients for s and p polarisations (r_s and r_p) can be extracted from the matrix M_{Total} in equation 4.4 (this was more thoroughly discussed in chapter 3) [10, 13, 51]. These reflection coefficients are used to calculated the

reflectance ratio,

$$\rho = \frac{r_p}{r_s}. \quad (4.5)$$

ρ was used to determine *psi* ψ and *delta* Δ which are parameters used in ellipsometry calculations. ψ and Δ are calculated by [51];

$$\psi = \tan^{-1}(|\rho|), \quad (4.6)$$

$$\rho = \tan(\psi)e^{i\Delta}, \quad (4.7)$$

$$\Delta = \tan^{-1}\left(\frac{\text{Im}(\rho)}{\text{Re}(\rho)}\right). \quad (4.8)$$

The orientations of the polariser P and analyser A are related to ψ and Δ by the following equations;

$$P = \frac{\psi}{2} - 45^\circ. \quad (4.9)$$

$$A = 90^\circ - \Delta. \quad (4.10)$$

Figure 4.11 is a plot of P vs A of modelled (solid line) and measured (data-points) ellipsometry data for spin-cast PVP films. Each data-point corresponded to a sample with a different film thickness d . A range of modelled P and A values were calculated for films with refractive index n , but different values of d . Plotting these values (over a wide range of different d values) resulted in a ‘loop’ which increased/decreased in size when the modelled refractive index n was larger/smaller respectively. The least squares method was used to fit the size of the loop to the measured data-points. This was used to extract the refractive index of the samples.

The film thickness of samples were extracted by comparing measurements to modelled data. P and A were modelled for samples which had refractive index n . The modelled film thickness d was varied to calculate a range of corresponding P and A values. These modelled values were compared with measurements to extract the film thickness of the samples.

Each sample was measured five times and an average value was used as the final result. The standard deviation of these measurements was calculated and

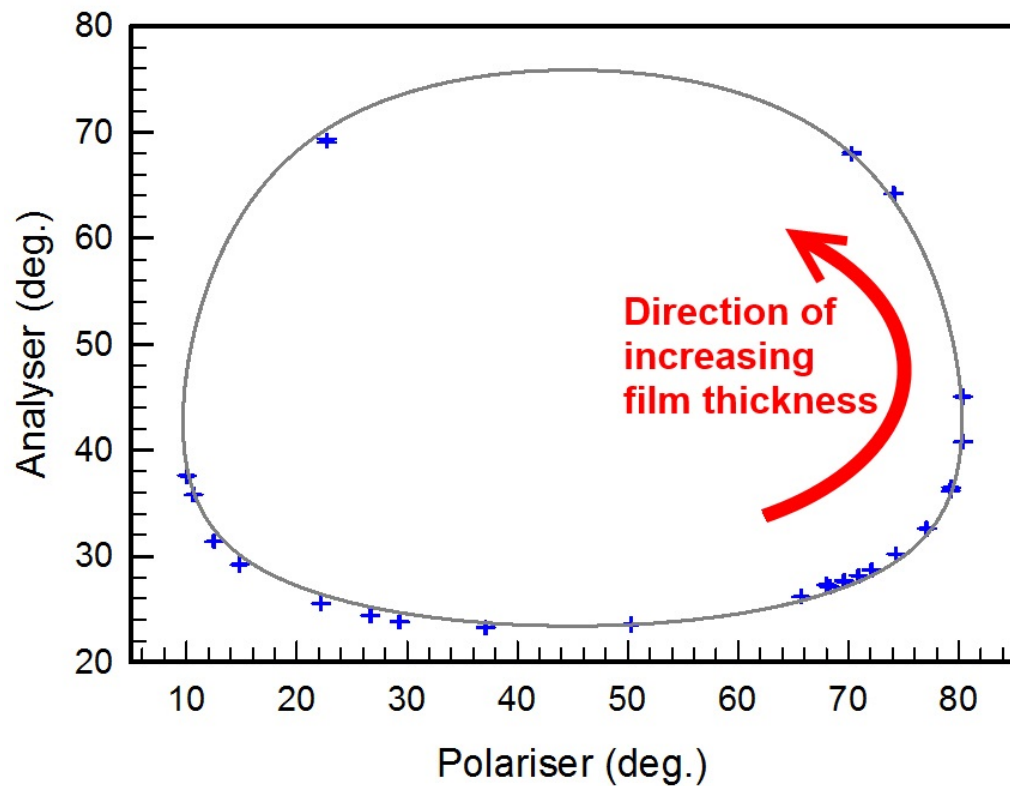


Figure 4.11: The refractive index of PVP ($n_{PVP} = 1.516 \pm 0.001$) was measured using ellipsometry. Each data-point corresponds to P and A measurements of samples with a different PVP layer thickness. The grey ‘loop’ corresponds to modelled P and A values for a film with refractive index n .

used as the error.

4.4.1 Film thickness calibration

Ellipsometry was used to measure the thickness of polymer films which were spin-cast at different spin-speeds and solution concentrations. Figure 4.12 shows that the film thickness decreased as the deposition spin-speed increased. The film thickness also decreased if the solution concentration was reduced.

Samples were initially prepared from solutions of 4.0% wt PVP and 4.0% wt PS. DBRs were prepared with reflection bands between 450nm and 650nm by depositing films between 1.0krpm and 4.5krpm (this is discussed further in chapter 3.7). Sample preparation was later improved by reducing the concentration of the PVP solution to 3.2% (this is discussed further in chapter 6). The concentration of the polymer solutions were kept constant and spin-speed was used to control layer thickness during sample preparation. Figure 4.12 was used to calculate the film thickness of spin-cast films within the multi-layer structure (by recording the spin-speed used during preparation). This data was also used to prepare samples with a specific structure/spectra by controlling the thickness of deposited films.

Ellipsometry was also used to measure the film thickness of bi-layers. Specifically, it was used to test if film thickness was the same whenever spin-coating onto both polymer and silicon substrates. Film thickness measurements were used to model the reflection spectra of DBR samples. The modelled spectra would be inaccurate if there were large errors in the film thickness measurements. Two sets of single layer samples were prepared, which were $265 \pm 1nm$ PVP and $221 \pm 1nm$. PS layers were then spin-cast on top of the single layer PVP films to make bi-layer samples. Likewise, PVP films were also spin-cast on top of the single-layer PS films. These bi-layer samples were prepared with a variety of different top layer film thickness. Figure 4.13 is a diagram of a polymer bi-layer which has been prepared on a silicon substrate. The ellipsometry model was extended to include the bottom polymer film in the bi-layer as part of the substrate structure (polymer film \rightarrow oxide \rightarrow silicon). This was because the thickness of the bottom layer was kept constant for all samples. The bi-layer samples were measured using ellipsometry and the film thickness of the top layer was calculated using the extended model.

Figures 4.14 and 4.15 show the thickness of the top film in a bi-layer sample when cast at different spin-speeds. The film thickness of single layer samples is

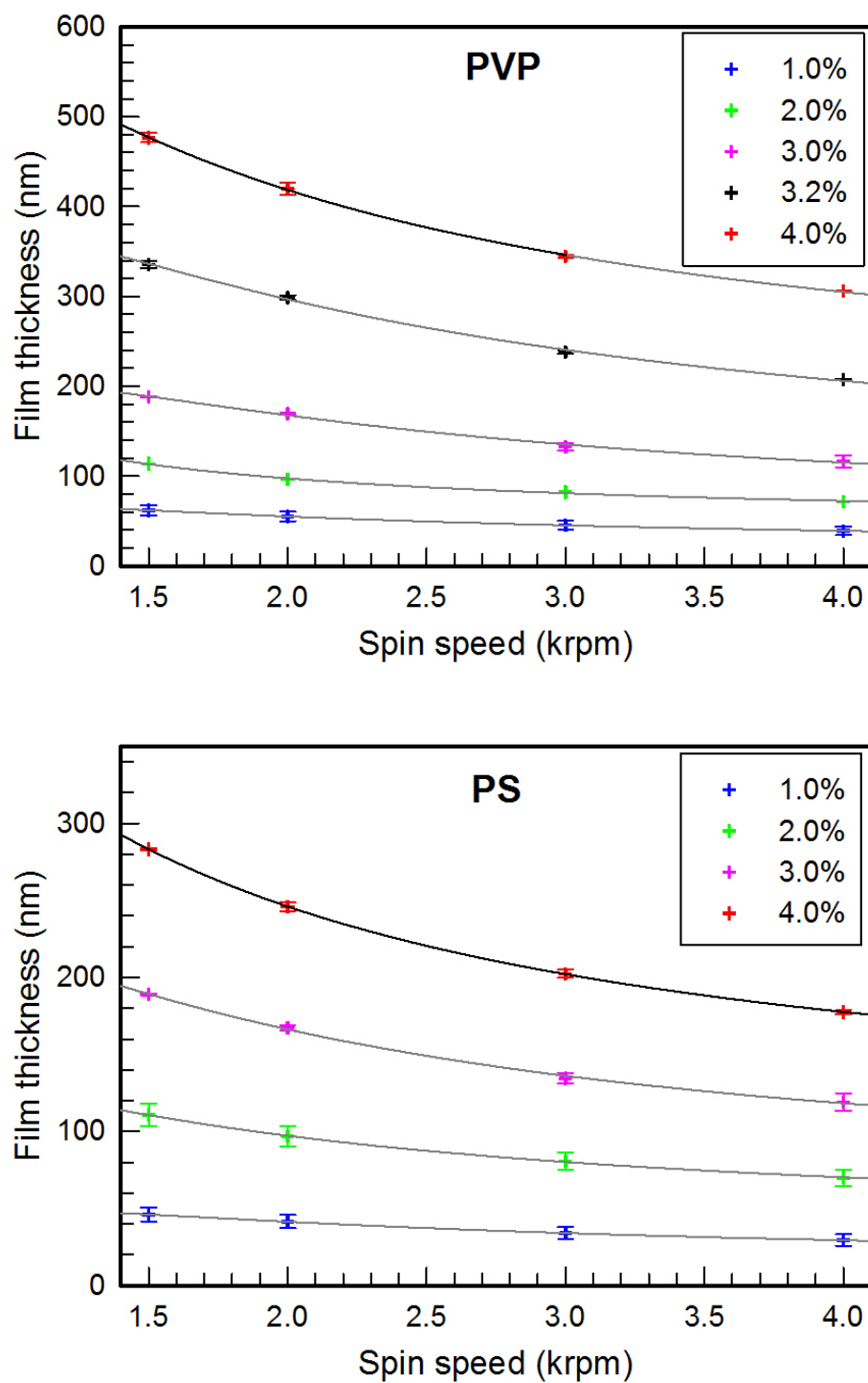


Figure 4.12: Ellipsometry film thickness measurements of PVP (top panel) and PS (bottom panel) films which were spin-cast at different spin-speeds and concentrations. The curves are free-hand plotted and the errors in the data-points were calculated using the standard deviation of five repeat measurements.

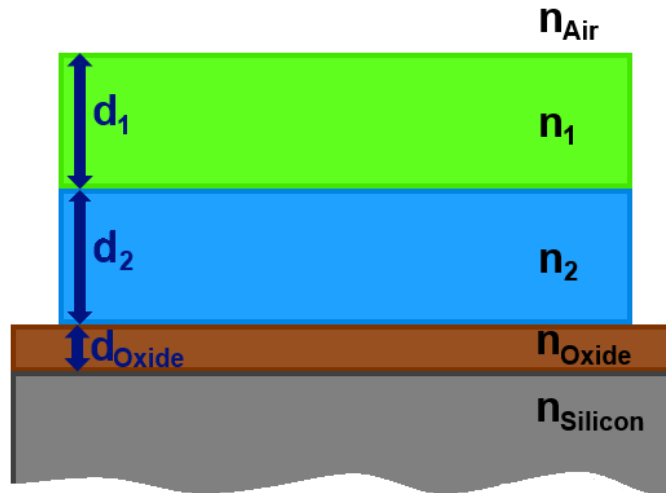


Figure 4.13: This diagram represents a polymer bi-layers which was spin-cast on to a silicon substrate. The thickness of the top layer d_1 was calculated by carefully measuring the thickness and refractive indices of all the other layers.

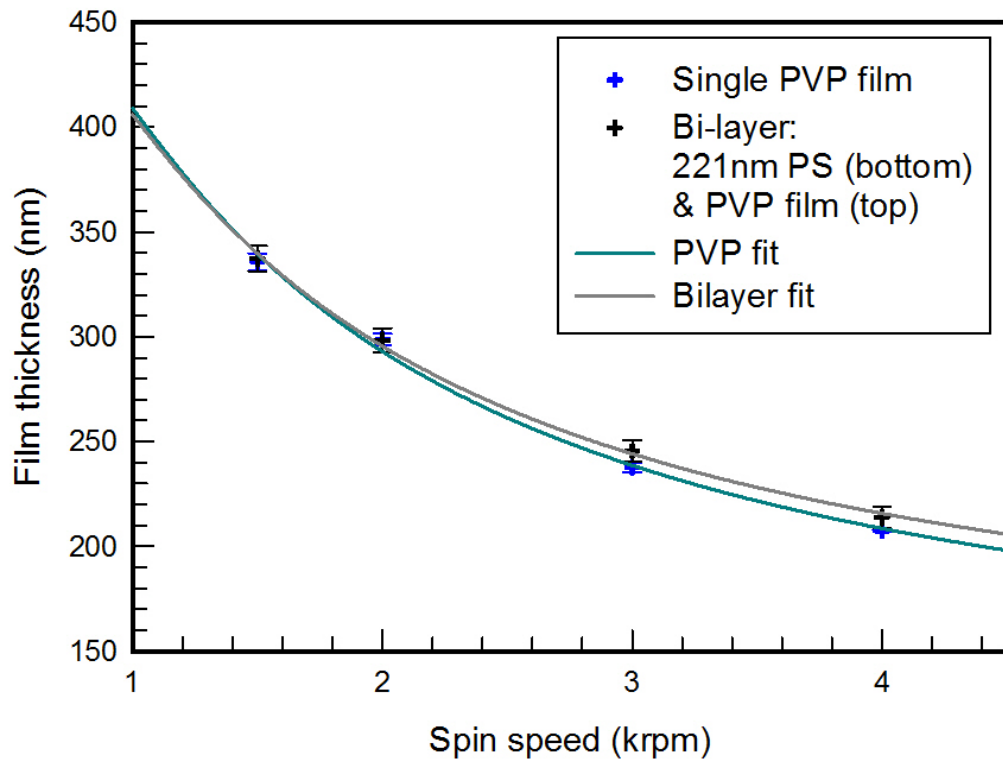


Figure 4.14: Comparison of the PVP layer thickness when spin-cast on top of silicon (blue data-points) and PS substrates (black data-points). The curves are free hand plotted and the errors were calculated using the standard deviation from 5 repeat measurements.

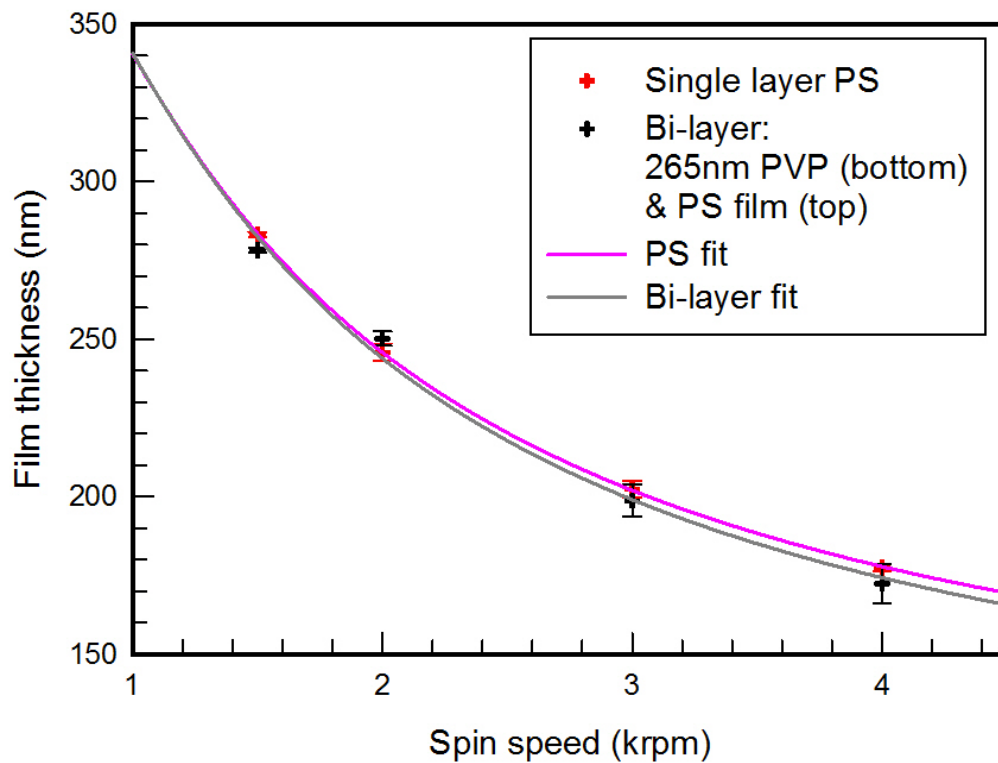


Figure 4.15: Comparison of the PS layer thickness when spin-cast on top of silicon (red data-points) and PVP substrates (black data-points). The curves are free hand plotted and the errors were calculated using the standard deviation from 5 repeat measurements.

also shown for comparison. These results showed that the thickness of PVP and PS did not significantly change when spin-cast on top of the alternate polymer layer. Therefore, the samples could be modelled using thickness values obtained from ellipsometry measurements of single layer PVP and PS films.

4.4.2 Spectroscopic ellipsometry

The home-built-ellipsometer could only measure the refractive index of samples at the wavelength of its laser light ($\lambda = 633nm$). However, the refractive index of a sample is not the same for all wavelengths. There is no general equation to model the dispersion of the refractive index with respect to wavelength for an arbitrary material [11]. A *J. A. Woolman Alpha-SE spectroscopic ellipsometer* (shown in figure 4.16) was used to measure the dispersion of the refractive index for spin cast polymer films and glass slide substrates.

The spectroscopic ellipsometer measures the optical properties of samples at various wavelengths of light. Psi Ψ and Delta Δ (which were discussed in section 4.4) were measured between wavelengths of $350nm$ and $900nm$ for each sample. The *CompleteEASE* software on the spectroscopic ellipsometer was used to model the optical properties of the samples. The number of layers, film thickness, refractive index and angle of incidence are parameters which could be fitted or constrained in the software. A variable is more accurately fitted when the error/uncertainty in the other variables are small. Independent measurements (the home-built ellipsometer was used to measure layer thickness) and accepted literature values (refractive indices of silicon and its native oxide layer [68]) were used to reduced the number of free-parameters when fitting data.

Figure 4.17 illustrates the modelled sample structure of the single layer polymer samples. Accepted literature values were used to model the wavelength dispersion of the refractive indices for the silicon dioxide $n_{SiO_2}(\lambda)$ and silicon substrate $n_{Si}(\lambda)$ [68]. The film thickness of the silicon dioxide layer d_{SiO_2} was measured with the home-built ellipsometer. Furthermore, the film thickness d_{Film} and refractive index (at $633nm$) of the polymer film were also measured using the home-built ellipsometer. Only the wavelength dispersion of the refractive index of the polymer $n_{Film}(\lambda)$ film was unknown.

Measurements of Ψ and Δ were compared with the optical model of the sample to calculate $n_{Film}(\lambda)$ for each wavelength measured. The dispersion curve of $n_{Film}(\lambda)$ was modelled using a Cauchy function (2^{nd} order approxima-

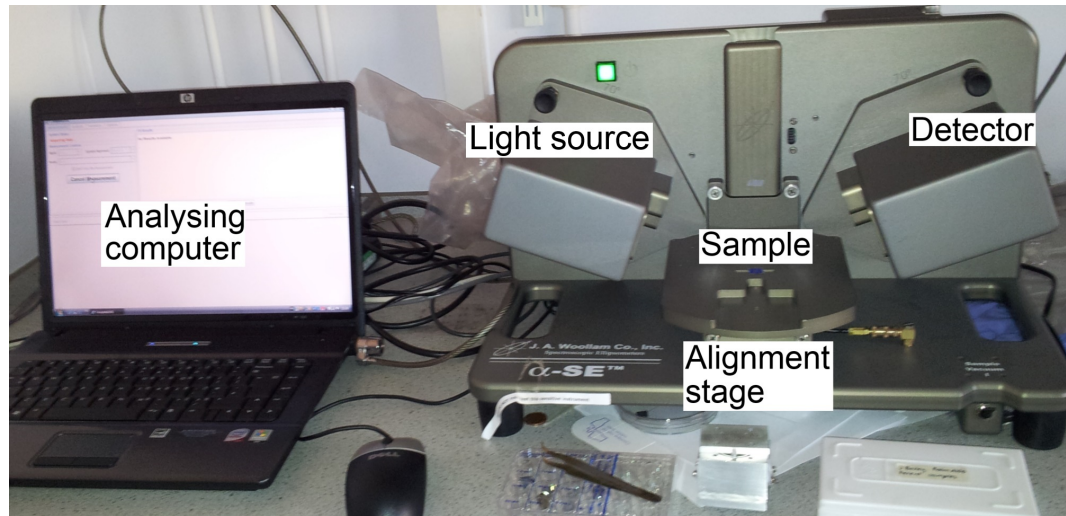


Figure 4.16: The J. A. Woolman Alpha-SE spectroscopic ellipsometer. A white light source was incident on the spin-cast polymer sample which was then measured using the detector. It is capable of measuring changes in refractive index with respect to wavelength for polymer samples.

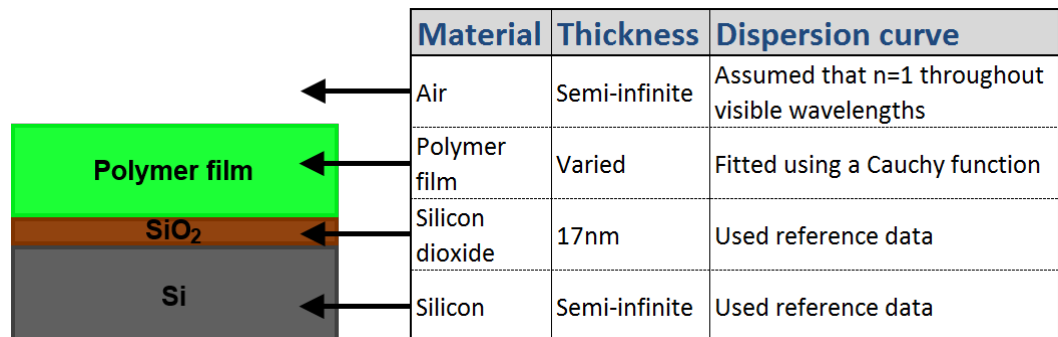


Figure 4.17: A diagram of sample structure and a table of properties values/modelling assumptions used to calculate the refractive indices of the polymers. The thickness of the polymer films were measured using the home-built ellipsometer. ‘Reference data’ from well established literature were used to model the refractive indices of the silicon substrate and its native oxide layer [68].

tion) [10],

$$n_{Film}(\lambda) = A + \frac{B}{\lambda^2} + \frac{C}{\lambda^4} + \dots \quad (4.11)$$

Where n = wavelength dispersion of the refractive index for the polymer film, λ = wavelength of light, A , B and C = coefficients which are material dependent.

Unfortunately, measurements of Ψ and Δ for the polymer films were not reproducible when using the spectroscopic ellipsometer. There were large errors when attempting to fit $n_{Film}(\lambda)$. Sample quality was tested by remeasuring the film thickness at 6 different sections of each sample using the homebuilt ellipsometer. Each measurement had an error of $\pm 1nm$ and the standard deviation of the measurements was $\pm 2nm$ for all samples. This indicated that the films were relatively flat over the sample surface.

The refractive index of the polymer films were previously measured at $\lambda = 633nm$ using the home-built ellipsometer. These refractive index measurements were comparable with literature values [65] and should have also been consistent with the spectroscopic ellipsometer measurements. The spectroscopic ellipsometry data was re-fitted so the refractive index was equal to the home-built ellipsometer measurement at $\lambda = 633nm$. Increasing/decreasing the modelled film thickness respectively decreased/increased the calculated refractive index of the polymer film. This was used to fit the spectroscopic ellipsometer model to the home-built ellipsometer measurements of the refractive index at $\lambda = 633nm$. The film thickness error was increased to $\pm 10nm$ to fit the refractive index at $\lambda = 633nm$. This was despite the home-built ellipsometer measuring the error in film thickness to be $\pm 2nm$ over the entire sample. The reason for the large increase in film thickness error needed to fit the refractive indices of the polymer was not completely understood. However, the technique improve the quality of the measured refractive index data.

Each sample was measured 10 times (repositioning the sample after each measurement) and fitted at $\lambda = 633nm$ by changing the modelled film thickness. An average was calculated to reduce the occurrence of any errors from the measurements. Two different thickness films were prepared and measured for all of the polymer materials tested. Figure 4.18 is a plot of the refractive index for two PVP samples with respect to wavelength. These samples were analysed using the techniques which were previously discussed. The results showed that these measurements were reproducible, despite the overestimated error when modelling the film thickness.

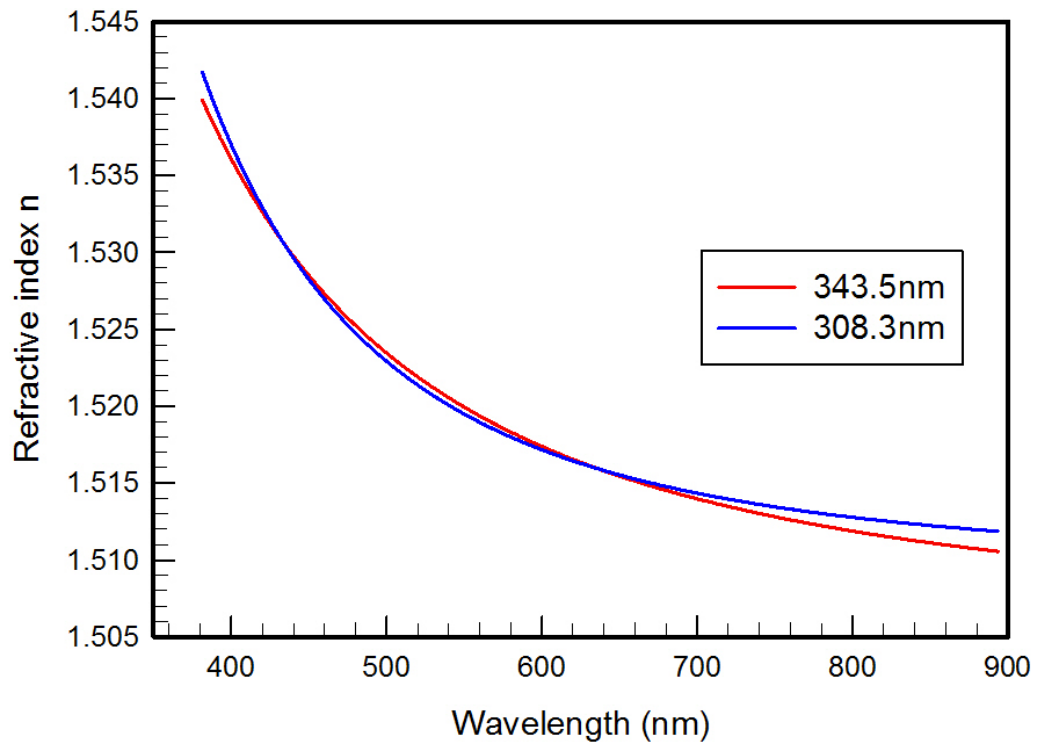


Figure 4.18: Comparison of the dispersion for two PVP films of thickness $343.5 \pm 1\text{nm}$ and $308.3 \pm 1\text{nm}$ (film thickness was measured using the home-built ellipsometer). Both curves are an average of ten measurements whereby the sample was repositioned in between each measurement using the spectroscopic ellipsometer. Comparing the curves demonstrates that the results are reproducible. This is despite inaccuracies in the sample alignment and the modelled film thickness adjustments when calculating the dispersion.

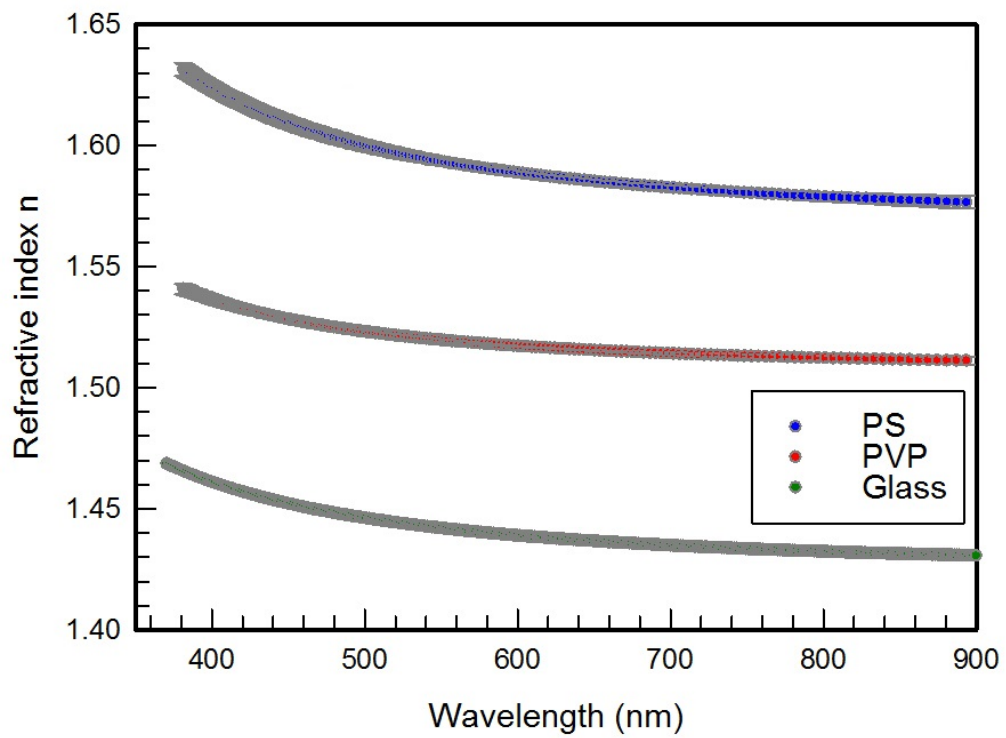


Figure 4.19: The dispersion PVP, PS and glass. These samples were measured using the spectroscopic ellipsometer. Two different samples (with different thickness films) were prepared for each polymer. Each sample was measured ten times and repositioned after each measurement. The dispersion curve for the polymers is an average of twenty measurements, because two different samples were prepared for each polymer.

The wavelength dispersion of the refractive index for PS, PVP and a glass slide are shown in figure 4.19. The analysis of the glass slide only had a single interface (the substrate was a semi-infinite medium). Black tape was attached to the underside of the glass slide to reduce secondary reflections from the bottom interface (glass \rightarrow air). The secondary reflections would otherwise interfere with the reflections from the top interface and change the measurements (air \rightarrow glass) [10].

4.5 UV/visible spectrometry

UV/visible spectrometry was used to measure the optical properties of polymer films and DBR samples. This technique can be used to measure the optical absorption, transmission and reflection of a sample. The materials used in this research needed to be non-absorbing in the UV/visible spectrum. Absorption bands would reduce the reflectance of a DBR reflection peak (if the reflection peak and absorption bands overlapped). This equipment was also used to measure the UV/visible reflection bands of DBR samples.

A white light source emitting in the UV/visible wavelengths and a *Ocean Optics RedTide USB650* spectrometer were integrated into two different optical set-ups. The optical spectra were recorded and analysed on a computer.

A transmission spectrometer was built to measure samples prepared on top of transparent glass slide substrates. A reflection spectrometer set-up (a.k.a. reflectometer) was also built and used to measure samples which were prepared on opaque substrates. The set-ups were aligned so the beam from the light source reflected off the sample and into the spectrometer. A high reflectance silver mirror was used to align the beam for the reflectometer. A background was recorded before the optical properties of the samples were measured. The sample was then placed into the spectrometer set-up (replacing the silver mirror in the reflectometer) and the spectra was measured. Reflectance and transmittance were measured by calculating the ratio of the intensities obtained in the sample and the background spectra.

4.5.1 UV/visible spectra measured in transmission

The optical spectra of samples which were spin-cast onto glass slide substrates could be measured in transmission. Spectroscopic measurements of thick poly-

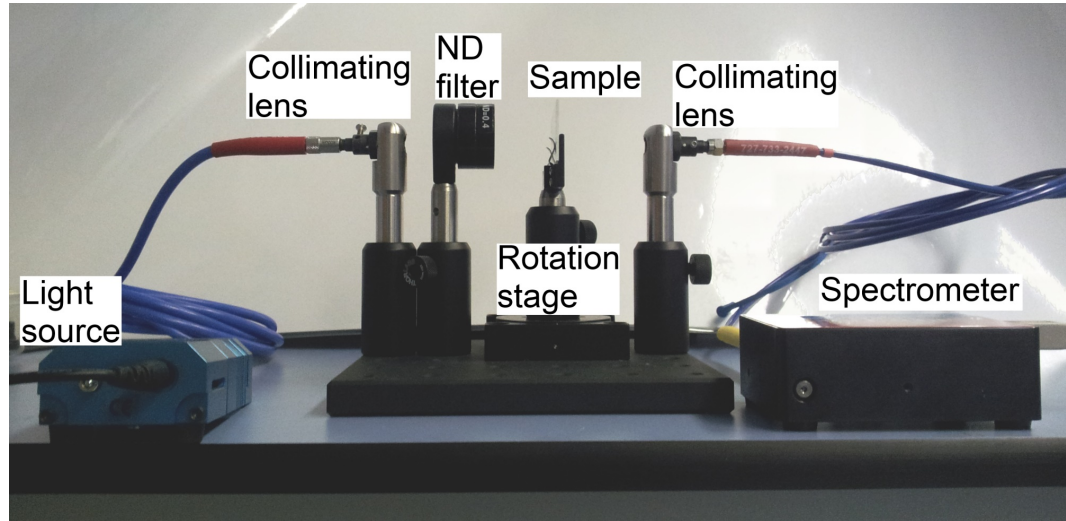


Figure 4.20: Optical arrangement for the transmission set-up spectrometer. This was used to measure the UV/visible transmission of samples which had transparent substrates. The beam from a white light source was passed through and collimating lens via an optical cable. This was transmitted through the sample and another collimating lens focused the light into the spectrometer. The spectra was recorded using a computer.

mer films, cast onto glass-slide substrates, were used to measure any absorption in the spectra of the samples in the UV/visible wavelengths. These results showed that the polymer films were non-absorbing between $350nm \rightarrow 900nm$ wavelengths. Optical microscopy, ellipsometry and atomic force microscopy (AFM) showed that the films were uniform, homogeneous and defect free. Absorption and scattering losses were negligible, so light was either transmitted or reflected by the sample. The following approximation was used to calculate the reflectance of a sample when measuring it with the transmission spectrometer set-up [10],

$$R = 100\% - T. \quad (4.12)$$

Where R = reflectance [%] and T = transmittance of the sample [%].

Figure 4.20 shows the transmission UV/visible spectrometer set-up. White light was passed through a collimating lens via an optical fibre. The intensity of the light beam was attenuated using a neutral density filter to prevent the spectrometer from saturating. A sample was secured onto a rotation mounting stage (for angular measurements which are discussed more thoroughly in section 5.5). The transmitted light was collected using another collimating lens. Light

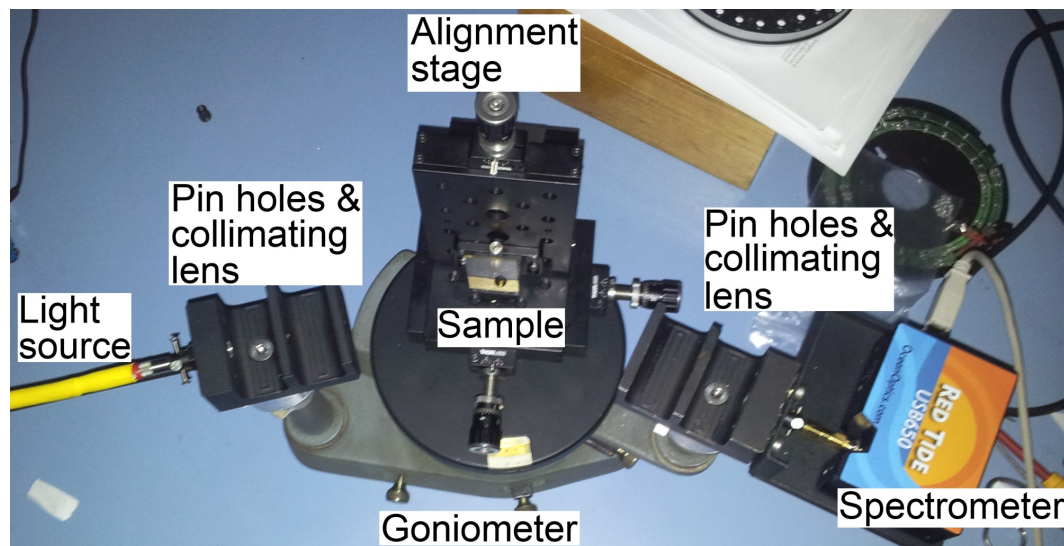


Figure 4.21: The reflectometer optical set-up. This used various components which were mounted onto a goniometer. The beam from a white light source was passed through two pinholes to align and collimate the beam. A sample was placed onto a sample stage which intercepted the incident light. The sampled was aligned by adjusting the translation stages which were built into the sample stage. Reflected light was passed through two aligning pin-holes and into the spectrometer. The orientation of the light source, sample stage and detector could be changed and measured by using the goniometer.

was then passed to the spectrometer via an optical fibre. *Spectra Suite* (Ocean Optics) software was used to analyse the spectrometer data.

The equipment was designed so that it would be possible for angular measurements of the sample. Rotating the sample stage changes the angle of incidence. This also changes the angle of refraction for light propagating through the sample (Snell's law of refraction $n_1 \sin(\theta_1) = n_2 \sin(\theta_2)$ [10]). The path of the beam was diverged slightly as the sample was rotated away from normal incidence. The path of the transmitted light id deviated/shifted. A large collection lens was used to collect all of the transmitted light. This included when the transmitted beam path was deviated by rotating the sample.

4.5.2 UV/visible spectra measured in reflection

Some samples could not be measured in transmission because their substrates were opaque. The optical spectra of these samples had to be measured in reflection. A purpose built reflectometer was constructed (figure 4.21). The white light source illuminated the sample with a collimated beam. This set-

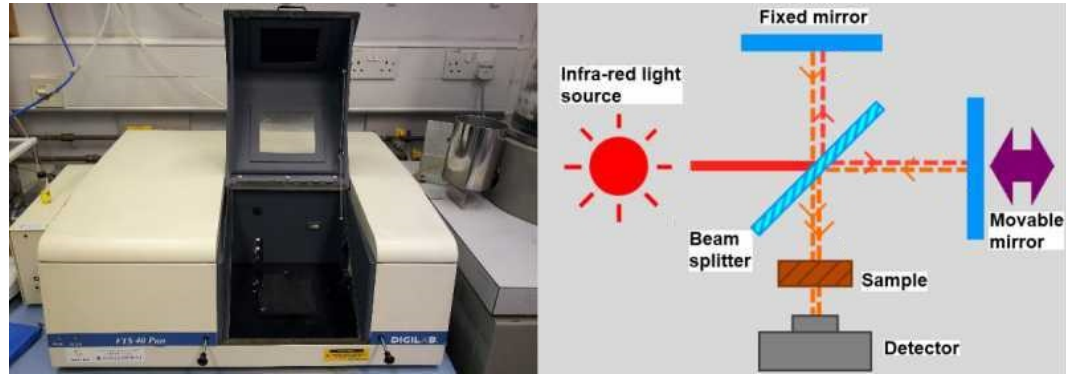


Figure 4.22: [Left panel] The Digilab FTS4000 FTIR spectrometer which was used to measure the infra-red properties of polymer DBR samples. [Right panel] Schematic of the infra-red beam path in a FTIR set-up [69].

up used 3 translation and 2 rotation stages were used to adjust the position of the sample and align the path of the beam. The reflected light was then measured using the *Ocean Optics RedTide USB650* spectrometer. All of the components were mounted onto a goniometer. This enabled the light source and the spectrometer to be rotated about the sample which was positioned at the centre of rotation. Pin-holes were used to collimate and align the beam so the samples reflectance could be measured at different angles of incidence and/or reflection. This is discussed in greater detail in chapter 10.

4.6 Fourier transform infra-red spectroscopy

Fourier transform infra-red (FTIR) spectrometers are used for measuring the chemical composition of samples [69]. Most FTIR spectrometers consist of a broadband infra-red light source, Michelson interferometer, sample stage and detector (illustrated in the right panel in figure 4.22). The measured spectra is analysed using a computer [69, 70]. A *Digilab FTS4000* spectrometer was used to measure the samples described in this thesis (shown in the left panel in figure 4.22).

The right panel in figure 4.22 illustrates the FTIR spectrometer set-up. A beam from a broadband infra-red light source is transmitted into a Michelson interferometer [69, 70]. For simplicity, a mono-chromatic infra-red light source with a well defined wavelength λ is initially considered. The two reflected beams in the interferometer undergo recombination and constructively interfere when the path difference between the beam splitter and both mirrors is

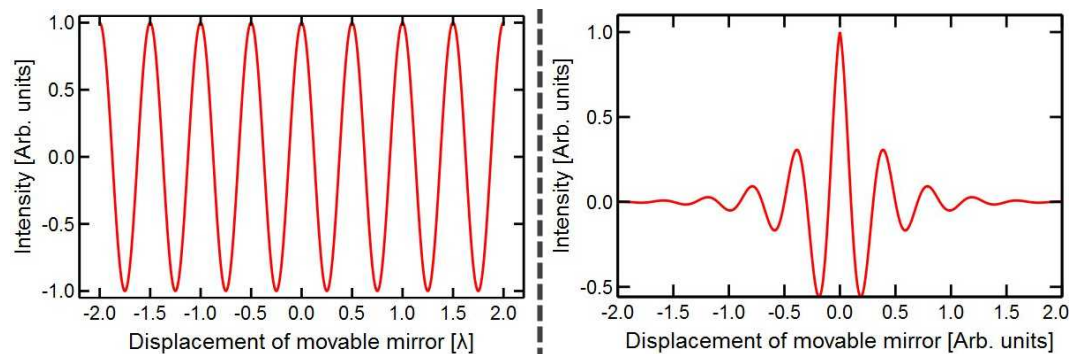


Figure 4.23: [Left panel] Representation of the intensity of a monochromatic beam as it is being modulated by the movable mirror changing position. [Right panel] A representation of a broadband beam which has been modulated by varying the position of the movable mirror.

equal to one another. However, if the movable mirror were displaced by $\lambda/4$, the optical path difference would change by $\lambda/2$. This is due to the beam travelling twice the spatial distance. De-constructive interference occurs when the optical path difference between the two beams is $\delta = \lambda/2$. The two beams will constructively interfere when the mirror is moved by a distance of $n\lambda/2$ (where $n = 0, 1, 2, \text{etc}$), which results in the optical path difference between the two beams becoming $\delta = n\lambda$ [70]. Moving the mirror in a constant direction causes the intensity of the measured beam to oscillate sinusoidally (illustrated in figure 4.23 [left]). The same process occurs for broadband sources, but moving the mirror would cause the intensity of each wavelength to modulate (figure 4.23 [right]). Therefore, the interferogram (measured intensity signal) of the beam incident onto the sample is changed by varying the mirror position in the interferometer [69]. FTIR measures the intensity at all wavelengths with respect to mirror position. This data is analysed using a Fourier transform to calculate the intensity of the spectra with respect to wavelength [70]. Measurements of samples must be ratioed to background measurements before being analysed with the Fourier transform. This is so only the properties of the sample are analysed and effects due to instrumentation and optics are removed. Equations 4.13 and 4.14 are calculations for the intensity of the beam incident on the detector ($I(\delta)$) and the spectral power density for a particular wave-number ($B(\bar{\nu})$) respectively [70];

$$I(\delta) = \int_{-\infty}^{+\infty} B(\bar{\nu}) \cos(2\pi\bar{\nu}\delta) d\bar{\nu} \quad (4.13)$$

and

$$B(\bar{\nu}) = \int_{-\infty}^{+\infty} I(\delta) \cos(2\pi\bar{\nu}\delta) d\delta \quad (4.14)$$

Where $I(\delta)$ = intensity of the beam incident on the detector [%], $B(\bar{\nu})$ = intensity of the beam with respect to wave-number [%], $\bar{\nu}$ = wave-number of the wavelength being analysed [cm^{-1}] and δ = optical path difference between the reconstructed beams from the interferometer [cm].

The wave-number $\bar{\nu}$ is the inverse of the wavelength and conventionally written in units of cm^{-1} [70]. However, the results in this thesis are plotted with respect to wavelength instead of wave-number. This is so the FTIR data is easier to compare with the UV/visible data. The wavelength was calculated by;

$$\lambda = 1/\bar{\nu} = c/\nu \quad (4.15)$$

where c = speed of light [cm/s], ν = frequency of the wave [s] and the wavelength is written in units of cm .

FTIR can be used to measure the infra-red absorption bands of molecules to help identify its chemical composition and structure. The incident infra-red energy excites the molecule from its ground state into a vibrational and/or bending mode. These discrete absorption states correspond to the ‘missing’ absorption bands measured in the transmission spectra [69, 70]. Changing any of the following will also change the absorption spectra of a molecule;

- *Mass of the atoms*: Like a mass on a spring, more energy would be needed to drive a system with larger massed bodies than one consisting of smaller masses [70].
- *Strength of the bond between atoms*: More energy is required to drive a system which has a stronger bond between two atoms [70]. This is equivalent to trying to oscillate two masses coupled with a spring of high spring constant.
- *Geometry of the molecule*: A polar molecule has more rotational degrees of freedom than a linear molecule. More degrees of rotation results in higher orders of vibrational modes [69].

The components of a molecule (like O – H in water) have their own absorption bands due to rotational and vibrational energy modes. Literature values

and FTIR measurements can be cross-compared to determine the chemical composition of a sample [69, 70].

The absorption spectra of a sample is different when there has been a chemical change. For example, swelling will introduce a new chemical into the sample and new absorption bands will appear. Likewise, de-swelling will remove absorption bands as the chemical has been removed. The absorption spectra also changes if there has been a chemical reaction. This is due to the chemical structure of the sample being changed by the chemical reaction [69, 70].

The O – H bond in water is a strong infra-red absorber. Its presence can dominate the spectra and prevent more discrete absorption peaks from being detected (such as C – H). Removal of water was needed to measure smaller peaks. The FTIR sample chamber was continuously purged with dry air to improve the quality of results [69]. This was necessary for the PVP/PS DBRs because PVP swells with water.

4.7 Neutron reflectivity

Neutron reflectometry is used to measure the properties of thin films which may be difficult to measure with other techniques such as x-ray reflectometry. X-rays are easier to produce, focus, filter and are readily available [55]. However, despite having a wavelength comparable to atomic spacing ($\sim 1\text{\AA}$), x-ray reflectivity experiments are not able to resolve smaller atoms such as hydrogen. Polymer samples are also difficult to measure as, like hydrogen, they only weakly scatter x-rays because of their low electron density. Large doses of x-ray radiation are needed to measure polymer samples. This can burn and damage the samples while they are being measured. Furthermore, the contrast between different polymer samples is very low as they have similar chemical structures and composition. Hence, x-ray reflectometry is not a suitable technique for measuring the structure of multi-component polymer samples [55, 71]. Neutron reflectivity is a better technique for investigating polymer structures. Using deuterated polymer adds contrast between polymer samples (which is discussed in greater detail later in this section). Soft matter samples, such as polymers, can be scanned without being burnt.

A typical neutron reflectometer set-up is shown in figure 4.24. The polymer samples were measured using the *Inter* reflectometer at the ISIS facility in Oxfordshire, UK. Neutrons are produced at that facility by bombarding a tungsten

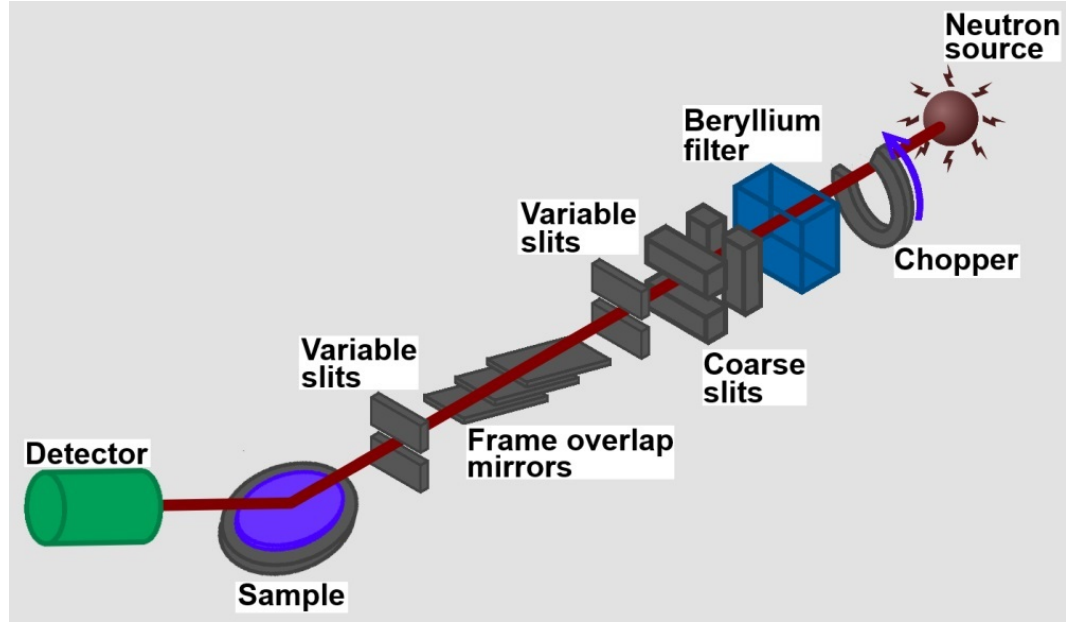


Figure 4.24: This diagram represents a typical neutron reflectometer set-up [71]. Measurements from this type of set-up were used to measure the polymer-polymer interface widths within polymer multi-layers.

target which accelerated protons. The production of neutrons was pulsed so that the high velocity neutrons can be removed by using a ‘chopper’. Neutrons allowed past the chopper were slowed using a beryllium filter. Beryllium has a large scattering cross section which inelastically scatters the neutrons for them to lose a sufficient proportion of their energy. The beam passed through coarse and variable slits to focus it onto the sample. Slow moving neutrons were removed by passing the beam through frame overlap mirrors. Without these mirrors, the slow neutrons would fall incident onto the sample in between pulses. This would add unnecessary background noise to the measurements. The remaining neutrons were reflected from the sample and measured with the detector [71].

Neutrons have a *de Broglie* wavelength which is comparable to atomic spacing ($\sim 1\text{\AA}$) and a high penetration depth [55,71]. The wavelength of a neutron is calculated by [71],

$$\lambda_{Neutron} = \frac{h}{m_n v}. \quad (4.16)$$

Where m_n = mass of a neutron [$1.675 \times 10^{-27} \text{kg}$] and v = neutron velocity [ms^{-1}].

Neutrons have no electric charge and are not scattered by electrons. Instead, the reflection of neutrons is by inelastic scattering with the nuclei of the sample [55]. Incident neutrons collide with, but do not penetrate into the nuclei of samples. The neutron scattering properties of nuclei are not the same for different isotopes of the same element. This is because of the differences in the atomic mass [55]. Polymer molecules are predominantly made from carbon and hydrogen atoms. It would be difficult for neutron reflectivity experiments to differentiate between different polymers because they share similar chemical composition and structures. However, the hydrogen atoms in a polymer molecule can be replaced with its heavier isotope *deuterium*. Deuterating the polymer does not change its chemical properties as deuterium is a isotope of hydrogen. Samples made from a deuterated polymer can be prepared using the same techniques as their non-deuterated equivalent. Neutron reflectivity is able to measure the difference in scattering properties between deuterated and non-deuterated polymers [55, 71]. The structure of the multi-layer polymer samples was measured using neutron reflectivity by replacing the PS layers with a fully deuterated equivalent (this is discussed more thoroughly in section 4.7.1).

Neutrons have a magnetic moment of $\mu = -1.913\mu_N$ (where the nuclear magneton $\mu_N = 5.051 \times 10^{-27} JT^{-1}$), which is due to its quantum mechanical spin $S = 1/2$ [55]. Magnetic fields are used to control the path direction and focus a neutron beam. However, the magnetic moment of the samples nuclei is not strong enough to significantly scatter the neutron beam. The neutron beam is scattered by elastically colliding with the nuclei within a sample. This enables the neutron beam to penetrate deep into the sample, as only a fraction of the space within a sample is occupied by its nuclei [55].

Elastic neutron scattering occurs when a slow moving electron is scattered by a collision with a nucleus and no/little energy is lost (shown in figure 4.25). The magnitude of the incident wave-vector is equal to the scattered/final wave-vector [71];

$$k = |\mathbf{k}_i| = |\mathbf{k}_f| = \frac{2\pi}{\lambda}. \quad (4.17)$$

Where $|\mathbf{k}_i|$ = initial neutron wave-vector [m^{-1}], $|\mathbf{k}_f|$ = final neutron wave-vector [m^{-1}] and λ = wavelength of neutron [m].

For intuitive simplicity, it is easier to approach the problem as if it were an optical system with multiple interfaces and differing refractive indices. This

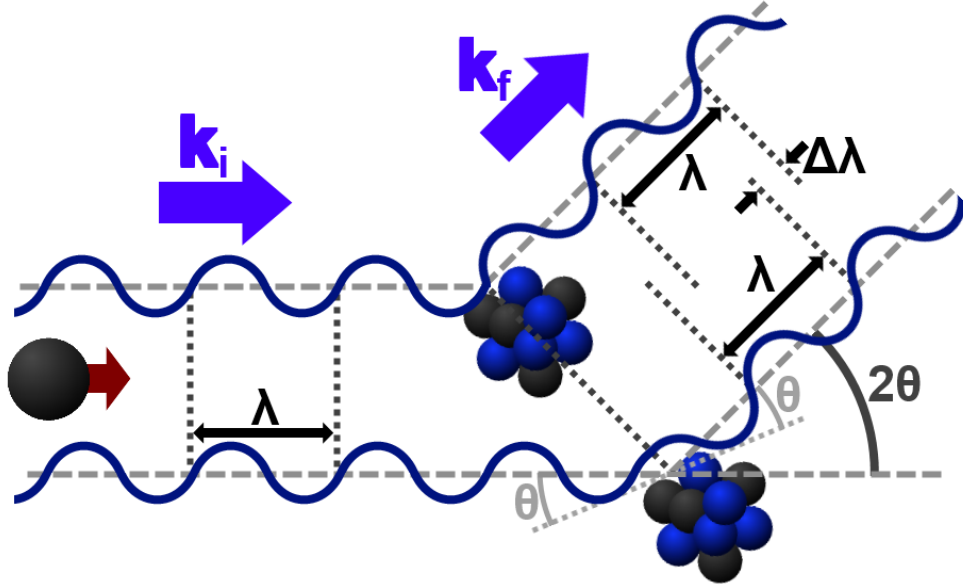


Figure 4.25: Diagram of an incident beam of neutrons which are scattered by the nuclei of the sample. \mathbf{k}_i and \mathbf{k}_f are the initial and final neutron beam wave-vectors respectively. λ is the wavelength of the neutron beam. $\Delta\lambda$ is the phase difference between scattered beam which undergo interference. The beam is scattered by 2θ since the x-axis of the reference frame is parallel to the path of the incident neutron beam.

approach makes it easier to calculate the properties of multi-layer samples and it is also comparable to the modified optical transfer matrix method used throughout this research (which is discussed in chapter 3). Figure 4.26 is a diagram of a neutron beam as it is reflected by multiple interfaces. The ‘*refractive index*’ of the media are calculated by the wave-vector of the neutron beam as it passes through air (\mathbf{k}_0) and the polymer layer (\mathbf{k}_j , where $j = 1, 2, 3, \dots$, etc). Therefore, the ‘refractive index’ of a neutron beam in air is $n_0 = 1$. The ‘refractive index’ for a neutron beam passing through a media j is [55],

$$n_j = \frac{k_j}{k_0}. \quad (4.18)$$

This is also written as [72],

$$n = 1 - \lambda^2 A + i\lambda B. \quad (4.19)$$

Where [72];

$$A = \frac{Nb}{2\pi}, \quad (4.20)$$

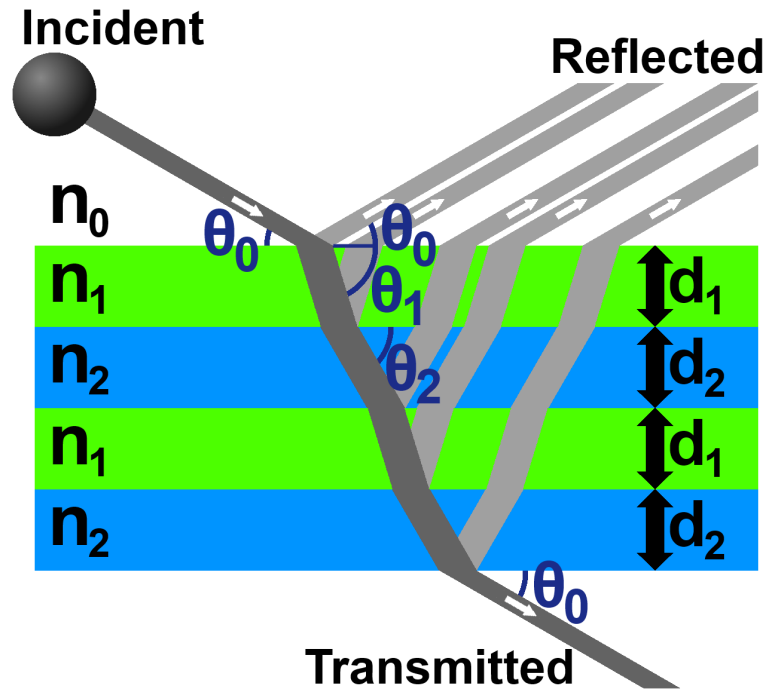


Figure 4.26: Diagram of an incident neutron beam which is partially reflected and transmitted by multi-layer interfaces. This occurs for whenever the beam encounters an interface (only beams which have been partially reflected once are shown in the diagram). Partial reflections from each interface constructively interfere to contribute towards the total reflection. Unlike optics, the angle of the incident and refracted beams was measured with respect to the surface and not the surface normal.

and

$$B = \frac{N\sigma_a}{4\pi}. \quad (4.21)$$

Where N = atomic number density [m^{-3}], b = bound coherent scattering length [m], σ_a = absorption cross-section [m^2] and λ = neutron wavelength [m].

The absorption cross-section σ_a is often ignored ($B = 0$) unless the sample is a strong neutron absorber ($B \neq 0$). Equation 4.19 can be extended to include magnetic scattering. However, this is also unnecessary for the analysis of polymer samples [72].

Fresnel's law of refraction predicts the existence of a critical angle θ_c which results in total internal reflection when the angle of incidence $\theta > \theta_c$. This occurs when the incident light is not refracted into the second medium and is only reflected from the interface [10]. There is an equivalent *critical glancing angle* for neutron reflectivity and it is conventionally measured with respect to the sample surface [71] (whereas optical measurements are conventionally measured with respect to the surface normal). The critical glancing angle θ_c is calculated by assuming that the initial interface is air-polymer [72];

$$\begin{aligned} n_1 \sin(\theta_1) &= n_2 \sin(\theta_2), \\ n_1 \sin(\pi - \pi/2) &= 1 \times \sin(\pi - \theta_c), \\ n_1 \cos(\pi/2) &= 1 \times \cos(\theta_c), \\ n_1 &= \cos(\theta_c). \end{aligned} \quad (4.22)$$

It is assumed that the small angle approximation $\cos(\theta) = 1 - (\theta^2/2)$ is suitable for θ_c [72]. Hence,

$$\begin{aligned} 1 - \frac{\theta_c^2}{2} &= 1 - \frac{\lambda^2 N b}{2\pi}, \\ \theta_c &= \lambda \sqrt{\frac{N b}{\pi}}. \end{aligned} \quad (4.23)$$

Neutron reflectivity measures the sample at an angle which is close to but not smaller than θ_c . Measuring at smaller angles of incidence increases the resolution of the experiment [55, 71]. However, the neutron beam is totally internally reflected if the sample is measured at an angle below θ_c . This results

in non of the internal structure of the sample being measured. Samples are measured at a grazing angle of incidence which is slightly greater than θ_c [55,71]. Solid surfaces are typically measured at 0.5° and above with respect to the surface [71].

The reflectance for a single interface of two bulk media is equivalent to the reflectance obtained from Fresnel's equations [10, 72],

$$R_{01} = \left| \frac{n_0 \sin(\theta_0) - n_1 \sin(\theta_1)}{n_0 \sin(\theta_0) + n_1 \sin(\theta_1)} \right|^2. \quad (4.24)$$

Samples consisting of more than a few layers are better calculated using the modified optical matrix method (which is discussed further in chapter 3). Each layer is calculated as [72],

$$M_j = \begin{bmatrix} \cos(\beta_j) & -(i/p_j) \sin(\beta_j) \\ -(ip_j) \sin(\beta_j) & \cos(\beta_j) \end{bmatrix}. \quad (4.25)$$

where,

$$p_j = n_j \sin(\theta_j), \quad (4.26)$$

and

$$\beta_j = \left(\frac{2\pi}{\lambda} \right) n_j d_j \sin(\theta_j) \quad (4.27)$$

Where d_j = the thickness of the layer j which the neutron beam is propagating through, β = *optical path length* of layer j .

The entire multi-layer sample is calculated by multiplying all of the matrix components of equation 4.25. Hence,

$$M_{total} = M_1 M_2 M_3 \dots M_n \quad (4.28)$$

The total reflectance is calculated by the components of the matrix [55,72],

$$R = \left| \frac{(M_{11} + M_{12}p_s)p_a - (M_{21} + M_{22})p_s}{(M_{11} + M_{12}p_s)p_a + (M_{21} + M_{22})p_s} \right|^2. \quad (4.29)$$

Where p_a and p_s correspond to equation 4.26 to include the initial air and final substrate interfaces respectfully.

However, the matrix method used thus far has assumed that interfaces are have no roughness and are sharp. The intensity of a reflected beam from a

single interface is calculated as [72];

$$I(\lambda) = I_0(\lambda)e^{-q_0q_1\langle\sigma\rangle^2}, \quad (4.30)$$

Where,

$$q_j = 2k_j\sin(\theta_j). \quad (4.31)$$

Where I_0 = reflection intensity without roughness [*counts*], $\langle\sigma\rangle$ = root mean square roughness of the interface [m^2].

It was assumed that the roughness of an interface could be suitably modelled by a Gaussian curve (shown in equation 4.30). The following equation is a single interface Fresnel coefficient which has been modified using equation 4.30,

$$r_{ij} = \left(\frac{p_i - p_j}{p_i + p_j}\right) e^{-0.5q_0q_1\langle\sigma\rangle^2}. \quad (4.32)$$

Where p_i & p_j are given in equation 4.26.

This is comparable to the diffuse interface approximations which were discussed for optical calculations (See section 3.7). However, it is difficult to substitute equation 4.32 into equation 4.29. This method does not calculate the reflectance using a series of single reflectance coefficients. Instead, a similar matrix technique known as *Abeles method* is used [72],

$$C_m = \begin{bmatrix} e^{i\beta_{m-1}} & r_m e^{i\beta_{m-1}} \\ r_m e^{-i\beta_{m-1}} & e^{-i\beta_{m-1}} \end{bmatrix}. \quad (4.33)$$

Each layer m is defined by a 2×2 matrix C_m . Multiplying all of the matrices together results in a 2×2 matrix which characterises the entire sample (as was shown in equation 4.28). The reflectance was calculated by taking the ratio of the appropriate components and multiplying them by their complex conjugate [10, 72],

$$R = \frac{M_{21}M_{21}^*}{M_{11}M_{11}^*}. \quad (4.34)$$

Finally, it is conventional to measure neutron reflectivity data with respect to the scattering-vector \mathbf{Q} [55],

$$\mathbf{Q} = \mathbf{k}_f - \mathbf{k}_i. \quad (4.35)$$

The magnitude of the wave-vector for inelastic scattering ($|\mathbf{k}_f| = |\mathbf{k}_i|$) is

calculated by;

$$\begin{aligned}
Q^2 &= |\mathbf{Q}|^2 = (\mathbf{k}_f - \mathbf{k}_i)^2 \\
&= |\mathbf{k}_f|^2 + |\mathbf{k}_i|^2 - 2\mathbf{k}_f\mathbf{k}_i \\
&= |\mathbf{k}_f|^2 + |\mathbf{k}_i|^2 - 2|\mathbf{k}_f\mathbf{k}_i| \cos(2\theta) \\
&= 2k^2 - k^2 \cos(2\theta) \\
&= 2k^2 [1 - \cos(2\theta)] \\
&= 2k^2 [2 \sin^2(\theta)] \\
&= 4k^2 \sin^2(\theta).
\end{aligned} \tag{4.36}$$

Note that the wave was scattered by an angle of 2θ since the x-axis is parallel to the direction of the incident wave (see figure 4.25). Also, the trigonometric relation $\cos(2\theta) = 1 - 2\sin^2(\theta)$ [73] was used to solve the previous equation.

Hence,

$$\begin{aligned}
Q &= 2k \sin(\theta) \\
&= \frac{4\pi}{\lambda} \sin(\theta).
\end{aligned} \tag{4.37}$$

The reflectance of the sample was measured with respect to changes in the neutron wave-vector. Q is a dispersive function, which is dependent upon the neutron wave-length λ . The dispersion is measured by varying the angle of incidence θ , or energy of the scattered neutrons (which can also calculate λ) [55].

The equations provided in this section can be used to build a computer model of the sample. The properties of the sample were calculated by fitting variables in the model. A fitting program was used (Motofit [74]) to analyse the measured neutron data for different polymer samples.

4.7.1 Preparation of neutron reflectivity samples

Single layer and multi-layer polymer samples were prepared for neutron reflectivity experiments. The polymer-polymer interfaces between spin-cast polymer layers were measured using the samples discussed in this section. PS was replaced with *fully deuterated PS* (dPS) to increase the contrast in neutron scattering length density between PVP/PS layers. The only difference between

the two molecules is the hydrogen atoms being a heavier isotope. Therefore, deuterated PS has the same chemical and optical (refractive index) properties as non-deuterated PS.

The thickness of layers within the neutron reflectivity samples were thinner (reduced to between 140nm and 200nm) than previously prepared PVP/PS multi-layers (typically between $200\text{nm} \rightarrow 530\text{nm}$). This was because thinner films were needed to measure *Kiessig fringes* for single and multi layer films (which are shown in section 8.2). Kiessig fringes occur from the interference between partial reflections from interfaces and are useful for measuring the film thickness [55].

Unfortunately, changes to sample preparation (compared with the PVP/PS multilayer preparation discussed in section 4.3) were needed to make the PVP/dPS multi-layer samples. The deuterated PS was a close, but not an exact, approximate to the non-deuterated PS polymer. For example, the molecular weight of the non-deuterate polystyrene was $\sim 192,000$, whereas the molecular weight of the deuterate polystyrene was $\sim 190,000$. However, PS and dPS are chemically the same so the two materials were comparable. It was more challenging to prepare defect free multi-layer samples which were made from thinner spin-cast polymer layers. The sample preparation technique was modified slightly to improve sample quality (which is discussed later in this section). However, the preparation of PVP/dPS multi-layers was not significantly different from when PVP/PS multi-layers which were previously prepared. UV/visible spectroscopy measurements of a PVP/dPS DBR showed that it had similar optical properties to a PVP/PS DBR. This indicated that the properties of the polymer multi-layer were not significantly changed by the modified sample preparation technique.

The spin-cast films were made thinner by reducing the concentration of the polymer solutions to 2.9% PVP and 3.0% dPS which were dissolved into a mixture of 50:50 ethanol:acetonitrile and toluene respectively. Using the same preparation technique which was used to make the PVP/PS multi-layers resulted in inhomogeneous cracked multi-layers. This was due to the previously deposited films being swollen by solvent when depositing new layers. The sample was protected by reducing its exposure to large quantities of solvent. This was achieved by depositing the solution while the sample was being rotated at 4.0krpm . Most of the solution was ejected off the substrate during the first few moments of exposure to the sample. The sample was spun for 30 seconds

after deposition to ensure that the film was dry. In comparison, the PVP/PS multi-layers were prepared by depositing solutions onto the substrate when it was stationary. HCl vapour was used to swell/protect the PVP layers during both PVP/PS and PVP/dPS multi-layer preparation techniques. The samples were also annealed for 5 hours at 110°C under a $\sim 1\text{mtorr}$ vacuum after all of the layers were deposited.

Six samples were prepared, but only three could be measured using neutron reflectivity. This was because experimental time was lost when the neutron beam went down. We were informed that an error had occurred during routine maintenance. The beam was switched off to enable repairs. However, three samples were measured and their analysis lead towards useful results.

The following samples were prepared and measured using neutron reflectivity. The purpose for each measurement is provided after each sample name;

- *Single deuterated PS layer*: The film thickness and surface roughness of the deuterated polystyrene was measured using neutron reflectivity. These results were later compared with ellipsometry and AFM measurements.
- *PVP (top)→dPS (bottom) bi-layer*: This sample was prepared to measure the PVP→dPS interface. The width of the PVP→dPS interface may not have been the same as the dPS→PVP interface due to how the samples were prepared using solution processing.
- *10 layer PVP/dPS structure*: A multi-layer sample was prepared to test if the interfacial width changes with respect to the number of layers within the structure. For example, does adding more layers increase the interface widths? Does topographical roughening and/or residual solvent broaden the interfacial widths?

The following samples were also prepared, but were not measured using neutron reflectivity. A more complete set of data would have been gathered if the samples were measured because of the following reasons;

- *Uncoated silicon substrate*: The silicon substrate has a native oxide layer which is measurable when using neutron reflectivity. The same type of silicon wafer were used as substrates for the polymer layer samples. This substrate should have be measured independently so the polymer samples could have been more accurately modelled and measured.

- *Single PVP layer*: The film thickness of the PVP films were measured using ellipsometry. The surface roughness of the PVP film was also measured using an AFM. Neutron reflectivity would have been used to complement the previous measurements.
- *dPS (top) →PVP (bottom) bi-layer*: This sample was prepared to measure the dPS→PVP interface. The interfacial width of dPS→PVP may not be the same as PVP→dPS because of the sample being solution processed.

4.8 Time of flight secondary ion mass spectrometry

Time of flight secondary ion mass spectrometry (TOF-SIMS) was used to measure the internal structure of the DBR multi-layers. This included the film thickness of layers and polymer-polymer interface widths. The multi-layer samples were also ideal for testing a new TOF-SIMS sputtering source. It was concluded that TOF-SIMS was useful for measuring complex structures, despite having a poor resolution (when compared with ellipsometry and neutron reflectivity for example). Unfortunately, it could not accurately measure the polymer-polymer interface widths. This is discussed further in chapter 9.

Samples are *depth profiled* by controlled etching using electrons, ions, neutral particles or high energy photon beams. The research in this thesis used clustered beams of ionised atoms (Ar_{2000}^+) to sputter neutral and ionised atoms away from the sample surface (illustrated in figure 4.27). These experiments must be done in a high vacuum so the ionised particles ejected from the sample can be measured [75]. TOF-SIMS usually uses two different etching beams. The *sputter source* was used to etch through the sample with high precision, but it does not yield a large quantity of ionised particles which are detectable. The *analysis beam* was used to produce a large yield of ionised particles, but the sample etch rate was not easily controlled [75]. Alternating between the two beams enables controlled etching and analysis. Both beams raster over the surface ($100\mu m \times 100\mu m$ area), etching through the sample and scanning its freshly sputtered surface. The secondary ions produced by the analysis beam were measured using an ion detector (illustrated in figure 4.28) and recorded onto a computer.

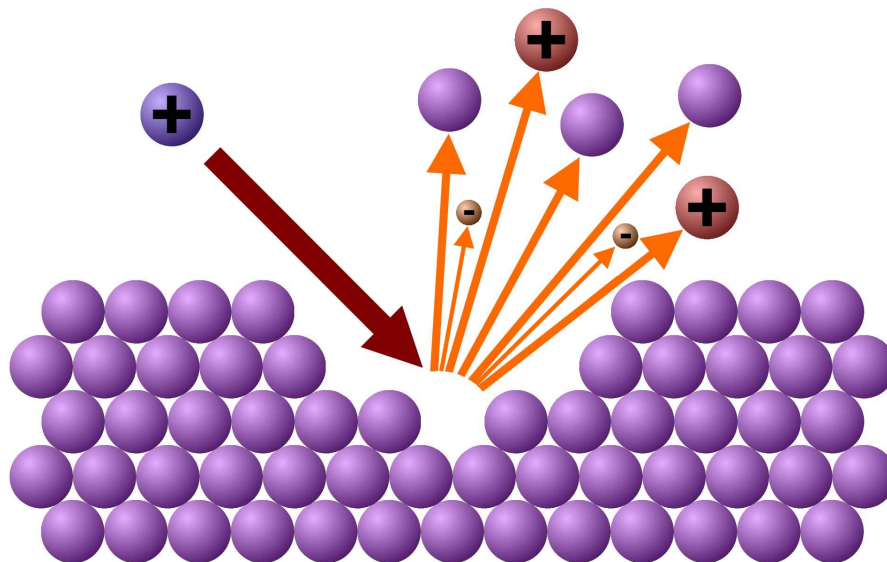


Figure 4.27: An incident ion beam (blue) strikes the surface of a sample (purple). This ejects a mixture of neutral (purple) and charged/secondary ions (red) and electrons (yellow) off the sample. The charged ions are then detected using a mass spectrometer. Analysis was used to measure which ionised molecular fragments had been sputtered off the surface by the ion beam. This was used to determine which chemicals are in the sample and where.

The analysis beam used bismuth as an ion since it produces some of the best ionised atoms/molecules for organic materials [76]. An Argon cluster Ar_{2000}^+ beam was used to etch through the samples. The beam fires a cluster of atoms which is approximately 2000 argon atoms per ion. This was an improvement over the popular C_{60}^{n+} sputter beam, which is unable to etch through materials such as polyethylene, polystyrene and conjugated polymers (which will be referred to as ‘challenging polymers’ in this thesis) [77, 78, 79]. However, it is capable of etching through other polymers like PVP. The inability of ion beams, like C_{60}^{n+} , to etch through challenging polymers is because the beam breaks molecular bonds within the polymer sample whilst etching. The radical polymer chains have unstable electron structures (due to unpaired valence electrons or an electron shell which has not been filled) which causes them to be highly reactive [49]. The radical chains chemically react with the other polymer chains in the sample which causes them to ‘cross-link’. These intermolecular polymer bonds increase the rigidity and integrity of the polymer sample. Cross-linking of challenging polymers decreases the etching rate of ion beams, like C_{60}^{n+} , to near negligible. Ar_{2000}^+ overcomes this problem by significantly reducing the number of radical polymer chains created during etching [78, 79]. This is due

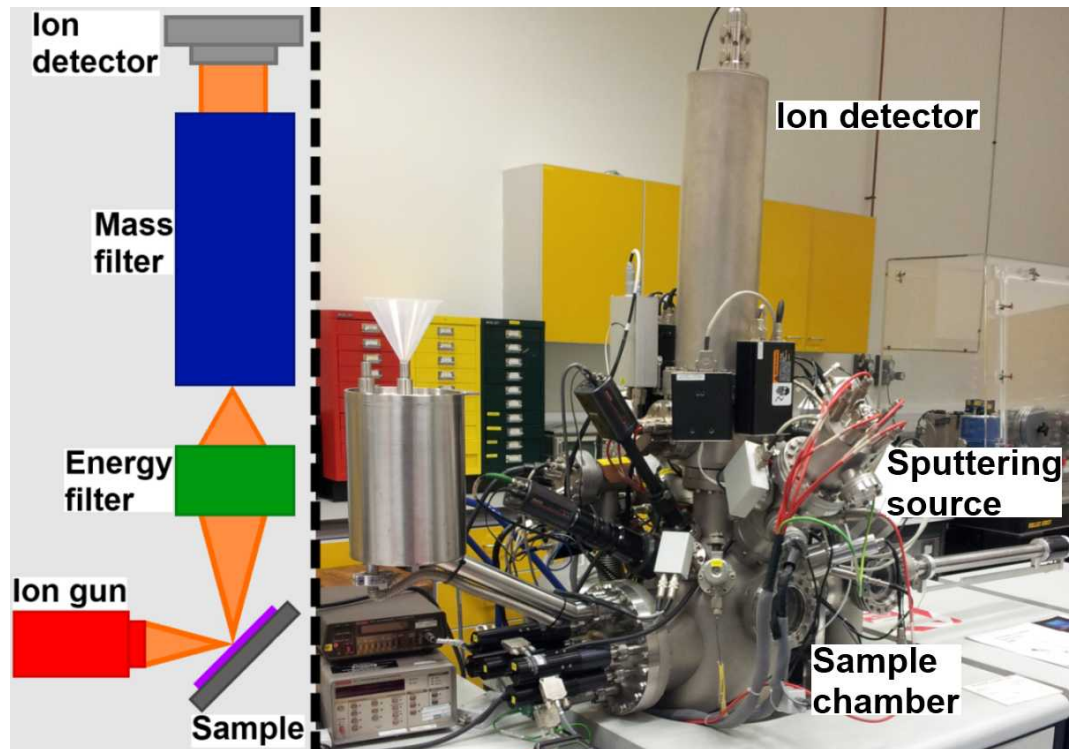


Figure 4.28: [Left panel] A controlled cluster of ions is fired from the ion gun at the surface of the sample. Secondary ions are ejected off the sample and passed through filters. The remaining ions are measured using an ion detector. The ion beam etches in pulses as it rasters over the surface of the sample. [Right panel] Photograph of the TOF-SIMS set-up used at NPL for measuring the polymer DBRs.

to the ion cluster mass/charge ratio being larger.

Experiments had already shown that Ar_{2000}^+ has a relatively constant sputter yields and excellent resolution [80,81]. This made the beam an ideal technique to measure the structure of layered polymer samples. The polymer DBRs which were previously made are also simple multi-layer 1D polymer structures. The film thickness of the polymer layers was previously measured using ellipsometry. UV/visible spectroscopy of these samples showed that the thickness of the polymer films within the multi-layers were well defined. These samples were used to test the depth profiling capabilities and accuracy of the Ar_{2000}^+ sputter source through a multi-layer polymer sample.

Analysis of TOF-SIMS data is often lengthy and requires several processes. Therefore, each process is discussed in the following subsections;

4.8.1 Chemical analysis of mass spectra

TOF-SIMS can be used to chemically profile a sample while etching through it. The mass spectrometer detected the secondary ions which were sputtered off the sample during etching. Each ionised atom and molecule has its own distinct peak with respect to the detected mass of the ionised molecular component. It was possible to determine which chemicals are in a sample by the constituent parts of the mass spectrometer peaks [82]. The spectra shown in figure 4.29 is the mass spectrometry of a PVP/PS multi-layer (shown in the *ION-TOF* software used to analyse the TOF-SIMS measured data). These peaks represent some of the detected ions throughout the experiment over a $100\mu m \times 100\mu m$ sputtered sample surface area. A significant number of the peaks will be shared between the two polymers, since they are both predominantly hydrocarbon structures. However, there are distinct chemical differences between the two polymers which are each represented by their own mass peaks. The best chemical peak markers for PVP and PS were $C_5H_{10}N_3^+$ and $C_7H_7^+$ respectively. Furthermore, the Si^+ peak was also considered so that the substrate could be detected during measurements. The intensity of the $C_5H_{10}N_3^+$, $C_7H_7^+$ and Si^+ peaks were measured while the sputter beams raster and etched through the samples. A large $C_5H_{10}N_3^+$ peak and a low $C_7H_7^+$ peak would indicate that the sputter beams were etching through a PVP layer. Likewise, large $C_7H_7^+$ peak and a low $C_5H_{10}N_3^+$ peak would indicate that the sputter beams were etching through a PS layer. A large Si^+ would indicate that the sputter beams had etched through all of the polymer layers and was in contact

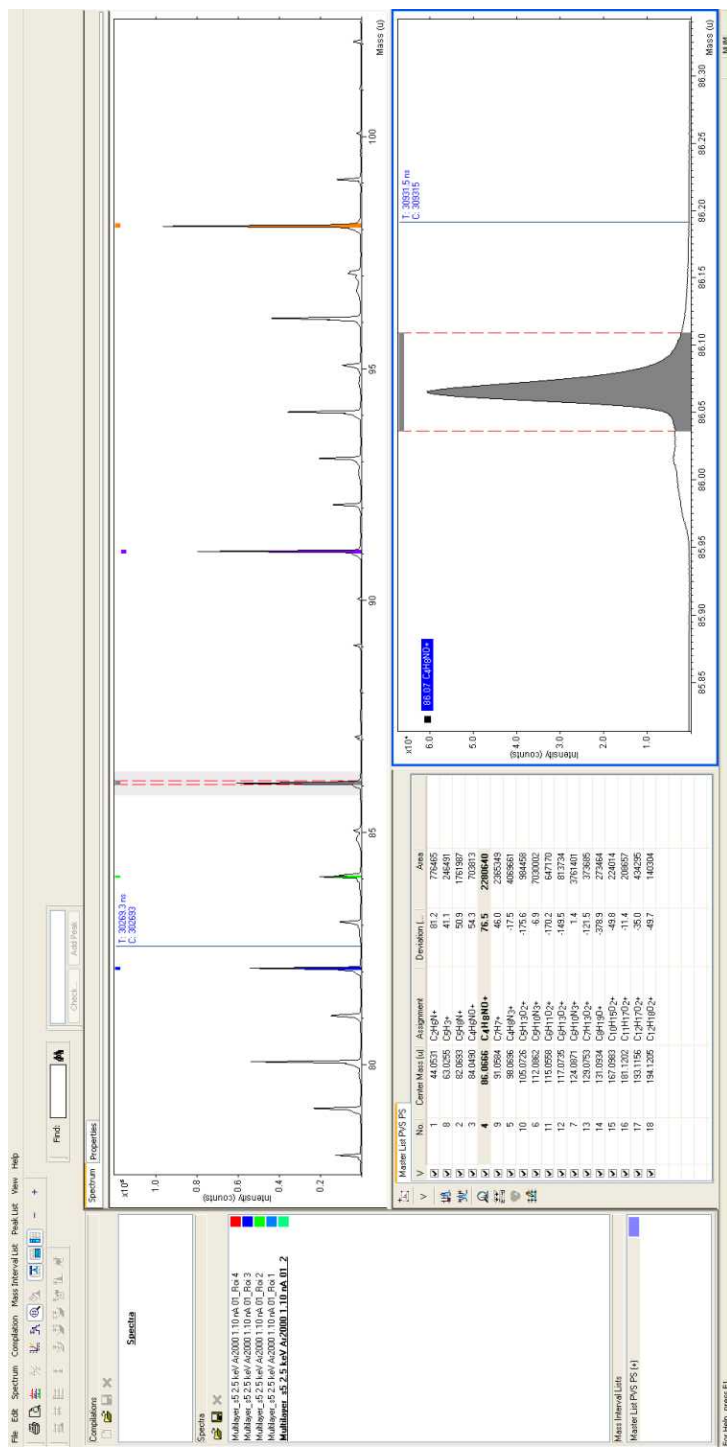


Figure 4.29: Screen caption of the *ION-TOF* software. The top panel (with respect to the screen caption) represents a portion of the mass spectroscopy data for a PVP/PS multi-layer sample. Each peak corresponded to a different ionised molecule which as been detected. The panel on the bottom right was a peak which has been selected for further chemical analysis. Each peak was measured with respect to its ion mass. This was compared to a library to determine which molecule or atom was being measured.

with the substrate. It is important to note that the magnitude of the peak (ion counts with respect to ion mass) does not necessarily indicate that more material is being sputtered from the sample. For example, it does not mean that there is twice as much of material ‘A’ when compared with material ‘B’, if the measurement for peak ‘A’ were twice as large as peak ‘B’. Material ‘A’ may more readily ionise than material ‘B’, which results in a stronger signal for ‘A’ being measured [82]. The ‘etch rate’ (sputtered sample ion count with respect to incident ion beam dose) is a more important measurement, as it calculates how quickly the ion beam etches through a material. This is discussed later in this thesis.

4.8.2 Selecting regions of interest

There were problems with the experimental set-up of TOF-SIMS which caused the depth profile to be misinterpreted. Careful analysis was used to improve the quality of results by understanding the limitations of the TOF-SIMS experimental technique. Unfortunately the TOF-SIMS ion beam was not able to independently measure lateral variation in the topography of a surface. This caused errors in how depth profiling data was analysed. It assumed that any measured samples had a flat surface [82]. Previous measurements of PVP/PS spin-cast multi-layer samples showed that there was a surface roughness between $1\text{nm} \rightarrow 4\text{nm}$. These samples were measured over a $40\mu\text{m} \times 40\mu\text{m}$ surface area using the AFM (which is comparable to the $100\mu\text{m} \times 100\mu\text{m}$ surface area measured using TOF-SIMS). All of the samples were spin-cast onto silicon wafers which had a surface roughness less than 1nm . Therefore, the samples were not perfectly flat and there is a measurable roughness on their surface. However, TOF-SIMS measured the underlying films as being rough, instead of the surface (illustrate in figure 4.30).

Controlled etching was used to measure the structure of a sample when using TOF-SIMS. However, the etch rate of the ion beam can be disturbed by inhomogeneity in density of the film and/or contaminants from unwanted chemicals. This may also include the chemical composition of the film not being uniform, such as trapped solvent within the layers. These defects would change the etch rate through the sample and result in the film thickness being incorrectly measured [82, 83]. The quality of results also degraded during the experiment, as the surface of the sample was continuously roughened by the sputter beams [82]. Anomalies in results are often difficult to correct since the

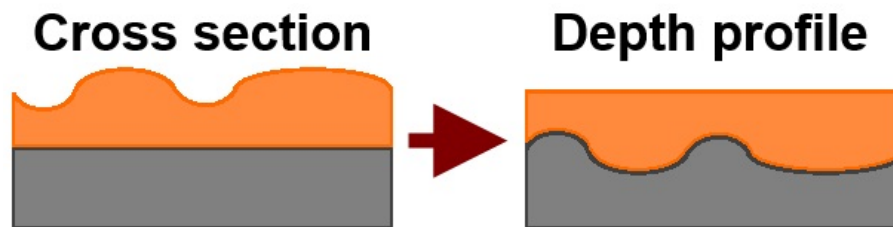


Figure 4.30: [Left panel] An illustration of a rough film which was cast on top of a silicon substrate when viewed as a cross section. The image is a cross-section of the hypothetical sample. [Right panel] The TOF-SIMS depth profile representation of the same hypothetical sample which was illustrated in the left panel. TOF-SIMS is unable to measure the initial topography of the sample's surface. It assumes that the top of the sample is flat and any roughness at the surface is not measured. The ion beam etches through the sample and inadvertently measured the flat interface (film→substrate) as being rough.

proportions of the depth profile are misaligned for subsequent measurements [82]. Any disruption in depth profiling are carried through with the rest of the experiment as it is being etched (illustrated in figure 4.30).

'Regions of interest' were selected to reduce the effects of poor depth profile homogeneity. It was assumed that the top and the bottom of the polymer multi-layers were relatively flat (using the results from previous AFM measurements). A cross section of the silicon-polymer interface was analysed after measuring the sample by depth profiling through it (shown in figure 4.31). Topographically flat regions were selected and are represented in figure 4.31 as 'islands' of continuous 'hue'. Five large (and non-square) regions of interest were selected and each were between 10% → 20% of the total scanned surface area for each sample. These large areas were analysed to minimise experimental noise and repeats were used to improve the quality of results. The depth profile was re-calculated so that each region of interest was re-analysed as if it were an independent sample.

4.8.3 Depth profiling and calibration of sputter rate

The intensity of the mass spectra for PVP ($C_5H_{10}N_3^+$), PS ($C_7H_7^+$) and silicon (Si^+) for each region of interest were plotted with respect to sputter dose of the ion beam. The sputter dose is the number of incident ions (Ar_{2000}^+) per square meter which were fired onto the surface of the sample. The dose of the incident Ar_{2000}^+ etching beam increases with respect to time. Figure 4.32

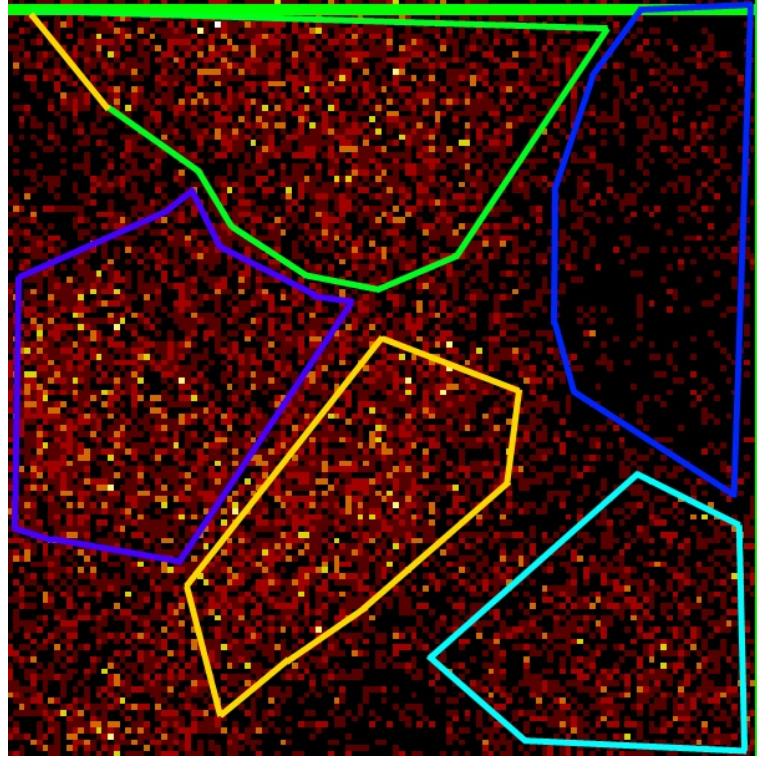


Figure 4.31: This is a cross section of the PVP→silicon interface for a single layer PVP films. TOF-SIMS had measured topographical roughness in the PVP→silicon interface. However, AFM measured a low surface roughness for the silicon substrate and the single layer PVP film. The TOF-SIMS measured roughness of the PVP→silicon interface is a defect in the sputtering technique. Results were improved by measuring five different regions of interest (represented by the coloured outlines in the figure) and calculating the average. Regions were selected by their homogeneity, as it was known the the PVP→silicon interface should have been flat. Each region was between 10% → 20% of the total surface area scanned ($100\mu m \times 100\mu m$).

Material	Ellipsometry: Thickness (nm)	Depth profile: Thickness (dose $\times 10^{18}$)	Depth profile: Interface (dose $\times 10^{18}$)	Etch rate ($\times 10^{-18}$ nm/dose)	Film thickness (nm)	Interface width (nm)
PVP	206.3 ± 1.0	17.67 ± 0.12	0.58 ± 0.03	11.66	206.0 ± 1.4	6.8 ± 0.4
PS	218.7 ± 1.0	14.83 ± 0.17	0.30 ± 0.06	14.77	219.0 ± 5.3	9.3 ± 2.0

Table 4.3: TOF-SIMS dose calibration of PVP and PS spin cast films. The thickness of the films were measured using ellipsometry and were used to calculate the etch rate of the polymers with respect to incident Ar_{2000}^+ ion dose.

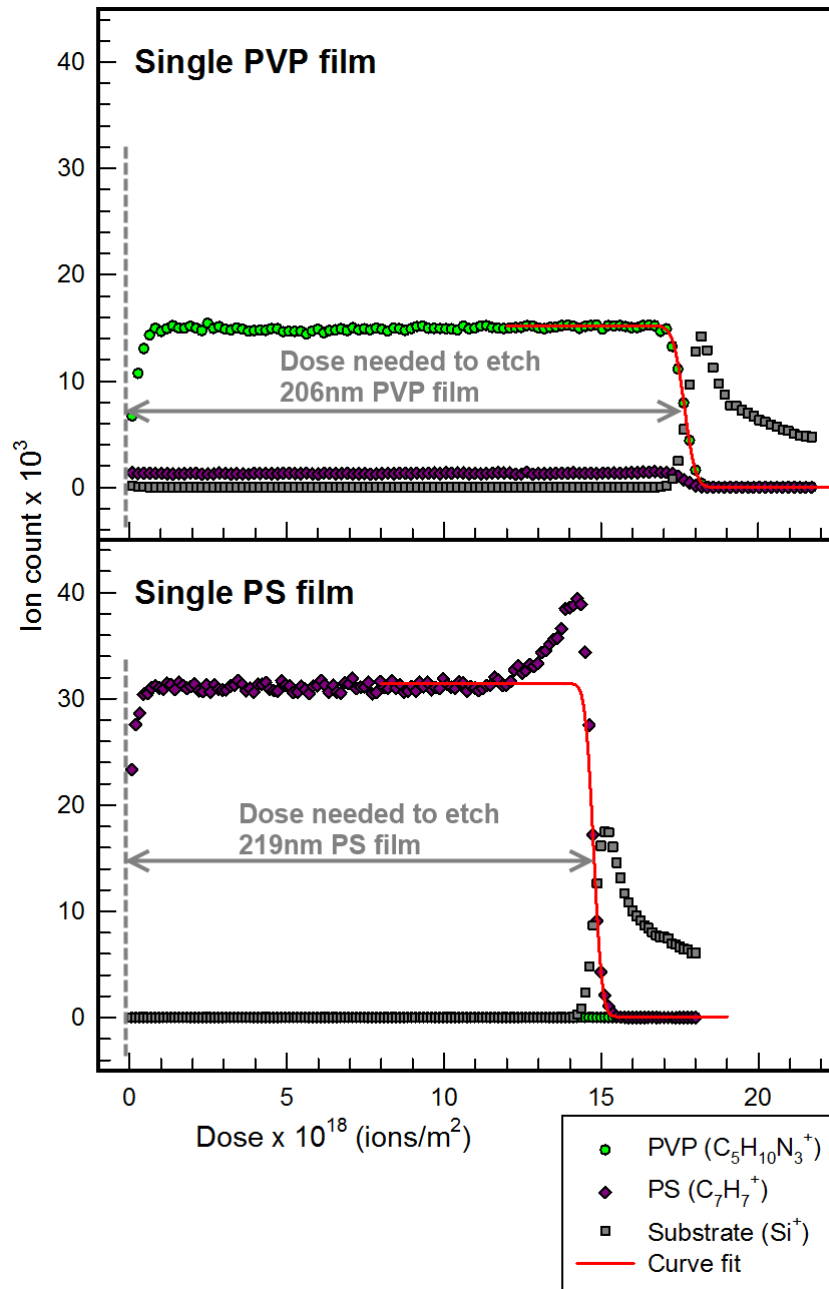


Figure 4.32: [Top panel] TOF-SIMS depth profiling of a single layer PVP film (green data-points). [Bottom panel] Depth profile of a single layer PS film (purple data-points). Both samples were measured over a $100\mu\text{m} \times 100\mu\text{m}$ surface area. The polymer \rightarrow silicon interfaces were fitted with a error function to calculate (red curve) its position (with respect to sputter dose) and interface width. The widths of these depth profile curves are proportional to the thickness of the polymer films. These depth profile measurements were compared with ellipsometry measurements of the same samples. This was used to calculate the etch rate of the incident Ar_{2000}^+ ion dose for both polymer films.

shows the depth profile for single layer PVP and PS films. It was assumed that the Ar_{2000}^+ sputter beam was capable of etching through both PVP and PS at a constant rate. The widths of each curve correspond to when the relevant material was being sputtered off the sample by the Ar_{2000}^+ etching beam. However, the transition from one medium to another is not immediate (which is discussed in greater detail later in this section). Instead, there is an interface width which was modelled by a error function (represented by the red curves in figure 4.32) [73],

$$f(x) = \frac{1}{2} \left[1 + \operatorname{erf} \left(\frac{x - \mu}{\sigma_{S.D.} \sqrt{2}} \right) \right]. \quad (4.38)$$

Where μ = mean of the error function and $\sigma_{S.D.}$ = standard deviation of error function.

Equation 4.38 was modified to consider the analysis of TOF-SIMS,

$$f(d) = \frac{A}{2} \left[1 + \operatorname{erf} \left(\frac{\sqrt{2}(d - \mu)}{\sigma_{Int}} \right) \right] + C. \quad (4.39)$$

Where A = amplitude of depth profile curve [*sputtered ion counts*], d = dose of Ar_{2000}^+ ions, [*ion beam counts*], μ = dose of Ar_{2000}^+ needed to etch through layer [*ion beam counts*], $2\sigma_{S.D.} \equiv \sigma_{Int}$ = width of interface between layers [*ion beam counts*] and C = baseline of the depth profile [*sputtered ion counts*].

The mid-point of an interface μ is the transition point where one material changes to another. Equation 4.39 was always calculated with respect to the bottom of a film (which corresponds to the intensity of the curve reducing). The separation between the interfaces μ was used to measure the thickness of the films. It was assumed that any intermixing of the two polymers would not significantly change the etch rate.

The sharp peak at the bottom of the PS film (at the PS→Si interface, shown in figure 4.32) was not due to the quantity of PS rapidly increasing. Instead, the sputtered material is more readily ionised when it is closer to the silicon interface. The peak was due to an increase in the number of ions being detected [82]. The inflection was ignored when fitting the Gaussian function since it is a error in the measurement system.

The widths of the depth profile curves (shown in figure 4.32) from five dif-

ferent regions of interest each were compared with ellipsometry measurements of the same PVP and PS samples. This was used to calculate the etch rates for each of the polymers. The etch rate of PVP was 11.66×10^{-18} nm/dose and PS was 14.77×10^{-18} nm/dose (shown in table 4.3). This was used to measure the film thickness of polymer layers from TOF-SIMS depth profile data. This calculation was also used to measure the widths of interfaces, using TOF-SIMS.

Chapter 5

UV/visible properties of PVP/PS DBRs

5.1 Introduction

PVP/PS DBRs were prepared using the techniques discussed in section 4.3. The optical properties of the samples were measured in the UV/visible spectrum using the transmission spectrometer described in section 4.5.1. Samples with different numbers of layers and different layer thickness values were prepared, measured and analysed. These experiments were used to measure and control the reflection properties of polymer DBR samples [84].

5.2 Controlling the wavelength of the reflection bands

The graph at the top of figure 5.1 shows the UV/visible reflectance spectrum of a 30 layer DBR. Each layer was spin-cast from 4.0% w.t. PVP in 50:50 ethanol:acetonitrile and 4.0% w.t. PS in toluene, using the preparation techniques which were discussed in chapter 4.3. Single layer samples were also prepared by spin-casting the films onto silicon substrates. These samples were prepared using the same solution concentrations and spin-speeds as the multi-layer samples for comparison. The thickness of the single layer films were

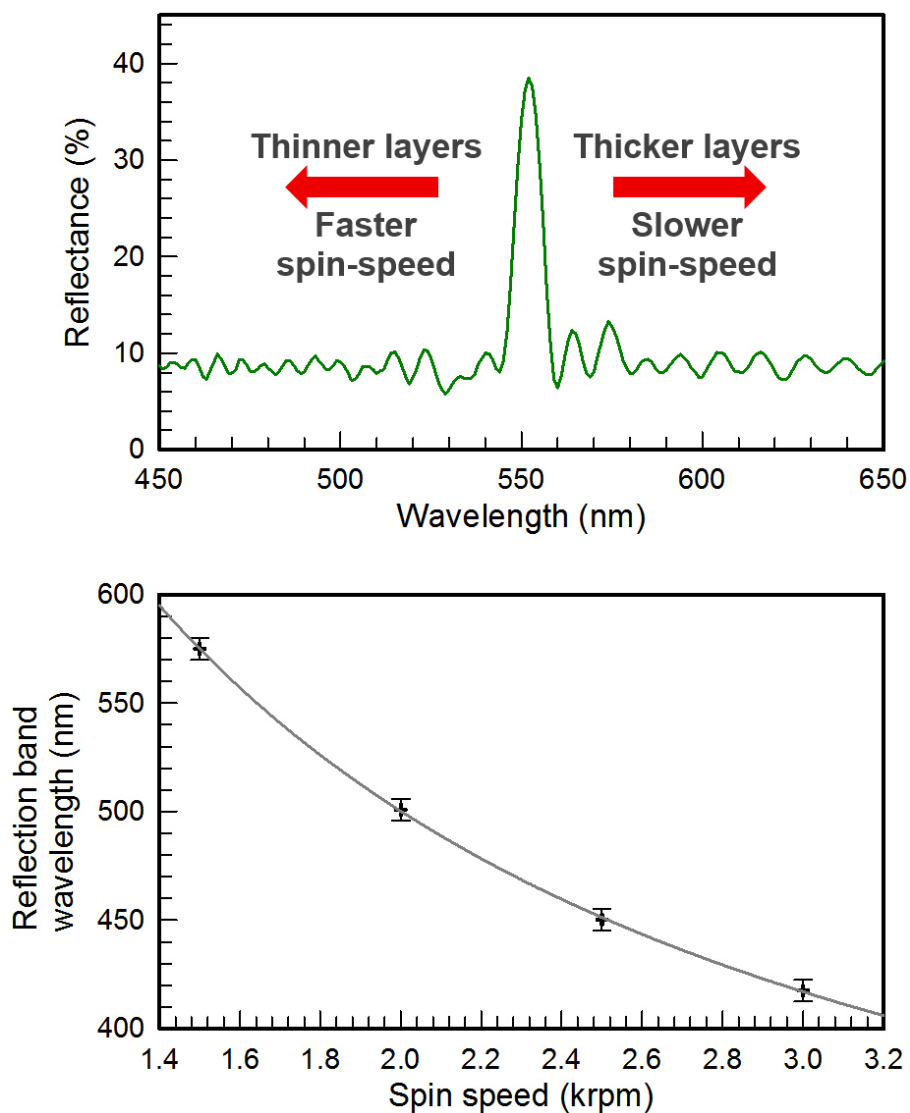


Figure 5.1: [Top panel] The UV/visible spectrum of a 30 DBR made from layers of $439 \pm 1\text{nm}$ PVP and $271 \pm 1\text{nm}$ PS. The position of the reflection band can be controlled by keeping the solution concentrations constant and changing the deposition spin-speed. Depositing thinner/thicker layers will blue-shifted/red-shifted the wavelength of the reflection peak respectively. [Bottom panel] Wavelength of the reflection peak plotted with respect to deposition spin speed. The data points represent sample measurements. Each sample was measured five times and the standard deviation was used as the error. The curve was free-hand drawn.

$d_{PVP} = 459 \pm 1nm$ and $d_{PS} = 271 \pm 1nm$, which were measured using ellipsometry (discussed in section 4.4). These results were used as a measurement of the corresponding thickness of layers in the DBR sample. The 30 layer polymer DBR at the top of figure 5.1 had a reflection peak at $550nm$ (when measured at normal incidence). A series of other 30 layer samples were also prepared using the same techniques and polymer solution concentrations. However, the deposition spin-speed was changed to make the layers thicker or thinner.

The graph at the bottom of figure 5.1 is the wavelength of the peak reflection band with respect to the deposition spin-speed. The thickness of the spin-cast PVP layers were between $\sim 360nm$ and $\sim 530nm$. Likewise, the thickness of the PS layers were between ~ 210 and ~ 320 . Each data-point (in the plot at the bottom of figure 5.1) corresponds to a different 30 layer DBR sample which was prepared using a different spin-speed. Layer thickness increased/decreased when then deposition spin-speed was faster/slower respectively.

The following equation is used to calculate the position of the reflection peak with respect to wavelength. However, this equation only applies for when the sample is being measured at normal incidence. The wavelength position of the reflection peak is calculated by [10],

$$\lambda = \frac{2}{N} (n_1 d_1 + n_2 d_2), \quad (5.1)$$

Where n_1 = refractive index of alternating layer 1, n_2 = refractive index of alternating layer 2, d_1 = film thickness of alternating layer 1, d_2 = film thickness of alternating layer 2 and N = reflection peak number 1, 2, 3, ..., etc. The reflection peak with the largest possible reflection peak wavelength is when $N = 1$.

A DBR sample which has thinner/thicker layers would respectively blue-shift/red-shift the wavelength of the reflection peak. Samples were prepared with reflection band wavelengths between $450nm \rightarrow 650nm$ by depositing solutions at spin-speeds between $1.0krpm \rightarrow 4.0krpm$. The calibration curve in the bottom plot in figure 5.1 was used to prepare samples with targeted peak reflection band wavelengths. This was controlled by keeping the solution concentrations constant and changing the deposition spin-speed for different wavelength reflection bands.

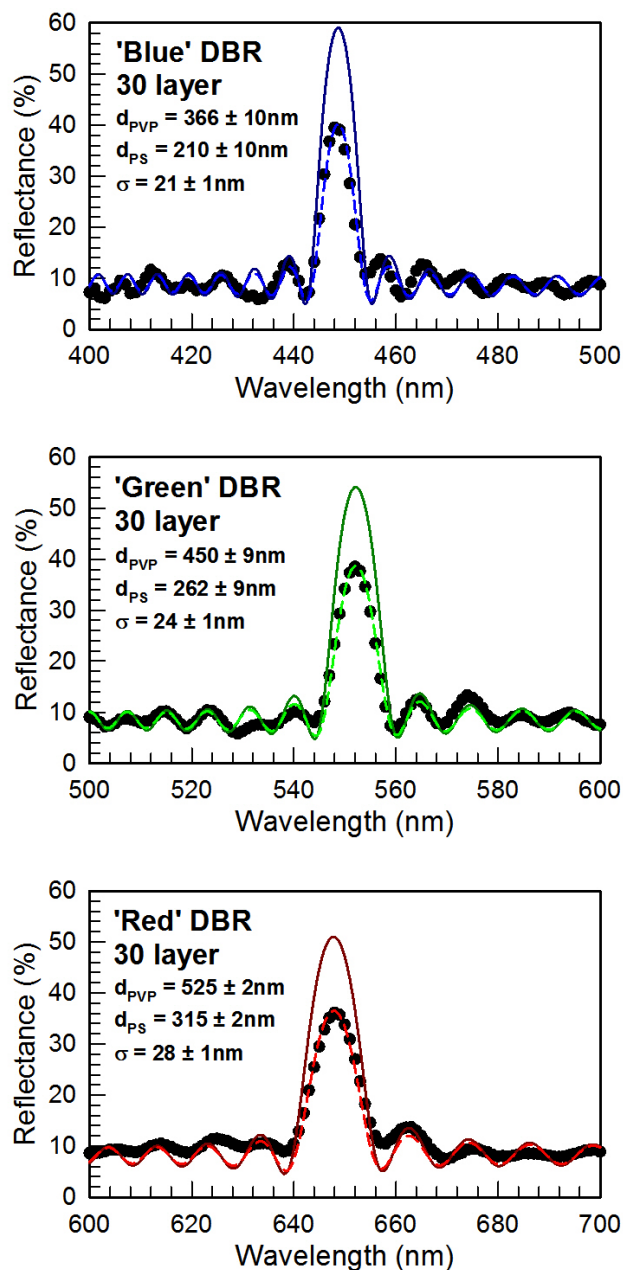


Figure 5.2: Three different samples were prepared using the calibration curve in figure 5.1. ‘Blue’ [top panel], ‘Green’ [middle panel] and ‘Red’ [bottom panel] were prepared with reflection peaks positioned at wavelengths $\sim 450\text{nm}$, $\sim 550\text{nm}$ and $\sim 650\text{nm}$ respectively. The black data-points correspond to the spectroscopic measurements of three different 30 layer samples. The solid lines represent spectra which was modelled using the modified optical transfer matrix method (which was discussed in chapter 3). Calculations which include estimates for polymer-polymer interface widths (discussed in section 3.7) are represented by the dashed lines.

Sample	Reflection band position (nm)	Deposition spin-speed ($krpm$)	Single layer PVP thickness d_{PVP} (nm)	PVP thickness used in model d_{PVP} (nm)	Single layer PS thickness d_{PS} (nm)	PS thickness used in model d_{PS} (nm)	Diffuse interface σ (nm)
Blue	~ 450	2.51 ± 0.01	376 ± 1	366 ± 10	220 ± 1	210 ± 10	21 ± 1
Green	~ 550	1.64 ± 0.01	459 ± 1	450 ± 9	271 ± 1	262 ± 9	24 ± 1
Red	~ 650	1.17 ± 0.01	527 ± 1	525 ± 2	317 ± 1	315 ± 2	28 ± 1

Table 5.1: Parameters used to model the 30 layer PS/PVP DBR sample shown in figure 5.2. Single layer polymer film measurements (using ellipsometry) were used to model the reflection band of the DBR samples. However, small corrections were needed to fit the modelled reflection band to the spectroscopic measurements. Furthermore, the polymer-polymer diffuse interface widths were estimated to improve the modelled fit (see section 5.3.1). The ellipsometry errors are calculated using a standard deviation of five different measurements.

Three 30 layer samples were prepared with targeted reflection peak wavelengths at $450nm$, $550nm$ and $650nm$ (which are respectively labelled as ‘Blue’, ‘Green’ and ‘Red’ DBRs throughout this thesis). The UV/visible reflection spectra of these three samples are shown in figure 5.2. Spectroscopic measurements of the reflectance from each sample are represented by the data-points. The solid curves represent spectra which were modelled using the modified optical transfer matrix method (discussed in chapter 3). Those calculations assumed perfectly sharp interfaces ($\sigma = 0$). Models which did include polymer-polymer interface width estimates σ were calculated separately. The spectra from these calculations are represented by the dashed curves in figure 5.2. Polymer-polymer interface width estimates are discussed more thoroughly in section 5.3.1.

The modified optical transfer matrix method used film thickness (figure 4.12) and dispersion of the refractive index measurements (figure 4.19) to calculate the reflection properties of the DBRs. However, the film thickness measurements were adjusted to fit the modelled spectra with spectroscopic measurements of the DBR samples. It was not possible to determine the thickness corrections needed for each individual layer in the DBR sample. Instead, the film thickness corrections were applied equally to all of the modelled layers. The layer thickness measurements and corrections used to improve the fit of the model are shown in table 5.1.

The small difference between the modelled and measured reflection band (when using the ellipsometry measurement of single layer films) could be caused by a number of different factors;

- *Errors in ellipsometry measurements:* Typically, errors in ellipsometry measurements of the film thickness of single layer polymers were between $1nm$ and $4nm$. Measuring the thickness of the top layer film in a bi-layer is more difficult than measuring a single layer film. The optical properties of these samples are sensitive to small changes. Film thickness of the bottom layer and the refractive index of all the layers in the bi-layer sample must be accurately measured. Inaccurate measurements of these parameters/quantities would increase the top layer film thickness error when measuring the bi-layer sample. Comparisons between polymer layers which were spin-cast on top of silicon or polymer substrates were

discussed in section 4.4.1. Figures 4.14 and 4.15 showed that there was a small change in film thickness when spin-coating onto silicon or polymer substrates. Although, these changes could have contributed towards the film thickness errors used in the calculations.

- *Wavelength dependence of refractive index:* The error of the film thickness was overestimated to fit the dispersion measurements 4.4.2. This suggests that there could be errors within the dispersion measurements. The dispersion measurements were used to model the UV/visible spectrum of the DBR samples. A layer would need to be thicker/thinner if the refractive index was under/over estimate respectively to maintain the same optical path length $OPL_{Film} = d_{Film}n_{Film}$ of the layers [10].
- *Residual solvent:* All samples were annealed at $110^{\circ}C$ for 5 hours under vacuum. This is above the glass transition temperature of PS ($T_g \simeq 100^{\circ}C$ [65]) but not the T_g of PVP ($T_g \simeq 150 - 180^{\circ}C$ [65]). Solvent would not as readily diffuse out of the PVP layers as it would have for the PS layers. Furthermore, the multi-layer structure may restrict the toluene diffusing out of the sample. Residual solvent within the polymer layers would swell the polymers (increasing the layer thickness) and reduce their refractive index (decreasing their optical path length). This would change the optical properties of the photonic structure, such as the wavelength of the reflection peak.

5.3 Inefficiencies and defects which reduce DBR peak reflectance

The measured reflectance of the DBR reflection peak was not as large as the modified optical transfer matrix method had calculated (spectra shown in figure 5.2). This indicated that there were other properties of the DBR samples which should be considered. For example, the polymer-polymer interfaces being broad instead of sharp (discussed in section 5.3.1), lower refractive index contrast between layers (discussed in section 5.3.2) and disorder in the photonic structure (discussed in section 5.3.3).

5.3.1 Polymer-polymer interfaces

The modified optical transfer matrix model previously assumed that the polymer-polymer interfaces between layers were sharp. However, the layers are made from polymer films which were spin-cast on top of polymer substrates (which are also previously deposited layers). Previous experiments have measured broad polymer-polymer interface widths, which were $\sim 10nm$, for similar spin-cast polymer layered samples [85]. Interfaces between spin-cast polymer layers should be considered when modelling the optical properties of DBR samples. The following points are different types of interfaces which also correspond to the illustration in figure 5.3;

- *Sharp interfaces*: The two materials are not intermixed and the surfaces between the two layers are perfectly flat.
- *Diffuse interfaces*: This is a intermixed blend of both of the materials at the interface. The transition from one material to another is gradual and can be modelled using an error function [86]. Polymer chains can intermix and broaden the interface. Solution processing swells the surface polymer chains and increases their mobility [18, 86]. Furthermore, the polymer chains between two separate polymers will tend to intermix when they are swollen by residual solvent.
- *Roughened interfaces*: The topography of the sample is not flat and the surfaces of the polymers at the interface are naturally rough. This causes the two materials to penetrate into one another. Solvent evaporation during spin-coating will cause roughening on the surface of a spin-coated film [62, 85]. Spin-coating a film on top of rough films will not remove the roughness at the newly formed interface.
- *Diffuse and roughened interfaces (combined)*: The polymer-polymer interfaces are likely to be a combination of both the diffuse and roughened interface [18, 86].

AFM was used to measure the surface roughness of multi-layer polymer films. The root mean square surface roughness measurements were between $\sim 1.2 \pm 0.4nm$ and $4.1 \pm 0.3nm$. Unfortunately, AFM is only able to measure the surface of a sample. The internal polymer-polymer interfaces would have

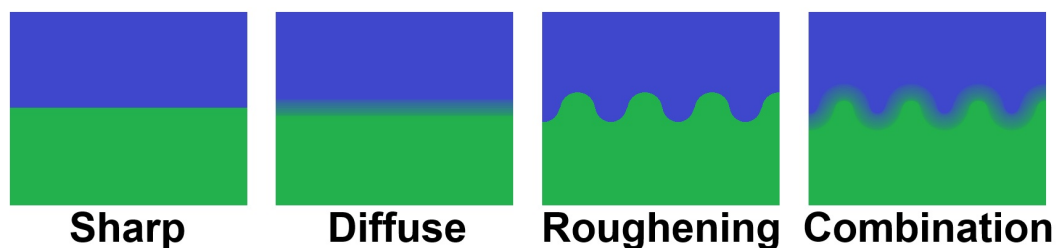


Figure 5.3: These diagram represent the different types of interfaces which should be considered for spin-coated polymer multi-layers. Sharp interfaces are when the transition from one medium to another is well defined. Diffuse interfaces are caused by the two materials intermixing. Rough interfaces are caused by the topography of the interfaces penetrating into both materials. The interface of the polymer films is likely to be a combination of both diffuse and roughened interfaces.

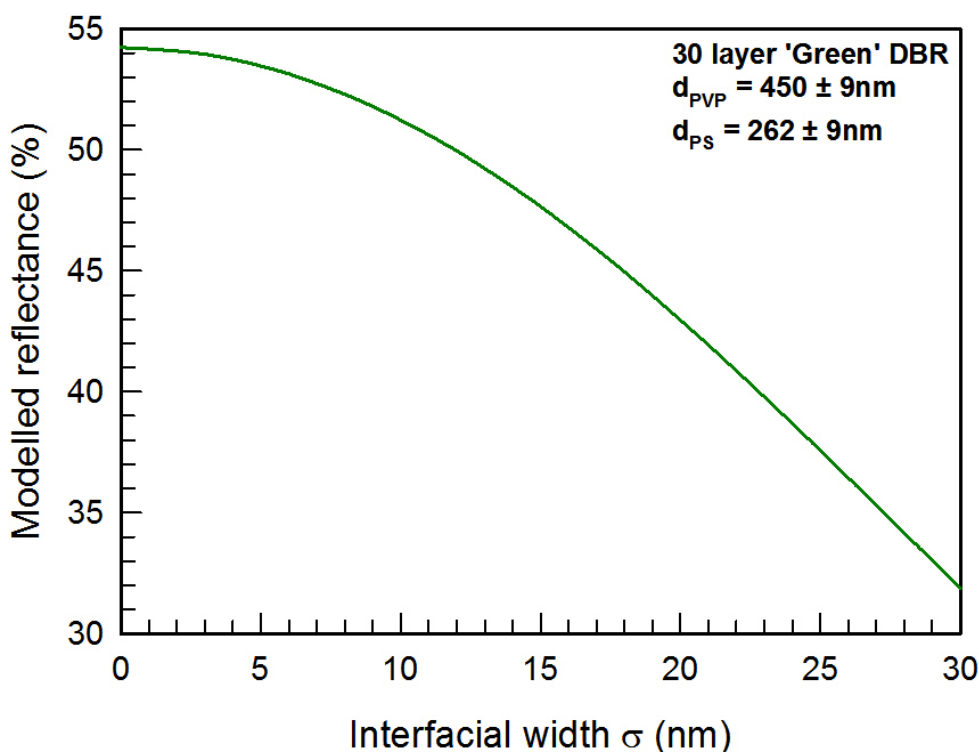


Figure 5.4: The reflectance of the reflection peak from a modelled 30 layer 'Green' $\sim 550nm$ ($d_{PVP} = 450 \pm 9nm$ and $d_{PS} = 262 \pm 9nm$) DBR was plotted with respect to changing polymer-polymer interface width. Increasing the modelled polymer-polymer interface width reduces the total reflectance of the modelled reflection peak.

to be measured using other techniques such as neutron reflectivity (see chapter 8) and TOF-SIMS (see chapter 9). Measuring the surface roughness after each film deposition would not be an accurate technique to measure the interface widths between layers. The polymer films could swell and intermixing (at small length scales) during sample preparation. Polymer chains on the surface of a sample can still be mobile when in an orthogonal solvent [18, 87]. Hence, the two different polymer materials could have mixed when depositing layers.

The surface roughness of the spin-cast films were two orders of magnitude less than the wavelength of incident light. Reflected light was considered to be specular as the quantity of scattered light was negligible because of the relatively small surface roughness [54]. In this case, the optical properties of topographical roughness are indistinguishable and significantly less than the optical effects of diffuse interfaces. The calculations for polymer-polymer interface widths were simplified by treating the roughening and diffuse interface as a single problem. A single approximation for diffuse interfaces, which corrects the reflection coefficient r , was used to model the combined effects of diffusion between layers and roughening (which was also discussed in section 3.7),

$$r_{int} = r \exp \left[-8 \left(\frac{\pi \sigma n_{N+1}}{\lambda} \right)^2 \right]. \quad (5.2)$$

Increasing the interface width σ results in the magnitude of the reflection coefficient at a given interface being reduced. This reduces the total reflectance of the reflection peak. Figure 5.4 illustrates the reduction in the reflectance of a modelled reflection peak of a 30 layer ‘Green’ DBR sample as σ increases. The widths of all the interfaces were assumed to be the same throughout the sample. This would not necessarily be the case for real samples. For example, depositing a PVP film on top of a PS layer could result in a broader interface than when depositing a PS film on top of a PVP layer (or vice versa). This is because one polymer may be more or less orthogonal to the solvent used to dissolve the alternate polymer [18, 86]. The difference of the two cannot be measured by modelling optical spectra, so neutron reflectivity or TOF-SIMS measurements must be used instead.

The dashed lines shown in figure 5.2 are modelled curves which include estimates for polymer-polymer interfaces widths. These calculations were used to

improve the modelled fit with respect to the UV/visible spectrometry measurements. Changing the widths of the interfaces does not change the wavelength position of the reflection bands. This is because the average/effective film thickness and refractive index of the layers are unchanged. Values for the interface widths estimates used to fit the measurements in figure 5.2 are shown in table 5.1. The polymer-polymer interface widths were estimated to be between $20nm \rightarrow 30nm$. These estimated interface widths were larger than those measured from comparable polymer layered samples [85].

The polymer-polymer interface widths of the PVP/PS multi-layer samples were later measured using neutron reflectivity (discussed in chapter 8). The interface width of PS(top) \rightarrow PVP(bottom) interfaces were $0.61 \pm 1nm$. Whereas the PVP(top) \rightarrow PS(bottom) interfaces were $0.96 \pm 1nm$. These measurements are significantly smaller than the estimates calculated by fitting the modelled spectra to UV/visible measurements. The samples were remodelled using the measured interface widths. However, there is negligible difference between the remodelled spectra (using neutron reflectivity measurements) and modelled spectra which assumed the sample had sharp interfaces.

The reduction in the reflectance of the measured DBR reflection band (when compared with modelled spectra) was not due to large polymer-polymer interface widths. Instead, the reduction in reflectance could be due lingering solvent left over from sample preparation. This is discussed further in the next subsection.

5.3.2 Reduction of refractive index contrast

Neutron reflectivity measured the polymer-polymer interfaces to be small (all of the measured interfaces were less than $1nm$ wide). The measured reflectance of the reflection bands were lower than what the modelled spectra had estimated. This could have been due to trapped solvent reducing the refractive index contrast between layers. Solvent may have lingered within the polymer layers during sample preparation. It was later discovered that the reflectance of the DBRs increased towards the modelled reflectance (see section 6.2). This could have been due to the lingering solvent diffusing out of the sample over time.

The refractive indices of ethanol ($n = 1.363$), acetonitrile ($n = 1.344$) and

toluene ($n = 1.496$) are smaller than the refractive indices of PVP ($n = 1.516$) and PS ($n = 1.586$). Trapped solvent would have lowered the refractive index of the polymer films. This could also reduce the refractive index contrast between the polymer materials. Figure 5.5 shows the reflectance spectra of the ‘Blue’, ‘Green’ and ‘Red’ 30 layer DBRs with reflection peaks at wavelengths $\sim 450nm$, $\sim 550nm$ and $\sim 650nm$ respectively (which are the same samples shown previously in figure 5.2). The data-points represent the measured UV/visible reflection spectra of the DBR samples. The dashed lines are modelled spectra with the refractive index contrast between the polymer layers Δn reduced.

The modelled spectra in figure 5.5 were fitted by decreasing the contrast of the refractive index between the layers ($\Delta n = n_{PS} - n_{PVP}$) by a value $\delta(\Delta n)$, using the following equations;

$$[n_{PVP}(\lambda)]_{Corrected} = [n_{PVP}(\lambda)]_{Measured} + \delta(\Delta n)/2, \quad (5.3)$$

and,

$$[n_{PS}(\lambda)]_{Corrected} = [n_{PS}(\lambda)]_{Measured} - \delta(\Delta n)/2. \quad (5.4)$$

Where $\delta(\Delta n)$ = change in the refractive index contrast between layers, $[n_{PVP}(\lambda)]_{Measured}$ and $[n_{PS}(\lambda)]_{Measured}$ is the measured wavelength dispersion of the refractive index for PVP and PS respectively.

These ‘corrected’ refractive index values are approximations for changes in the refractive index of the polymer layers. It was not possible to measure the refractive index of the solvent swelled polymer layers within the sample. Instead, these calculations were only used to model the effects of a smaller optical contrast between layers Δn . The refractive index of PVP decreases when it is swelled with 50:50 ethanol:acetonitrile. However, it was simpler to increase the modelled refractive index of PVP to reduce Δn . Likewise, the modelled refractive index of PS was reduced to lower Δn . The magnitude of $\delta(\Delta n)$ was applied equally to the measured refractive index of PVP and PS. Table 5.2 shows the film thickness and refractive index contrast changes used to model the spectra. The thickness of the layers had to be increased to keep the position of the reflection peak constant. This was due to the optical path

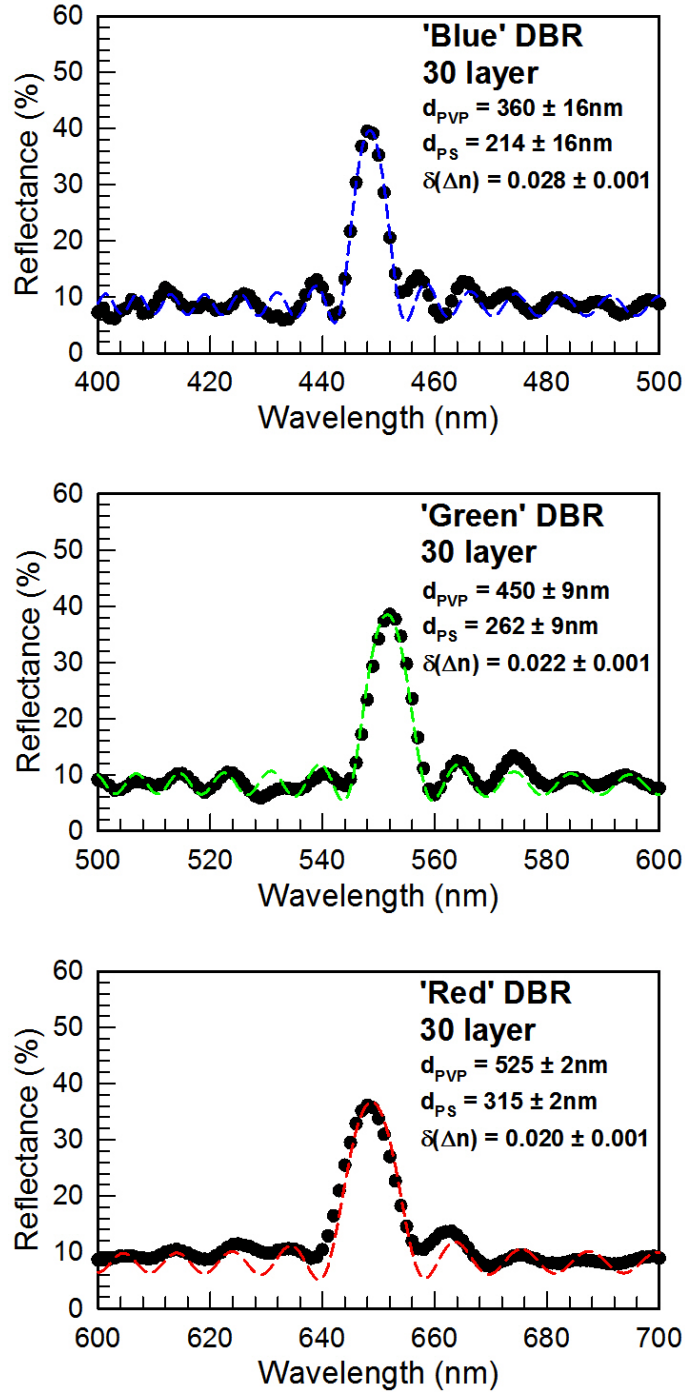


Figure 5.5: The UV/visible reflectance measurements (data-points) of the ‘Blue’ [top panel], ‘Green’ [middle panel] and ‘Red’ [bottom panel] were remodelled using the modified optical transfer matrix method (dashed curves). This included estimates for reductions in the refractive index contrast Δn between the polymer layers. Changes in the refractive index contrast as large as $\delta(\Delta n) = 0.028 \pm 1$ were needed to reduce the modelled reflectance to fit measured spectra. The reduction in contrast may have been due to residual solvent trapped in the multi-layers.

Sample	Reflection band position (nm)	Single layer PVP thickness d_{PVP} (nm)	PVP thickness used in model d_{PVP} (nm)	Single layer PS thickness d_{PS} (nm)	PS thickness used in model d_{PS} (nm)	Change in refractive index contrast $\delta(\Delta n)$
Blue	~ 450	376 ± 1	360 ± 16	220 ± 1	214 ± 16	0.028 ± 0.001
Green	~ 550	459 ± 1	450 ± 9	271 ± 1	262 ± 9	0.022 ± 0.001
Red	~ 650	527 ± 1	525 ± 2	317 ± 1	315 ± 2	0.020 ± 0.001

Table 5.2: The refractive index contrast between PVP and PS layers was changed by using equations 5.3 and 5.4. Values of these variables are not representative of measured DBR samples. This is because the refractive index of the PVP layers wouldn't increase if there were trapped solvent in the films. Instead, these modelling experiments were used to test how large a change in refractive index contrast $\delta(\Delta n)$ was needed to fit the reflectance of the modelled to the measured spectra. The reflectance of the modelled reflection peaks had reduced when the refractive index contrast was lowered.

length ($\text{OPL}_{Film} = n_{Film}d_{Film}$) of the polymer layer reducing as the refractive index decreased [10].

Reductions of Δ_n between 0.020 and 0.028 were needed to fit the modelled spectra with UV/visible spectrometry measurements. The following Lorentz-Lorenz equation was used to calculate the refractive index of a polymer/solvent mixture [88];

$$\frac{n_{Mix}^2 - 1}{n_{Mix}^2 + 2} = \phi_{Poly} \frac{n_{Poly}^2 - 1}{n_{Poly}^2 + 2} + \phi_{Solv} \frac{n_{Solv}^2 - 1}{n_{Solv}^2 + 2}. \quad (5.5)$$

Where n_{Mix} , n_{Poly} and n_{Solv} are the refractive indices of the polymer/solvent mixture, polymer and solvent respectively. ϕ_{Poly} and ϕ_{Solv} are the volume fractions of the polymer and solvent components in the mixture.

Up to 20% of the volume in a spin-cast PS film can consist of residual toluene [89]. A literature refractive index value for toluene and the ellipsometry measurement of PS were used to calculate the refractive index of a swelled PS film [65]. The calculated reduction in refractive index for a swelled PS film was $\Delta n_{PS} = 0.018$. This is slightly lower than the $\delta(\Delta n)$ which was used to fit the optical transfer matrix method to measured spectra. However, residual solvent in the PVP films would reduce the refractive index contrast between the layers. The Lorentz-Lorenz equation indicates that the reduction in reflectance could be due to trapped solvent. Therefore, more experiments are needed to measure the refractive index and film thickness of the swelled PVP and PS layers in the DBR samples. This would help model and understand the optical properties of the DBR samples further.

5.3.3 Effects of disorder in layer thickness

All of the DBR modelling data previously assumed that the thickness of the PVP (d_{PVP}) and PS (d_{PS}) remain constant. However, the film thickness of the deposited layers may change throughout the DBR. This could be due to an increased error when spin-coating on of polymer layers, differences in swelling from residual solvent, or warping because of residual stresses [86]. Disorder in the layer thickness would change the photonic structure and shape of the reflection peak (which is similar to the chirped reflection spectra shown in

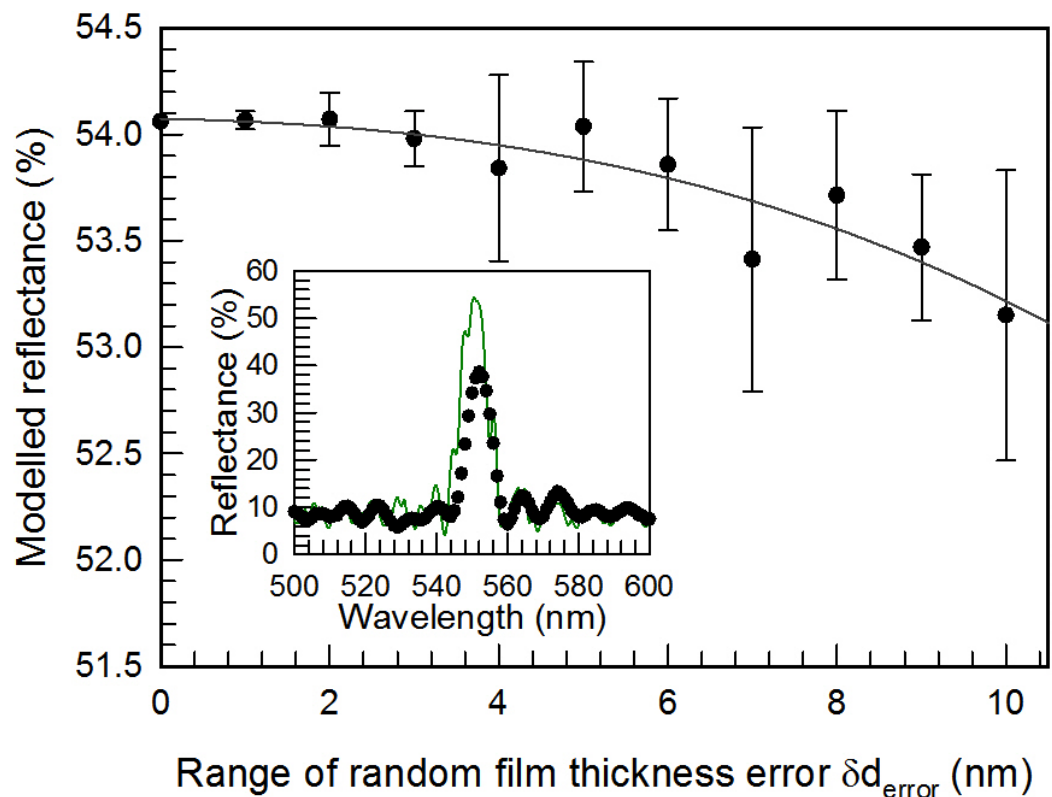


Figure 5.6: The reflectance of modelled reflection peaks are reduced as the thickness of the modelled DBR layers become disordered. Each modelled layer was modified by randomly changing the thickness within a range of error δd_{Error} . This plot models disorder in a hypothetical 30 layer ‘Green’ DBR ($d_{PVP} = 410nm$ and $d_{PS} = 262nm$ when $\delta d_{Error} = 0nm$). Each data-point was the average of reflectance from ten modelled samples with random layer thickness disorder applied. Standard deviation was used to calculate the errors. The curve is a quadratic polynomial fit. UV/visible measurements of a 30 layer ‘Green’ DBR (data-points) and the modelled spectra when $\delta d_{Error} = 10nm$ (green curve) are shown in the inserted panel.

section 5.6). A 30 layer ‘Green’ DBR sample was remodelled with included layer thickness disorder. Each layer thickness was modified by;

$$d_{Modified} = d_{Initial} \pm \frac{\delta d_{Error}}{2}. \quad (5.6)$$

Where $d_{Modified}$ = layer film thickness after being adjusted by applying a small error, $d_{Initial}$ = original single layer film measurement and δd_{Error} = size of the random film thickness error.

The initial film thickness of the layers were consistent with the modelled ‘Green’ DBR sample shown in table 5.1. Each film thickness was modified slight by adding or subtracting a random error within a pre-determined range δd_{Error} . For example, the thickness of each film would be changed by a random error within $-1nm$ and $+1nm$ if $\delta d_{Error} = 2nm$. The reflectance of a 30 layer $550nm$ ‘Green’ DBR (with sharp interfaces) was modelled for different ranges of δd_{Error} . Each test of δd_{Error} was modelled 10 times. The average and standard deviation were calculated to demonstrate the variation in results. Figure 5.6 shows that the reflectance decreased when δd_{Error} had increased. The reflectance only decreased by $\sim 1\%$ when $\delta d_{Error} = 10nm$. Irregularities in the modelled reflection spectra start to occur when δd_{Error} is increased as the model diverges away from the shape of the measured spectra. This is illustrated by the caption in figure 5.6 which is a model of a 30 layer ‘Green’ DBR which has a random film thickness error range of $\delta d_{Error} = 10nm$. The modelled spectra (solid line) does not fit the shape or reflectance of the measured spectra (data-points). Hence, the reduction in reflection between measured and modelled data is unlikely to be entirely due to random variations in film thickness.

5.3.4 Asymmetry in the layer thickness

The single layer ellipsometry measurements were used to model the reflection band of 30 layer DBRs (shown in figure 5.2). Slight corrections to the film thickness measurements (shown in table 5.1) were needed to improve the fit of the modelled spectra with respect to measured spectra. Corrections to film thickness were applied equally to both PVP and PS layers. However, any variation between modelled and actual film thickness may not have been equal for all the polymer layers. The film thickness correction for one of the polymer

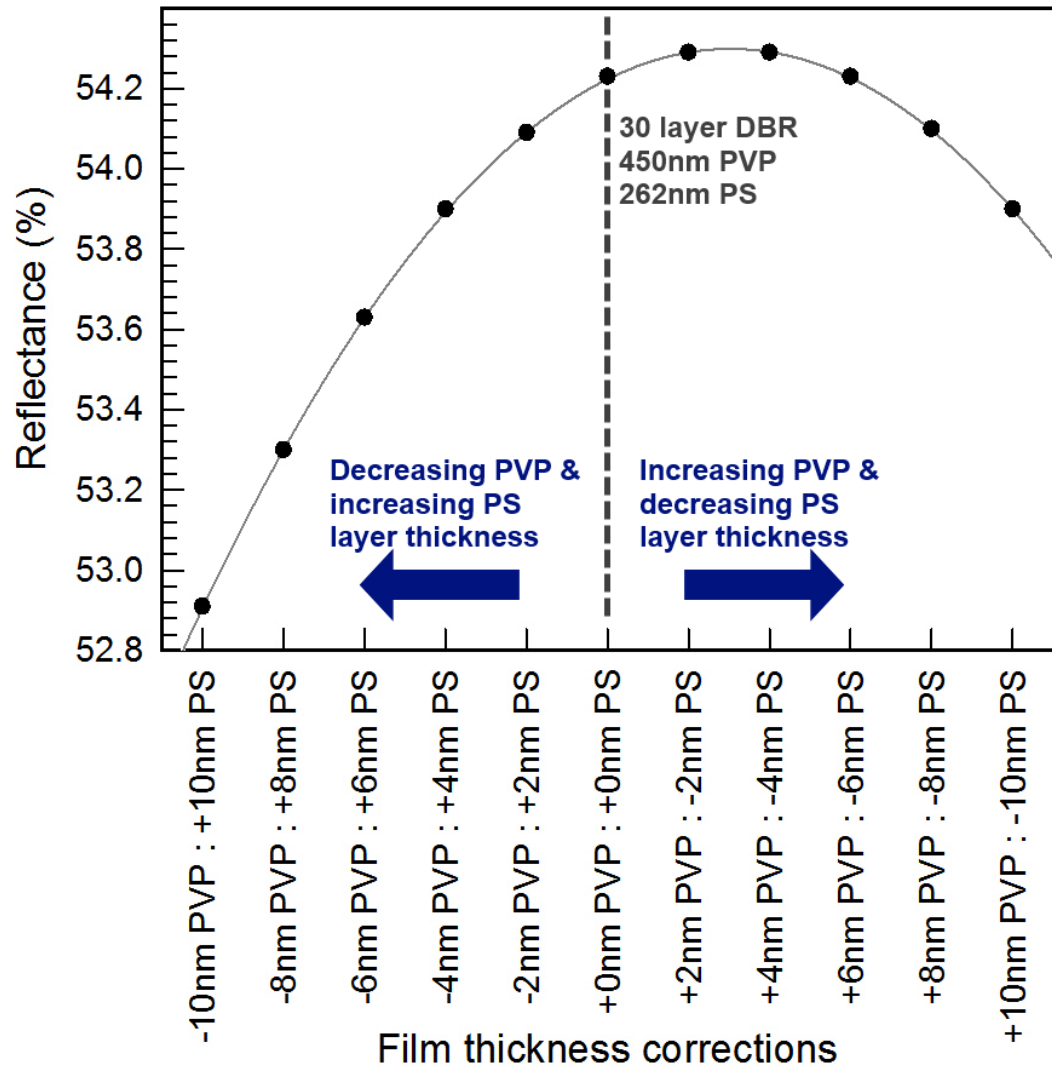


Figure 5.7: The modelled reflectance of a 30 ‘Green’ DBR (originally $d_{PVP} = 410nm$ and $d_{PS} = 262nm$) was calculated for small changes in layer thickness. Reflectance of the reflection peak was calculated for different layer thickness values, which were within error of the calculations. However, equal and opposite changes were needed to keep the wavelength of the modelled reflection band consistent with the measurements. Changes in the film thickness (within error) were not large enough to significantly reduce the modelled reflectance, to fit the measured data.

layers may have needed to be larger than the alternate polymer layers. For example, the PVP or PS layers may be swollen by trapped solvent. A hypothetical 30 layer ‘Green’ DBR was modelled for this experiment. Layers with thickness $d_{PVP} = 440nm$ and $d_{PS} = 262nm$ from table 5.1 were used to model the reflection spectra. Asymmetry was then introduced adding or subtracting incremental changes in layer thickness δd . The position of the reflection band was kept within $550 \pm 1nm$ by decreasing the layer thickness of PVP/PS by δd , when the layer thickness of PS/PVP was increased by δd respectively. Hence, the total film thickness of each PVP/PS bi-layer was kept constant. However, the ratio between the PVP and PS film thickness was changed.

Figure 5.7 is a plot of the modelled reflectance of a ‘Green’ 30 layer DBR reflection band with respect to changes in the film thickness of PVP and PS. The reflectance changed as the asymmetry between d_{PVP} and d_{PS} was varied. However, corrections as large as $\delta d = \pm 10nm$ were needed to significantly change the reflectance of the DBR reflection peak by $\sim 1.3\%$. Large changes in the film thickness may have occurred if the films were swollen with residual solvent. Although, the refractive index of the polymer layers would have also reduced. Therefore, the optical path length should be considered $OPL_{Film} = n_{Film}d_{Film} / \cos(\theta_{Film})$ as it would change the optical properties of the sample [10]. A combination of changing film thickness and refractive index, by residual solvent, may have reduced the reflectance of the DBR reflection peaks.

These results also demonstrated that more efficient photonic structures can be prepared by tuning the thickness of layers. This is discussed further in section 6.3.

5.4 Controlling the reflectance

Increasing the number of layers in a sample also increases the number of interfaces. This also increases the number of partial reflections which contribute to the total reflectance of the sample. Therefore, the magnitude of the reflection peak is increased by adding more layers to the sample. Figure 5.8 shows the reflectance of the reflection peaks for ‘Red’, ‘Green’ and ‘Blue’ DBRs, which were each prepared with different numbers of deposited layers (10, 20, 30, 40 and 50). Each data-point represents the reflectance of a measured reflection peak

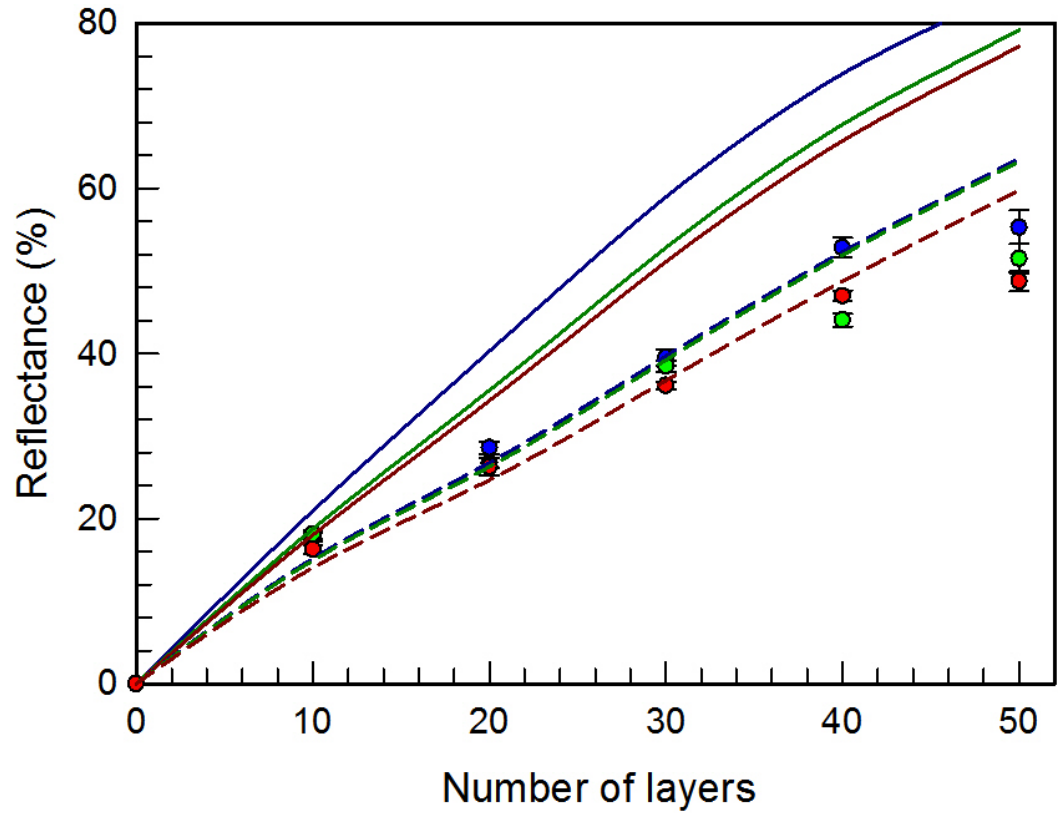


Figure 5.8: The reflectances of ‘Blue’, ‘Green’ and ‘Red’ DBRs (coloured appropriately in this figure) with reflection bands at $\sim 450nm$, $\sim 550nm$ and $\sim 650nm$ respectively, are plotted with respect to the number of layers deposited. UV/visible spectrometry measurements are represented by the data-points. Result is an average of five measurements and the errors are their standard deviations. The solid lines represent the reflectance of modelled samples which have sharp interfaces. The dashed lines represent modelled spectra which have had refractive index contrast between layers reduced (using the values in table 5.2).

from a DBR sample. All of the samples were modelled using the modified optical transfer matrix method. Values from table 5.1 were used to model samples which had sharp interface widths (represented by the solid curves in figure 5.8). Likewise, the values in table 5.2 were used to model any possible reduction in refractive index contrast between the layers Δn . Lingering solvent within the samples would have lowered the refractive indices of the polymer layers (see section 5.3.2). Reducing the refractive index contrast of the polymer layers by $\delta\Delta n$ had improved fitting the modelled spectra to sample measurements (represented by the dashed curves in figure 5.8).

All of the measurements and modelled data in figure 5.8 show that the reflectance of the reflection peak increases when more layers are added to the sample. However, the sharp interface model overestimates the reflectance of the DBR reflection peaks. This worsens as the number of layers increases because of additional properties which are not being modelled. Adding more layers could reduce the reflectance decrease by, trapping more solvent and adding defects (such as contaminants). Furthermore, the thickness of the sample is increasing, which approaches above the coherence length of the reflected light [10, 11, 14].

The modelled data which included reduced refractive index contrast $\delta\Delta n$ had improved fitting with measured results. However, this model underestimated the reflectance of the DBR peaks when the number of layers is less than 30. It also over estimated the reflectance of the DBR peaks when the number of layers is greater than 30. This was due to all of the curves being calculated using the 30 layer spectra fit. Hence, the reduction of the refractive index between layers may be smaller/larger for less/more than 30 layers deposited during sample preparation respectively. It is more difficult for residual solvent to diffuse out of the sample when there are more layers [66].

The reflectance of the DBR can be controlled by changing the number of layers deposited (shown in figure 5.8). However, there were no significant gains in reflectance for samples of more than 50 layers, when using this sample preparation technique. This was most likely due to trapped solvent within the layers of the DBR (discussed in chapters 6 and 8). The total reflectance of the DBRs was later improved by periodically annealing during sample preparation. This allowed more layers to be added to the sample and increased the total reflectance possible (this is discussed further in section 6.4).

5.5 Angular dependence of DBR spectra

Changing the angle of incident light will change the wavelength of a reflection peak from a DBR sample. This is known as *iridescence* [10, 12]. The transmission UV/visible spectrometer shown in figure 4.20 was built to include variable angle measurements. Rotating the sample changes the angle of incidence with respect to the sample surface. This would cause the beam path of the transmitted light to slightly deviate away from the centre of the collection lens (due to the initial air→polymer and final glass→air interfaces being different). However, the collection lens was large enough for this problem to be neglected.

The reflection spectra of the 30 layer ‘Blue’, ‘Green’ and ‘Red’ DBRs were measured at different angles of incidence. These samples were also modelled using the modified optical transfer matrix method. This included modelling samples with sharp interfaces (values were provided in table 5.1) and reducing the refractive index contrast between the polymer layers Δn (values were provided in table 5.2). Reducing the refractive index contrast between the layers improved the fit of the modelled spectra to the corresponding reflection measurements.

Figure 5.9 shows the wavelength of the reflection peak for the 30 layer ‘Red’, ‘Green’ and ‘Blue’ samples with respect to the angle of incident light. All of the measurements showed the reflection peaks blue-shift when the angle of incident light deviated/increased away from the normal of the sample surface (data-points). Only the modelled spectra for samples with sharp interfaces are shown in figure 5.9 (solid curves). Modelled spectra for samples with reduced refractive index contrast Δn were also calculated. However, there was negligible difference between the two different types of modelled samples. The data from both models had accurately calculated the wavelength dependence/iridescence of reflection spectra measured from DBR samples.

Blue-shifting of the reflection peaks would appear to be counter intuitive as the optical path length between interfaces increases as the light moves away from normal incidence ($\text{OPL}_{\text{Film}} = n_{\text{Film}}d_{\text{Film}}/\cos(\theta_{\text{Film}})$ [10]). Figure 5.10 illustrates that the optical path length of the transmitted light increases when the angle of refraction θ_r is raised. However, this causes a phase difference δ between the rays reflected from the top and bottom of the film. Only rays

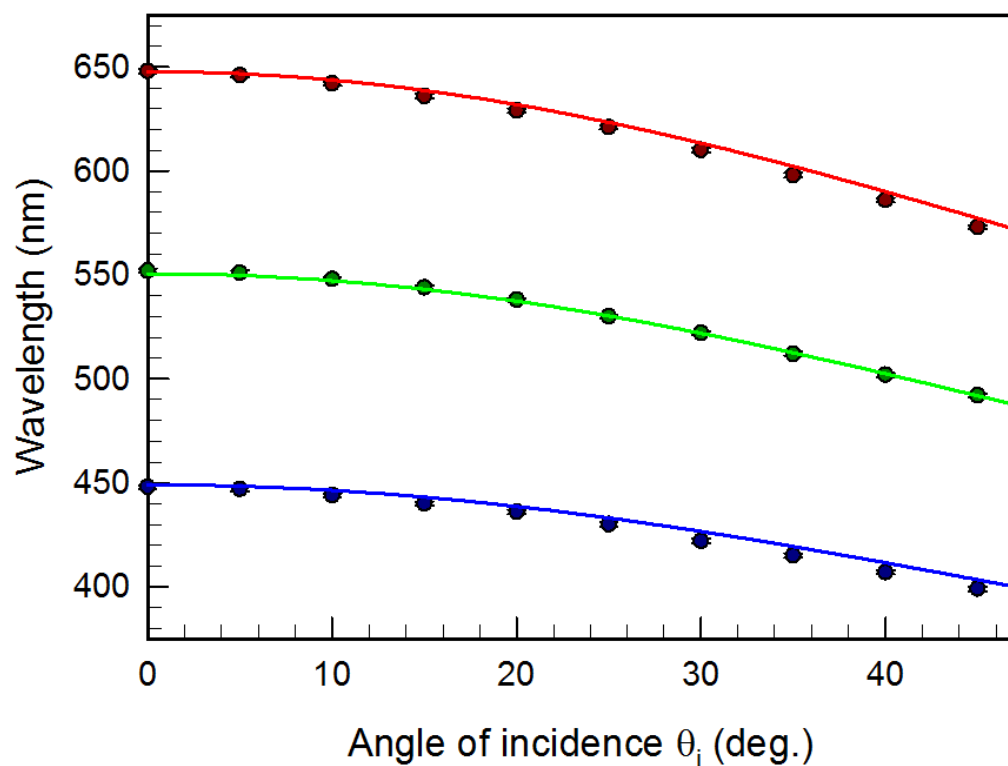


Figure 5.9: The wavelength of measured reflection bands for the 30 layer ‘Red’, ‘Green’ and ‘Blue’ DBRs (represented by data-points and coloured appropriately in the figure) plotted with respect to the angle of incident light. The modified optical transfer matrix method was used to model the measured data (solid curves). Only modelled results for sharp interfaces are shown. Modelled samples which had a reduced refractive index contrast were also calculated. However, the difference, when compared to the sharp interface model, was negligible. All of the results showed the wavelength of the reflection band blue-shifting as the incidence increased.

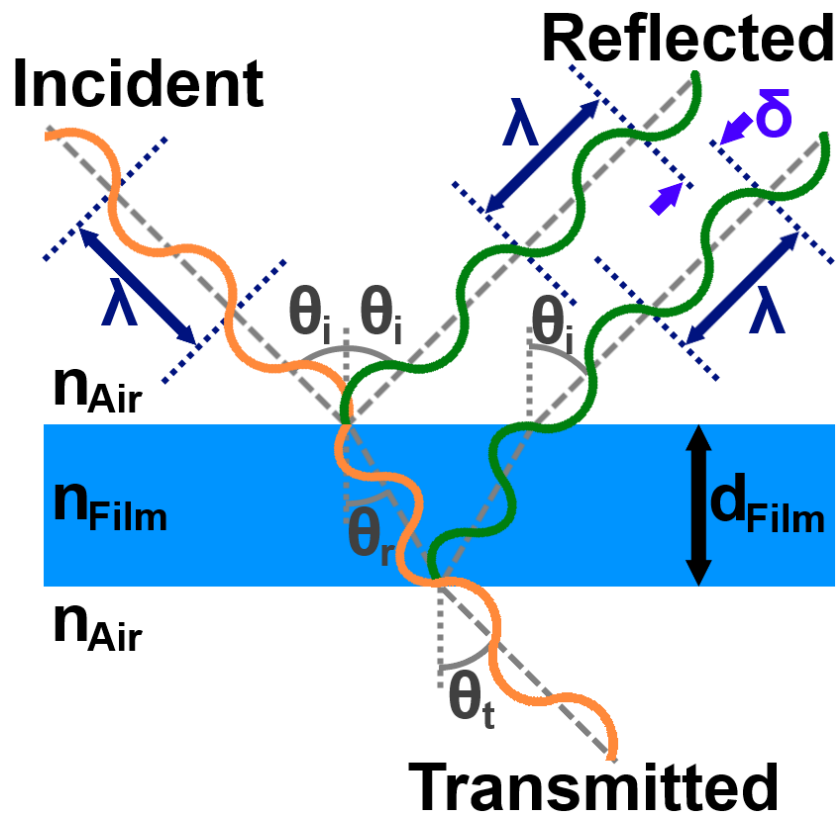


Figure 5.10: Changes in the reflected colour (irridescence) are discussed for a single layer thin film for simplicity. However, these same principles would apply for a multi-layer sample. Moving the light source away from normal incidence (θ_i) changes the optical path length of transmitted light in the film and also the angle of refraction (θ_r). The top and bottom reflected waves interfere, but only rays which constructively interfere are reflected by the sample. The reflected wave is blue-shifted to maintain constructive interference.

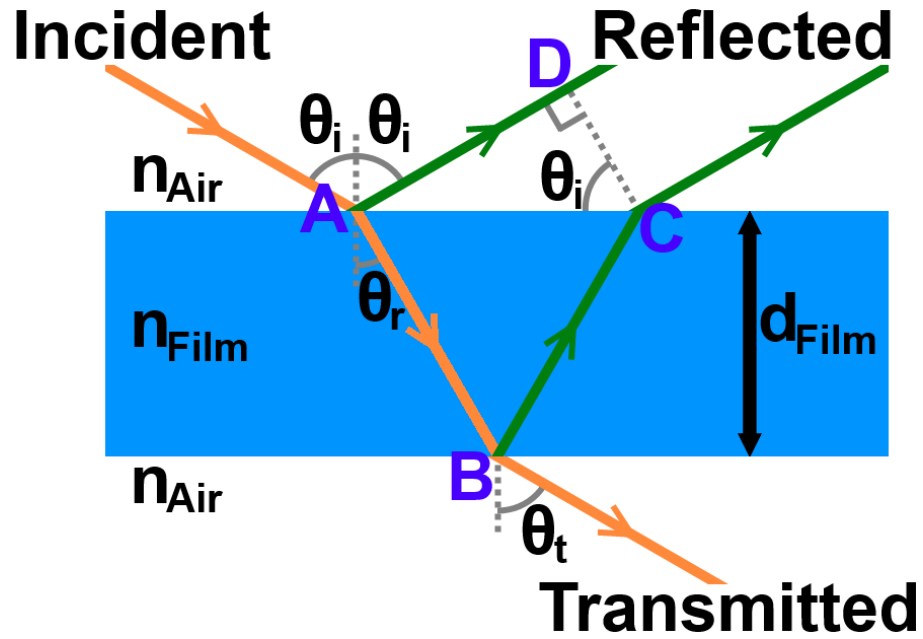


Figure 5.11: This diagram illustrates the phase difference between the top and bottom reflected waves when changing the angle of incidence. The increased optical path length $A \rightarrow B$ does not red-shift the reflected light. Instead, the path length $A \rightarrow D$ causes a phase difference between the two reflected rays. Only waves which constructively interfere are reflected by the thin film. Therefore, the reflection band is blue-shifted to compensate for the changes in phase.

which constructively interfere are reflected by the DBR samples. A given wavelength of light which was previously reflected at normal incidence would not constructively interfere when $\theta_i \neq 0$. However, a smaller wavelength would constructively interfere and is reflected by the DBR sample.

The iridescent properties of photonic structures can be explained using simple geometrical arguments. A single thin film is considered for simplicity, but the effect of iridescence would be the same for a multi-layer. However, the modified optical transfer matrix method should be used when calculating the angular properties of reflection spectra of a multi-layer sample. Figure 5.11 is provided as a visual aid for calculating the iridescence of a single layer film. Consider the two rays coming out of the film and have the magnitude E_{1r} and E_{2r} . For simplicity, we consider the two rays to be emitted from a light source which is beneath the thin film. The optical path difference Λ between the two reflected beams is given by [10];

$$\Lambda = n_{Film}[(\overline{AB}) + (\overline{BC})] - n_{Air}(\overline{AD}). \quad (5.7)$$

Where n_{Film} = refractive index of the film and n_{Air} = refractive index of air.

This is expanded by,

$$(\overline{AB}) = (\overline{BC}) = \frac{d_{Film}}{\cos(\theta_r)}. \quad (5.8)$$

Where d_{Film} = thickness of film and θ_r = angle of refraction

Hence, equation 5.7 becomes,

$$\Lambda = \frac{2d_{Film}n_{Film}}{\cos(\theta_r)} - n_{Air}(\overline{AD}). \quad (5.9)$$

The magnitude of (\overline{AD}) is also re-written as,

$$(\overline{AD}) = (\overline{AC}) \sin(\theta_i). \quad (5.10)$$

Where θ_i = angle of incidence.

This is changed by substituting $\sin(\theta_i)$ into Snell's law [10],

$$(\overline{AD}) = (\overline{AC}) \frac{n_{Film}}{n_{Air}} \sin(\theta_r). \quad (5.11)$$

Using figure 5.11, the magnitude of (\overline{AC}) is also calculated by,

$$(\overline{AC}) = 2d_{Film} \tan(\theta_r). \quad (5.12)$$

Substituting this into equation 5.11 results in,

$$(\overline{AD}) = \frac{2d_{Film}n_{Film}}{n_{Air}} \tan(\theta_r) \sin(\theta_r). \quad (5.13)$$

Which is substituted into equation 5.9

$$\begin{aligned}
\Lambda &= \frac{2d_{Film}n_{Film}}{\cos(\theta_r)} - n_{Air} (\overline{AD}) \\
&= \frac{2d_{Film}n_{Film}}{\cos(\theta_r)} - n_{Air} \left[\frac{2d_{Film}n_{Film}}{n_{Air}} \tan(\theta_r) \sin(\theta_r) \right] \\
&= \frac{2d_{Film}n_{Film}}{\cos(\theta_r)} [1 - \sin^2(\theta_r)] \\
&= \frac{2d_{Film}n_{Film}}{\cos(\theta_r)} [\cos^2(\theta_r)] \\
&= 2d_{Film}n_{Film} \cos(\theta_r).
\end{aligned} \tag{5.14}$$

The phase difference of the optical path length δ is calculated by multiplying the wave-vector of the ray when it is reflected into the air medium k_{Air} with the optical path length difference Λ . The wave-vector in air is;

$$k_{Air} = \frac{2\pi}{\lambda_{Air}}. \tag{5.15}$$

Where λ_{Air} = wavelength of the light in air.

Furthermore, waves will undergo a phase shift of $\pm\pi$ radians when reflected from an interface if the incident medium has a lower refractive index than the transmitted medium [10]. Therefore, for a thin film suspended in air, there is a relatively phase shift of $\pm\pi$ radians. Hence, the phase difference between the two reflected beams is;

$$\begin{aligned}
\delta &= k_0\Lambda \pm \pi \\
&= \left[\frac{2\pi}{\lambda_{Air}} \right] [2d_{Film}n_{Film} \cos(\theta_r)] \pm \pi \\
&= \frac{4\pi d_{Film}n_{Film}}{\lambda_{Air}} \cos(\theta_r) \pm \pi,
\end{aligned} \tag{5.16}$$

The two rays constructively interfere when the phase difference is $\delta = 2m\pi$ (where $N = 0, 1, 2, 3...$ etc). Furthermore, the $\pm\pi$ is simplified to $-\pi$ since there is no difference in which sign π it takes. Hence,

$$\delta = 2m\pi = \frac{4\pi n_{Film}}{\lambda_{Air}} d_{Film} \cos(\theta_r) - \pi, \tag{5.17}$$

Hence,

$$\begin{aligned}
\frac{4\pi n_{Film} d_{Film} \cos(\theta_r)}{\lambda_{Air}} - \pi &= 2m\pi, \\
\frac{2n_{Film} d_{Film} \cos(\theta_r)}{\lambda_{Air}} - 1 &= m, \\
d_{Film} \cos(\theta_r) &= (m + 1) \frac{\lambda_{Air}}{2n_{Film}},
\end{aligned} \tag{5.18}$$

This shows what the wavelength of reflected light (λ_{Air}) decreases with respect to increasing angle of refraction θ_r (which decreases $\cos(\theta_r)$). Interference such as this is why the curve in figure 5.9 is a maximum at $\theta_i = 0$ and decreases in wavelength when $\theta_i > 0$.

Figure 5.12 is a plot of the measured and modelled reflectance for 30 layer ‘Blue’, ‘Green’ and ‘Red’ DBR reflection peaks with respect to angle of incident light. Reflectance of the measured sample reflection peaks (data-points) started to decay as θ_i increased. This was most likely due to imperfections in the sample which reduced the reflectance of the DBR. Moving the incident light towards a grazing angle illuminates a larger area of the sample. Therefore, unwanted imperfections may have been measured by mistake. Modelled data with sharp interfaces (represented by solid lines) were relatively constant as θ_i increased. However, the modelled data which had the refractive index contrast between layers reduced (dashed lines), increased as the incident light deviated away from the normal of the sample surface. It was difficult to model the reflectance of the DBR samples which are swelled with residual solvent. This thickness of the layers increases and the refractive index decreases. Hence, the optical path length of the layers is changed $OPL = n_{Film} d_{Film} \cos(\theta_{Film})$. This changes how the partially reflected waves constructively interfere. The reflectance will increase if the constructive interference of the partially reflected light is more efficient. This is comparable to tuning the layers of the DBR sample into a more efficient structure, which was discussed in section 5.3.4.

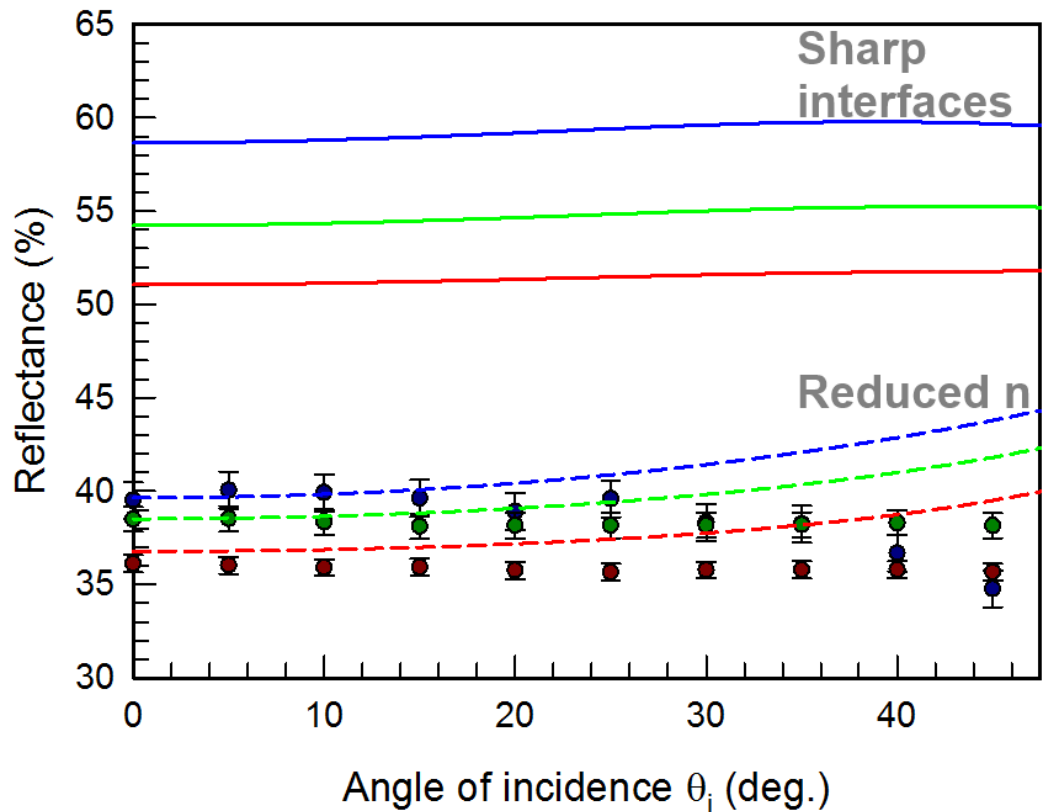


Figure 5.12: Reflectance of 30 layer ‘Red’, ‘Green’ and ‘Blue’ DBR reflection peaks were measured with respect to angle of incidence. Measurements of DBR samples are represented by the data-points. The average of five repeat measurements were used. Errors were calculated using the standard deviation. The modelled data with sharp interfaces is represented by the solid line. Both results showed the reflectance of the DBR staying relatively constant as they were rotated. The measured ‘Blue’ sample did drop in reflectance, but this could be due to the incident beam measuring a surface defect. Results were also calculated for modelled samples which have a reduced refractive index contrast (dashed lines). The reflectance from these samples was increased when the angle of incidence was larger. This is probably due to the optical path length of the layers being changed by modifying the value of the refractive indices.

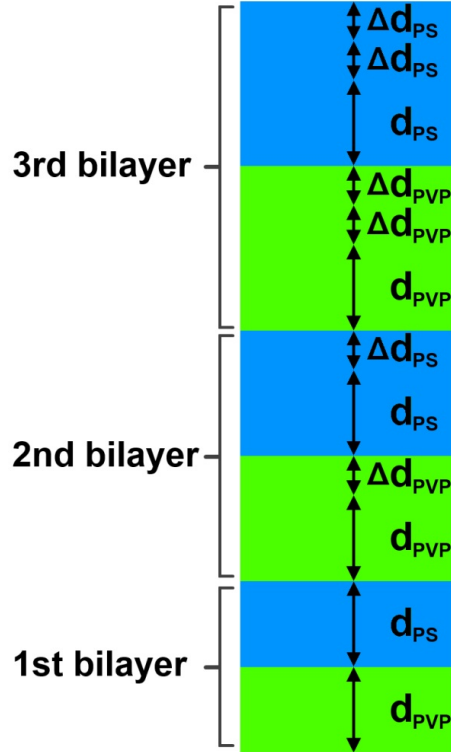


Figure 5.13: A representation of the incremental increase in the bi-layer film thickness of chirped structures. The thickness of each bi-layer increases slightly by Δd after each bi-layer deposition. This was achieved during sample preparation by decreasing the deposition speed when spin-casting a film. Changes in the spin-speed were controlled using a self written Matlab program and the automated spin-cater set up.

5.6 Chirping the photonic structure

Sample preparation was modified by designing and building an automated spin-coater (which was discussed in section 4.3.1). The data in figures 4.12 and 4.19 were used to calibrate the automated system. This technique was extended to make *chirped samples*. The narrow reflection bands of the polymer DBRs may be of benefit to some applications such as optical filters [1,2]. However, some applications which may require a broader reflection bands. This can be achieved by chirping the photonic structure. Chirping is when there are small incremental changes in the thickness of the multi-layer films are added while they are being prepared (illustrated in figure 5.13). This results in a broader reflection band which is composited of discrete reflection peaks.

A chirped sample was prepared for the purpose of optical measurements

Initial layer thickness (nm)	PVP thickness d_{PVP}	Initial layer thickness (nm)	PS thickness d_{PS}	Chirp per bi-layer δd (nm)	Fitted change in refractive index contrast $\delta(\Delta n)$
250 ± 1		250 ± 1		$+1 \pm 1$	18 ± 1

Table 5.3: The variables used to model the chirped DBR sample (UV/visible spectra of the sample is shown in figure 5.14). The refractive index contrast was reduced to improve the fit of the DBR model.

and modelling. This sample was made by initially depositing a bi-layer with $d_{PVP} = 250 \pm 1nm$ and $d_{PS} = 250 \pm 1nm$ thickness layers. More bi-layers were deposited onto the sample as it was being prepared. However, each bi-layer deposition was increased by $\delta d = +1 \pm 1nm$ until 25 bi-layers (50 layers in total) were deposited. The sample was annealed for 5 hours at $110^{\circ}C$ under a $\sim 1mtorr$ vacuum.

A UV/visible spectrum measured from the chirped DBR sample (data-points) is shown in figure 5.14. The reflection properties of the sample were modelled using the optical transfer matrix method (discussed in section 3), which was modified to include the incremental changes in film thickness. A chirped sample with sharp interfaces was modelled and is represented in figure 5.14 by the solid grey curve. Another model was calculated to improve the reflectance fit by changing the refractive index contrast between the polymers (represented by the dashed black curve). The variables used to model the data are shown in table 5.3.

The measured and modelled spectra showed how chirping the structure broadens the reflection band. Non-chirped samples had reflection bands which were $\sim 15nm$ wide (FWHM), whereas the chirped samples had reflection bands which were $\sim 40nm$ wide. The discrete peaks of the chirped reflection band were not accurately modelled using the modified optical transfer matrix method. This was likely due to be limited by the film thickness resolution obtained during spin-coating (which is typically $\pm 1nm$). The samples were chirped by adding $+1 \pm 1nm$ to each bi-layer during sample preparation. It was not possible to model the spectra of the chirped sample with high precision because of the errors in spin-cast film thickness.

The reflectance of the chirped DBR sample ($\sim 32.7\%$) was significantly less than a comparable non-chirped 50 layer sample ($\sim 52\%$). All of the partial re-

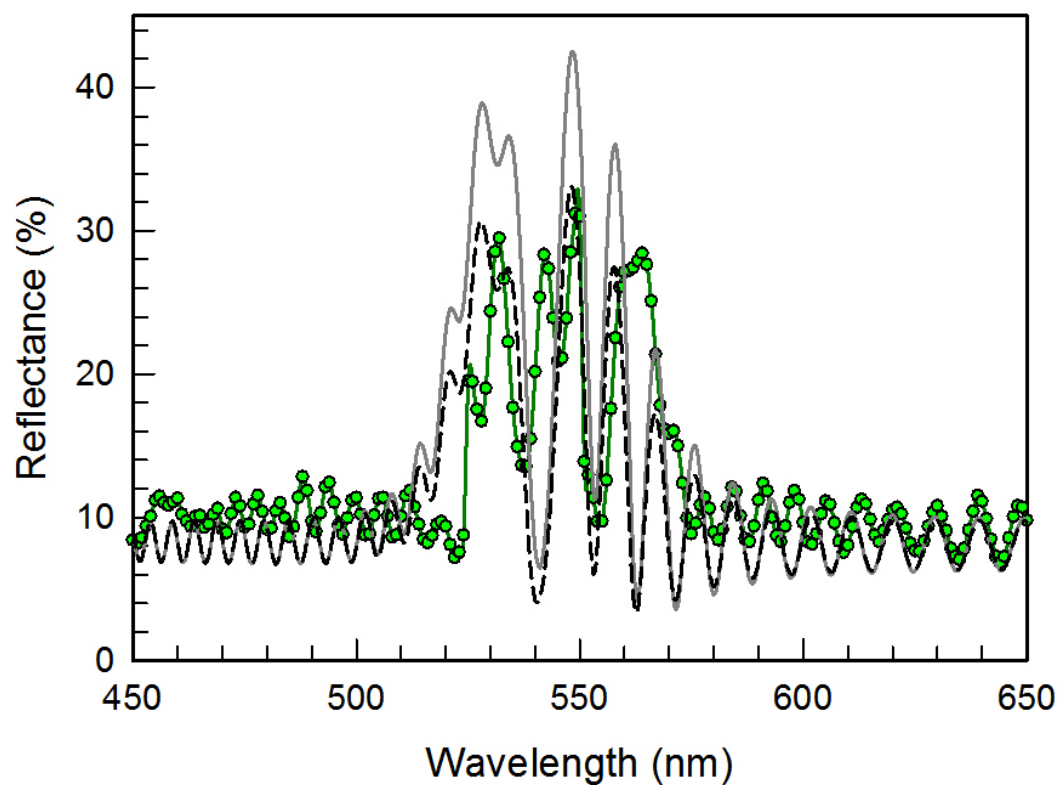


Figure 5.14: UV/visible reflection spectra of a chirped DBR. This is a 50 layer sample whereby, the initial thickness of the PVP and PS layers were both $250 \pm 1\text{nm}$. The thickness of both layers increased by $1 \pm 1\text{nm}$ per bi-layer deposited. This broadens the reflection band. The data-points and interconnecting green curve are the UV/visible spectroscopic measurements of the sample. The solid grey curve are the results for a modelled sample with sharp interfaces. The dashed black curve is spectra which was modelled for a sample with reduced refractive index contrast between layers.

flections are contributing towards a single wavelength in a non-chirped sample. Whereas, the partial reflections in a chirped sample are contributing towards a broader range of wavelengths.

5.7 Summary

Polymer DBR samples were successfully prepared by spin-coating PVP and PS films into a multi-layer structure. The wavelength of the reflection band could be controlled by varying the thickness of the polymer layers. This was possible by controlling the spin-speed when depositing layers. Thinner/thicker films were prepared by spin-coating at a faster/slower spin-speed respectively. Making the DBR layers thicker/thinner would red-shift/blue-shift the wavelength position of the reflection peak respectively.

The reflectance of the DBR was controlled by the number of layers deposited onto the sample. Increasing the number of layers also increases the number of interfaces. More partial reflections occur when there are more interfaces. These partial reflections contribute towards the total reflectance of the DBR sample. A total reflectance of $\sim 55\%$ was possible with a 50 layer sample. Adding more than 50 layers did not increase the reflectance when using this technique. However, this was later improved by changing the sample preparation technique (which is discussed in the next chapter).

There was a large difference between the reflectance of measured and modelled reflection peaks. Various possible explanations were investigated to determine why the reflectance of the samples were reduced. This included large polymer-polymer interface widths, disorder in the layer thickness and disproportionate layer thickness. However, it was concluded that residual solvent (left over from sample preparation) was the most likely cause of the problem.

The angular dependence of the DBRs was measured by using the rotation stage in the transmission set-up spectrometer (see section 4.5.1). Diverging the incident light away from the surface normal of the sample had blue-shifted the wavelengths of the reflection peak. The measurements showed the reflectance of the DBRs staying constant when the angle of incidence was changed. However, this was difficult to model because of the refractive index being changed by the residual solvent in the DBRs layers. These values were different from the

spectroscopic ellipsometry measurements which were used in the calculations. Attempting to correct for changes in the refractive index (by reducing Δn) resulted in the model misrepresenting the reflectance of the measured spectrum when changing the angle of incidence.

The bandwidth of the reflection peak was increased by chirping the multi-layer structure. This technique used the automated spin-coater set-up to incrementally increase the layer thickness per bi-layer deposition. The width of the reflection band was increased from $\sim 15nm$ to $\sim 40nm$ wide.

Chapter 6

Improving the preparation and reflectance of PVP/PS DBRs

6.1 Introduction

The optical measurements in chapter 5 showed that the PVP/PS DBRs had a lower reflectance than what was predicted by the model. Those samples were prepared using techniques discussed in section 4.3. A total reflectance of $\sim 55\%$ was possible with a 50 layer DBR. However, adding more than 50 layers did not increase the reflectance, when using the same preparation technique. A larger reflectance would be needed before integrating these DBRs into devices [4]. This chapter discusses preparation techniques used to increase the reflectance of PVP/PS DBR samples. The total reflectance of PVP/PS DBRs was increased to $\sim 93\%$ (with a 100 layer DBR) by modifying the sample preparation procedure.

6.2 DBR samples after ageing

The DBR samples in sections 5.2 and 5.4 were remeasured approximately one year after their preparation. It was discovered that the reflectance of the samples reflection peaks had increased over time. The wavelength of the samples reflection peaks had also slightly red-shifted after ageing. Figure 6.1 shows the UV/visible spectra of a ‘Green’ 30 layer (top caption) and 50 layer (bottom

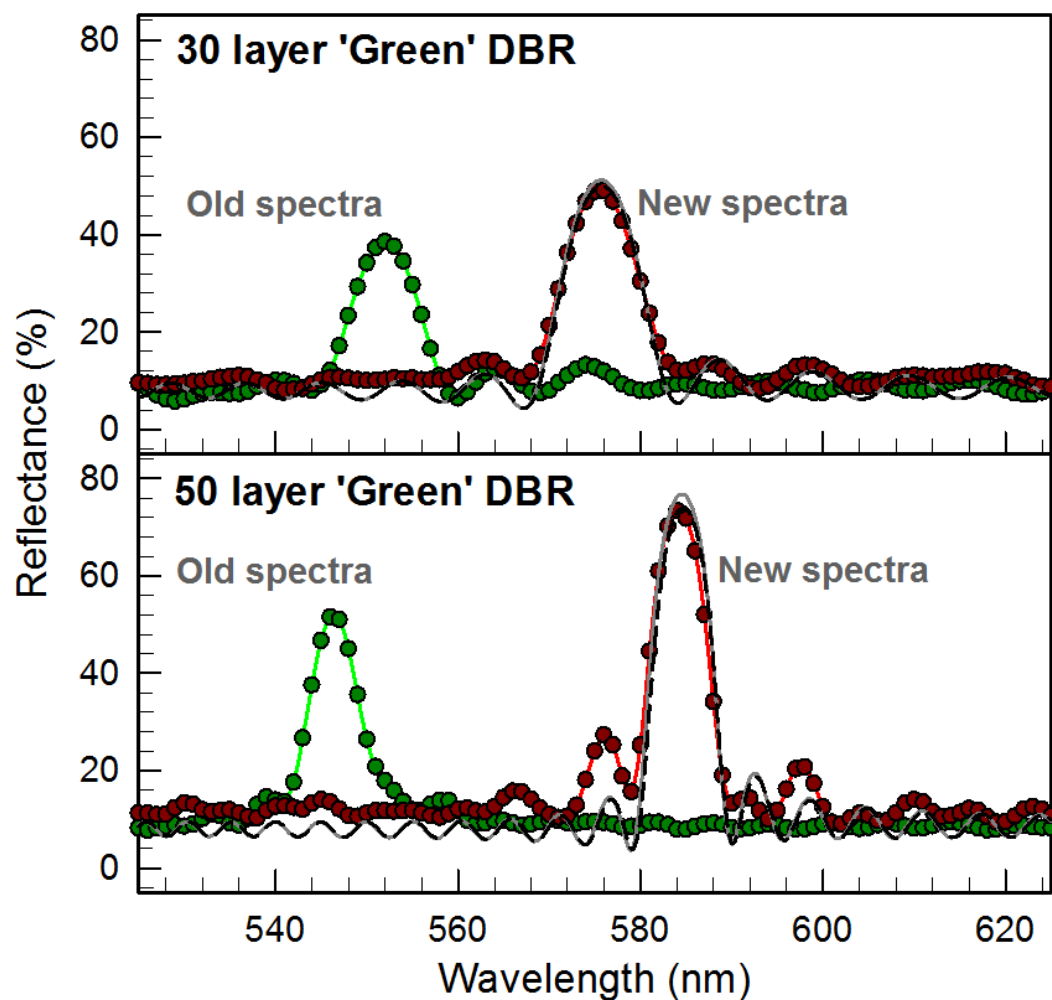


Figure 6.1: The reflection spectra of the 30 layer [top panel] and 50 layer [bottom panel] ‘Green’ DBR samples were remeasured approximately one year after their preparation (red data-points and curves). These measurements were compared with the original results (green data-points and curves) for comparison. The wavelength of the reflection bands had red-shifted and their reflectances had increased. Results for a modelled DBR with sharp interfaces (grey curves) were calculated for the remeasured spectra. Likewise, a modelled DBR with reduced refractive index contrast (grey curves) were calculated for the remeasured spectra. There was only a small change in refractive indices ($\delta(\Delta n) = 0.006 \pm 0.001$ for the 30 layer sample and $\delta\Delta n = 0.007 \pm 0.001$ for the 50 layer sample). This suggested that trapped solvent was diffusing out of the samples as they aged.

Spectra measured	Modelling technique	PVP layer thickness values used d_{PVP} (nm)	PS layer thickness values used d_{PS} (nm)	Reduction in refractive index contrast $\delta(\Delta n)$
‘Old’	Sharp interfaces	450 ± 9	262 ± 9	NA
	Reduced Δn	450 ± 9	262 ± 9	0.022 ± 0.001
‘New’	Sharp interfaces	466 ± 7	278 ± 7	NA
	Reduced Δn	466 ± 7	278 ± 7	0.006 ± 0.001

Figure 6.2: Values used to model the 30 layer ‘Green’ DBR samples for their ‘original’/‘old’ and ‘remeasured’/‘new’ reflectance measurements. The thickness of the modelled layers had increased and the change in refractive index contrast $\delta(\Delta)$ had decreased.

Spectra measured	Modelling technique	PVP layer thickness values used d_{PVP} (nm)	PS layer thickness values used d_{PS} (nm)	Reduction in refractive index contrast $\delta(\Delta n)$
‘Old’	Sharp interfaces	447 ± 12	259 ± 12	NA
	Reduced Δn	446 ± 13	258 ± 13	0.031 ± 0.001
‘New’	Sharp interfaces	472 ± 13	284 ± 13	NA
	Reduced Δn	472 ± 13	284 ± 13	0.007 ± 0.001

Figure 6.3: Values used to model the 50 layer ‘Green’ DBR samples for their ‘original’/‘old’ and ‘remeasured’/‘new’ reflectance measurements. The thickness of the modelled layers had increased and the change in refractive index contrast $\delta(\Delta)$ had decreased.

caption) DBR. The original/old spectrometry measurements are represented by the green data-points and interconnecting solid green curves. The remeasured/new spectra are represented by the red data-points and interconnecting solid red curves. Both samples were modelled using the modified optical transfer matrix method. The values used to fit the model to the measured spectra of the 30 and 50 layer samples are shown in tables 6.2 and 6.3 respectively. However, only the models for the remeasured/new spectra are shown in figure 6.1. The solid grey curves represent modelled DBR samples with sharp interfaces. The dashed black curves are modelled spectra which were fitted to measured spectra by reducing the refractive index contrast between the polymers by $\delta(\Delta n)$ (shown in tables 6.2 and 6.3).

The reflection spectra of both the 30 and 50 layer samples were measured shortly after their preparation. The calibration curve from figure 4.12 was used to calculate the film thickness of the polymer layers in the DBR samples. These layer thickness values were corrected (up to $\pm 12nm$) to improve the fit of the modelled reflection peak. The measured reflectance, of the reflection peak, for the 30 layer DBR sample was $38 \pm 1\%$. This reflectance was $15 \pm 1\%$ less than the modelled reflection peak for a 30 layer DBR sample with sharp interfaces ($53 \pm 1\%$). The reflectance of the modelled reflection peak was improved/decreased by reducing the refractive index contrast of the polymer layers by $\delta(\Delta n) = 0.022$. Likewise, the measured reflectance of the reflection band for the 50 layer sample was $52 \pm 1\%$. This was $28 \pm 1\%$ smaller than the reflection peak of a modelled 50 layer sample with sharp interfaces ($80 \pm 1\%$). The agreement between the measured and modelled reflectance of the reflection peaks was improved by reducing the refractive index contrast of the polymers by $\delta(\Delta n) = 0.031$. A larger value of $\delta(\Delta n)$ was needed to fit the reflectance of the 50 layer sample, compared to the value of $\delta(\Delta n)$ needed to fit the 30 layer sample. It would be more difficult for solvent to diffuse out of a sample which has more layers/interfaces. There was proportionally more trapped solvent in the 50 layer sample than the 30 layer sample.

The reflection peaks of both the 30 and the 50 layer ‘Green’ DBR samples had red-shifted after ageing. The wavelength of the 30 layer DBR reflection peak had red-shifted by $23 \pm 1nm$. Likewise, the wavelength of the 50 layer DBR reflection peak had red-shifted by $38 \pm 1nm$. The refractive index of the polymer layers would have increased when residual solvent diffused out of the

sample as it aged. However, the layers would have also de-swelled and their thickness would have decreased. However, the optical path length of the layers ($\text{OPL}_{\text{Film}} = n_{\text{Film}}d_{\text{Film}}/\cos(\theta_{\text{Film}})$ [10]) would have increased if the change in refractive index was proportionally greater than the change in film thickness. Furthermore, changes in the refractive index could have increased the refractive index contrast between the layers. This would have increased the reflectance of the reflection peaks.

The remeasured spectra were re-modelled using the modified optical transfer matrix method. Tables 6.2 and 6.3 show a comparison of the values for film thickness (d_{PVP} and d_{PS}) and change in refractive index contrast ($\delta(\Delta n)$) for modelled spectra of ‘Old’ and ‘New’ measurements. The thickness of the layers for the modelled 30 layer DBR had increased by 16nm when recalculated for the remeasured spectra. Likewise, the layer thickness of the modelled 50 layer DBR had increased by 25nm . There was a greater change in the optical properties of the 50 layer DBR than the 30 layer DBR over time. This was due to more solvent lingering in the 50 layer sample after preparation.

The peak reflectance value for the 30 and 50 layer samples had increased after ageing. Furthermore, the difference between the reflectance of the reflection peaks for the measured and modelled (with sharp interfaces) DBRs were reduced after ageing. The measured and modelled reflectance of the 30 layer DBR were $49 \pm 1\%$ and $53 \pm 1\%$ respectively after ageing. A reduction in the refractive index contrast of $\delta(\Delta n) = 0.006 \pm 0.001$ was needed to improve the modelled reflectance (shown in figure 6.1). Likewise, the measured and modelled reflectance of the reflection peak for the 50 layer sample were $73 \pm 1\%$ and $79 \pm 1\%$ respectively after ageing. A reduction in the refractive index contrast of $\delta(\Delta n) = 0.007 \pm 0.001$ was needed to improve the modelled reflectance. This could be due to trapped solvent still lingering in the sample and/or errors in the ellipsometry measurements of refractive index and layer thickness. These magnitude of changes in refractive index contrast were much smaller than those previously calculated for the 30 layer ($\delta(\Delta n) = 0.022 \pm 0.001$) and 50 layer ($\delta(\Delta n) = 0.031 \pm 0.001$) modelled reflection spectra. The refractive index of the polymer layers had increased because of residual solvent diffusing out of the sample as it aged. The refractive indices of the layers in the DBRs (after ageing) were more comparable with the previous measurements of single layer films (discussed in section 4.4.2).

The calculated thickness of layers used to model the remeasured DBR spectra were larger than the original single layer measurements. An increase of $7nm$, compared to the single layer measurement, was needed to fit the model to the remeasured spectra of the 30 layer sample. Likewise, an increase of $13nm$ was needed to fit the model to the remeasured spectra of the 50 layer sample. This may be due to increases in the film thickness and/or refractive index, as both increase the optical path length of the layer. There are several explanations which could cause changes in thickness and/or refractive index of the polymer layers;

- *Removal of residual solvent:* The solvents used to process the polymer solutions have a much lower refractive index than their respective polymers ($n_{toluene} = 1.496$, $n_{ethanol} = 1.360$ and $n_{Acetonitrile} = 1.344$). Both the single layer and the multi-layer samples were annealed at $110^{\circ}C$ for 5 hours under a $1mtorr$ vacuum. This is above the glass transition temperature of PS (T_g of PS = $97^{\circ}C$ [65]), but not PVP (T_g of PVP = $170^{\circ}C$ [65]). Some of the solvent could have been trapped within the multi-layer sample as PVP remained in a glassy state [18]. It would have been more difficult for solvent to diffuse out of/through the PVP layers. Most of the solvent should have diffused out of the PS single layer films as they were not capped with layers of PVP. However, there may have been residual solvent in the PVP layers during ellipsometry measurements. Residual solvent would have changed the optical path length of the films. This would have also changed film thickness and refractive index measurements of the PVP films. Unfortunately, a series of aged PVP samples were not able to be remeasured using ellipsometry.
- *Swelled by water vapour:* PVP is known to readily swell in the presence of water vapour, which includes room humidity [90]. The multi-layer structure may have had the water removed during annealing. However, the water may have then diffused back into the structure from the surrounding humidity of the air. This would swell the PVP layers, reduce its refractive index and increase the optical contrast between polymer layers. However, all of the DBR samples were capped with a layer of PS which is also hydrophobic. This would repel and water trying to penetrate into the sample [18]. The PS layers were also relatively thick, so it would be very difficult for water to penetrate through the layers and

swell the PVP films. Although, experiments did show the positions of the reflection bands red-shift when the sample was swelled in water vapour (results are not shown). The reflection bands also blue-shifted when the sample was placed in a dry air atmosphere. However, the reflection band relaxed into it's original reflection band wavelength within a few minutes after each experiment. This demonstrated that water vapour is able to penetrate through the multi-layer sample.

6.3 Asymmetry and symmetry of film thickness

The samples which were discussed previously in chapter 5 were prepared by spin casting solutions of 4.0% wt PVP in 50:50 ethanol:acetonitrile and 4.0% wt PS in toluene. All of the films were spin-cast at spin-speeds between 1.0*krpm* and 4.5*krpm*. The DBR samples from these experiments partially reflected light from each interface, which constructively interfered and resulted in the reflection peak. Each bi-layer within the DBR samples had an optical path length which was double the wavelength of light (2λ). There are also reflection peaks at other wavelengths which are calculated by,

$$\lambda_M = \frac{2}{M} [d_1 n_1(\lambda) + d_2 n_2(\lambda)], \quad (6.1)$$

Where n_1 and n_2 are the refractive indices of media '1' and '2' respectively, d_1 and d_2 are thickness of alternating polymer layers '1' and '2' respectively and $M = 1, 2, 3, \dots, \text{etc.}$

The reflection peaks which occur from even values of ' M ' disappear when $d_1 n_1 = d_2 n_2$. DBRs which have $d_1 n_1 = d_2 n_2$ structures are referred to 'symmetric samples' in this thesis. Likewise, samples which have a $d_1 n_1 \neq d_2 n_2$ are referred to as asymmetric samples. The wavelength position of reflection peaks from a symmetric DBRs are calculated by,

$$\lambda_M = \frac{2}{2M - 1} [d_1 n_1(\lambda) + d_2 n_2(\lambda)], \quad (6.2)$$

DBR samples were prepared with a layer thickness of $d_{Film} = 3\lambda/4n_{Film}$.

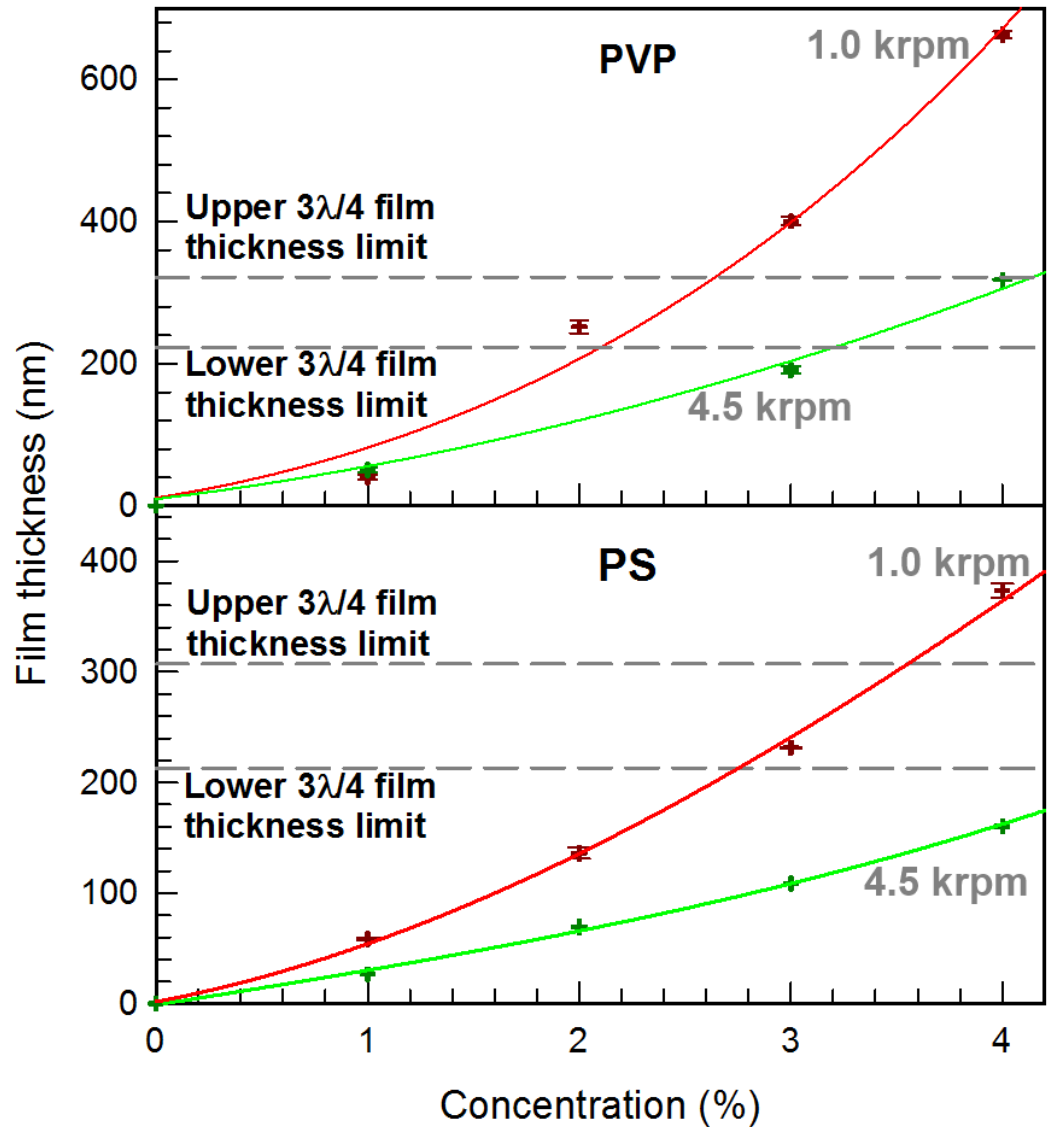


Figure 6.4: Film thickness of spin-cast polymer films with respect to polymer concentration. This experiment was used to select the best concentration for sample preparation. Specifically, when the thickness of the layer is $d = 3\lambda/4n$ for reflection peaks that are between wavelengths of 450nm and 650nm . This is within a layer thickness between 223nm to 322nm for PVP and 213nm to 307nm for PS (which are shown by the dashed lines on both plots). The curved lines are free hand drawn.

It was not possible to make samples with a layer thickness of $d_{Film} = \lambda/4n_{Film}$ without cracks forming during sample preparation. However, DBR samples should be prepared with the smallest layer thickness as possible. Thicker films deviate away from the coherence length of light, which reduces the efficiency of the DBR [12, 14]. The coherence length of light reflected by the DBR sample is calculated using the following equation [11],

$$\ell_C = \frac{2 \ln 2}{\pi n_{Film}} \frac{\lambda}{\Delta\lambda}, \quad (6.3)$$

Where ℓ_C = coherence length, n_{Film} = refractive index of film, λ = wavelength of reflection peak and $\Delta\lambda$ = full width half maximum of reflection peak.

Equation 6.3 was used to calculate the coherence length of light reflected by a 30 layer ‘green’ DBR (shown in figure 5.2). The coherence length was $10\mu m$, which is much larger than layers which are $3\lambda/4n_{Film}$ thick.

Layers with optical path length of $3\lambda/4$ could not be prepared by spin-casting from solution concentrations of 4.0% wt PVP and 4.0% wt PS. Reducing the film thickness further would have required spin-speeds greater than $4.5krpm$. This was not possible as the vacuum seal on the spin-coater could not keep the sample secure at faster spin-speeds. Instead, the concentration of the polymer solutions were reduced to decrease the layer thickness.

Figure 6.4 shows different thickness of films which were spin-cast from different concentrations of PVP and PS solutions. The red curves correspond to samples which were spin-cast at the lower spin-speed limit ($1.0krpm$). The green curves correspond to samples which were spin-cast at the upper spin-speed limit ($4.5krpm$). A film of thickness d can be prepared by any of the solutions within the red and green curves. Figure 6.4 was used to calculate the best concentration to prepare films with an optical path length of $3\lambda/4$ when measured at normal incidence. The thickness of a film with a optical path length of $3\lambda/4$ at normal incidence for reflected light of wavelength λ is calculated by,

$$d_{Film} = \frac{3\lambda}{4n_{Film}} \quad (6.4)$$

DBRs were prepared with reflection peaks at wavelengths between $450nm$

and 650nm . Equation 6.4 was used to calculate the thickness of the PVP and PS layers needed to make DBRs with reflection peaks at wavelengths between 450nm and 650nm . The lower (DBRs with reflection bands at $\lambda = 450\text{nm}$) and upper (DBRs with reflection bands at $\lambda = 650\text{nm}$) are indicated by the guidelines in figure 6.4. The blue coloured regions indicate the film thickness and solution concentration ranges needed make a DBR with a reflection peak between wavelengths of 450nm and 650nm . The PS concentration was kept at 4.0% wt. However, the PVP concentration was reduced to 3.2% wt. The film thickness with respect to spin-speed calibration curve for films spin-cast from a 3.2% wt PVP solution was shown in figure 4.12.

The dispersion of the refractive index (shown previously in figure 4.19), layer thickness with respect to spin-speed (shown previously in figure 4.12) and equation 6.4 were used to calculate the spin-speed used to prepare a layer with optical path length $3\lambda/4$ at normal incidence. This was written into a computer program which was used to control the automated spin-coater. The thickness of each deposited layer was controlled by changing the spin-speed. Samples with the same optical path length for ever layer could be prepared using this technique.

Figure 6.5 shows the UV/visible reflection spectra of two different DBR samples. The red curve represents the reflection spectra from a 50 layer ‘Green’ DBR. It had a bi-layer optical path length of 2λ and the optical path length of each layer were not all equal ($d_{PVP}n_{PVP} \neq d_{PS}n_{PS}$). This was named as a asymmetric sample. The grey curve represents a 50 layer DBR sample which has a bi-layer optical path length of $3\lambda/2$. All of the layers have same optical path length ($d_{PVP}n_{PVP} = d_{PS}n_{PS}$) and this was named as a symmetric DBR sample.

The reflectance of the asymmetric 50 layer DBR reflection peak was $52 \pm 1\%$. This was only 2% smaller than the reflectance of the symmetric DBR reflection peak (which is within error of the two spectrometer measurements). The symmetric DBR structure did not significantly increase the reflectance of the DBR samples. All of the layers are swelled with trapped solvent, which changes their optical path lengths. The symmetric sample is not likely to have the intended $d_{PVP}n_{PVP} = d_{PS}n_{PS}$ structure, unless the solvent has diffused out of the sample. However, the photonic structure is distinctively different from the asymmetric sample. This was demonstrated by the symmetric sample not

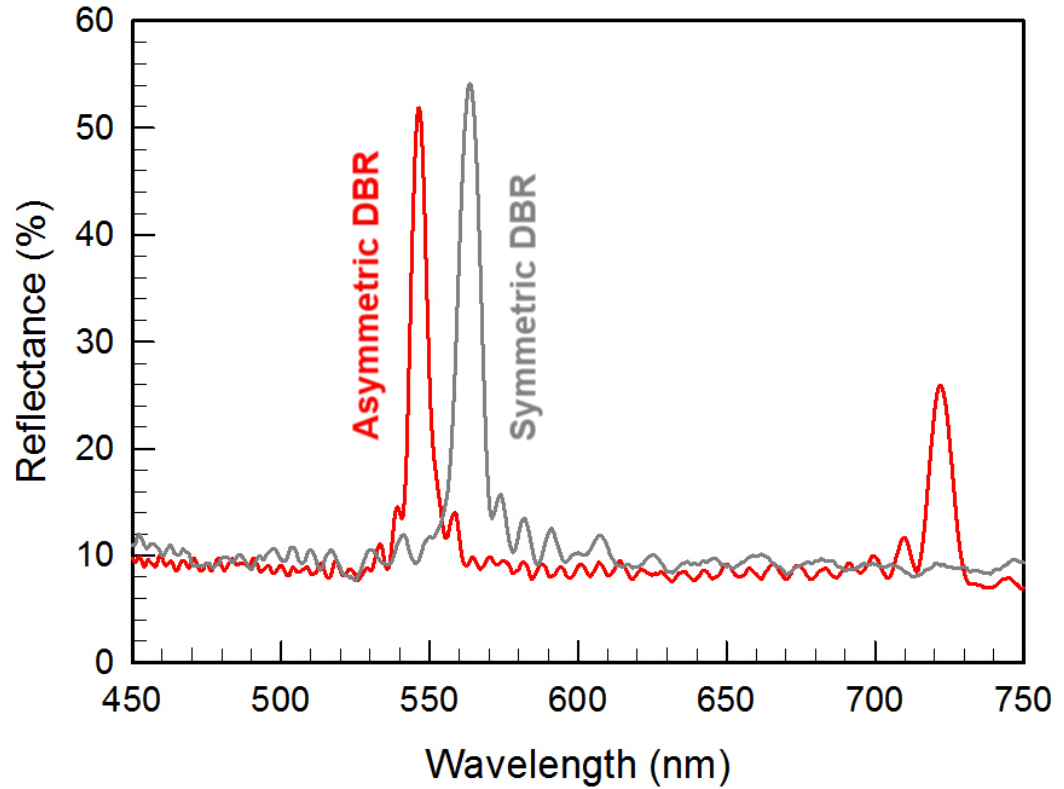


Figure 6.5: Comparison of two samples which are tuned close to 550nm . The red curve the reflection spectra from a 50 layer DBR with layers of thickness $n_{PVP}d_{PVP} \neq n_{PS}d_{PS}$, where $d_{PVP} = 360 \pm 16\text{nm}$ and $d_{PVP} = 214 \pm 16\text{nm}$ (optical thickness asymmetry). The black curve spectra is 50 layer DBR where the optical thickness of the layers is closer to $n_{PVP}d_{PVP} = n_{PS}d_{PS}$, where $d_{PVP} = 272 \pm 1\text{nm}$ and $d_{PVP} = 259 \pm 1\text{nm}$ (optical thickness symmetry). Furthermore, the DBR structure was changed by reducing the optical thickness of the bi-layer from λ (red curve) to $3\lambda/4$ (black curve). Both changes improve the reflectance of the DBR spectra slightly.

having a reflection peak at $722 \pm 1nm$. Changing the photonic structure and removing unwanted ‘secondary’ reflection peaks could be useful for applications such as notch filters [1,2].

6.4 Periodically annealing during sample preparation

It was discussed in section 5.4 that the reflectance from PVP/PS DBRs could not be increased by adding more than 50 layers. There was also a large difference between reflectance of the reflection peaks for measured and modelled DBRs. This worsened as the number of layers increased (which was illustrated in figure 5.8). The reflectance of the reflection peaks increased as the samples aged. Trapped solvent from sample preparation may have slowly diffused out of the sample as it aged (which was discussed in section 6.2). Waiting a year for the reflectance of the reflection bands to increase is impractical. Furthermore, the wavelength of the reflection peaks would red-shift as the sample ages. Annealing the samples above the glass transition temperature of PVP ($T_g = 170^\circ C$) was attempted. However, the samples would burn despite being annealed in a $\sim 1mtorr$ vacuum.

The DBR samples in chapter 5 were prepared by depositing all of the layers onto the substrate and then annealing the whole sample at once. This resulted in lingering solvent being trapped in the DBR sample. Trapped solvent would more readily diffuse out of samples which have less layers deposited. This is because the solvent would not have to penetrate through as many layers to diffuse out of the sample. The preparation technique was changed by periodically annealing the sample after approximately every 20 layers deposited. All annealing stages were at $110^\circ C$ for 5 hours under a $\sim 1mtorr$ vacuum. This allowed the solvent from freshly deposited layers to diffuse out of the sample during annealing.

Initial experiments demonstrated that the top layer would always have to be PVP when depositing more layers after annealing. The sample would crack if more layers were added to an annealed multi-layer which was capped with a PS film. This was due to top PS film being de-swollen after annealing. The un-swollen layer was unprotected when depositing the PVP solution on

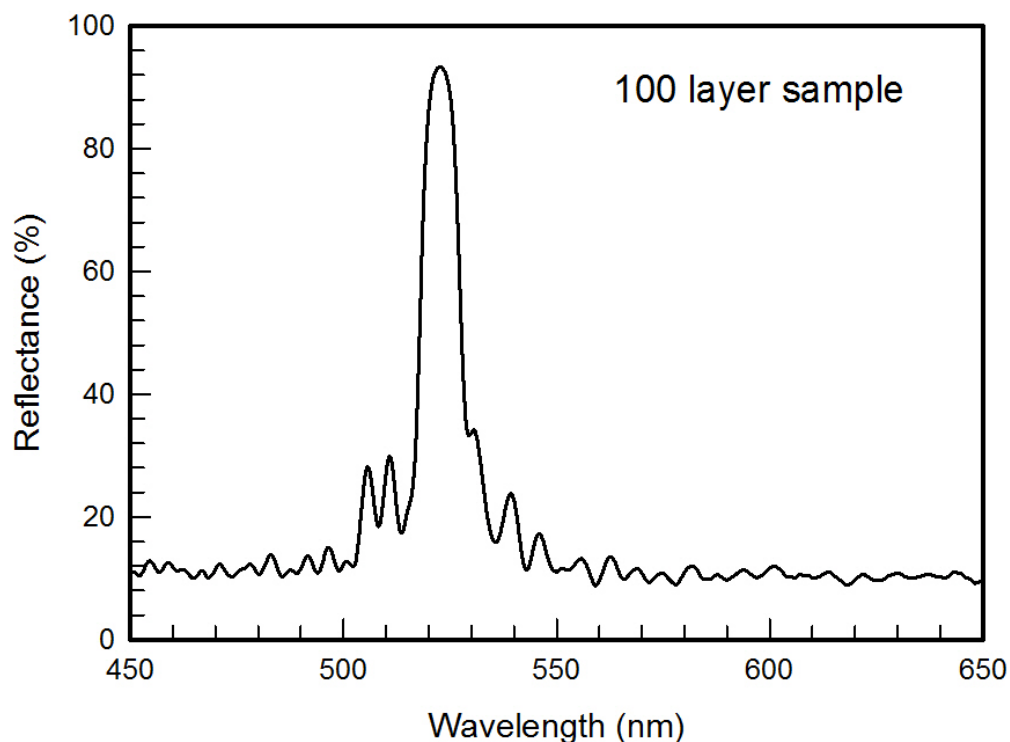


Figure 6.6: Reflection spectra from the 100 layer PVP/PS DBR. This samples was made by annealing at 110°C for 5 hours under a $\sim 1\text{mtorr}$ vacuum every 20 layers (approximately). Periodically annealing the sample during preparation helps to removed more residual solvent within the DBR. This improved the reflectance of the sample and allowed more than 50 layer (the previous limitation) to be added. $\sim 93\%$ (shown here) was the highest reflectance measured. A 150 layer DBR sample did not increase the reflectance any further.

top. Solvent from the PVP solution would attempt to penetrate through the unprotected PS layer and swell the underlying PVP films. This would strain the PS film and crack the sample. However, an annealed PVP layer could still be protected by swelling the film with HCl vapour. The samples were always capped with a PVP layer for annealing steps before the end of sample preparation. A final layer of PS was used to cap the sample at the end of its preparation. This PS capping layer was used to protected the underlying PVP layers from being swollen by air humidity.

Annealing periodically during sample preparation improved the reflectance of DBR reflection peaks. Furthermore, it enabled more layers to be deposited onto the sample. This increased the total reflectance possible with PVP/PS

DBRs. Figure 6.6 show the UV/visible reflection spectra of a 100 layer PVP/PS DBR. All of the layers were tuned to have the same optical thickness $n_1d_1 = n_2d_2 = 3\lambda/4$. The total reflectance of the reflection peak was $\sim 93 \pm 1\%$. A 150 layer sample (data not shown) was also prepared, but it did not increase the reflectance beyond $\sim 93 \pm 1\%$. Adding more than 50 layers did not increase the reflectance of the reflection peaks when using the previous sample preparation technique (discussed in section 4.3). The number of layers which contributed to the reflectance was increased by periodically annealing during sample preparation. A maximum of 100 ‘useful’ layers can be prepared using the preparation technique discussed in this section. However, adding more than 100 layers (using this preparation technique) did not increase the reflectance of the DBR reflection peaks. This could be due the quality of the sample degrading as each new layer is added. Specifically defects are carried through to any new layers which are deposited on top of the sample. It become increasingly more difficult to add more layers to a sample whilst also improving its reflectance.

6.5 Summary

Both the reflectance and wavelength position of the DBR reflection peaks was shown to increase as the PVP/PS DBR samples aged. This was due to residual solvent diffusing out of the DBRs over time. Removal of the solvent de-swells the polymer layers and increases their refractive index. The increase in refractive index had also increased the optical path length of the layers. This red-shifted the position of the reflection peaks. The refractive index contrast between the layers had also increased when the solvent diffused out of the sample. This increased the reflectance of the DBR reflection peaks. Changes in the reflection peak wavelength, for example, may be a problem when using these devices in applications, such as band-stop mirrors. Ideally, there would have been no residual solvent trapped in the DBR layers during sample preparation.

The reflectance was only slightly improved when the optical path length of the bi-layer was reduced to $3\lambda/4$, instead of 2λ . However, the number of reflection peaks in the UV/visible spectrum was reduced because of the differences in photonic structure. This may be useful in applications such as band-stop mirrors, which may only want a single wavelength removed from a spectrum.

The reflectance of the DBR reflection peak was increased by periodically annealing the sample during preparation. A total reflectance of $\sim 93\%$ was measured from a 100 layer sample which was prepared using this technique. Periodically annealing helped remove residual solvent during sample preparation. Less solvent was left lingering in the sample after preparation. However, there were only a small number of experiments which tested this preparation technique. This could be investigated further to determine why periodically annealing the sample enables more ‘useful’ layers (which increase the reflectance of the sample) to be deposited onto the sample.

Chapter 7

Infra-red measurements and properties of polymer DBRs

7.1 Introduction

The RGB DBR samples in figure 5.2 were designed to function as UV/visible reflectors. Light was partially reflected by the interfaces in the DBR sample. Each bi-layer in the structure had an optical path length of $n_{PVP}d_{PVP} + n_{PS}d_{PS} = 2\lambda$ (where λ is the wavelength of UV/visible light). However, other wavelengths of light can also be reflected by the DBR. The largest wavelength which can be reflected by a DBR is when $n_{PVP}d_{PVP} + n_{PS}d_{PS} = \lambda/2$ [12]. This corresponds to a wavelength which is twice the optical path length of the repeating bi-layer in the DBR. The RGB DBRs were able to reflect wavelengths which were in the infra-red. A Fourier transform infra-red (FTIR) spectrometer was used to measure the infra-red reflection peaks of the DBRs [91].

FTIR spectrometry was also used to measure the chemical composition of the DBR samples. Specifically, to determine if the polymer films underwent chemical changes when swelled with HCl vapour [91].

7.2 Measuring the effects of HCl swelling

The PVP layers were swollen with HCl to protect the films during sample preparation (which was discussed in section 4.3). FTIR was used to measure any chemical changes which could have occurred when swelling the samples with HCl vapour. Thick ($\sim 500nm$) films of PVP and PS were spin-cast onto calcium fluoride optical windows (CaF_2). The CaF_2 substrate is often used in FTIR studies since it is non-absorbing in the Infra-red spectrum. Each of the samples were placed into the FTIR and their infra-red absorption spectra were separately measured. The samples were then taken out of the FTIR sample chamber and swelled using a large reservoir of HCl vapour. DBRs which were swollen with HCl vapour (which were previously made for the experiments in chapter 5) had a different reflection colour from samples which were not swollen with HCl vapour. This was due to the film thickness and refractive indices of the layers changing after being swollen with HCl vapour. The reflection colour did not change any further after a few seconds of exposure. This was because the polymer layers were saturated with HCl vapour. It was assumed that a few seconds of HCl vapour exposure was an adequate length of time to saturate thick single layer polymer films. The samples were placed back into the FTIR spectrometer and the absorption spectra were remeasured. Each sample was remeasured at different time intervals to measure the effects of swelling PVP with HCl vapour over time.

Carboxylic acid (such as Acyl chloride) are used to cross-link polymers [49]. HCl is a highly reactive acid which may have cross-linked, degraded and/or chemically reacted with the polymers. Any of these examples would have changed the chemical structure of the polymers. FTIR was used to measure changes in the absorption spectra of the polymer films before and after being swollen with HCl vapour. Chemical reactions (such as cross linking and/or degradation) would have changed the intensity of the absorption bands, because the chemical structure of the sample would have changed. New absorption peaks would indicate that there are new chemical structures in the sample. This could be due to a chemical reaction, or a new chemical being introduced into the sample [69, 70].

Results showed that the PS film was unaffected by its exposure to HCl vapour (results not shown). The polymer did not undergo a chemical reac-

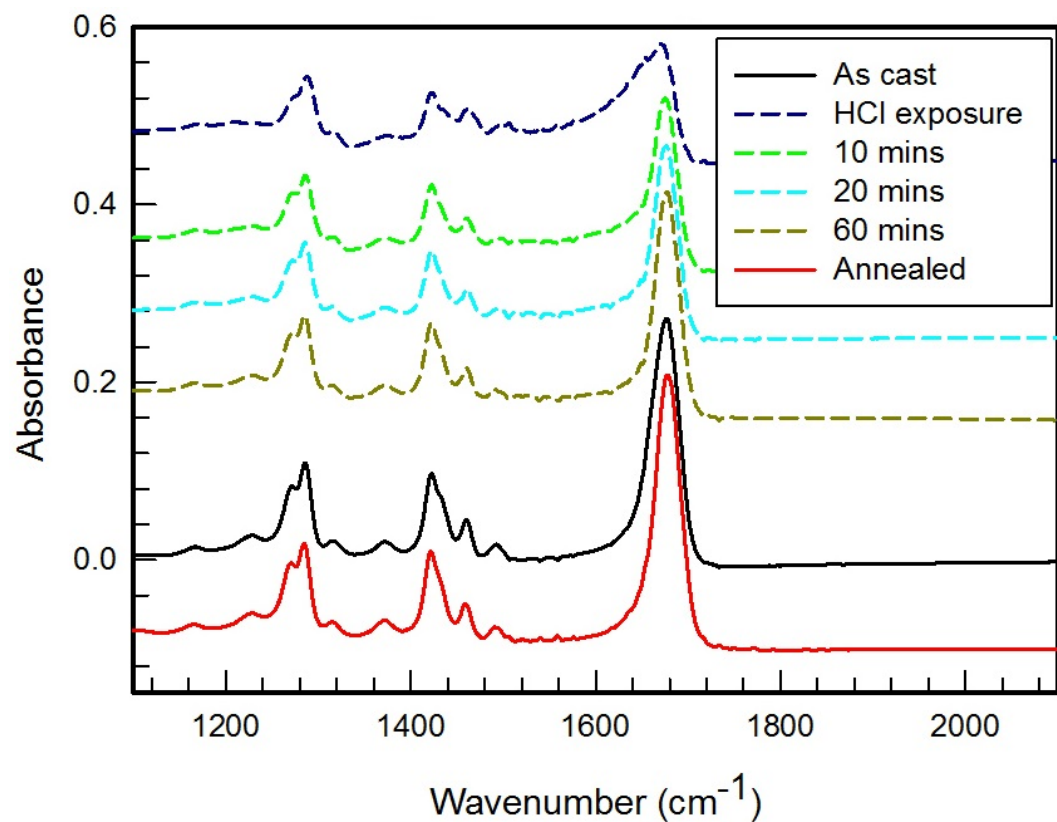


Figure 7.1: FTIR spectra of a PVP film measured under different conditions. The peaks at $\sim 1280\text{cm}^{-1}$ and $\sim 1420\text{cm}^{-1}$ correspond to the C – N and C – H vibration bonds respectively. Likewise, the large peak at $\sim 1670\text{cm}^{-1}$ is due to the C = O carbonyl group [92, 93].

tion, retain any HCl vapour, or swell in HCl vapour at all. FTIR absorbance measurements did show changes in the PVP film when it was exposed to HCl vapour. However, this was not due to any chemical reactions. The changes in absorption spectra were due to lingering HCl vapour within the polymer film. Figure 7.1 shows the FTIR absorbance spectra of the PVP sample measured at different time intervals after HCl vapour exposure.

There were 3 distinctive peaks which were measured in the FTIR absorbance spectra of the the PVP film (shown in figure 7.1). Each peak corresponded to an absorption from different chemical bonds in the PVP molecule. The chemical formula for PVP is $(C_6H_9NO)_n$ and the chemical structure was shown in figure 4.2. The first FTIR absorption bands were at $\sim 1280cm^{-1}$ and $\sim 1420cm^{-1}$ which correspond to the accepted C – N and C – H vibrations respectively [70]. The final peak was measured at $\sim 1670cm^{-1}$, which corresponds with vibrations from carbonyl groups within the polymer [70].

Swelling the PVP film with HCl vapour caused the absorption peaks to broaden and decrease in absorbance. This also occurred when measuring the FTIR spectra of as cast PVP films, which were not annealed before FTIR measurements. These samples were swollen with residual 50:50 ethanol:acetonitrile solvent in the PVP film. The intensity of the absorption peaks increased and also their widths decreased when residual 50:50 ethanol:acetonitrile solvent diffused out of the PVP film by annealing the sample. This also occurred when the HCl vapour diffused out of the PVP film when the sample was annealed.

Comparison of the pre-swollen and annealed (which was previously swollen) spectra showed that the intensity of the absorption peaks were unchanged. New peaks in the PVP absorbance spectra did not appear after HCl vapour exposure. No chemical reactions had occurred (including cross-linking) in the PVP film during/after HCl vapour exposure. The HCl vapour only swelled the PVP layers during sample preparation.

The FTIR experiments showed that the HCl vapour slowly diffused out of the PVP film over time without annealing. A single layer PVP film should take a few hours to de-swell HCl vapour after exposure. It takes ~ 30 seconds to spin-cast a new polymer layer during sample preparation. A 50 layer sample took approximately an hour to prepare. The multi-layer would have retained a lot of HCl vapour and also residual organic solvent (50:50 ethanol:acetonitrile

and toluene) during sample preparation. UV/visible reflectance of the reflection peaks from DBR samples did not increase when adding more than 50 layers (which was discussed in section 5.4). However, more layers could be added, which increased the reflectance of the DBR, by annealing the sample after approximately every 20 layers were deposited (which was discussed in section 6.4). Residual solvent more readily diffused out of the DBR when it was periodically annealed during sample preparation. Therefore, too much lingering solvent may reduce the quality of samples during their preparation.

7.3 DBR reflection bands in FTIR spectra

Figure 7.2 shows the FTIR measurements for 50 layer ‘Red’, ‘Green’ and ‘Blue’ PVP/PS DBR samples. They are the same samples which were measured using UV/visible spectroscopy. Measurements of single layer PVP and PS showed that there are no chemical absorption bands for those materials between $1.6\mu m$ and $2.7\mu m$ in these samples (data not shown). The FTIR spectra measured between $1.6\mu m$ and $2.7\mu m$ are DBR reflection bands. These results are shown with respect to wavelength instead of wave-number. Wavelength was used so that the results could be compared with UV/visible measurements. Note that the samples were measured with respect to transmittance. However, the following figures show the results with respect to reflectance, which were calculated by using the following equation,

$$R = 100\% - T - A, \quad (7.1)$$

Where R = reflectance and A = absorbance of the sample.

There were no absorption bands within the $1.6\mu m$ and $2.7\mu m$ wavelengths, so $A = 0$.

7.3.1 Position of the reflection bands

The infra-red spectra of the 50 layer ‘Blue’, ‘Green’ and ‘Red’ DBRs are shown in figure 7.2. The data-points represent data which was measured using the FTIR spectrometer. Like the UV/visible spectra, the infra-red reflec-

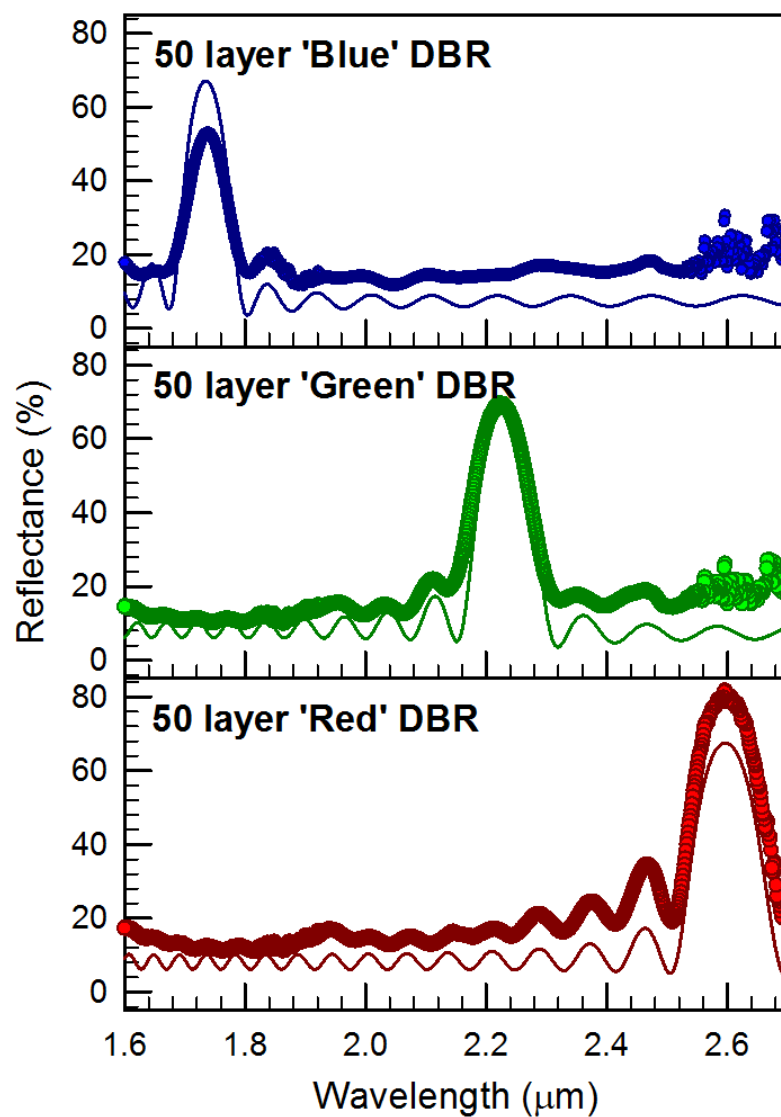


Figure 7.2: The 50 layer ‘Blue’ [top panel], ‘Green’ [middle panel], and ‘Red’ [bottom panel] DBRs were measured using FTIR (data-points). They are the same samples which were measured in UV/visible spectroscopy experiments. FTIR measurements of single layer polymers and the glass substrate showed that there were no absorption bands between $1.6\mu\text{m}$ and $2.7\mu\text{m}$. Therefore, the curves in the figure are reflection bands from the DBR structure and controlled by the film thickness of the samples. All of the spectra was modelled using the optical transfer matrix method (solid curves). The ‘noisy’ spectra near $2.6\mu\text{m}$ in the ‘Blue’ and ‘Green’ samples were due to absorption from residual water.

Sample	Single layer PVP thickness (nm)	PVP thickness used in model (nm)	Single layer PS thickness (nm)	PS thickness used in model (nm)
'Blue' DBR	$376 \pm 1nm$	$362 \pm 14nm$	$220 \pm 1nm$	$206 \pm 14nm$
'Green' DBR	$459 \pm 1nm$	$459 \pm 1nm$	$271 \pm 1nm$	$271 \pm 1nm$
'Red' DBR	$527 \pm 1nm$	$530 \pm 3nm$	$317 \pm 1nm$	$320 \pm 3nm$

Table 7.1: Ellipsometry film thickness measurements and adjusted film thickness corrections used to model 50 layer 'Blue', 'Green' and 'Red' PVP/PS DBR samples. Large corrections for the modelled film thickness may have been due to the infra-red refractive index measurements. The film thickness would have been reduced if the measured refractive index was too high (so that the optical thickness of the sample nd was the same). This is discussed further in section 7.4.

tion bands are ‘blue-shifted’/‘red-shifted’ when the thickness of the layers in the DBR are made thinner/thicker respectively. The thickness of the layers were controlled by the rotation speed during spin-coating. Spin-cast films are made thinner/thicker by increasing/decreasing the deposition spin-speed respectively. The ability to control the position of narrow ($\sim 0.15\mu m$) reflection bands within $1.6\mu m$ and $2.7\mu m$ may be useful to telecommunications using fibre optics [10, 22]. These reflection bands could be used as notch filters in fibre optics to select or remove signals at specific wavelengths and remove noise.

The widths of the reflection peaks were between $120nm$ and $180nm$ when measured in the infra-red spectrum. This is much larger than the widths measured in the UV/visible spectrum, which were between $10nm$ and $17nm$. The increase in bandwidth is due to an increase in coherence length, which is discussed more thoroughly in the next section.

Infra-red spectrometry measurements were modelled using the modified optical transfer matrix method (which was discussed in chapter 3). Ellipsometry film thickness measurements and modelling film thickness adjustments are shown in table 7.1. The film thickness corrections used to improve the fit between the measured and modelled spectra (shown in table 7.1), are not the same as those used for the UV/visible spectrum calculations (shown in table 5.1). Residual solvent in the DBR samples would have changed the refractive index, layer thickness (due to swelling) and optical path length ($OPL = nd/\cos(\theta)$) of the polymer layers. The optical path length in the UV/visible is not the same as in the infra-red wavelengths, because of differences in the refractive index values. This was compensated by adjusting the thickness of the layers.

Only spectra for modelled DBRs with sharp polymer-polymer interface widths are shown in the figures (represented by the solid curves in figure 7.2). Modelled spectra which included possible changes in the refractive index contrast ($\delta(\Delta n)$) were not calculated. This was because of uncertainty in the refractive indices when modelling infra-red spectra of the samples. The refractive index of the polymers (and contrast between layers) would have changed because of lingering solvent. There are also errors in the infra-red refractive index calculations, which are discussed further in section 7.4.1.

7.3.2 Controlling the reflectance of infra-red DBRs

The infra-red reflectance of the PVP/PS DBR samples (shown in figure 7.2) increased by adding more layers to the DBR structure. Adding more layers adds more interfaces, which increases the reflectance of the DBR reflection peaks. Therefore, the magnitude of the reflectance can be controlled by increasing or decreasing the number of layers deposited.

The reflectance of the reflection peaks in the infra-red (shown in figure 7.3) are much larger than the reflectance of the UV/visible reflection peaks (shown in figure 5.4). The largest reflectance measured in the infra-red was $\sim 80\%$ from the 50 layer ‘Red’ DBR sample. Whereas $\sim 55\%$ was the largest reflection peak measured in the UV/visible from the 50 layer ‘Blue’ DBR sample. The reflectance would have increased if the refractive index contrast Δn between the layers was larger. However, the refractive index contrast in the infra-red ($\Delta n \sim 0.062$) was smaller than the contrast in the UV/visible ($\Delta n = \sim 0.075$). The increase in reflectance is not entirely due to the refractive index of the layers changing. Instead, it is due to the properties of how the partially reflected light interferes from each interface.

Constructive interference occurs when two ‘light sources’ are emitting light which are coherent with respect to one another. This is comparable to reflections from two separate interfaces in a DBR sample. Constructive interference is more prominent when the separation between the interfaces is much less than the *coherence length* [10, 13]. The coherence length of infra-red is larger in these DBR samples (with respect to UV/visible light) because of a longer wavelength and smaller refractive index (see equation 6.3). This leads to the interference of reflected infra-red light being more prominent than the UV/visible reflections [10, 13].

The reflectance was modelled using the optical transfer matrix method (which was discussed in section 3). This is represented in figure 7.3 by the solid lines. The model suggested that there should only be a small difference in the reflectance of the 50 layer ‘Blue’ ($R = 67 \pm 1\%$), ‘Green’ ($R = 69 \pm 1\%$) and ‘Red’ ($R = 67 \pm 1\%$) reflection peaks. However, there were large differences between the measured reflectance of the reflection peaks of the 50 layer ‘Blue’ ($R = 52 \pm 1\%$), ‘Green’ ($R = 68 \pm 1\%$) and ‘Red’ ($R = 81 \pm 1\%$) DBRs. Differences between the measured and modelled spectra could have been due to

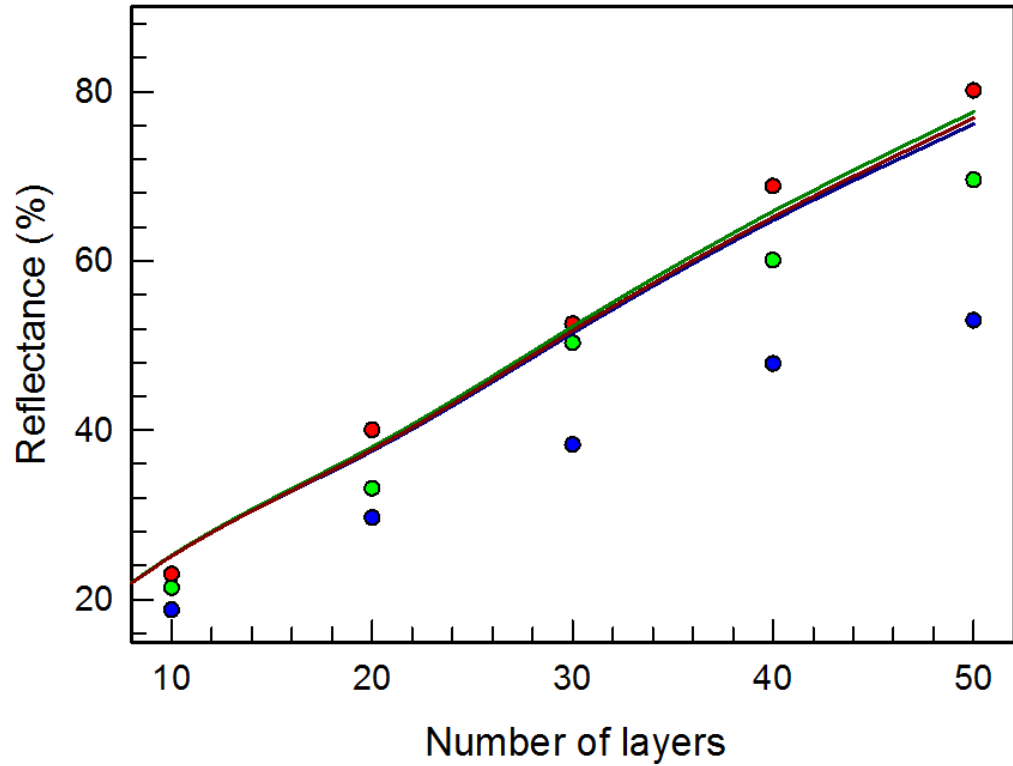


Figure 7.3: Reflectance of the ‘Blue’, ‘Green’ and ‘Red’ DBR samples were measured in the infra-red (data-points) with respect to the number of layers deposited. Each sample ‘colour’ is appropriately labelled in the plot. All of the curves were free hand drawn. The reflectance of the samples were also modelled for a sample with sharp interfaces (solid lines). Increasing the number of layers also increases the reflectance of the DBR. The differences between the measured and modelled data are due to errors in the values used to model the reflectance.

residual solvent in the DBR layers, which changes their refractive indices. This would have also changed refractive index contrast between the polymer layers. Reducing/raising the refractive index contrast would have increased/decreased the reflectance of the reflection peaks respectively. Section 7.4.1 discusses the method used to calculate the refractive index of the polymer in the infra-red spectrum. These calculations were used to model the DBR infra-red spectrum. Errors in the refractive index calculations would have inaccurately modelled the reflectance of the infra-red reflection spectra.

7.4 Modelling infra-red DBR spectra

The modified optical transfer matrix method was used to model the infra-red spectra of PVP/PS DBRs. The film thickness and refractive index of the polymer layers were measured for use in the calculations. Film thickness was measured by spin-casting single layer polymer films onto silicon wafers and using ellipsometry. The film thickness were corrected slightly to improve modelled data fit (shown in table 7.1). These values were slightly different from the corrections used to model the reflection peaks in the UV/visible measurements. This was because the refractive indices of the films are not the same for different wavelengths. The optical path length of the DBRs layers, when transmitting infra-red light, is not the same as when transmitting UV/visible light through the layers ($OPL_{Film} = d_{Film}n(\lambda)_{Film}$ at normal incidence [10]).

7.4.1 Wavelength dependence of refractive index

Unfortunately, it was not possible to get access to equipment which is an infra-red analogue of a spectroscopic ellipsometer. Instead, alternative methods were used to determine the refractive indices of the polymer films at infra-red wavelengths.

A free-standing PS film was prepared in an effort to calculate the refractive index of the polymer in the infra-red. The infra-red reflection spectra of the free-standing PS film was measured using the FTIR spectrometer. A duplicate of the free-standing PS film was spin-cast on a silicon substrate and the film thickness was measured using ellipsometry. The infra-red reflection spectra of

the free-standing polymer was modelled using the modified optical transfer matrix method. This model could be used to calculate the refractive index values of PS as it was the only unknown variable. However, the FTIR measurements of the free-standing film were not reproducible. It was not possible to measure the refractive index values of PS in the infra-red spectrum using the equipment available.

The spectroscopic ellipsometer (which was discussed in section 4.4.2) measured the dispersion of the refractive index from the UV/visible to the near infra-red ($0.9\mu m$). Refractive index measurements from the spectroscopic ellipsometer were fitted using a Cauchy function. The data was re-analysed for wavelengths measured in the μm instead of the nm length scale. Ideally, the measurements would have been in the infra-red wavelengths. However, it was assumed that the dispersion functions for both UV/visible and infra-red wavelengths are the same. The following equations are the Cauchy fits for PS, PVP and glass calculated to the 3rd order approximation with respect to μm wavelengths;

$$\begin{aligned} n_{PS}(\lambda) &= 1.568 + \frac{6.270 \times 10^{-3}}{\lambda^2} + \frac{0.428 \times 10^{-3}}{\lambda^4}, \\ n_{PVP}(\lambda) &= 1.507 + \frac{2.702 \times 10^{-3}}{\lambda^2} + \frac{0.315 \times 10^{-3}}{\lambda^4}, \\ n_{glass}(\lambda) &= 1.425 + \frac{4.563 \times 10^{-3}}{\lambda^2} + \frac{0.201 \times 10^{-3}}{\lambda^4}. \end{aligned} \quad (7.2)$$

The second and third terms become very small when λ is large. Therefore, the refractive index is nearly constant when extrapolating the refractive index values into the infra-red. Hence, these extended dispersion curves were used to model the refractive index of the materials in the infra-red.

These assumptions are supported by previous studies which measured the refractive index of various polymer (polystyrene, Polycarbonate and Poly(methyl methacrylate)) within wavelengths of $0.4\mu m$ and $1.6\mu m$ using a purpose built interferometer. Their results demonstrated that the refractive indices were approaching a constant magnitude in the near infra-red ($1.6\mu m$). The data was also analysed using a Cauchy fit to calculate refractive index values of the polymers [94].

The refractive index calculations were used with the optical transfer matrix method to calculate the reflection spectra of the DBRs in the infra-red. Figure 7.2 showed that the model could calculate the wavelength position of the reflection peaks. However, more thorough measurements of the refractive indices in the polymers should be used to accurately model the reflectance of the reflection peaks.

7.5 Summary

DBR reflection peaks were measured between $1.6\mu\text{m}$ and $2.7\mu\text{m}$ in the infra-red spectrum. The wavelength position of the reflection peaks were controlled by changing the layer thickness of the films in the DBR samples. This was controlled by the deposition spin-speed when preparing samples.

The infra-red reflectance of the DBR samples was controlled by changing the number of layers deposited onto the sample. Adding more layers increases the reflectance of the reflection peak, because more interfaces are added to the DBR structure. A total reflectance of $\sim 81\%$ was measured in the infra-red spectra from a 50 layer sample. The 100 layer sample which was discussed in section 6.4 was not measured using FTIR spectroscopy. It may have had a greater reflectance than the 50 layer sample when measured in the infra-red spectrum.

The wavelength of the reflection peaks were successfully modelled using the modified optical transfer matrix method. However, the reflectance of the infra-red reflection peaks could not be adequately modelled. This was due to errors in how the refractive indices of the polymer layers were calculated. Unfortunately, it was not possible to measure the refractive indices of the polymer layers in the infra-red wavelengths at the time of these experiments. Measuring the refractive indices (rather than extracting values from extended UV/visible wavelength measurements and equations) would be more accurate when modelling the reflection spectrum of the DBRs in the infra-red spectrum.

The chemical absorption bands of the polymers were measured using FTIR spectrometry. Exposing the samples to HCl vapour (during sample preparation) did not cross-link or degrade the polymer layers. Only the PVP layers were swollen by the HCl vapour during sample preparation.

Chapter 8

Neutron reflectivity measurements of polymer multi-layers

8.1 Introduction

Neutron reflectivity was used to measure the polymer-polymer interfaces in PVP-PS bi-layers and multi-layers. The wavelength of neutrons is much smaller than visible light and fine-scale structures (like polymer-polymer interface widths) can be measured. Neutrons are able to penetrate into a sample to measure its internal structure [55, 71].

Diffuse polymer-polymer interfaces σ were suggested as a possible explanation as to why the measured reflectance was lower than predicted in chapter 5. Estimates for σ were calculated by fitting the modelled spectra to measurements. The polymer-polymer interfaces widths of 30 layer PVP/PS DBRs were estimated as between $21nm$ and $28nm$. These values were larger than experiments measuring the polymer-polymer interfaces widths of similar polymer samples [85].

8.2 Measuring and modelling polymer samples

Unfortunately, only 3 out of the 6 prepared samples could be measured (which was discussed in section 4.7.1). However, the samples which were measured were analysed and some useful information was extracted.

8.2.1 Deuterated PS

The properties of the single deuterated PS (dPS) sample were measured using neutron reflectivity and analysed using the Motofit fitting program [74]. Ellipsometry was used to measure the film thickness of the silicon oxide layer and polymer films. AFM was used to measure the surface roughness of the substrate and spin-cast polymer films. Literature values were used for variables such as the interface roughness between silicon and its native oxide layer [95]. The *Scattering length density calculator* within the MotoFit program [74] was used to calculate the neutron scattering length density ρ of all materials. Hence, as many variables as possible were measured or calculated before fitting the modelled spectra in the MotoFit program. The input and fitted variables are shown in table 8.1.

Specular neutron reflectivity cannot discern between rough and diffuse interfaces as the entire sample surface is measured simultaneously [71]. Off specular reflection spectra was not measured during these experiments. There is no diffuse interface between the SiO_2 and the polymer film, as the two materials cannot intermix. The surface roughness of the SiO_2 layer was measured using AFM. This was used to calculate the roughness between SiO_2 and the polymer film σ_{Si-dPS} and was kept constant during data fitting. Likewise, the dPS -Air interface was measured using an AFM, but this was fitted during modelling. This was to test the quality of the fit by comparing it with the AFM measurements.

The film thickness of the SiO_2 layer (measured using ellipsometry) was kept constant during modelling. Ellipsometry was used to measure the film thickness of the dPS layer. The thickness value of dPS was used as an initial guess in the fitting program. Its thickness was allowed to vary slightly to improve the quality of the fit with respect to neutron reflectivity measurements. Variations in film thickness, as small as $1nm$, can dramatically change the modelled reflection

Variable	Scattering length density ρ ($\times 10^{-6}$)	Input - Film thickness d (nm)	Fitted - Film thickness d (nm)	Input Roughness σ (nm)	Fitted Roughness σ (nm)
<i>dPS</i>	5.99 ± 0.01	147.0 ± 2.0	145.9 ± 0.1	0.48 ± 0.01	0.48 ± 0.01
<i>SiO₂</i>	3.47 ± 0.01	2.0 ± 1.0	2.0 ± 1.0	0.69 ± 0.07	0.69 ± 0.07
<i>Si</i>	2.07 ± 0.01	NA	NA	0.4 ± 0.1	0.4 ± 0.1

Table 8.1: Table of the variables used to model the dPS single layer film. The input film thickness values were measured using ellipsometry. The interface roughness of the layers was measured using AFM (except the *Si-SiO₂* interface was determined by using literature data [95]). The only parameters which were allowed to change during fitting were d_{dPS} and σ_{dPS} . Changes to the film thickness were within error of the ellipsometry measurement (calculated using the standard deviation of five repeat measurements). The surface roughness measurement σ_{dPS} did not change significantly. Measured and modelled neutron reflectivity spectra is shown in figure 8.1.

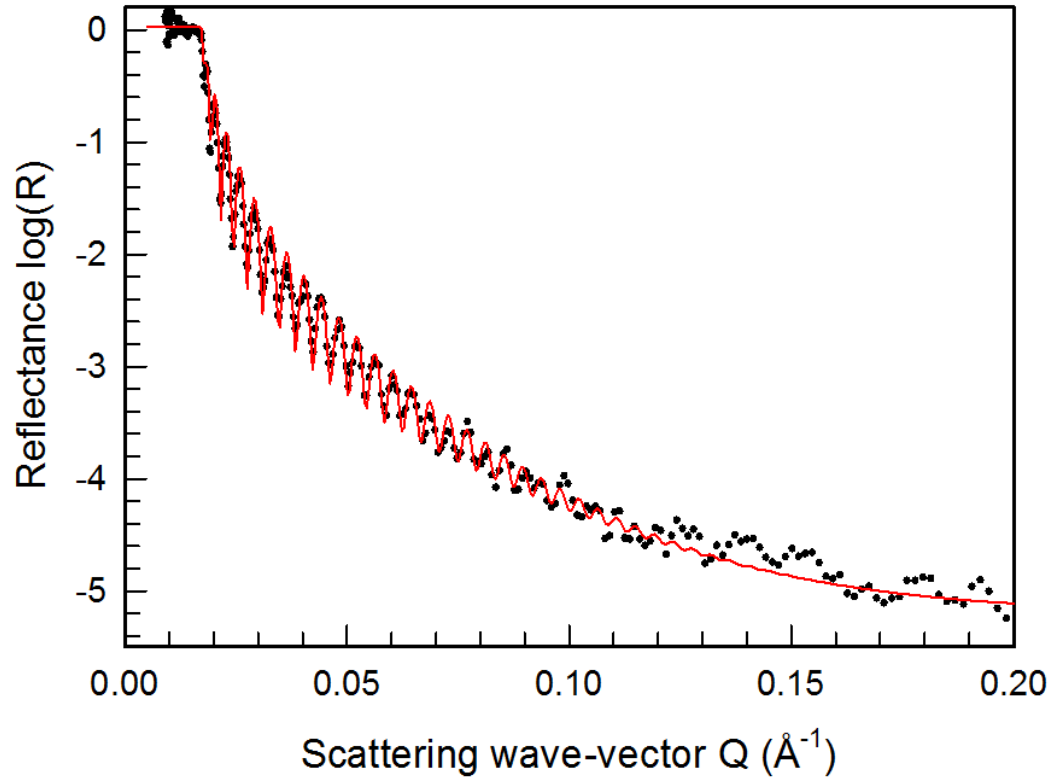


Figure 8.1: Neutron reflectivity measurements (data-points) and fitted model (red curve) for a single layer of deuterated PS which was spin-cast onto a silicon substrate. Keeping all of the variables were kept constant except for d_{dPS} and σ_{dPS} when fitting the model to the measurement. The neutron reflectivity and AFM measurement of σ_{dPS} were the same. The film thickness was modified slightly when fitting the data, but it was within error of the ellipsometry measurement.

spectra.

Figure 8.1 shows the neutron reflectivity measurements (data-points) and the fitted model using Motofit (red curve). The fitted data is within good agreement of the neutron reflectivity measurements. Surface roughness measurements of the dPS film were unchanged during fitting. Furthermore, the thickness of the dPS film only changed by $\sim 1nm$ which was within error of the ellipsometry measurements. Therefore, the measurements and assumptions of the Si and SiO_2 layers were a good approximation for the substrate.

8.2.2 PVP (top) \rightarrow dPS (bottom) bi-layer

Unfortunately, only one of the bi-layer samples was measured, which was the PVP (top) \rightarrow dPS (bottom) bi-layer. The input film thickness of each layer was measured using ellipsometry. A single layer dPS film was used to measure the film thickness of the bottom layer in the sample. Whereas, the thickness of the PVP (top layer) was measured using Ellipsometry measurements of the bi-layer were used to calculate the thickness of the PVP (top) layer. The surface roughness of the bi-layer was measured using AFM and was kept constant during fitting. The surface roughness of a single layer dPS was measured using AFM. This was used as an initial guess for the interface width of $\sigma_{PVP \rightarrow dPS}$. The initial film thickness and interface width variables are shown in table 8.2.

Figure 8.2 shows the neutron reflectivity measurements (data-points) and model (green curve) of the PVP(top) \rightarrow PS(bottom) bi-layer sample. The data was modelled by varying the thickness of the polymer films d_{PVP} and d_{dPS} and polymer-polymer interface width $\sigma_{PVP \rightarrow dPS}$ (shown in table 8.2 as the ‘Fitted - Roughness’ for dPS) with respect to the neutron reflectivity measurements. Both the neutron reflectivity measurements of the film thickness d_{PVP} and d_{dPS} were thinner than the ellipsometry measurements. The difference in d_{PVP} thickness was within error of ellipsometry. However, the change in the thickness of dPS (bottom layer) was from $147.0 \pm 2.0nm$ (measured using ellipsometry) to $142.9 \pm 0.1nm$ (measured using neutron reflectivity). The change in layer thickness was slightly larger than the ellipsometry measurement error. Furthermore, the neutron reflectivity measurement of dPS in this experiment was slightly less (by $3nm$) than the neutron reflectivity measurement from section 8.2.1. Preparing the sample by depositing the solution while the substrate is

Variable	Scattering length density ρ ($\times 10^{-6}$)	Input - Film thickness (nm)	Fitted - Film thickness (nm)	Input Roughness (nm)	Fitted Roughness (nm)	- σ
<i>PVP</i> (top film)	1.39 ± 0.01	183.0 ± 3.4	182.0 ± 0.1	1.27 ± 0.30	1.27 ± 0.30	
<i>dPS</i> (bottom film)	5.99 ± 0.01	147.0 ± 2.0	142.9 ± 0.1	0.48 ± 0.01	0.61 ± 0.01	
<i>SiO₂</i>	3.47 ± 0.01	2.0 ± 1.0	2.0 ± 1.0	0.69 ± 0.07	0.69 ± 0.07	
<i>Si</i>	2.07 ± 0.01	NA	NA	0.4 ± 0.1	0.4 ± 0.1	

Table 8.2: Variables used in the Motofit program and were subsequently fitted with respect to the neutron reflectivity measurements of a *PVP* (top) \rightarrow *dPS* (bottom) bi-layer. The polymer film thickness measurements d_{PVP} and d_{dPS} and polymer interface $\sigma_{PVP \rightarrow dPS}$ were allowed to vary to fit the model to the measured spectra. The film thickness of *dPS* decreased slightly below error and the thickness of *PVP* decreased within error. Interface roughness $\sigma_{PVP \rightarrow dPS}$ (shown in 'Fitted - Roughness' for *dPS*) increased slightly. The measured interface width was two orders of magnitude less than what was estimated in chapter 5. The neutron reflectivity measurements and modelled spectra are shown in figure 8.2.

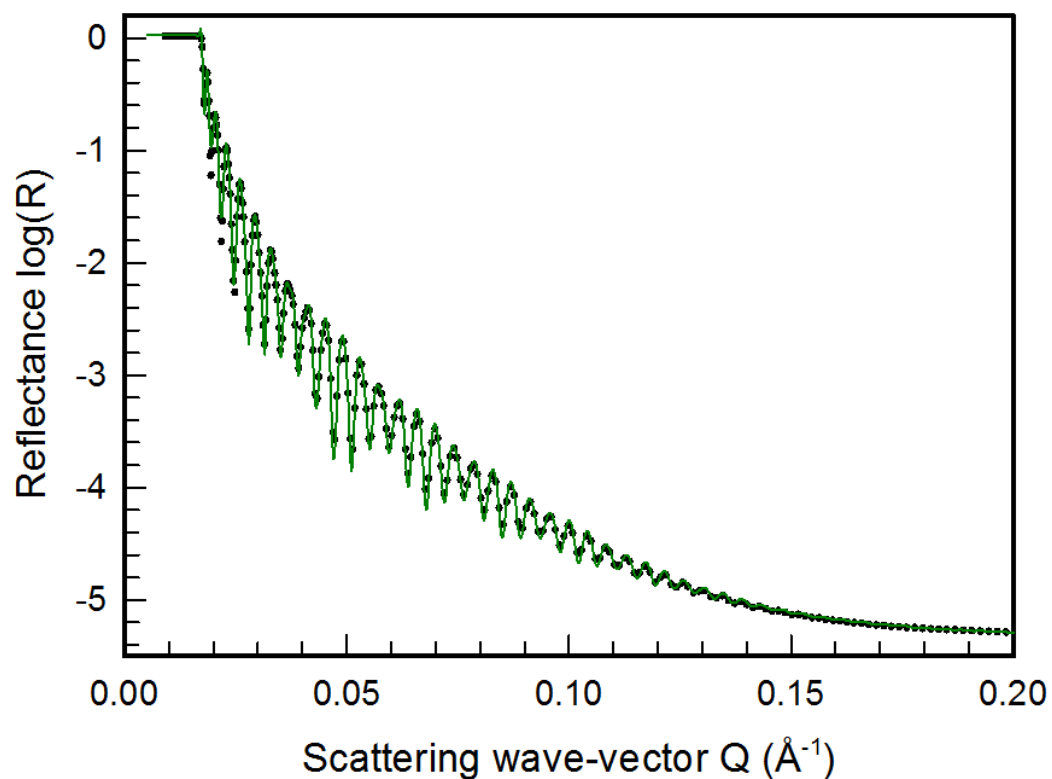


Figure 8.2: Neutron reflectivity measurements (data-points) and modelled data (green curve) of a PVP(top)→dPS(bottom) bi-layer. The modelled data was within good agreement of the neutron reflectivity measurements. Variables used to fit the data are shown in table 8.2. The film thickness of d_{dPS} and d_{PVP} were reduced to fit the measured data. Results showed that the interface width of $\sigma_{PVP \rightarrow dPS}$ increased slightly from the surface roughness of dPS . This suggested that a small increase in interface width did occur from diffuse polymer-polymer mixing at the interface.

spinning (discussed in section 4.7.1) may result in film thickness changes. This is when compared to depositing the solution onto a stationary substrate and then spin-casting.

The polymer-polymer interface width $\sigma_{PVP \rightarrow dPS}$ was slightly larger than the surface roughness σ_{dPS} measured in section 8.2.1. This shows that polymer-polymer diffuse intermixing is occurring when preparing the DBR multi-layers. However, neutron reflectivity measured the polymer interface widths as $\sigma_{PVP \rightarrow dPS} = 0.61 \pm 0.01 nm$ which is two orders of magnitude less than the initial diffuse interface estimates (which were approximately $\sim 25 nm$) obtained from optical methods. Neutron reflectivity spectra were calculated for larger interface widths, but the data was a poor fit of the measurements. Therefore, previous polymer-polymer interface width calculations using the DBR optical spectroscopy data are a huge over-estimate of the actual polymer-polymer interface widths. The low reflectivity of the DBR samples when compared to the model is likely due to other properties, such as lingering solvent in the polymer layers. This would change the refractive index contrast in the samples. A lower refractive index contrast would reduce the reflectance of the DBR reflection peaks.

8.2.3 10 layer PVP/dPS structure

The dPS(top)→PVP(bottom) bi-layer sample was not able to be measured due to time restrictions. However, the 10 layer PVP/dPS sample was measured which should allow the dPS→PVP interface $\sigma_{dPS \rightarrow PVP}$ to be estimated from the neutron data fit.

The sample was made from alternating layers of PVP and dPS which were spin-cast on top of a silicon substrate. PVP was the first polymer layer to be deposited and PS was the last. It was assumed that any small differences between each layer are negligible since it would not be possible to model each layer independently. The surface roughness of the 10 layer sample was $0.47 \pm 0.08 nm$, measured over a $40 \mu m \times 40 \mu m$ surface area using AFM. This was only $0.21 nm$ smaller than the PVP(top)→dPS interface $\sigma_{PVP \rightarrow dPS}$ (which was measured in section 8.2.2). The model was simplified by periodically stacking 5 dPS(top)→PVP(bottom) bi-layers on top of a silicon substrate to make the multi-layer. This replaced the modelled surface roughness of the sample with

Variable	Scattering length density ρ ($\times 10^{-6}$)	Input - Film thickness (nm)	Fitted - Film thickness (nm)	Input Roughness (nm)	Fitted Roughness (nm)	- σ
<i>dPS</i> (re-peats)	1.39 ± 0.01	147.0 ± 2.0	149.7 ± 0.1	0.61 ± 0.01	0.61 ± 0.01	
<i>PVP</i> (re-peats)	5.99 ± 0.01	183.0 ± 3.4	184.0 ± 0.1	1.27 ± 0.30	0.96 ± 0.01	
<i>SiO₂</i>	3.47 ± 0.01	2.0 ± 1.0	2.0 ± 1.0	0.69 ± 0.07	0.69 ± 0.07	
<i>Si</i>	2.07 ± 0.01	NA	NA	0.4 ± 0.1	0.4 ± 0.1	

Table 8.3: The initial variable values and fitted results when modelling the neutron reflectivity spectra of a 10 layer PVP/dPS structure. The film thickness used in the Motofit program were the same ellipsometry measurements to model the PVP (top)→dPS bi-layer. The interface roughness $\sigma_{PVP \rightarrow dPS} = 0.61 \pm 1nm$ (shown in the *dPS* row for the ‘Input - Roughness’ and also the ‘Fitted - Roughness’) was kept constant as it was measured in section 8.2.2. The AFM measurement of the surface roughness for the top layer PVP film in the bi-layer sample was used as an initial estimate of the $dPS \rightarrow PVP$ interface $\sigma_{dPS \rightarrow PVP}$ (shown in the PVP row). However, the fitted data suggested that the interface width was slightly less.

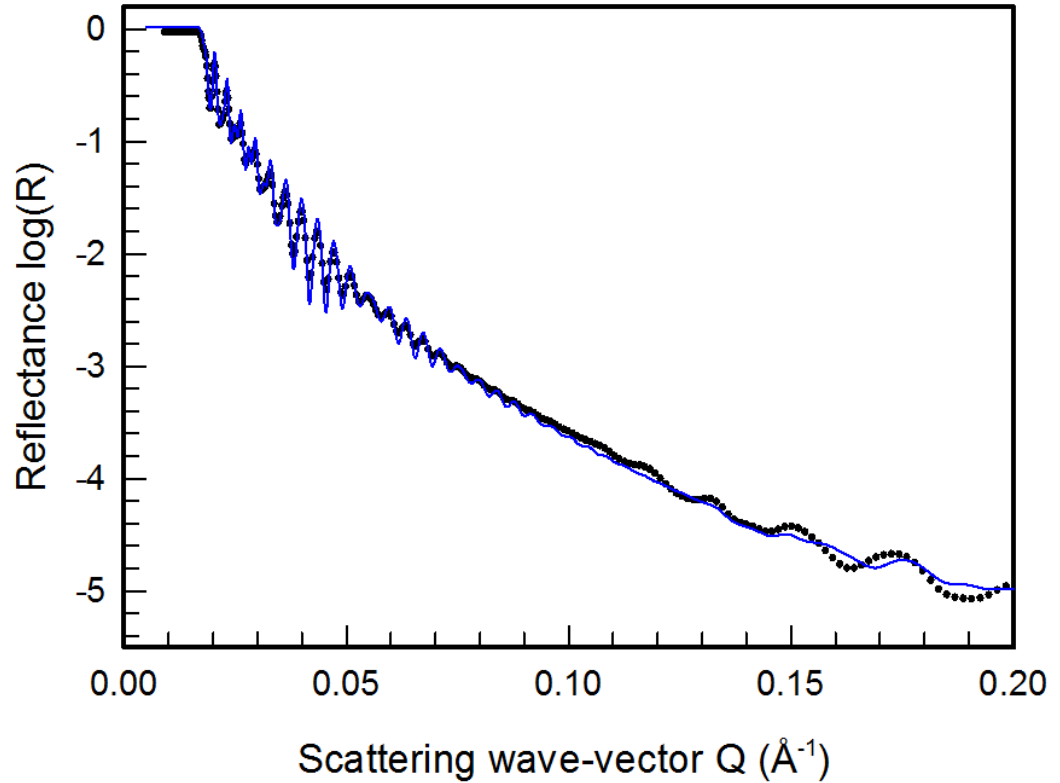


Figure 8.3: Neutron reflectivity measurements (data-points) and modelled spectra (blue curve) of a 10 layer PVP/dPS structure. The thickness of the polymer layers (d_{PVP} and d_{PS}) and the dPS \rightarrow PVP interface ($\sigma_{dPS\rightarrow PVP}$) were fitted whilst all other variables were kept constant. Table 8.3 shows the input and fitted values used to measure the film thickness and polymer-polymer interface widths. These results measured the dPS(top) \rightarrow PVP interface as $\sigma_{dPS\rightarrow PVP} = 0.96 \pm 0.01$. This was slightly smaller, but just under the error, of the surface roughness a dPS film which was measured using AFM.

a PVP→dPS polymer-polymer interface width for simplicity. However, the difference between the surface roughness and PVP(top)→dPS interface was considered to be negligible.

Figure 8.3 shows the neutron reflectivity measurements (data-points) and model (blue curve) of the 10 layer sample PVP/dPS sample. Table 8.3 shows the input and fitted values used to model the neutron reflectivity measurements. Ellipsometry measurements were used as the input film thickness values in the model (shown under ‘Fitted - Film thickness’ in table 8.3). Specifically, the thickness of the top layer in bi-layer samples were measured and used in the calculations. Hence, the measurements were of films which were spin-cast on top of polymer substrates.

Neutron reflectivity was previously used to measure the $\sigma_{PVP \rightarrow dPS}$ in a PVP(top)→PS(bottom) bi-layer (see section 8.2.2). This interface was equivalent to any $\sigma_{PVP \rightarrow dPS}$ interfaces in the multi-layer. The value of this interface was kept constant when modelling the neutron reflectivity measurements of the 10 layer sample.

The $\sigma_{dPS \rightarrow PVP}$ interface width was the only unknown variable for the 10 layer neutron reflectivity measurement. AFM was used to measure the surface roughness of a PVP(top)→PS(bottom) bi-layer. This was used as an initial approximation for the $\sigma_{dPS \rightarrow PVP}$ interface width. The neutron reflectivity model was fitted by varying the thickness of the layers (d_{PVP} and d_{PS}) and the $\sigma_{dPS \rightarrow PVP}$ interface width.

The extracted neutron reflectivity measurement of d_{PVP} was within error of the ellipsometry measurement. However, the extracted neutron reflectivity measurement of d_{dPS} was $0.7nm$ larger than the error of the ellipsometry measurement. The sample preparation technique was changed when making these samples (the solution was deposited while the substrate was spinning). This technique may not be as reproducible as when depositing the solution onto a stationary substrate. However, more investigation would be needed to confirm this.

The extracted neutron reflectivity measurement of the $\sigma_{dPS \rightarrow PVP}$ interface was slightly smaller than the surface roughness of the PVP(top)→PS(bottom) bi-layer. This change was within error of the AFM measurement, so the interface width may not have necessarily shrank. The results suggests that non

of the polymer-polymer interfaces do not broaden by solution processing the PVP/PS DBR samples.

Samples with larger interface widths of $\sigma_{dPS \rightarrow PVP}$ were simulated using the Motofit program. However, the neutron reflectivity calculations would not adequately fit to the measured reflection spectra. Therefore, the low reflectance of the PVP/PS DBRs (when compared with the modelled sharp interface spectra) was not due to polymer-polymer interface widths or surface roughness. The neutron reflectivity results support the argument that residual solvent is altering the reflection properties of the DBR samples.

8.3 Comparison with UV/visible spectra

A 50 layer DBR was prepared using the same techniques and polymer solutions (which was discussed in section 4.7.1) as those used to make the samples for neutron reflectivity measurements. However, the sample was prepared on a glass slide substrate. The reflection spectra of the 50 layer ‘neutron sample’ DBR was measured using the UV/visible spectrometer. Any significant changes in the UV/visible reflection spectra would indicate that the neutron reflectivity samples were not the same as the DBR samples from chapter 5. For example, the polymer-polymer interfaces could be different because of the slight change in sample preparation technique.

The layer thickness of the neutron reflectivity films/samples were reduced so that Kiessig fringes could be measured during neutron reflectivity measurements [55]. Unfortunately, this does not result in a large reflectance peak in the visible region of the EM spectrum (see figure 8.4). The measured peak was at the near infra-red ($\lambda = 986 \pm 1nm$), which was close to the cut-off wavelength of the UV/visible spectrometer. This resulted in some of the reflection peaks being cut-off from the spectra.

Table 8.4 shows the ellipsometry measurements used to model the reflection band using the modified optical transfer matrix method. This was the same technique used to model the spectra of PVP/PS samples in chapter 5. The film thickness of the PVP and dPS films were both reduced by $5nm$ to improve the modelled fit with the measured spectra. This is comparable with the film thickness corrections needed to fit the modelled data with spectra measured

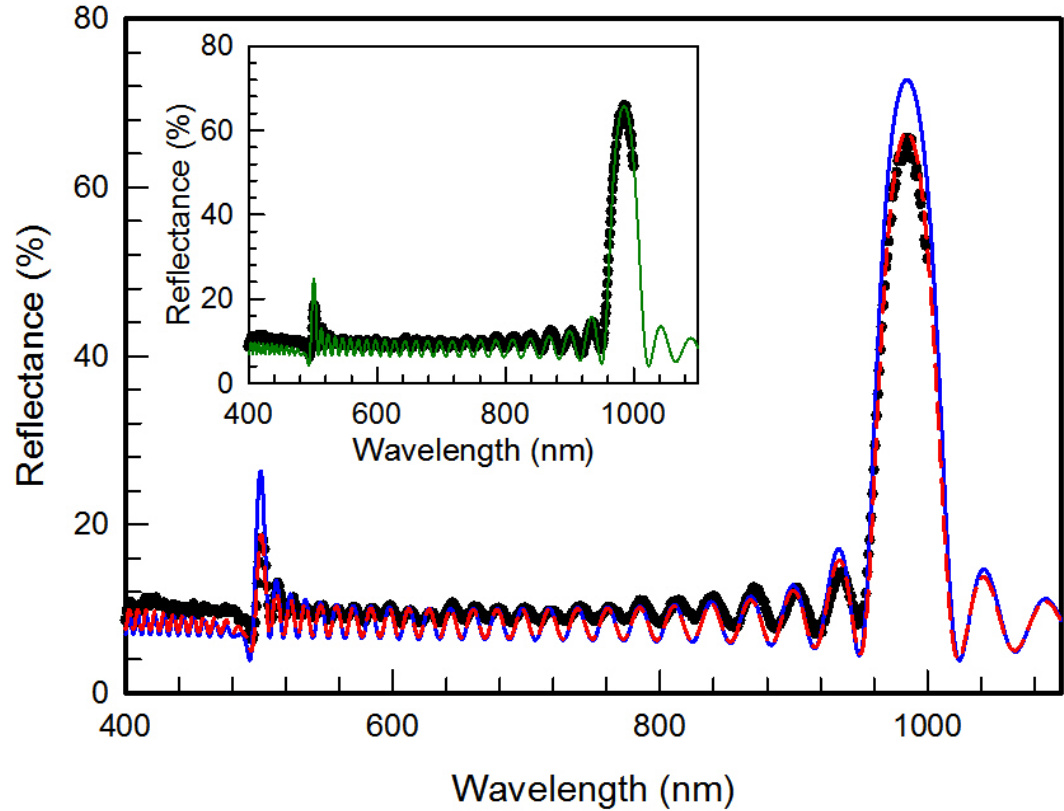


Figure 8.4: UV/NIR reflection spectra of a 50 layer DBR made from PVP and dPS which was spin-cast onto a glass slide substrate. The sample was prepared using the same techniques as those made for neutron reflectivity experiments (discussed in section 4.7.1). The reflection band is in the near infra-red and was measured using the transmission set-up spectrometer (data-points). Modelled spectra (using the modified optical transfer matrix method) with sharp interfaces is represented by the blue solid line. Spectra which assumed interface widths of $\sim 1nm$ were indistinguishable from modelled data with sharp interfaces (not shown). The dashed red curve represents modelled spectra which was fitted using large interface width approximations $\sigma = 25 \pm 1nm$. Therefore, the overestimation of large interface widths would have also been calculated for the 'neutron reflectivity' samples. A reduction in refractive index contrast of $\delta(\Delta n) = 0.008 \pm 1$ was needed to fit the model to the measured spectra (shown by the green curve in the caption).

	Thickness of PVP layers d_{PVP} (nm)	Thickness of PS layers d_{PS} (nm)	Interface width calculation σ (nm)	Reduced refractive index contrast $\delta(\Delta n)$
Ellipsometry measurements	183.0 ± 3.4	147.0 ± 2.0	NA	NA
Modelled spectra	178 ± 5	142 ± 5	25 ± 1	0.008 ± 1

Table 8.4: The values correspond to the ellipsometry measured and film thickness corrections used to model the DBR reflection band shown in figure 8.4. The interface width calculation σ was calculated using the modified matrix method model (discussed in chapters 3 and 5).

from PVP/PS DBRs (see table 5.1).

The modelled data initially assumed that the interfaces were sharp (shown by the blue curve in figure 8.4). However, the reflectance of the modelled spectra was larger than the measured spectra (represented by data-points in figure 8.4). $1nm$ interface widths were included in the calculations to measure the change in modelled reflectance. This was used as a comparison to the interface widths which were measured using neutron reflectivity experiments. Changes in the modelled spectra with respect to $1nm$ and sharp interface widths were negligible. Therefore, the lower reflectance, when comparing measurements to the predicted spectra, are not due to the finite interface widths.

The reflectance of the PVP/dPS DBR reflection peak (within the UV/visible wavelengths) was modelled with diffuse interface width approximations included (represented by the dashed red curve in figure 8.4). A polymer-polymer interface width of $\sigma = 25 \pm 1nm$ was needed to fit the model to the measured UV/visible reflection peak from the PVP/dPS DBR. This was comparable to the polymer-polymer interface width estimates which were calculated for PVP/PS DBRs (see table 5.1).

The UV/visible reflection spectra of the PVP/dPS DBR was also remodelled with reduced refractive index contrast $\delta(\Delta n)$ approximations (shown in the caption in figure 8.4). A reduction of $\delta(\Delta n) = 0.008 \pm 1$ was needed to model to the measured reflectance of the PVP/dPS DBR reflection peak. The reduction in refractive index contrast $\delta(\Delta n)$ required to fit the reflectance of the PVP/PS DBRs were between 0.020 and 0.030. Less of a change in $\delta(\Delta n)$ was needed when modelling the PVP/dPS DBR (when compared to the PVP/PS DBRs). This implies that there was less residual solvent in the PVP/dPS DBR sample. The thickness of the PVP/dPS layers were thinner than the layers in the PVP/PS DBRs. Thinner layers may have enabled the residual solvent to more readily diffused out of the PVP/dPS DBR during annealing.

The Bragg peak in figure 8.4 ($R = 66 \pm 1\%$) was larger than the 50 layer PVP/PS DBRs ($R \sim 55\%$) shown in chapter 5. This was due to the optical path length of each layer being $\sim \lambda/4$. A similar increase in the reflectance was observed when measuring the RGB DBRs in the infra-red (which was discussed in chapter 7).

The modified preparation technique for the PVP/dPS DBRs (see section

4.7.1) did not change the underlying problem which caused the reflectance to be lower than expected. Hence, the neutron reflectivity measurements are relevant to the PVP/PS DBRs discussed in chapter 5. The measurements also proved that the interface widths were significantly smaller than the previous diffuse interface width estimations. Trapped solvent was most likely the cause for losses in reflectance.

8.4 Summary

Not all of the samples which were prepared for neutron reflectivity experiments could be measured. This was due to experimental time being lost when the neutron beam was taken off-line. Measuring all of the samples would have lead to a more complete data-set. However, It was still possible to analyse the neutron reflectivity spectrum from the samples which were measured.

The polymer-polymer interface widths were not between $20nm$ to $30nm$, which were previously estimated by fitting modelled spectra to UV/visible measurements (see section 5.3.1). Instead, neutron reflectivity measured the all of the polymer-polymer interface widths to be less than $1nm$. It was not possible to fit the neutron reflectivity data with polymer-polymer interface widths that were between $20nm$ and $30nm$. Hence, the reduction in measured reflectance of the reflection peaks (when compared with the model), were definitely not due to large polymer-polymer interface widths.

A DBR sample was prepared using the same materials and preparation techniques as the deuterated (PVP/dPS) DBR samples. The reflection properties of the PVP/dPS sample was measured using the UV/visible spectrometer. Its optical properties were similar to the PVP/PS DBR samples prepared in chapters 5 and 6. Hence, variables which change the optical properties of a DBR (such as polymer-polymer interface widths) were comparable between the two samples.

Chapter 9

Using polymer multi-layers to calibrate TOF-SIMS experiments

9.1 Introduction

Time of flight secondary ion mass spectrometry (TOF-SIMS) is an analysis tool used to measure the chemical composition of a sample surface or thin film. It is often referred to as a *surface science* technique. Initially, TOF-SIMS was developed to measure the outer surface layers of materials [82]. This is important since surface atoms/molecules often contribute towards the properties of a bulk material, despite their low number compared with the rest of the sample [83]. Further work on depth profiling techniques extended it to be used to measure mono-layers, multi-layers and 3D structures. Samples are typically measured on the μm and nm length-scale.

TOF-SIMS is currently being used to research drug delivery systems [23,24], polymer electronics [26] and ink-jet printing [96]. These examples are made from nm length scale composite polymer structures. It is difficult to distinguish between different types of polymer in these structured sample. This is because polymers are predominantly hydrocarbon structures. TOF-SIMS etches through polymer samples with a resolution on the nm length scale. It is able to distinguish different polymers by measuring ions which are sput-

tered away from the sample surface during scanning [82]. However, there are a number of polymers that are used in applications (and are therefore of interest to investigate) that are challenging to etch through. This includes PS, as the polymer is susceptible to cross-linking during etching [77]. Several different types of etching beam and techniques have been previously developed to overcome these challenges in an effort to measure a broader range of materials.

In this chapter a new Ar_{2000}^+ etching beam source was used to depth profile through PVP/PS multi-layer structures. Depth profiling enabled the spatial structure of the DBR and individual layers to be measured. TOF-SIMS was also used to try and measure the polymer-polymer interface widths between layers.

9.2 Bi-layers

Bi-layers of PVP and PS were prepared using the spin-coating techniques discussed in section 4.3. This includes swelling the PVP layers with HCl vapour. These samples were prepared to test if there were differences in layer thickness when spin-cast onto a silicon or polymer substrates. Three samples were prepared;

- PVP(top)→PS(bottom): PVP was spin-cast on top of a previously spin-cast PS film.
- PS(top)→PVP(bottom): PS was spin-cast on top of a previously spin-cast PVP film.
- Floated PS(top)→PVP(bottom): A free-standing PS film was deposited onto a PVP substrate to make a bi-layer.

The floated PS(top)→PVP(bottom) sample was prepared by spin-coating a single layer PS film onto a glass slide substrate. A water bath was used to float the PS film off the glass slide. The PS film was lifted from the water bath using a ‘cradle’ (metal sheet with a $\sim 2cm$ hole at the center) and then left to dry. This free-standing PS film was transferred/deposited on top of a single layer spin-cast PVP film (illustrated in figure 9.1). Interfacial tension pulled the free-standing PS film flat onto the PVP film [97]. The bi-layer sample was

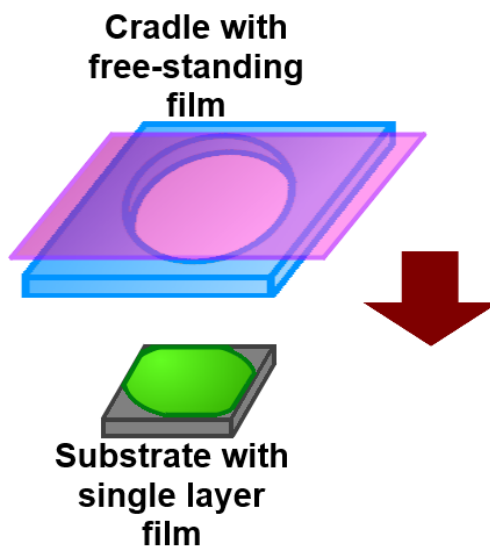


Figure 9.1: A free-standing film which is being held using a metal cradle. The free-standing film was lowered onto a single layer spin-cast film. Interfacial tension pulls the free-standing film flat onto the single layer film. This technique was used to prepared a bi-layer sample which did not involve the second/top layer being deposited by solution processing techniques.

annealed for 5 hours at $110^{\circ}C$ under a $\sim 1\text{mtorr}$ vacuum. This experiment was used to measure any polymer-polymer interface width changes when solution processing was not used to deposit films onto polymer substrates.

TOF-SIMS was used to measure the thickness of the polymer layers as well as polymer-polymer interface widths. Depth profile measurements of single layer films were used to calibrate the etch rate of the Ar_{2000}^{+} sputter beam (discussed in section 4.8.3). The etch rate of the two polymers were PVP= $(11.66 \pm 0.10) \times 10^{-18}nm/\text{dose}$ and PS= $(14.77 \pm 0.18) \times 10^{-18}nm/\text{dose}$. These values were used to extract the film thickness measured using TOF-SIMS. The depth profile width (which corresponds to layer thickness) was measured by calculating the dose of the sputtering beam between each interface. This value was multiplied by the etch rate to calculate the thickness of the layer.

The etch rate of the ion beam would change as it passed through an interface. This was due to the interface being a gradual blend of two different materials. However, it was not possible to measure the changes in the etch rate as it passed through the interface. This was especially true for the last polymer \rightarrow silicon interface, as the ion beam was not able to properly etch through silicon and cannot be calibrated. Instead, the width of the inter-

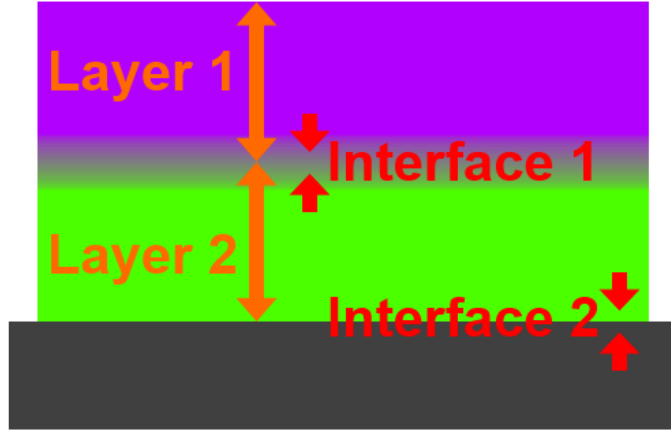


Figure 9.2: Illustration of a bilayer sample where each layer has a film thickness and is separated by an interface. The layers are numbered from top to bottom and the interface number are named from the previous medium.

face (with respect to dose) was multiplied by the sputter rate of the previous layer [78]. There was a 26.7% difference between the etch rate of PVP and PS, which would modify the measurement of the interface widths. This is discussed in more detail later in this chapter.

The sputtering beam etches from the top to the bottom of a sample. This corresponds to the last deposited layer being measured first, and the silicon interface being measured last. Each different layer was counted from the top down (illustrated in figure 9.2). The interfaces between each layer was numbered after the previous layer. For example, ‘interface 1’ is between layers 1 and 2. TOF-SIMS is unable to measure the surface topography of the sample, so the top air-polymer interface was assumed to be sharp (which is why it was ignored in analysis).

Results from the ellipsometry and TOF-SIMS measurements of the PVP(top) \rightarrow PS(bottom), PS(top) \rightarrow PVP(bottom) and floated PS(top) \rightarrow PVP(bottom) bi-layers are shown in tables 9.1, 9.2 and 9.3 respectively. Most of the TOF-SIMS depth profiling measurements were within good agreement with the ellipsometry measurements. However, the TOF-SIMS thickness measurement of the lower PS layer in the PVP(top) \rightarrow PS(bottom) bi-layer, was 7nm larger than the ellipsometry measurement. This may have been due to the sharp increase in measured ions at the PS \rightarrow silicon interface (see figure 9.3). The error function, which was used to measure interface position and width, was fitted to the shape of the depth profile (see figure 9.3). Changes in the depth profile

Layer (top → bottom)	Polymer	Ellipsometry: Film thickness (nm)	Depth profile: Thickness (nm)	Interface width (nm)
1	PVP	206.3 ± 1.0	207.5 ± 1.9	12.6 ± 0.7
2	PS	218.7 ± 1.0	225.6 ± 2.9	7.4 ± 0.9

Table 9.1: Each layer thickness of the the films in the PVP(top)→PS(bottom) bilayer were measured using ellipsometry. These errors were calculated using the standard deviation of five repeat measurements. The film thickness and interface widths were remeasured using TOF-SIMS depth profiling. Each interface was labelled with respect to the previous layer (illustrated in figure 9.2). In this case, interface 1 is between PVP and PS. Likewise, interface 2 is between PS and the silicon substrate. The TOF-SIMS measurements of the PS layer thickness was larger than ellipsometry measurement. This may have been due to the sharp increase in the measured PS ions at the PS→silicon interface.

Layer (top → bottom)	Polymer	Ellipsometry: Film thickness (nm)	Depth profile: Thickness (nm)	Interface width (nm)
1	PS	218.7 ± 1.0	220.8 ± 0.6	6.9 ± 0.5
2	PVP	206.3 ± 1.0	205.3 ± 1.0	6.8 ± 0.3

Table 9.2: Each layer thickness of the films in the PS(top)→PVP(bottom) bilayer were measured using ellipsometry. The film thickness and interface widths were also measured using TOF-SIMS depth profiling. Each interface was labelled with respect to the previous layer (illustrated in figure 9.2). In this case, interface 1 is between PS and PVP. Likewise, interface 2 is between PVP and the silicon substrate. The TOF-SIMS and ellipsometry film thickness measurements are within agreement of one another.

Layer (top → bottom)	Polymer	Ellipsometry: Film thickness (nm)	Depth profile: Thickness (nm)	Interface width (nm)
1	floated PS	218.7 ± 1.0	225.1 ± 0.8	6.7 ± 0.5
2	PVP	206.3 ± 1.0	203.2 ± 2.4	6.4 ± 1.0

Table 9.3: Floated PS(top)→PVP(bottom) bilayer was prepared and measured using ellipsometry and TOF-SIMS. The thickness of the PS layer was larger than the ellipsometry measurement. However, the film thickness would have been the same for a single layer film as it was not spun-cast on top of a polymer film. This indicates that there may be inaccuracies in the TOF-SIMS measurements.

would have also changed the error function and the extracted position of the interface.

The TOF-SIMS layer thickness measurement of the floated PS(top) → PVP(bottom) also showed some disagreement with the ellipsometry model. TOF-SIMS had measured the top PS layer to be $\sim 6nm$ less than the ellipsometry measurement. The thickness of the floated PS layer should have been the same as a single layer PS film. This was due to the floated film being originally spin-cast as a single layer, which was then transferred onto the PVP film. TOF-SIMS may not be able to etch through the polymer layers at a constant rate. This could be due to small imperfections in the film, such as inhomogeneity in the polymer density or film thickness. It could also be due to PS being a ‘challenging polymer’ [78]. However, there was only a $\sim 3\%$ difference between the TOF-SIMS and ellipsometry film thickness measurements of the floated PS film. TOF-SIMS is able to measure the distribution of layers in a sample, but more specialised equipment (such as ellipsometry) should be used for film thickness measurements.

The interface widths in TOF-SIMS measurements are much larger than the neutron reflectivity results (see section 8.2). Specifically, the polymer→silicon interface width. TOF-SIMS measured the polymer→silicon interface width as being between $6.4nm$ and $7.4nm$. However, the interface between polymer and silicon was known to be sharp ($\sim 1nm$). The region of interest selection (which was discussed in section 4.8.2) was used to remove large sputtering anomalies and anything which would smear the measurement of the interface (such as tilting and sample orientation). Errors in the interface width calculations may be due to the TOF-SIMS experimental method. There are several properties which can decrease depth profile resolution;

- *Sputter rate*: The sputtering beam etches in pulses over the sample surface. Each pulse may etch several nm deep into the sample [82]. PS had a larger etch rate than PVP, which would increase the length measured per sputtering dose. This suggests that the sputter rate can reduce the depth resolution of TOF-SIMS.
- *Roughening*: The sputter beam can cause the surface to roughen as it etches through the sample. This causes the sputtering resolution to worsen as the sample is being measured [82].

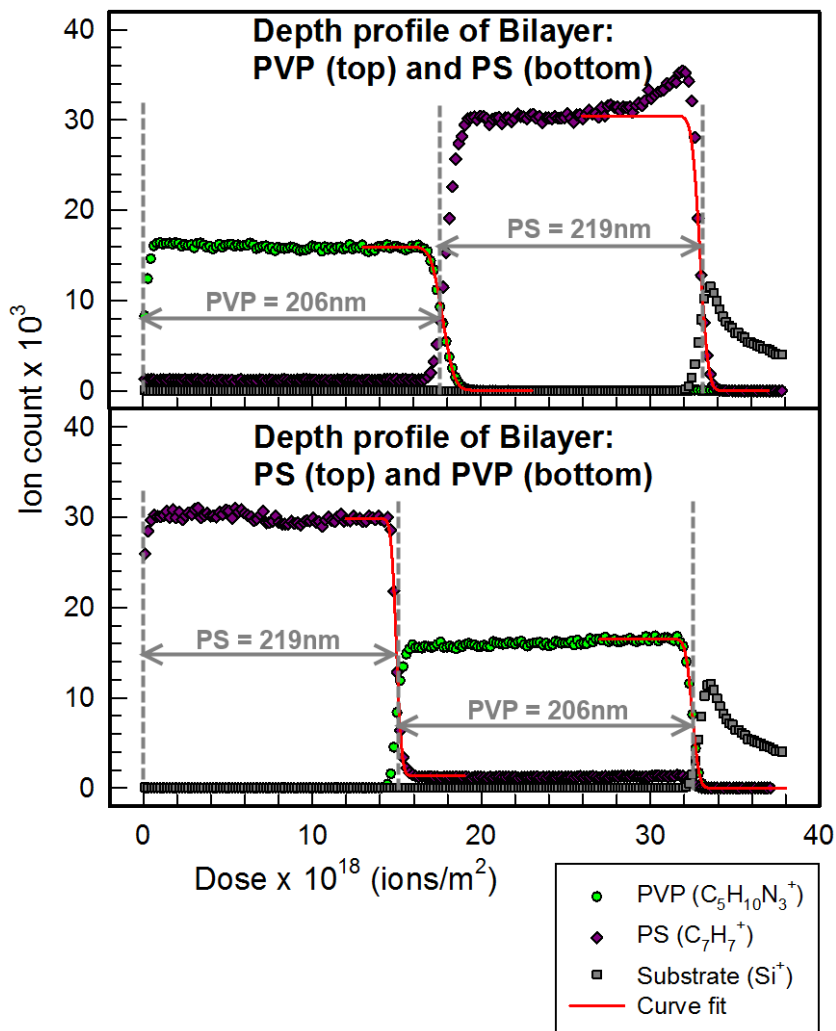


Figure 9.3: Depth profile of polymer bilayers. [Top panel] Depth profile of a PVP(top)→PS(bottom) bi-layer sample which was spin-cast onto a silicon substrate. [Bottom panel] Depth profile of a PS(top)→PVP(bottom) bi-layer sample which was spin-cast onto a silicon substrate. The red curves are the error functions which were fitted to measure the interface positions and interface widths with respect to ion dose.

- *Mixing*: The energy of the sputtering beam can penetrate through both materials and force them to mix. Secondary ions are detected from both materials due to them mixing. This causes the measured interfaces to widen [82].
- *Alignment*: Changes in the alignment of the substrate or any inhomogeneous layers should broaden the interface widths.

The interface widths measurements between polymer-polymer (including the floated PS sample) and polymer-silicon were all between $7nm$ and $13nm$. These measurements were less than the polymer-polymer interface width estimates (between $20nm$ to $30nm$) which were extracted from the UV/visible spectrometry measurements (see section 5.3.1). The reduction in measured reflectance (when compared to the model) were not due to polymer-polymer interfaces as wide as $20nm$ to $30nm$. However, the TOF-SIMS interface measurements were much larger than the neutron reflectivity measurements. This is due to TOF-SIMS not being able to resolve sharp interfaces. For example, this technique had measured the polymer-silicon interface between $6.4nm$ and $7.4nm$, when it was known to be closer to $\sim 1nm$. Correcting for changes in sputter rate through an interface would not significantly improve the TOF-SIMS results. The interfaces would still be too large, even if the etch rate of PVP (which was smaller than PS) was used to calibrate all of the interface widths in the sample.

9.3 Asymmetric multi-layers

The etch rate of the Ar_{2000}^+ sputter beam may not stay constant during depth profile measurements. Roughening, contamination variations in layer thickness and inhomogeneity in density will change the sputter rate of the etching beam through a sample [82,83]. Two thick 10 layer samples (with a total thickness of $\sim 1.25\mu m$) were prepared using the sample preparation techniques discussed in section 4.3. However, the PS layer was disproportionately smaller than the PVP layers. The thickness of the PS layers were between $40nm$ and $60nm$, whereas the PVP layers were between $180nm$ and $220nm$. These samples have been named as ‘asymmetric samples’, because of the large differences in PVP and PS layer thickness. The ratio between the thickness of the PVP and PS layers are

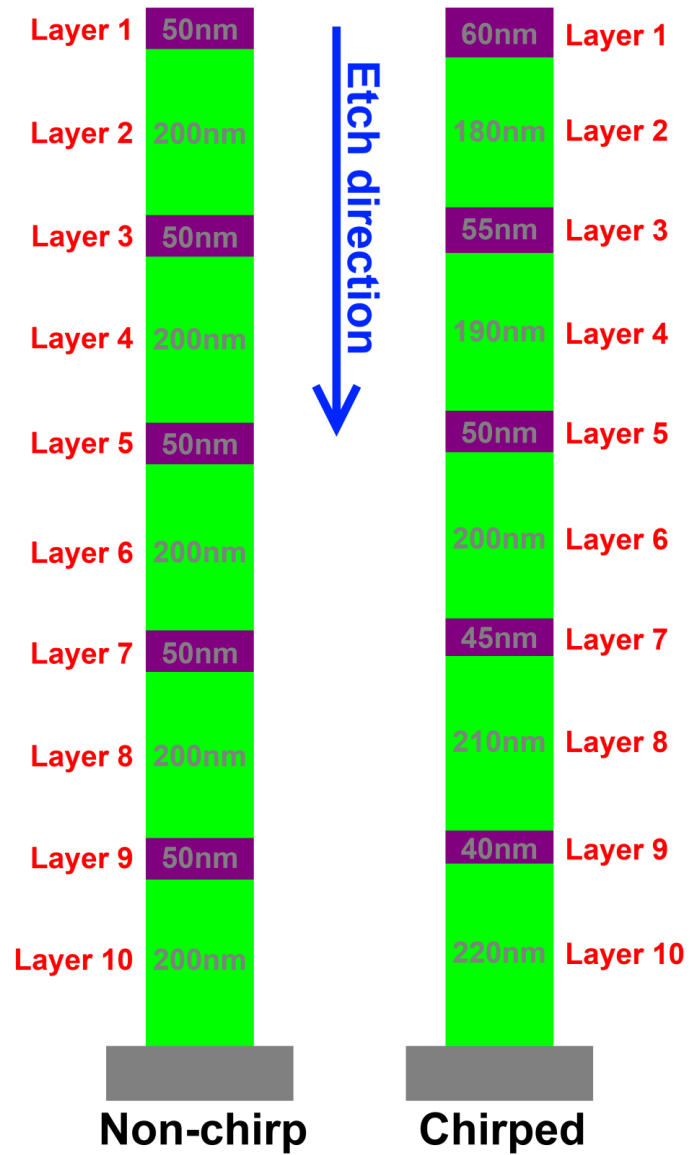


Figure 9.4: Illustration of multilayer samples with a large difference in the thickness between layers of PVP (green) and PS (purple). These samples were used to test the depth profiling accuracy when measuring the thickness of polymer composite samples.

not comparable with the previously prepared DBRs (see chapter 5). The thin PS layers in the asymmetric samples were used as ‘chemical markers’, which were used to measure different points in the sample during etching. These experiments were comparable to TOF-SIMS measurement by A. G. Shard [81]. He also used a Ar_{2000}^+ cluster beam to depth profile through a multi-layer polymer sample (made by vacuum deposition of alternating Irganox 1010 and Irganox 3114 layers [81]). The samples in this chapter were spin-coated and had PS layers which are ‘challenging’ to etch through when a Ar_{2000}^+ sputter source is not being used [77, 78].

The first polymer sample was prepared by spin-casting alternating layers with $200nm$ PVP and $50nm$ PS film thickness. This is called the ‘non-chirped sample’ as the thickness of PVP and PS layers were kept constant. The thickness of the PVP and PS layers were not kept constant when preparing the second polymer sample. This sample was used to test if TOF-SIMS could measure small changes in layer thickness. PVP was initially deposited with a layer thickness of $180 \pm 1nm$, which increased by $10 \pm 1nm$ after each PVP layer was deposited. The final PVP layer was deposited with a film thickness of $220 \pm 1nm$. Likewise, the initial PS layer thickness was $60 \pm 1nm$, which decreased by $5 \pm 1nm$ after each PS layer was deposited. The final PS layer was deposited with a film thickness of $40 \pm 1nm$. This was called the ‘chirped sample’ as the thickness of PVP and PS change throughout the multi-layer structure. The structure of both non-chirped and chirped structures are illustrated in figure 9.4.

9.3.1 Non-chirped samples

The TOF-SIMS depth profile results for the non-chirped sample are shown in figure 9.5. The periodicity of PVP and PS layers are clearly visible in the depth profile curves. Note that the PVP and PS layers have a different layer thickness. However, the magnitude of the PS depth profile bands (blue data-points in figure 9.5) were diminishing slightly as the sample was being etched. Reduction in ion count of the PS layers when depth profiling was due to them being too thin. This was due to the resolution of the system reducing while the ion beam was etching through the sample. This could have been caused by the etching beam roughening the surface of the sample, encountering a contaminant

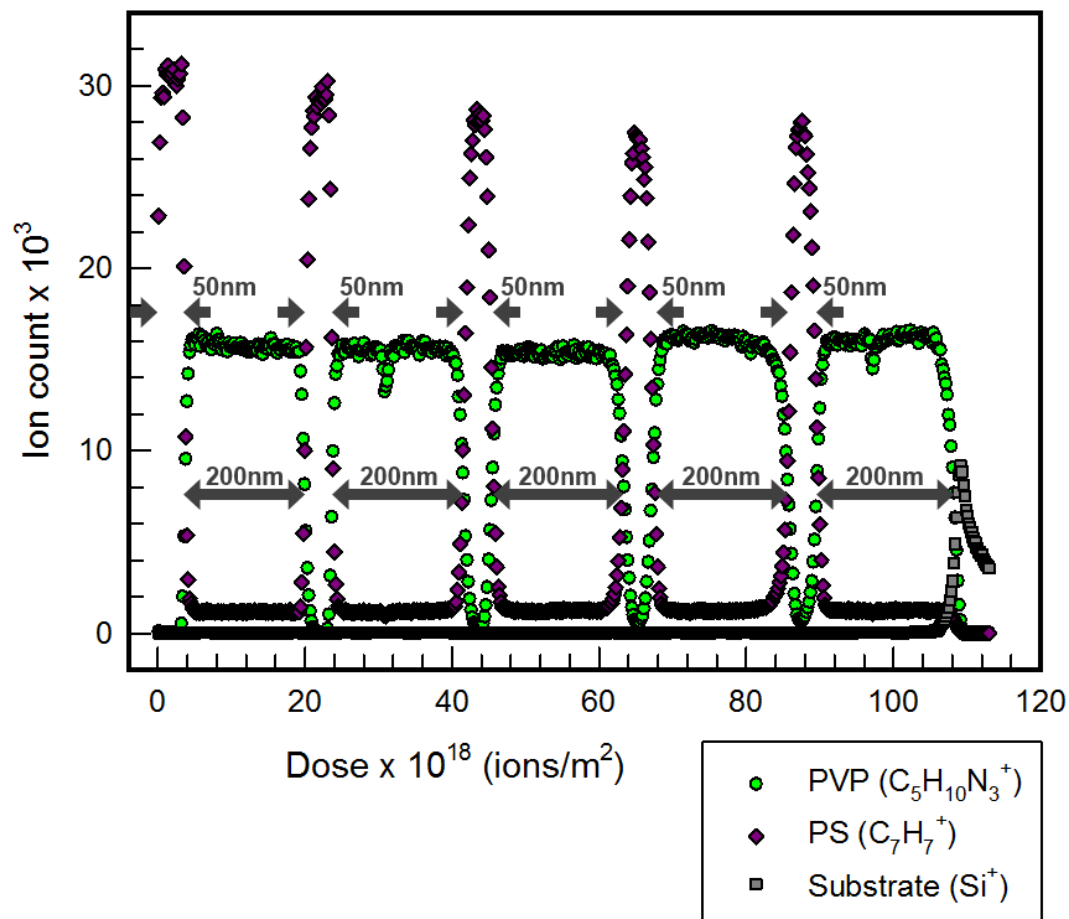


Figure 9.5: Depth profile of non-chirped 10 layer PVP/PS sample. These results are of the whole $100\mu\text{m} \times 100\mu\text{m}$ depth profiled area. PVP and PS films were spin-cast with a film thickness of $200 \pm 1\text{nm}$ and $50 \pm 1\text{nm}$ respectively. The intensity of the PS film decreases as the Ar_{2000}^+ beam continues to etch through the sample. An error in the sputtering measurement (possibly due to contamination) roughened the surface while the ion beam was etching. The PS layers were too thin for the reduced resolution of the ion beam to adequately measure.

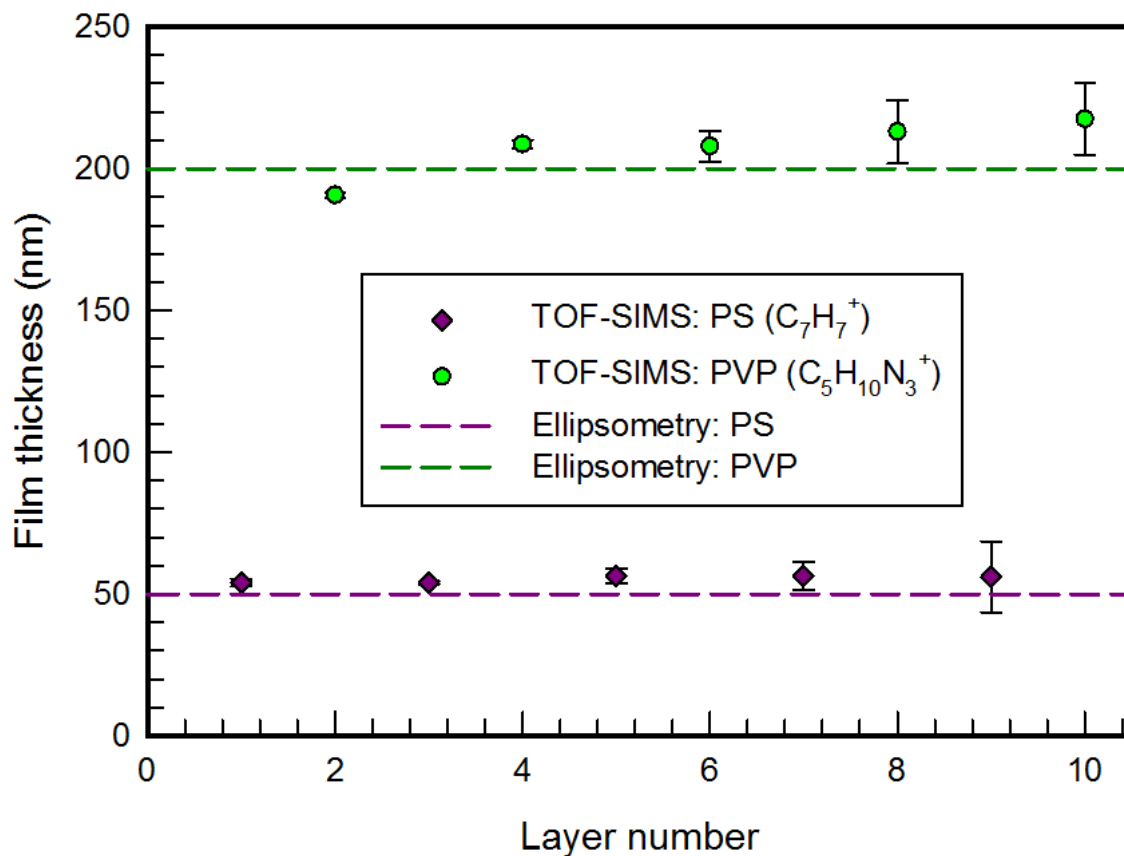


Figure 9.6: Film thickness measurements of 10 layer asymmetric PVP/PS non-chirped films using TOF-SIMS. The data points correspond to the average value measured from five regions of interest. The error was calculated using the standard deviation. Ellipsometry results from comparable single layer measurements are represented by the dashed lines.

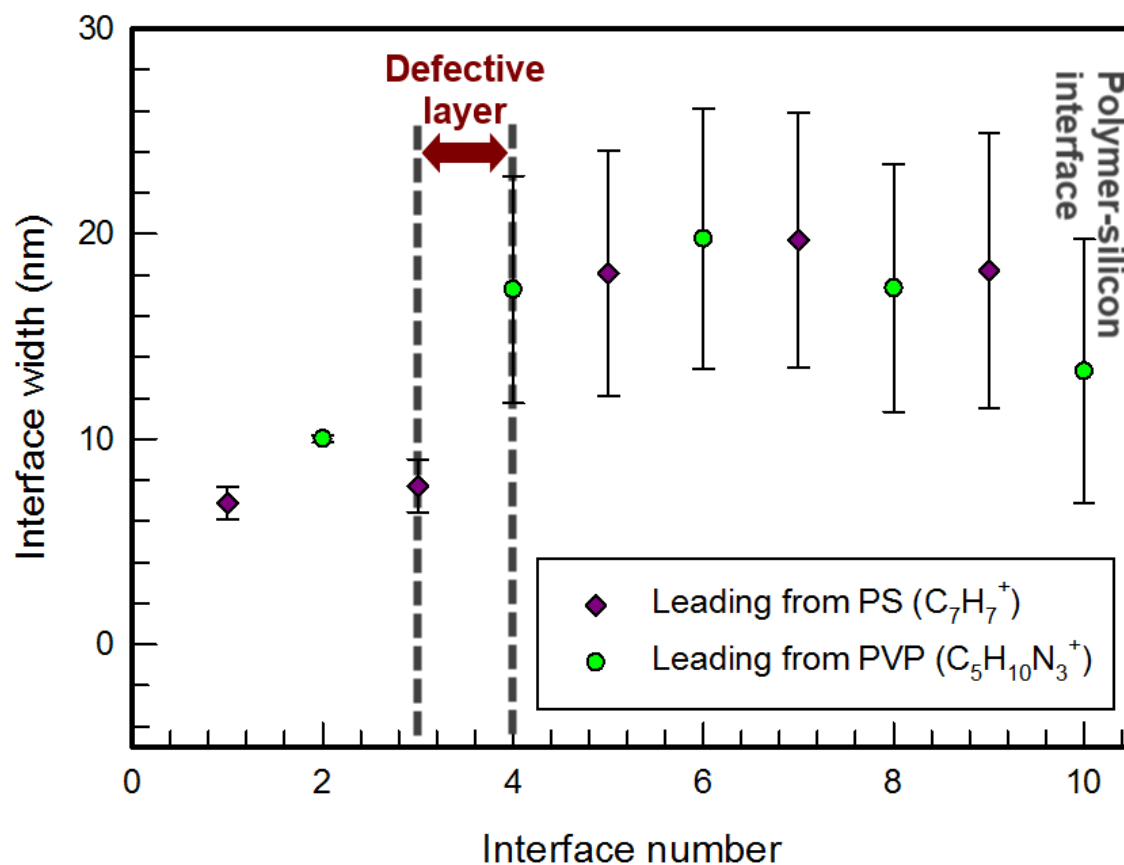


Figure 9.7: Widths of polymer-polymer and polymer-silicon interfaces for 10 layer asymmetric PVP/PS non-chirped sample. The first interface is PS→PVP and the second interface is PVP→PS. This alternates until the final tenth interface which is PVP→Si. Each data point represents an average of measurements from five regions of interest. Errors were calculated using the standard deviation. There is a large increase in measured width at the fourth interface. This may be due to a contamination and/or film thickness irregularity in the layer between the third and fourth interface.

and/or poor layer thickness uniformity [82,83].

The widths of the depth profile bands (shown in figure 9.5) were used to calculate the thickness of the layers (see section 4.8.3). Figure 9.6 shows the calculated TOF-SIMS film thickness (data-points), with the ellipsometry film thickness estimates (dashed lines). Both sets of results were in close agreement with one another. The thickness of the polymer films were constant during sample preparation.

The errors in the film thickness measurements had increased as the ion beam continued to etch through the sample. This is most likely a defect from data analysis. TOF-SIMS is unable to measure the surface topography of a sample and it was falsely assumed that it was flat. Any imperfections would continue to be measured as the beam etched through the sample. For example, consider a flat substrate which has a rough polymer film on top. TOF-SIMS would inadvertently measure the top of the polymer film as being flat and the substrate as being rough [82]. The same problem could be occurring for the layer thickness measurements in figure 9.6. Any variations in layer thickness would become more noticeable in depth profile measurements as the beam continued to etch through the sample.

Figure 9.7 is a plot of the extracted TOF-SIMS measurements of the interface widths with respect to the interface number. The interfaces are labelled from the top of the sample through to the bottom. This is interpreted with respect to the leading material. The polymer→air interface was not considered, because TOF-SIMS measures the layer as being flat. Therefore, PS→PVP and PVP→PS are the first and second interface respectively. The two interfaces alternative until the final/10th PVP→silicon interface.

The interface width measurements (shown in figure 9.7) were $8nm$ to $10nm$ for the first three interfaces measured. However, the interfaces had increased to widths between $15nm$ and $20nm$ after the third interface. This must have been due to a disruption in the interface width measurements between the third and fourth interface (which is the fourth layer from the top to bottom of the sample). Something in the sample changed the topography of the surface as it was being sputtered. This could have been contamination, or poor film thickness uniformity [82,83]. The profile of the roughness would have remained in the depth profile as the sputter through the rest of the sample. This is a

problem when measuring thick samples, as defects in the top layers are still visible when measuring the bottom layers.

9.3.2 Chirped

A chirped multi-layer sample was prepared to test the Ar_{2000}^+ sputter source's ability to measure a sample with varying film thickness. The depth profile of the chirped sample structure is shown in figure 9.8. The intensity of the PS ($C_4H_{10}N_3^+$) secondary ions did not diminish. This was despite some of the PS layers in the chirped sample (figure 9.8) being thinner than the non-chirped sample (figure 9.5). The surface of the chirped sample did not roughen as much as the non-chirped sample during etching. This may have been due to the chirped sample having fewer defects than the non-chirped sample. However, this would need to be investigated further for a more thorough conclusion.

Figure 9.9 shows the measured thickness of films using TOF-SIMS (data-points) and ellipsometry measurements (dashed-lines) with respect to layer number. The greatest difference between layer thickness measurements were approximately $\sim 20nm$ for the PVP layers. Layer thickness corrections which were needed to improve the fit of modelled data to UV/visible spectrometry measurements were not as large as $\sim 20nm$ (see chapter 5). The differences between the TOF-SIMS and ellipsometry measurements may have been due to small changes in the TOF-SIMS etch rate and/or calibration. Despite this, the general trend of the changing layer thickness (PVP increasing and PS decreasing from top to bottom of the sample) was observed. TOF-SIMS was able to measure the structure of the sample, but more suitable techniques (like ellipsometry) should be used for measuring film thickness.

Figure 9.10 shows the measured TOF-SIMS interface widths in the chirped sample. The first interface is PS(top) \rightarrow PVP(bottom) and the last is PVP(top) \rightarrow silicon(bottom). Interface widths for the chirped sample stayed relatively constant (between $8nm$ and $12nm$). These interfaces widths were narrower and less diverse than the interface widths from the non-chirped sample (between $15nm$ and $20nm$). The Ar_{2000}^+ beam may not have roughened the surface of the chirped sample as much as the non-chirped sample during etching. A rough surface would broaden the interface width. Although, the TOF-SIMS measurement of the polymer-silicon interface was broad ($10 \pm 1nm$). The in-

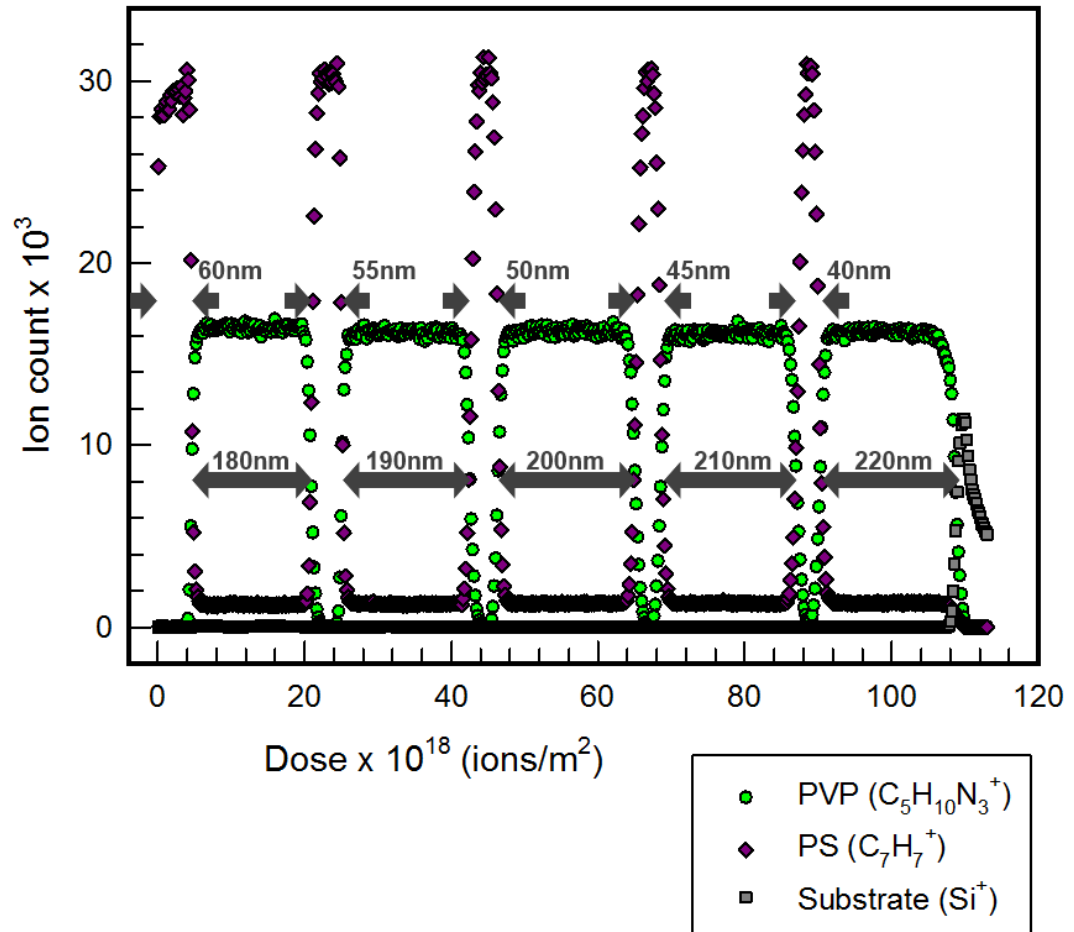


Figure 9.8: Depth profile of a chirped 10 layer PVP/PS sample. These results are of the whole $100\mu\text{m} \times 100\mu\text{m}$ depth profiled area. PVP and PS layers were spin-cast films with an initial thickness (bottom to top of sample) $d_{PVP} = 220 \pm 1\text{nm}$ and $d_{PS} = 40 \pm 1\text{nm}$. The PVP film was changed thickness by $-10 \pm 1\text{nm}$ per bi-layer deposited. Likewise, the PS film thickness was changed by $+5 \pm 1\text{nm}$ per bi-layer deposited. The thickness of the final layers deposited were $d_{PVP} = 180 \pm 1\text{nm}$ and $d_{PS} = 60 \pm 1\text{nm}$. Note that TOF-SIMS measures top \rightarrow bottom, so the measurement of the layer thickness is inverted when compared to the order of layers deposited..

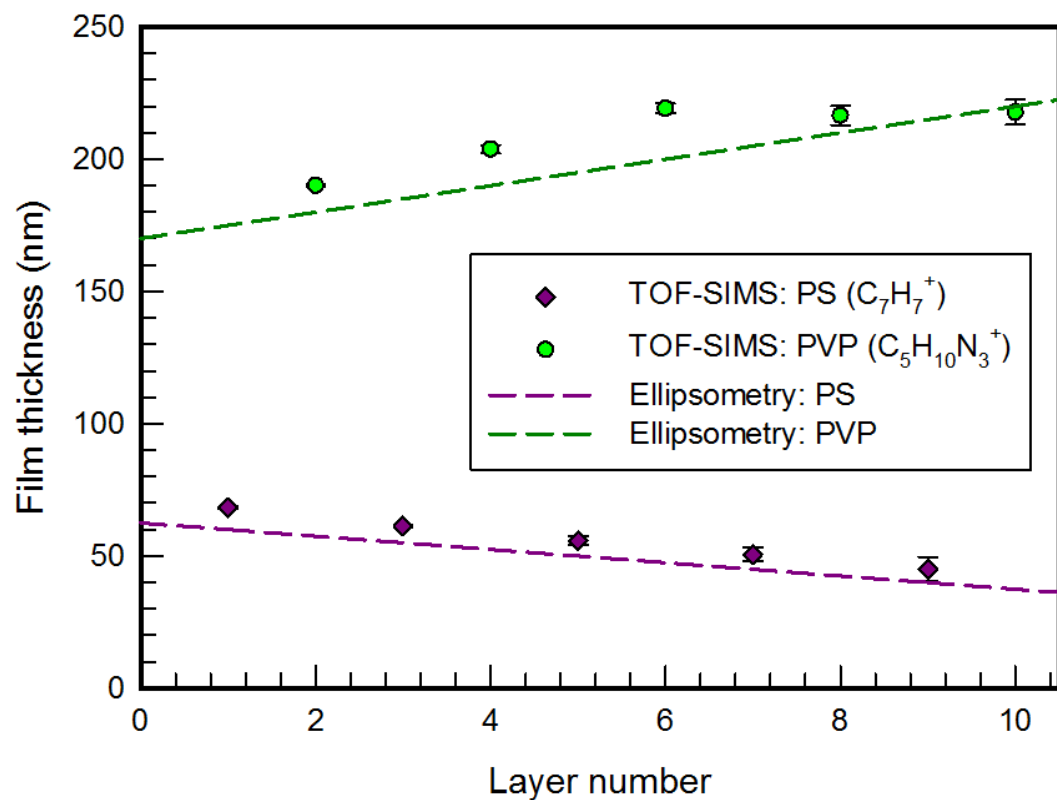


Figure 9.9: Film thickness measurements of a 10 layer asymmetric chirped PVP/PS sample structure. The data-points are an average of measurements from five regions of interest. Errors were calculated using the standard deviation. Single layer ellipsometry measurements are represented by the dashed lines. The largest difference in the film thickness measurements was $\sim 20nm$. However, the progressive changes in the film thickness of the chirped layers can be seen.

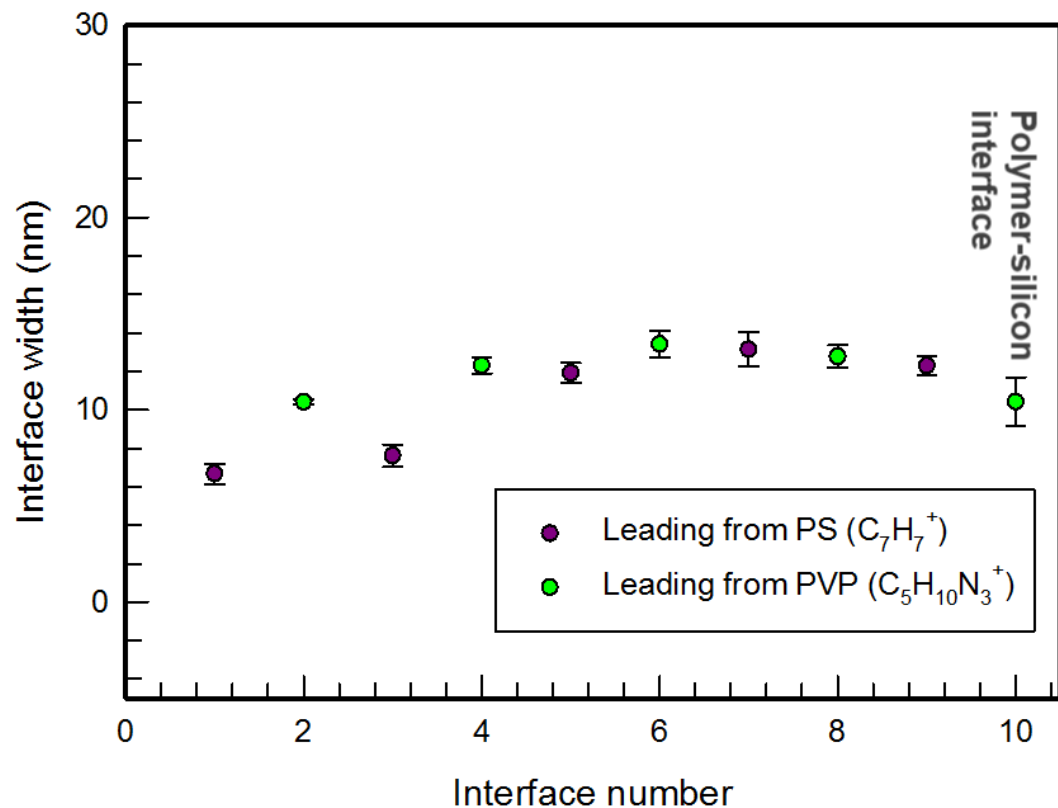


Figure 9.10: Widths of polymer-polymer and polymer-silicon interfaces for 10 layer asymmetric PVP/PS chirped sample. The first interface is PS→PVP and the second interface is PVP→PS. This alternates until the final 10th interface which is PVP→Si. Each data-point is an average of five measurements from different regions of interest. Errors were calculated using the standard deviation. The measurements of the interface widths were relatively constant at $\sim 10nm$. This data suggests that the etching beam did not significantly roughen the surface of the sample.

terface should have been measured as sharp ($< 1nm$), which TOF-SIMS was unable to resolve.

9.4 Multi-layers of thicker films

Multi-layer samples were prepared with films of a larger thickness (all films where approximately between $\sim 200nm$ and $\sim 380nm$). Three different six layer samples were prepared with differing thickness films. All of these samples were prepared using the same techniques as the polymer DBRs (discussed in section 4.3). The thickness of the layers in these TOF-SIMS sample were comparable to the layers in the polymer DBR samples (PVP layers between $360nm$ and $530nm$, PS layers between $210nm$ and $320nm$). These samples were used to test for variations in layer thickness in the DBR samples.

Figure 9.11 illustrates the depth profile for one of the samples. The Ar_{2000}^{+} beam was able to etch through the thicker PS layers without degradation in the secondary ion count. This would not be possible with pre-existing sputter beam types such as C_6O^{+} [78]. Those beams could have been halted by cross-linking.

Figure 9.12 shows a comparison of film thickness measurements using TOF-SIMS (data-points) and ellipsometry (dashed lines) for all 3 samples. The TOF-SIMS measurements of the film thickness are relatively constant for all samples. However, all of the TOF-SIMS measurements are larger ($\sim 25nm$) than the ellipsometry measurement of the PS layer thickness. This may be due to the etch rate of PS changing, or not being properly calibrated (PS = $(14.77 \pm 0.18) \times 10^{-18}nm/dose$). However, the thickness of the layers remained constant, which indicated that spatial separation between the layers was well defined. The reduction in DBR reflectance was not due to the thickness of the layers being disordered.

The polymer-polymer interface widths were measured for all 3 samples using TOF-SIMS. Figure 9.13 illustrates that the polymer interface widths are still relatively large ($\sim 10nm$), which also included the PVP \rightarrow silicon interface. Hence, TOF-SIMS was unable to measure sharp ($< 1nm$) interface widths. Although, the TOF-SIMS measured interface widths were less than the polymer-polymer interface widths which were estimated when modelling UV/visible reflectivity measurements (see section 5.3.1). The original estimates were wrong

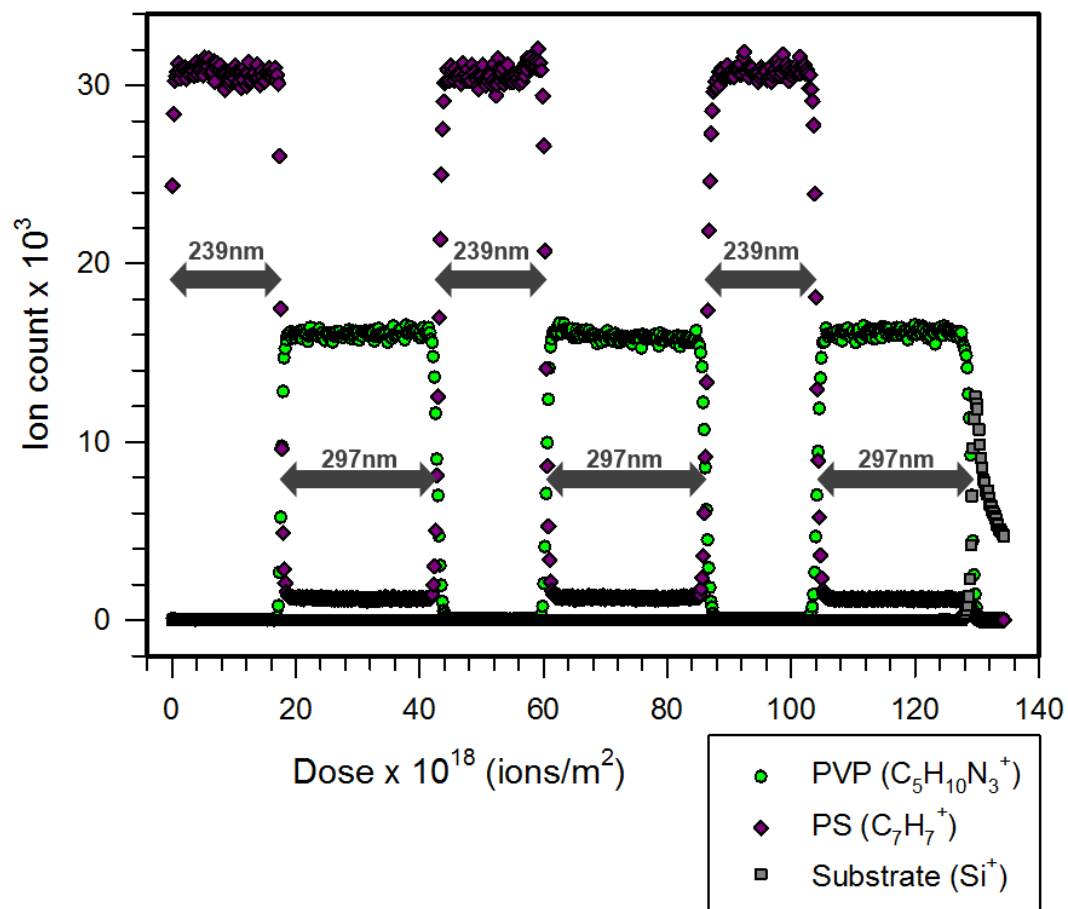


Figure 9.11: Depth profile measurement of a 6 layer PVP/PS over $100\mu\text{m} \times 100\mu\text{m}$ surface area. The thickness of the PVP layers are $d_{PVP} = 297.4 \pm 2.2\text{nm}$ and $d_{PS} = 239.0 \pm 1.3\text{nm}$ respectively. This sample is more comparable to the DBR samples which were measured in chapters 5 and 7. The ion count of PS remains constant despite PS being known as a ‘challenging polymer’ because it is susceptible to cross-linking when etched. The Ar_{2000}^+ etching beam is more capable of etching through PS than other etching beams like C_{60} [78].

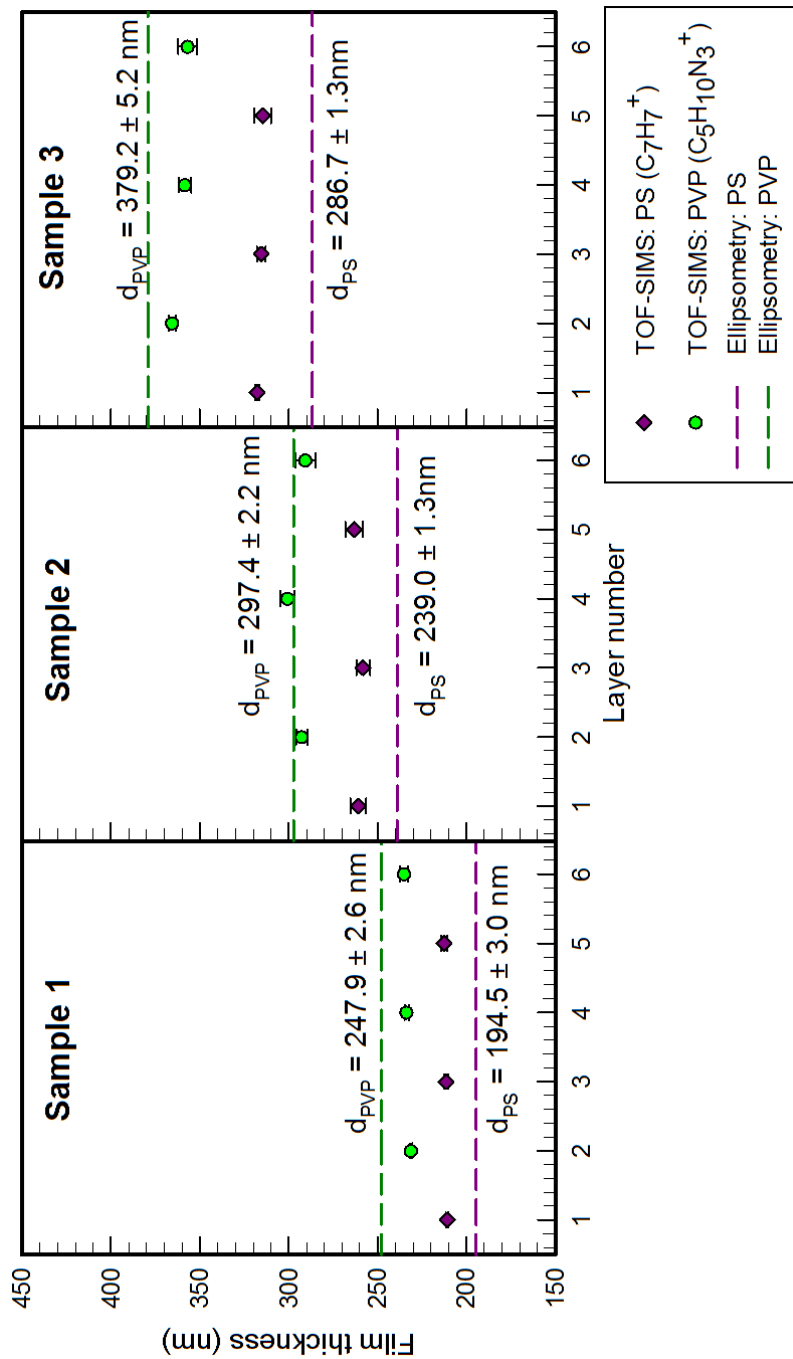


Figure 9.12: Film thickness measurements three different PVP/PS DBR samples. These samples were more comparable to the DBR samples which were measured in chapters 5 and 7. Samples 1 (layers with thickness $d_{PVP} = 247.9 \pm 2.6$ and $d_{PS} = 194.5 \pm 3.0$), 2 (layers with thickness $d_{PVP} = 297.4 \pm 2.2$ and $d_{PS} = 239.0 \pm 1.3$) and 3 (layers with thickness $d_{PVP} = 379.2 \pm 5.2$ and $d_{PS} = 286.7 \pm 1.3$) are shown in order of increasing repeating bi-layer thickness. Each data point is an average of TOF-SIMS measurements from five different regions of interest. Errors were calculated using the standard deviation. Dashed lines represent ellipsometry measurements.

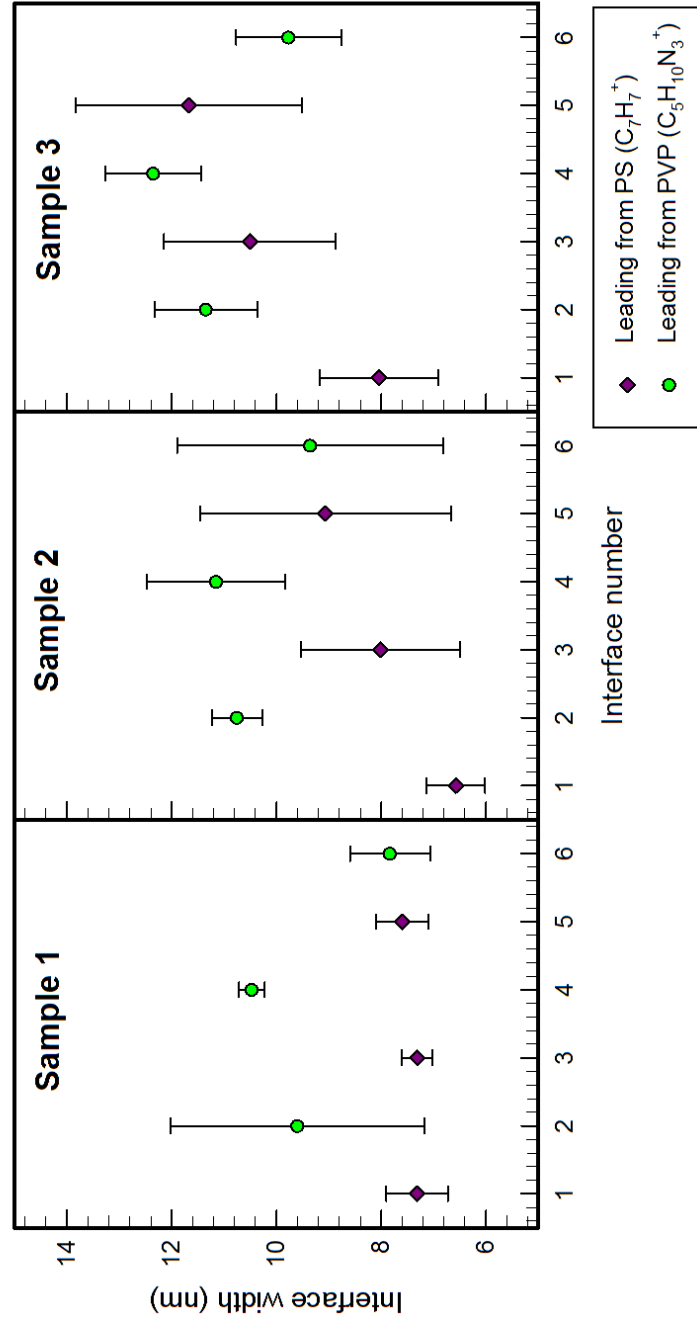


Figure 9.13: The TOF-SIMS measured interfaces for the 3 thicker film multi-layer samples. Each data-point is an average of TOF-SIMS measurements from five regions of interest. The errors were calculated using the standard deviation.

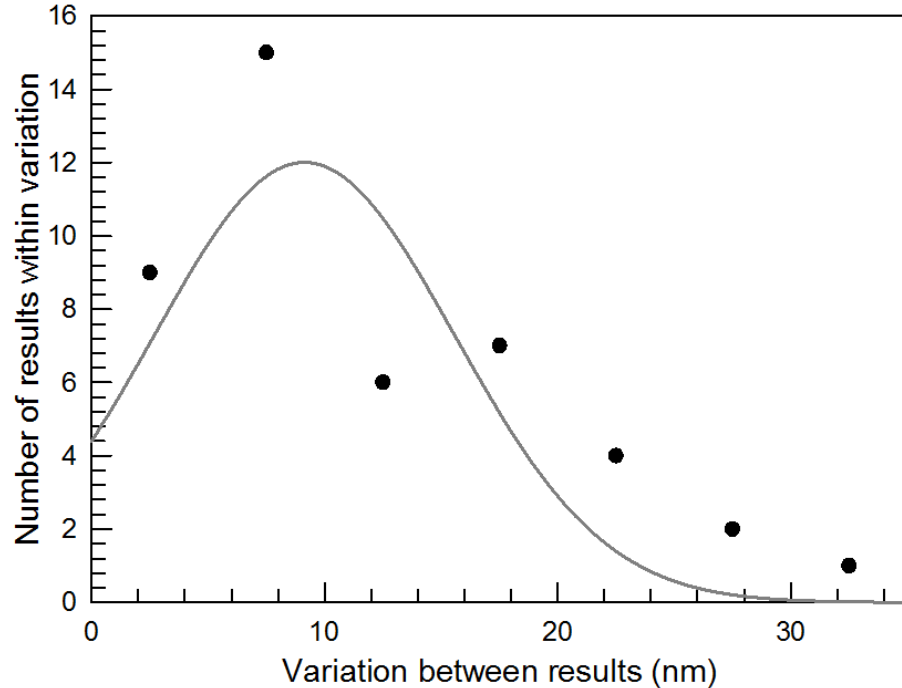


Figure 9.14: The layer thickness difference between the ellipsometry and TOF-SIMS results were calculated for all measurements. A Gaussian distribution (grey curve) was fitted using the measured data (data points) shown in this histogram. The most common difference between the two measurements were between $5nm$ and $10nm$.

and the reduction in reflectance was not due to large polymer-polymer interface widths.

9.5 Analysis of errors in TOF-SIMS measurements

The difference between the ellipsometry and TOF-SIMS layer thickness results were calculated for all measurements. Figure 9.14 shows a histogram of the difference between the two sets of measurements. The fitted Gaussian curve showed that the most frequent differences between ellipsometry and TOF-SIMS measurements were between $5nm$ and $10nm$. This indicates that the original calibration of the PVP and PS etch rates need improving. A more accurate measurement of the etch rates would improve results, such as using an average of several calibration samples/measurements. Although, the difference be-

tween the ellipsometry and TOF-SIMS measurements were shown to be large as $30nm$. The broad range between these measurements demonstrates that TOF-SIMS is not a good technique for accurately measuring film thickness.

9.6 Summary

The Ar_{2000}^+ ion beam was able to etch through the PS layers without the measurements degrading. This enabled the multi-layer structure of PVP/PS samples to be measured. However, the etch rate of the ion beam may have changed while the samples were measured. Only small changes were needed to off-set film thickness measurements. TOF-SIMS measurements of layer thickness were not always within error of the ellipsometry measurements. TOF-SIMS is capable of measuring the structure of multi-layer samples. However, more specialised/reliable techniques, like ellipsometry, should be used when measuring the thickness of films.

The TOF-SIMS measurements of layer thickness did not vary significantly with respect to one another. This demonstrated that the thickness of the spin-cast layers did not change significantly throughout the structure. Reductions in the measured sample reflectance were not due to disorder in the polymer layers.

Measurements of the interface widths was attempted by using TOF-SIMS. However, sharp interface widths, like the polymer-silicon interface, could not be resolved. The interface width measurements were typically $\sim 10nm$, when they should have been closer to $1nm$. Roughening of the sample surface (by contamination and/or inhomogeneity) had broadened the measured interface widths further. However, these measurements were smaller than the polymer-polymer interface width measurements which were extracted from UV/visible reflection measurements, which were between $20nm$ and $30nm$ wide (see section 5.3.1).

The measured reduction in DBR peak reflectance (when compared to the transfer matrix model) was not solely due to large polymer-polymer interface widths, or disorder in the structure. Other properties, such as trapped residual solvent, are more likely to be changing the optical properties of the DBR samples.

Chapter 10

Improving the angular dependence by corrugating DBR films

10.1 Introduction

It was shown in section 5.5 that flat DBR surfaces are susceptible to iridescence. This occurs when the reflection band blue-shifts due to changes in the angle of incidence. Iridescence can be a problem for various devices such as optical filters [1, 2], sensors [3], displays [4, 5] and solar cells [8, 9]. For example, the efficiency of LED's can be improved by encapsulating them within a photonic cavity using a Bragg reflector [4]. However, the Bragg reflector is susceptible to iridescence and the colour of the LED is only clearly seen when viewed at normal incidence.

One way to avoid this effect is to add curvature to the DBR. Ideally, the structure would be designed in such a way that incident light is always propagating parallel to the surface normal of the DBR. Other research groups have previously prepared curved DBR surfaces using various techniques. This includes rolling polymer bi-layers around a cylinder [21], spin-casting films onto a corrugated/blazed surface [98], blowing an elastomer multi-layer into a bubble [99] and swelling films to be moulded or patterned while being pressed with a pre-patterned PDMS stamp [100]. However, these techniques do not

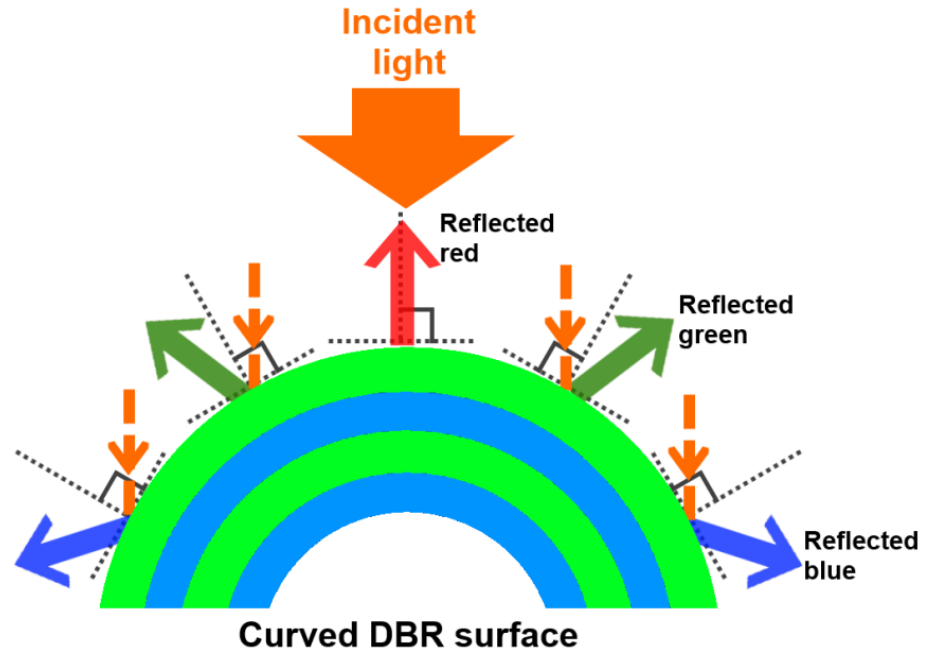


Figure 10.1: A curved DBR will reflect incident light into a wide range of directions. The wavelength of the reflections will blue-shift if the angle between the incident and reflected light is increased. Rotating the sample will not change the wavelength of the reflected light in the direction it is being measured. The curved DBR offers surfaces which are orientated over a wide broad of angles and this property is not lost when the sample is rotated.

have controlled film deposition over large surface areas. Applications, such as LED displays, would benefit from being prepared over large surface areas. Some of the previously mentioned techniques require the substrate to be pre-patterned [98, 100], which is a lengthy process.

10.2 Optical properties of curved DBRs

Figure 10.1 shows diagram of a curved DBR reflecting light. The spot size of the incident light covers the entire curvature of the sample. A curved DBR offers a broad range of angles of incidence on the sample surface. Likewise, the sample also offers a broad range of reflection angles. This is illustrated in the figure 10.1 by the DBR reflecting ‘red’, ‘green’ and ‘blue’ wavelength light. ‘Red’ is longest wavelength reflected by this example (this curved DBR would reflect ‘red’ light if it were made flat and measured at normal incidence). The longest wavelength is only measured when the angle of incidence and reflection

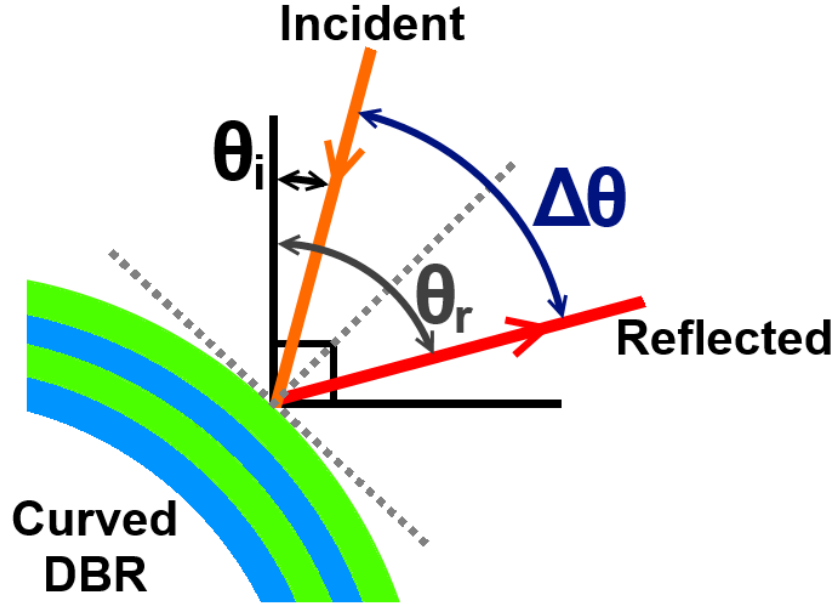


Figure 10.2: The wavelength of the reflected light is longest when the incident beam is normal to the curvature of the surface. However, the wavelength of the reflected beam is blue-shifted when the incident beam is not normal to the curvature of the surface. The angle between incident and reflected is $\theta_i + \theta_r = \Delta\theta$. This is used to calculate the wavelength of the reflection peak, by using the modified optical transfer matrix method.

are both perpendicular to the curved surface of the sample. This is comparable to when the DBR is flat and measured at normal incidence. The ‘green’ and ‘blue’ light are DBR reflections which have shorter wavelength reflection peaks because their angle of incidence is not normal to the curved surface. Different wavelengths of light are reflected at different angles of reflection.

Figure 10.2 is a diagram of a small section of a curved DBR film being illuminated at the angle of incidence θ_i . Light with wavelength λ is preferentially reflected at the angle of reflection θ_r by the DBR. The angle between θ_i and θ_r is calculated by,

$$\Delta\theta = |\theta_r + \theta_i|, \quad (10.1)$$

Where $\Delta\theta$ = angle between incident and reflected light [*degrees*], θ_i = angle of incidence [*degrees*] and θ_r = angle of reflection [*degrees*]. Note that by convention θ_i and θ_r are usually on opposite sides of the surface normal. The magnitude of either θ_i or θ_r is negative if they are both on the same side of the

surface normal.

The wavelength of the reflected light is blue-shifted when increasing the magnitude of $\Delta\theta$. Reflections from an infinitely small section of the surface are approximately specular. This infinitely small section of the surface can be approximated as a flat DBR. The modified optical transfer matrix method (discussed in chapter 3) was used to calculate the wavelength of light reflected from a small section of a curved DBR. Replacing the modelled angle of incidence with $\Delta\theta/2$ calculates the wavelength of the reflection peak λ from a curved DBR.

A curved DBR offers surfaces which enable a broad range of angles of incidence and reflection (unlike a flat DBR which has a single angle of incidence). This property is not lost when rotating a curved DBR. The wavelength dependence of the reflection peaks are unaffected when rotating the sample because of the curvature of its surface.

10.3 Corrugating thin films

Continuously curving the DBR's surface would provide a broad distribution of angled reflection surfaces. Making the sample flat over large surface areas (like on a chip) would be more practical for devices such as LEDs and solar cells. Corrugating the DBR films is a possible solution, as it adds curvature to a film over a flat area.

Previous experiments have corrugated unstrained thin films by using spontaneous pattern formation techniques [100,101]. A rigid film is deposited/bonded onto a pre-strained rubber substrate (illustrated by the diagram in figure 10.3). The rubber substrate attempts to return back to its original shape (due to entropic elasticity) when the pre-strain has been removed [18]. This adds an in-plane compressive stress to the previously unstrained thin film. The film attempts to resolve these stresses by bending. However, the substrate is much thicker ($\sim mm$ thick) than the thin film (between μm and nm thick) and it remains flat. This results in the film corrugating across the surface of the substrate as a result of the compressive stress [100, 101]. The spatial separation between each corrugation wrinkle is periodic. Previous experiments, using this technique, have measured corrugation wavelengths ℓ_c between μm and nm

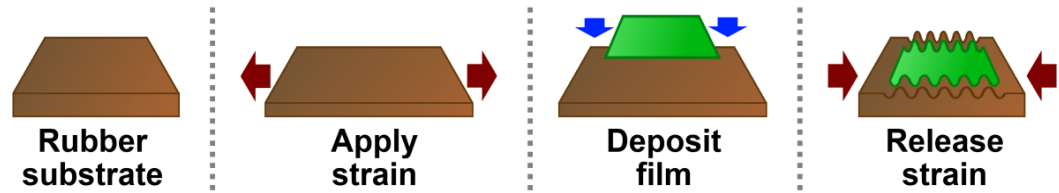


Figure 10.3: Diagram of a thin film being corrugated. Strain is applied to a rubber substrate by stretching it. An un-strained thin film is deposited onto the substrate. The substrate returns back to its original shape/size when the applied strain is removed. This applies a compressive stress to the thin film which causes it to corrugate.

length scales [101]. It was possible to corrugate a DBR (which is a multi-layer thin film) using this technique over a large surface area (approximately $1\text{cm} \times 1\text{cm}$).

10.3.1 Preparing the elastomer substrate

An elastomer was used as the rubbery substrate in this experiment. Elastomers consist of long molecular chains which are randomly cross-linked. These materials have a low Young's modulus (they are 'rubbery'), high strain failure (it is difficult to deform them permanently) and capable of storing strain energy [18, 49]. The elastomer will returned back to its original shape when the strain is removed.

Figure 10.4 shows the preparation procedure for the elastomer substrate. The elastomer was made from polyisoprene which was cross-linked by curing it with dicumyl peroxide in toluene. These substrates were placed into a purpose built 'strain-rig' (shown in figure 10.5). The in-built micrometer on the strain rig was used to apply a controlled strain to the elastomer substrate. A pre-strain of $\epsilon_{pre} = 0.025 \pm 0.001$ was used to prepared the corrugated sample which is discussed later in this chapter.

10.3.2 Preparing the CA/PVK DBR

Thicker films are more difficult to corrugate when compressing them with a pre-strained rubber substrate [100, 101, 102]. The PVP/PS DBRs were too thick (total thickness of $\sim 14\mu\text{m}$ for a 50 layer sample) to corrugated when using this

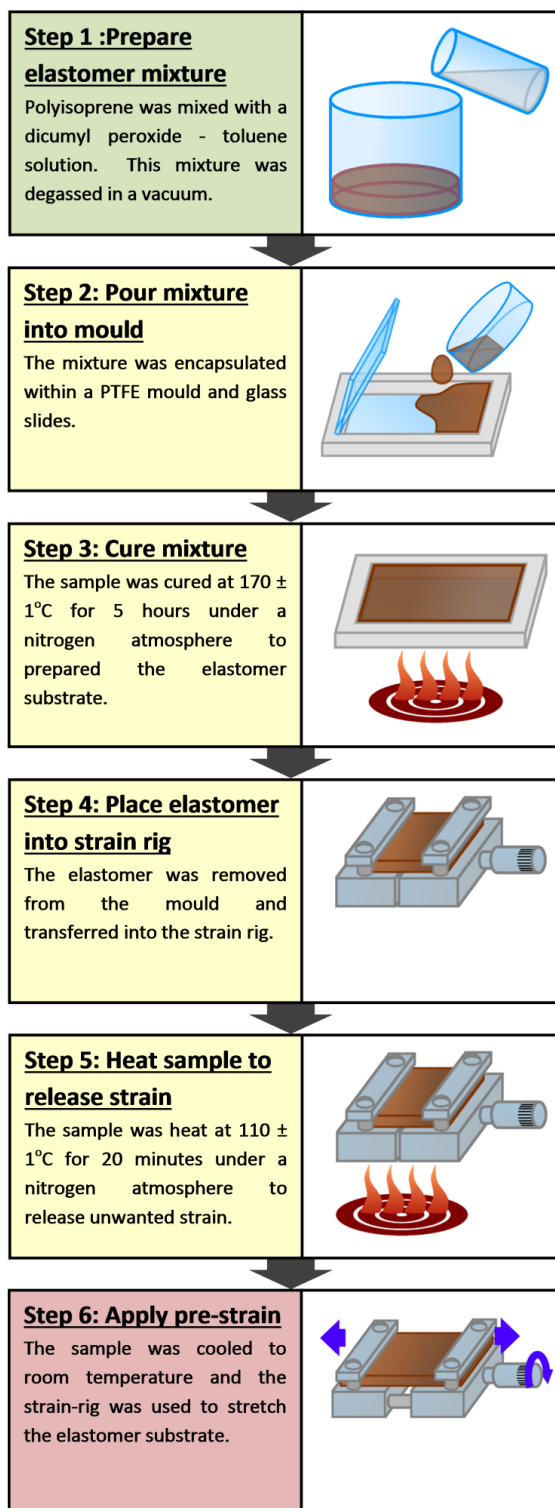


Figure 10.4: Flow diagram illustrating the sample preparation procedure of a cross-linked polyisoprene elastomer. The elastomer was transferred onto a *strain-rig* and stretched. This was used as the ‘pre-strain’ substrate for the corrugated DBR.

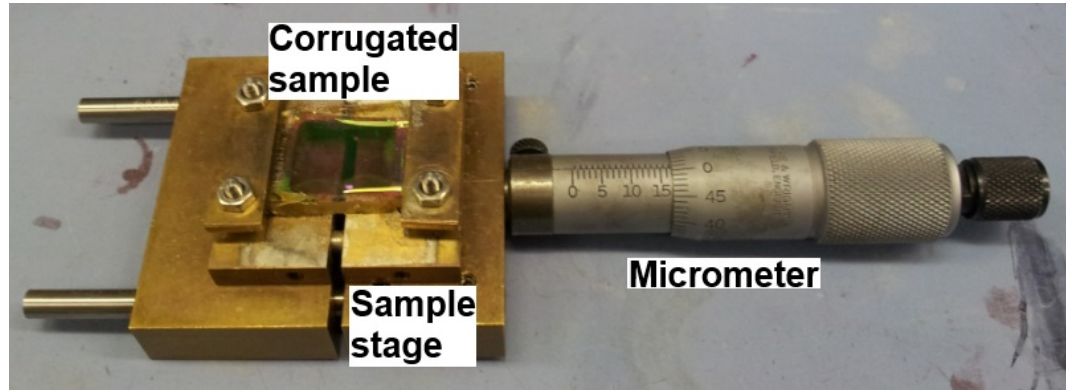


Figure 10.5: Photograph of the ‘strain rig’ which was used to apply strain to an elastomer substrate. The elastomer was placed into the sample stage. This is made from two sections which are interconnected by rails. A micrometer was used to push the opposing section away. Therefore, the sample stage separates outward. This stretched and strained the sample as it was ‘opened out’. Furthermore, the scale on the micrometer was used to calculate and control the applied strain. Turning the micrometer back into its original position enabled the sample stage to recede back into its unstrained position. This photograph also shows a DBR which had been corrugated using the strain-rig.

technique. Attempts to corrugate a 50 layer PVP/PS sample resulted in the films de-laminating from the substrate. A different polymer multi-layer system had to be used instead.

A DBR was prepared by spin-casting alternating layers of cellulose acetate (CA) and poly(9-vinylcarbazole) (PVK) [20,103]. The refractive index contrast between CA and PVK ($\Delta n_{CA/PVK} = 0.201 \pm 0.001$) was greater than the refractive index contrast between PVP and PS ($\Delta n_{PVP/PS} = 0.070 \pm 0.001$). Fewer layers were needed to prepare a CA/PVK DBR with a reflectance which was equal to a PVP/PS DBR. The layer thickness of the CA/PVK DBR layers were approximately four times thinner than the comparable PVP/PS DBR layers. Each layer in the CA/PVK DBRs had an optical path length of $\sim \lambda/4$, whereas the optical path length in each PVP/PS layer was $\sim \lambda$.

Figure 10.6 shows a comparison between a PVP/PS DBR and a CA/PVK DBR reflection spectra. The CA/PVK DBR has a much larger reflection peak when compared to the PVP/PS DBR. This is due to the CA/PVK sample having a larger refractive index contrast and the thickness of the layers ($d_{CA} = 107 \pm 6nm$ and $d_{PVK} = 66 \pm 6nm$) being much smaller than the coherence length of reflected light. Decreasing the layer thickness with respect to the

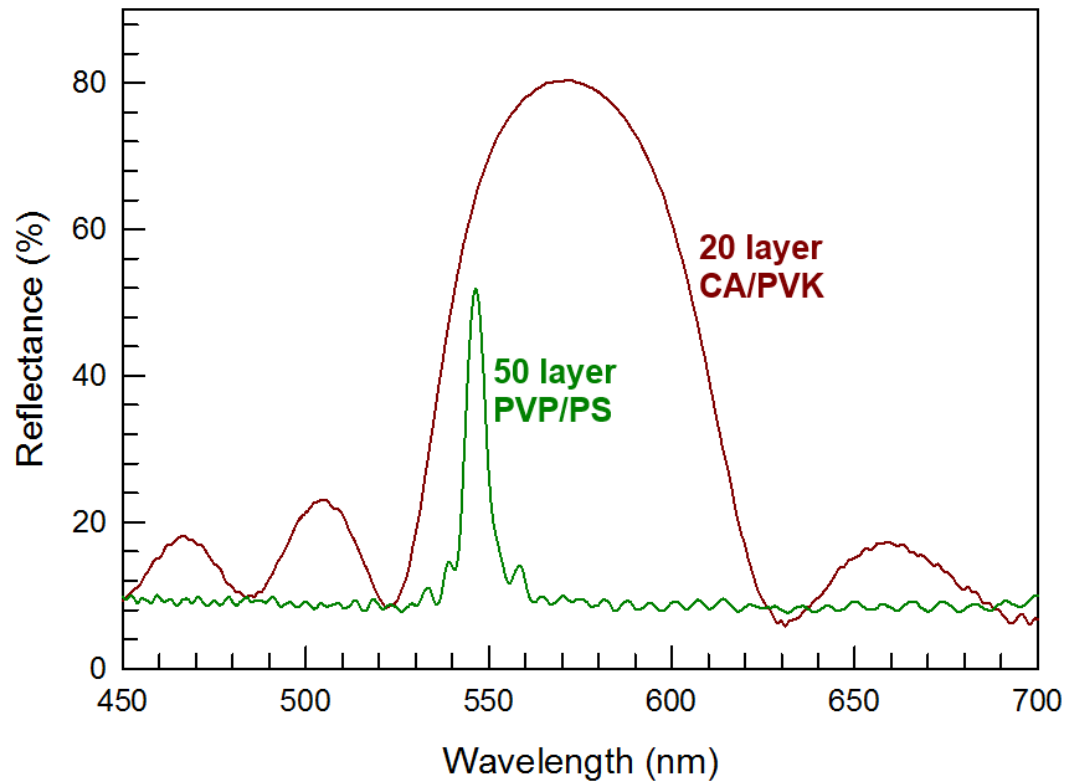


Figure 10.6: UV/visible reflection spectra of a 50 layer PVP/PS DBR and a 20 layer CA/PVK DBR. The CA/PVK DBR has a much larger reflection peak due to the layers being thinner and having a larger refractive index contrast. The increase in band-width is due to the thickness of each layer being much smaller than the coherence length of the reflected light.

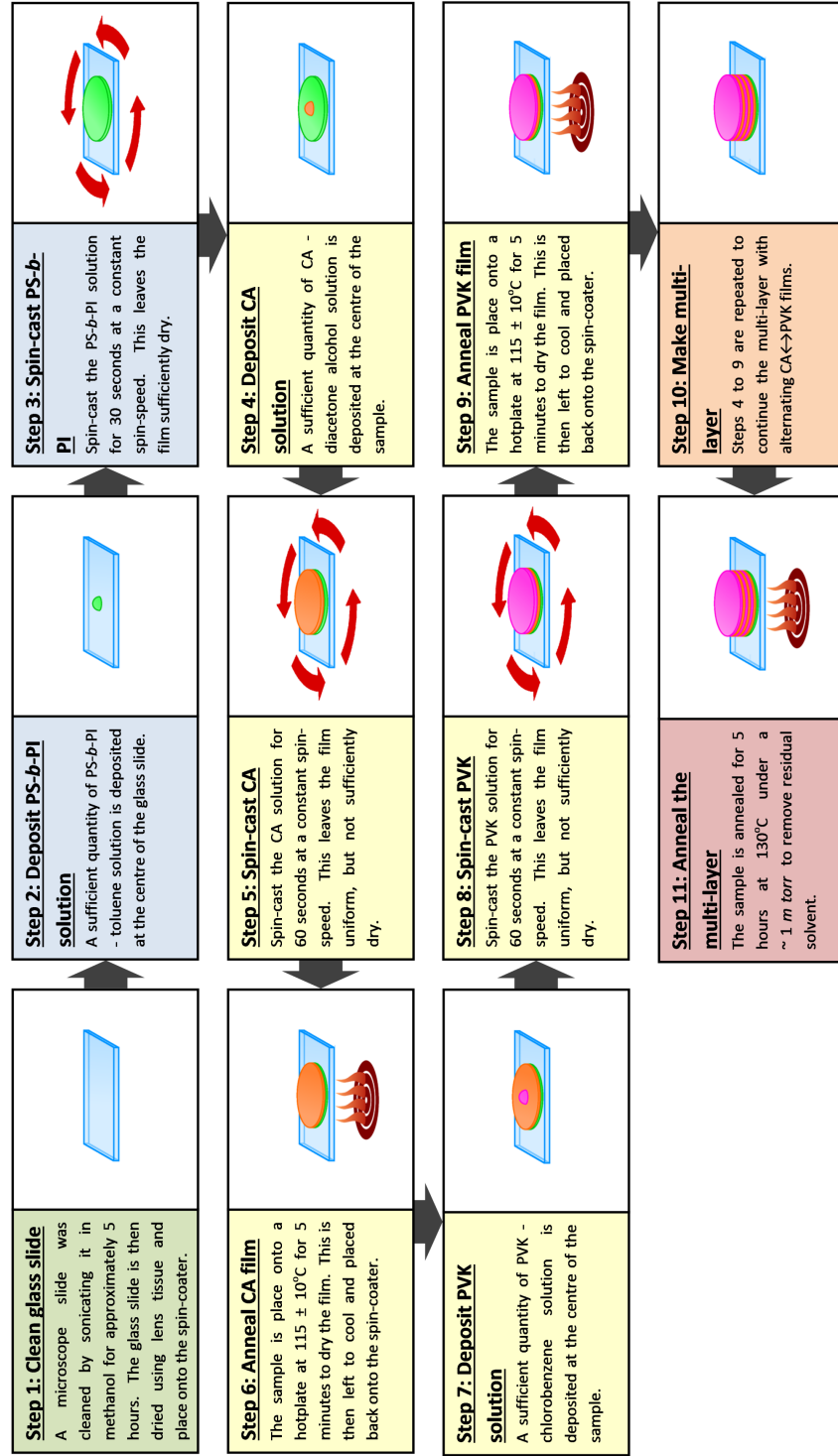


Figure 10.7: Flow diagram illustrating the sample preparation procedure for CA/PVK multi-layers. An initial PS-*b*-PI layer was spin-cast and used later as a binding layer to hold the DBR and elastomer substrate together. Preparation of the CA/PVK DBRs took longer than the PVP/PS DBR alternative because every deposited layer had to be heated on a hotplate.

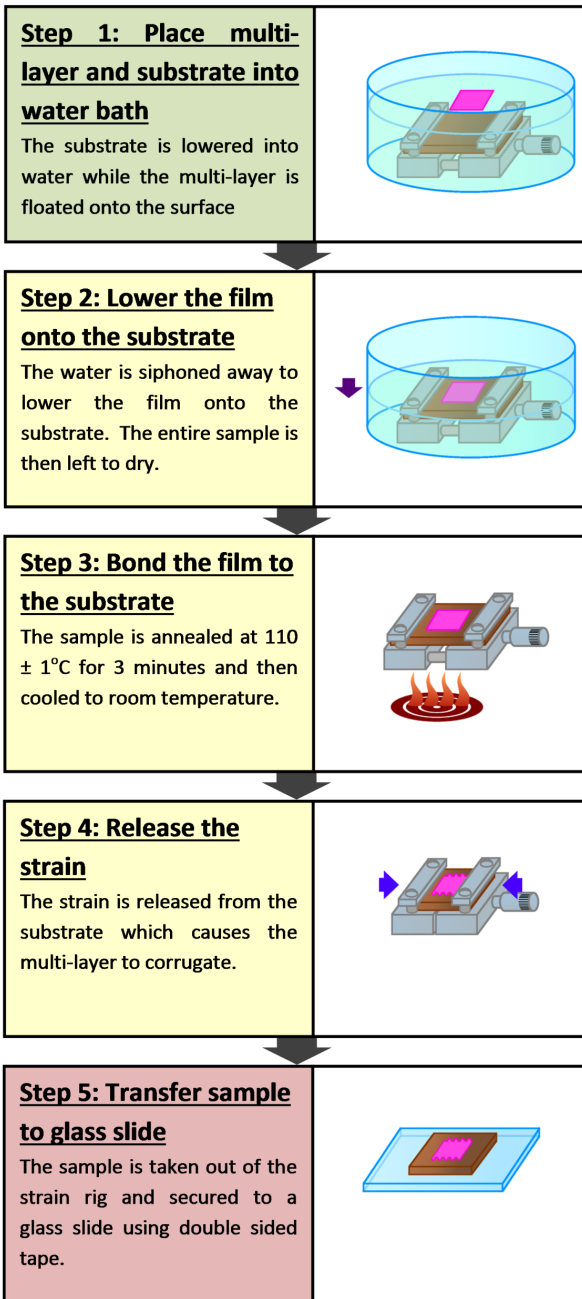


Figure 10.8: Flow diagram illustrating the DBR being deposited onto the elastomer substrate. The DBR film was bonded to the substrate by heating the sample for a short duration. Corrugations were created when the strain was removed from the elastomer substrate. The sample was transferred onto a glass slide so it could be easily handled during experiments.

coherence length also increases the bandwidth.

The benefits of using PVP/PS DBRs instead of the CA/PVK DBRs is that the sample preparation procedure is simpler (discussed later) and the solvents used are not as damaging to the environment. For example, chlorobenzene is less environmentally friendly than toluene [104, 105]. Another advantage may be the narrower reflection band of the PVP/PS DBRs, which may be useful for narrow-band filtering.

Figure 10.7 shows the sample preparation procedure for CA/PVK DBRs. Diacetone alcohol was used to dissolve CA into a solution and chlorobenzene was used to dissolve PVK. A 30 layer CA/PVK sample was prepared for the experiments discussed later in this chapter. The thickness of the CA and PVK layers used in the sample were $d_{CA} = 123.0 \pm 2.0nm$ and $d_{PVK} = 73.4 \pm 2nm$ respectively.

10.3.3 Corrugating the CA/PVK DBR

Figure 10.8 shows a flow diagram of the preparation procedure used to corrugate the DBR film. A water bath was used to lower the CA/DBR film onto the pre-strained elastomer substrate. This was then left to dry before heating the sample for 3 minutes at $110^{\circ}C$ to bond the film to the substrate. The sample was then released from the strain rig. Corrugations in the DBR film emerged as the elastomer relaxed back to its original shape.

10.4 Physical properties of the corrugated DBR

Figure 10.9 shows a optical microscope image of the corrugated DBR. Each bright fringe is either a maxima or a minima of the corrugated film. This micrograph image shows that the corrugations are equally spaced and parallel.

A profileometer was used to measure surface topography of the corrugated DBR. Measurements were along its path of corrugation (see figure 10.9). The data-points in figure 10.10 represent the profileometer measurements. The red sinusoidal curve is an approximation used to calculate the amplitude A_C and corrugation wavelength ℓ_C of the sample. These results showed that the

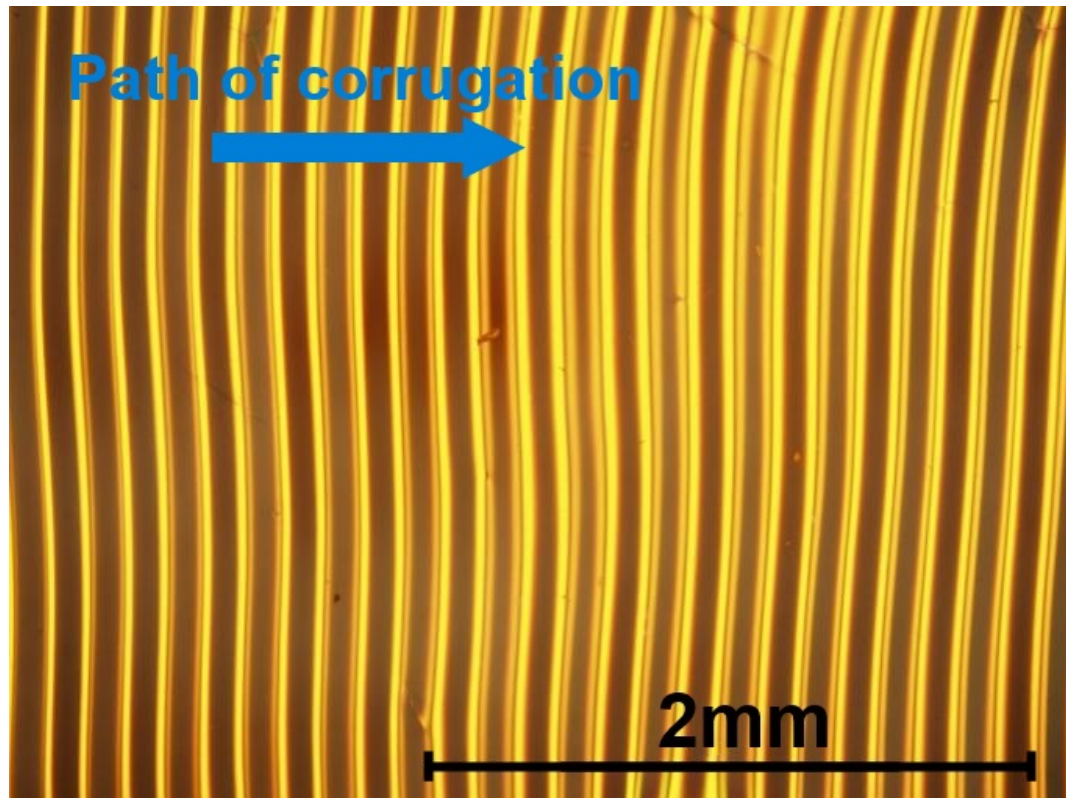


Figure 10.9: A $\times 5$ magnification optical microscope image of a 30 layer CA/PVK DBR which has been corrugated by a pre-strained polyisoprene elastomer. The bright fringes are reflections which are from surfaces orientated perpendicular to the incident light. Each bright fringe is from the alternate top and bottom peaks of the corrugated surface. The *path of corrugation* is label to clarify that it is in the direction of varying amplitude. This is also perpendicular to the direction of constant amplitude.

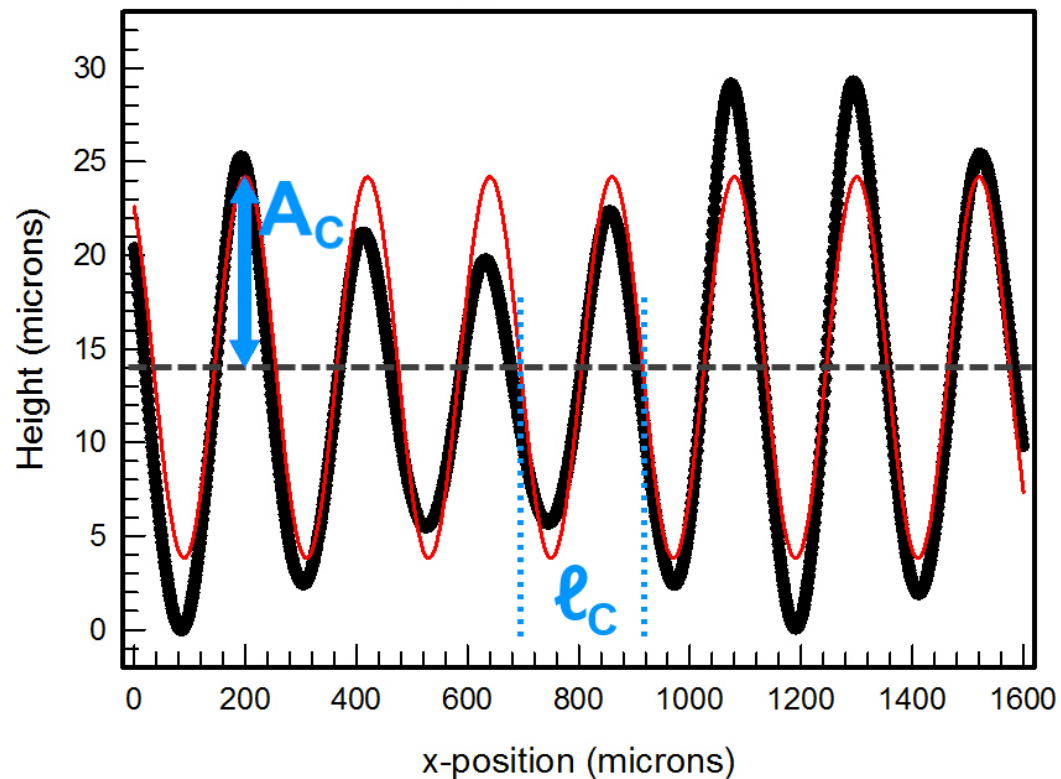


Figure 10.10: Profilometer measurement of a corrugated CA/PVK DBR (black data-points). The red curve is a cosine approximation used to determine the corrugation wavelength ($\ell_C = 220 \pm 5\mu m$) and average amplitude ($A_C = 10 \pm 3\mu m$). The wavelength of the corrugation was relatively periodic. However, the amplitude of the sample was shown to vary over the surface.

corrugations are periodic and have a corrugation wavelength of wavelength $\ell_C = 220 \pm 5\mu m$. This is much larger than the wavelength of visible light. The optical properties discussed later in this chapter are not due to diffraction from the corrugated surface [10].

The average amplitude of the corrugations was $A_C = 10 \pm 3\mu m$. This was 22 times smaller than ℓ_C . The corrugations are very shallow, but are still visible in the micrograph image (shown in figure 10.9).

10.5 UV/visible properties of corrugated DBRs

The UV/visible reflection properties of two CA/PVK DBR samples (deposited onto elastomer substrates) were measured and compared with each another. One of the samples was corrugated and the other sample was not. Both of the samples were made from 30 layer CA/PVK. The thickness of the CA layers where $d_{CA} = 123.0 \pm 2.0nm$ and the PVK layers where $d_{PVK} = 73.4 \pm 2.0nm$.

The reflection spectrum from these samples were measured using the refractometer (discussed in section 4.5.2). The angle of incidence θ_i is the angle of the incident light. Likewise, the angle of reflection θ_r is the angle of the detector. Both measurements are with respect to the surface normal of the substrate (not the curvature of the corrugations).

Various experiments were used to measure the optical properties of the samples. This included;

- *Specular reflection:* The optical properties of the samples were measured when the angle of incidence θ_i and angle of reflection θ_r were equal.
- *Changing measured angle of reflection θ_r :* Off specular measurements of the corrugated DBR were measured at different angle of reflection θ_r .
- *Changing angle of incidence θ_i :* The reflection properties of the corrugated DBR samples were measured when changing the angle of incidence θ_i .
- *Rotating the sample:* The corrugated DBR samples were rotated, which changed both the angle of incidence θ_i and reflection θ_r with respect to the

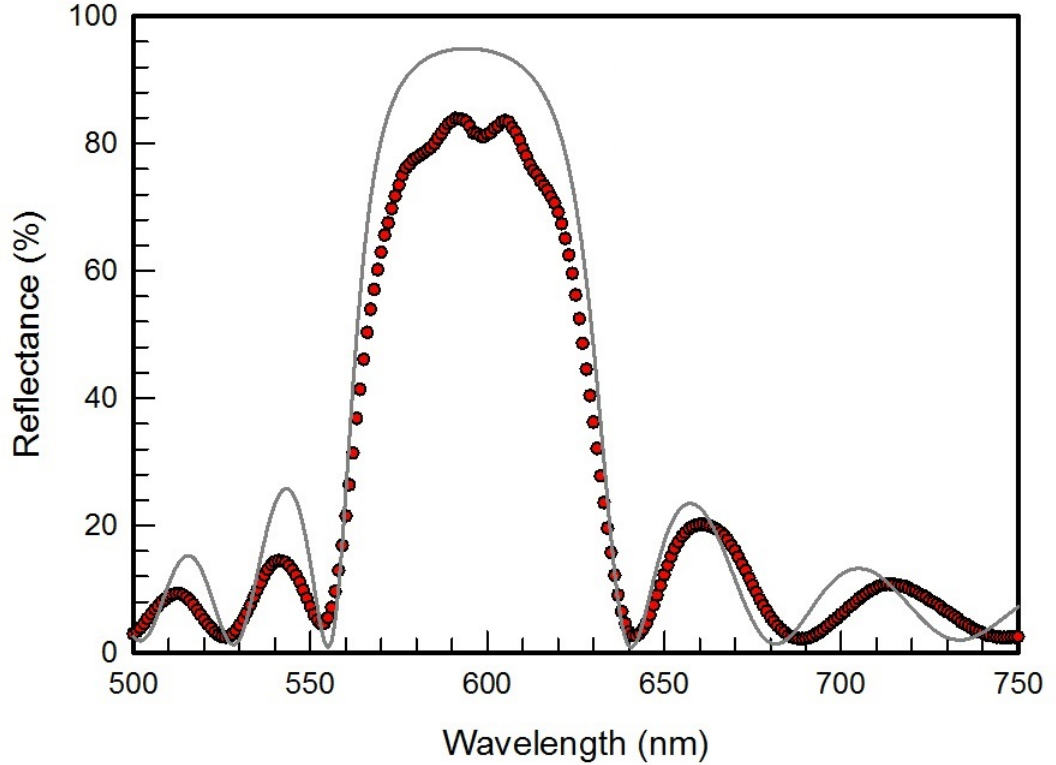


Figure 10.11: Reflectance of a 30 layer CA/PVK DBR which was deposited onto a un-strained elastomer substrate. The sample was measured at $\theta_i = \theta_r = 20 \pm 1^\circ$. UV/visible reflectance spectra was measured (red data-points) using the reflectometer. Reflectance spectra was also modelled using the modified optical transfer matrix method (grey curve). The optical properties of the CA/PVK DBR were not lost when depositing the CA/PVK DBR onto a un-strained elastomer substrate.

normal of the substrate. However, the angle between θ_i and θ_r remained constant.

The reflectance of the corrugated DBR was also discussed towards the end of this chapter.

10.5.1 Specular reflection measurements

Figure 10.11 shows the UV/visible reflection spectrum from the flat DBR when $\theta_i = 20 \pm 1^\circ$ (this is a specular reflection measurement so $\theta_i = \theta_r = 20 \pm 1^\circ$). It was not possible to measure light at normal incidence ($\theta_i = 0$) as the light source and spectrometer cannot occupy the same space on the reflectometer

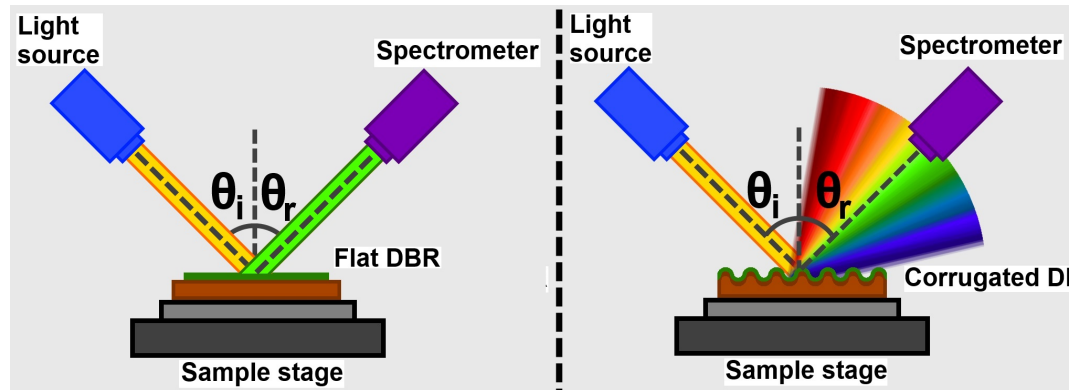


Figure 10.12: Illustration of the experimental set-up for measuring flat [left panel] and corrugated [right panel] DBRs. The experiment in this section measured the specular reflection ($\theta_i = \theta_r$) from the DBR samples. Results were measured with respect to the angle of incidence θ_i .

set-up. This CA/PVK DBR had a larger reflectance ($\sim 80\%$) and broader reflection band ($\sim 75nm$) than the PVP/PS DBRs. The modified optical transfer matrix method was able to model the wavelength position of the reflection peak by using ellipsometry measurements (data not shown). This experiment demonstrated that the CA/PVK could be transferred to an elastomer substrate without significant degradation in reflectance.

The flat PVP/PS DBRs showed iridescence when their angular dependence was measured in section 5.5. All of the reflections from the flat DBR were specular and can only be measured when $\theta_i = \theta_r$. Changing either θ_i or θ_r will misalign the reflected beam and nothing will be measured by the spectrometer.

Figure 10.12 is a diagram of the experimental procedure/set-up. The left panel is the collimated specular reflection of the flat DBR. The right panel is reflected light which is scattered over a broad range of different wavelengths. Both θ_i and θ_r are always with respect to the normal of the substrate. Reflection spectra was measured from both samples for different angles of incidence θ_i (between 20° and 70°). The measured angle of reflection θ_r was also changed so $\theta_i = \theta_r$ during this experiment.

The specular reflection measurements of the flat CA/PVK DBR (red data-pints) and corrugated DBR (blue data-pints) are shown in figure 10.13. Both results showed the wavelength of their reflection peaks blue-shift when θ_i had diverged away from the surface normal of the substrate. The angular dependence of both samples (wavelength of the reflection peak) were comparable.

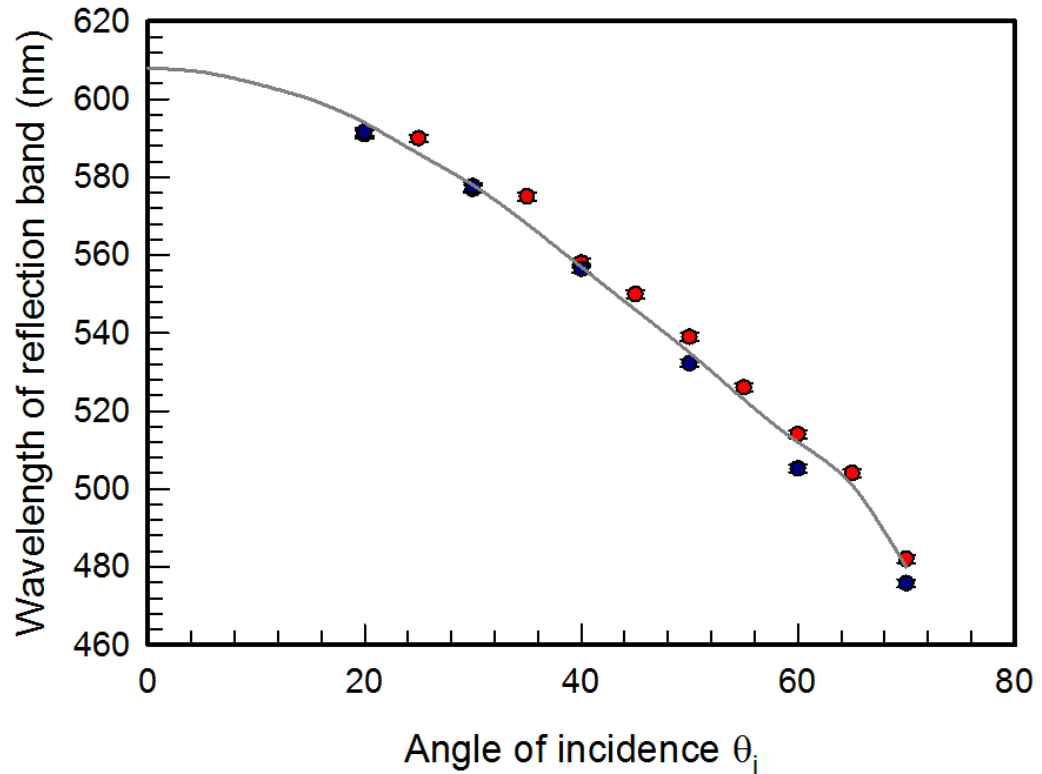


Figure 10.13: Comparison of the specular reflection measurements (when $\theta_i = \theta_r$) of the reflection peak wavelength from a flat CA/PVK DBR (red data-points) and corrugated DBR (blue data-points). The wavelength of the reflection band from both samples had blue-shifted when the angle of incidence diverged away from the normal to the substrate. These two results are comparable and were modelled using the modified optical transfer matrix method (grey curve).

This was modelled using the modified optical transfer matrix method (grey line). The model predicted that the longest wavelength of the reflection peak would have been $\lambda \approx 610nm$. This would occur in both samples if they were measured at normal incidence $\theta_i = 0$.

The flat CA/PVK DBR showed the same angular dependence as the PVP/PS DBRs discussed in section 5.5. Angular dependence was also measured in the corrugated DBR during specular reflection measurements. All of the measured spectra in this experiment would have been from the maxima and minima sections of the corrugated DBR. The surfaces of these small maxima and minima sections are parallel to the surface plane of the substrate. Hence, the wavelength properties of these reflection peaks are approximately the same as a flat DBR. The angular dependence of specular reflections was not improved by corrugating the DBR.

10.5.2 Changing measured angle of reflection θ_r

Figure 10.14 shows a diagram of a flat DBR being measured with a reflectometer. The reflection from the sample is specular and can only be measured when $\theta_i = \theta_r$. Changing the measured angle of reflection θ_r , misaligns the set-up and no reflection spectrum is measured.

Figure 10.15 shows a diagram of a corrugated DBR being measured with the refractometer. The reflected light was scattered (off specular reflection) along the direction of corrugation. Reflection spectra was still measured when changing the measured angle of reflection θ_r . However, the wavelength of the measured reflection peak changed.

The corrugated DBR sample was measured at different angles of reflection θ_r , with respect to the surface normal of the substrate. Incident light was kept at a fixed angle of $\theta_i = 40^\circ$ (also with respect to the surface normal of the substrate) during this experiment. Figure 10.16 shows the measured reflection spectrum from the corrugated DBR. The top, middle and bottom panels show the measured reflection spectrum at 60° , 40° and 20° angles of reflection θ_r , respectively. These results showed the wavelength of the reflection peak red-shifting when moving the angle of reflection θ_r closer to the angle to incidence θ_i . This is also illustrated in figure 10.17, which is a plot of the wavelength

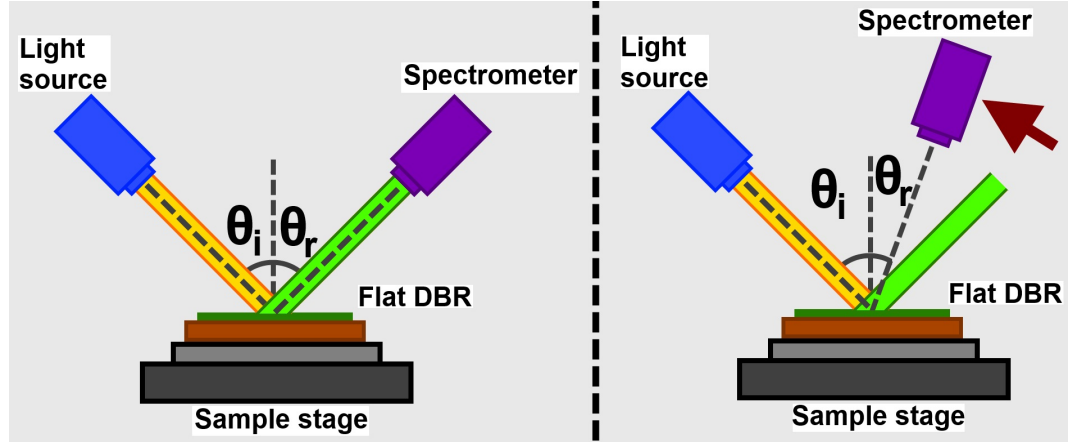


Figure 10.14: [Left panel] An incident collimated light beam at θ_i reflects off the sample at an angle of reflection θ_r . [Right panel] The spectrometer is moved to a new value of θ_r . No reflection spectrum is measured as the set-up is misaligned.

dependence of the corrugated DBR reflection peaks with respect to measured angle of reflection θ_r . The measurements are represented by the purple data-points. This data was also modelled using the modified optical transfer matrix method (grey curve). The modelled wavelength of the reflection peak was extracted by substituting the angle of incidence with the following correction,

$$\theta_{Model} = \frac{\Delta\theta}{2} = \frac{|\theta_r + \theta_i|}{2}, \quad (10.2)$$

Where θ_{Model} = angle of incidence used in the model (which should not be confused with the angle of incidence with respect to the surface normal of the substrate θ_i) and $\Delta\theta$ = difference between angle of incidence θ_i and reflection θ_r .

The corrugated DBR offers a broad range of angles of incidence with respect to the curvature of the surface. This curved surface reflects light over a broad range of angles and at different wavelengths. The measured beam of light, during the experiment, is reflected from a small section of the corrugated DBR's surface. This small section orientated perpendicular to the angle between θ_i and θ_r (shown previously in figure 10.1). The wavelength of the measured reflection peak was blue-shifted when the angle between θ_i and θ_r ($\Delta\theta$) had increased. Deviating θ_r away from θ_i increases $\Delta\theta$, which results in the wavelength of the measured reflection peak blue-shifting. The model predicted that the longest wavelength would have occurred if the angle incidence were parallel to the

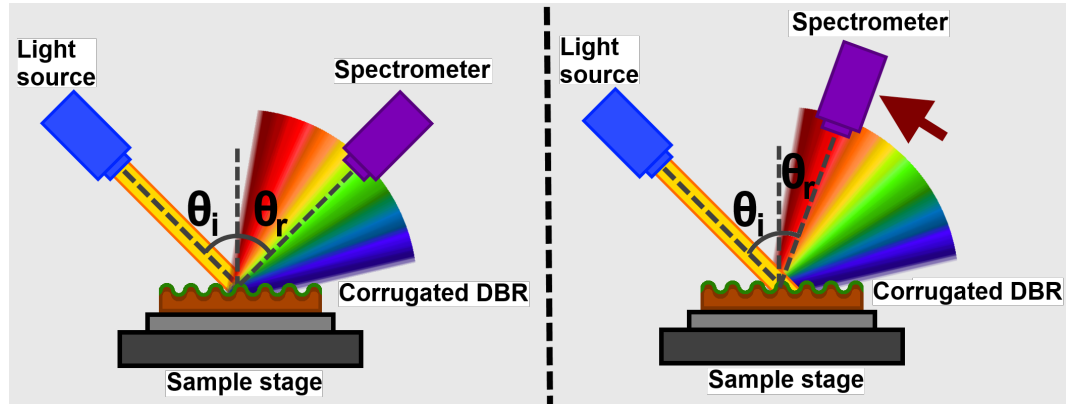


Figure 10.15: [Left panel] A collimated light beam illuminating a corrugated DBR at θ_i . A small sample of the reflected light is being measured with the spectrometer. [Right panel] The wavelength of the measured reflection peak is red-shifted when the detector θ_r is moved towards the angle of the incident light θ_i .

angle of reflection ($\Delta\theta = 0$). This would have also been the same wavelength of the reflection peak ($\lambda \approx 610nm$) if the corrugated DBR were made flat and measured at normal incidence.

No reflection spectrum was measured from the flat DBR when $\theta_i \neq \theta_r$ (off-specular). The corrugated DBR was able to reflect light over a broad range of reflection angles. However, the wavelength of the reflection peak changed with respect to θ_r . This is unique to the corrugated DBR, as the same optical properties were not possible with the flat DBR. Although, there was still angular dependence in the wavelength of reflection peaks during in this experiment.

10.5.3 Changing angle of incidence θ_i

Figure 10.18 is a diagram showing incident light reflecting off a flat DBR sample. The wavelength of the reflected light will red-shift when the light source approaches normal incidence. However, the reflection is specular, so the beam path is misaligned by moving the light source. No reflection spectrum is measured when $\theta_i \neq \theta_r$.

Figure 10.19 is a diagram of light being reflected by a corrugated DBR. Reflection spectra was still measured when changing the angle of incidence θ_i as the corrugated DBR reflects light over a broad range of angles. However, changing the angle of incidence also changes the the angle between θ_i and θ_r ,

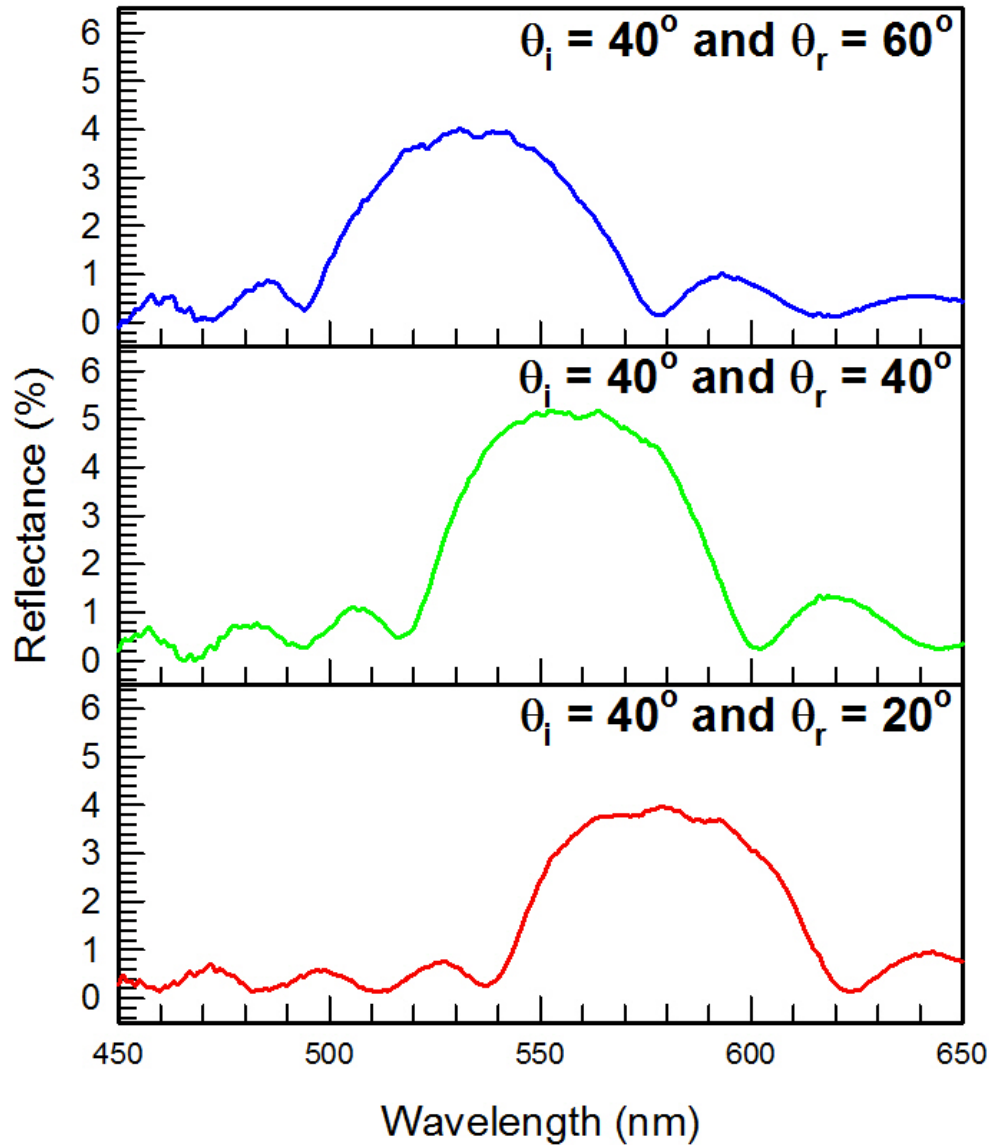


Figure 10.16: UV/visible spectrum measured from a corrugated DBR at different angles of reflection θ_r , which were 60° [top panel], 40° [middle panel] and 20° [bottom panel]. The angle of incidence was fixed at 40° with respect to the surface normal of the substrate (see figure 10.15). Moving the angle of reflection θ_r closer to the angle of incidence θ_i red shifts the measured reflection peak.

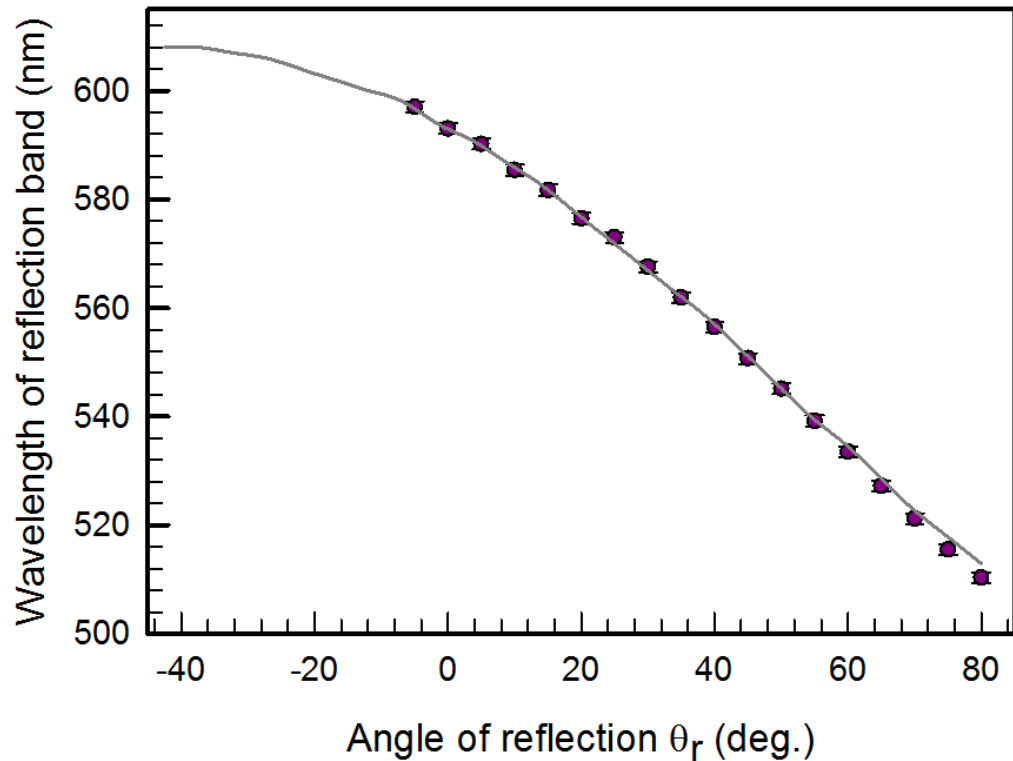


Figure 10.17: The wavelength of the reflection peak was measured with respect to the angle of reflection θ_r . Reflection measurements from the corrugated DBR are represented by the purple data-points. Error bars were determined by the resolution of the spectrometer. Moving the angle of reflection θ_r closer to the angle of incidence θ_i red-shifted the measured reflection peak (see figure 10.15). This angular dependence was modelled using the modified optical transfer matrix method (grey curve). The model predicted that the longest wavelength ($\lambda \approx 610nm$) would have been measured if there were not separation between the angle of incidence and reflection ($\Delta\theta = |\theta_r + \theta_i| = 0$).

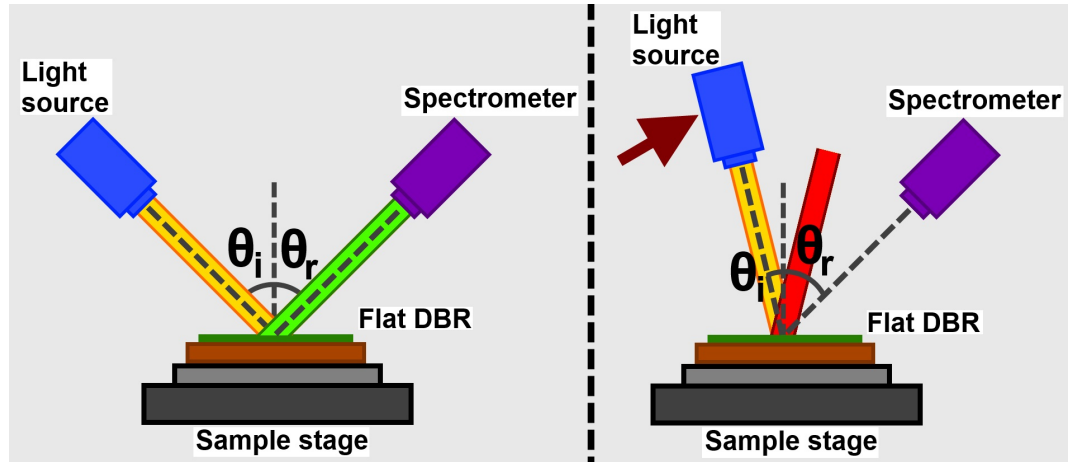


Figure 10.18: [Left Panel] The angle of incidence equals the angle of reflection for a flat DBR ($\theta_i = \theta_r$). [Right panel] The set-up is misaligned by changing the angle of incidence θ_i , but not reflection θ_r .

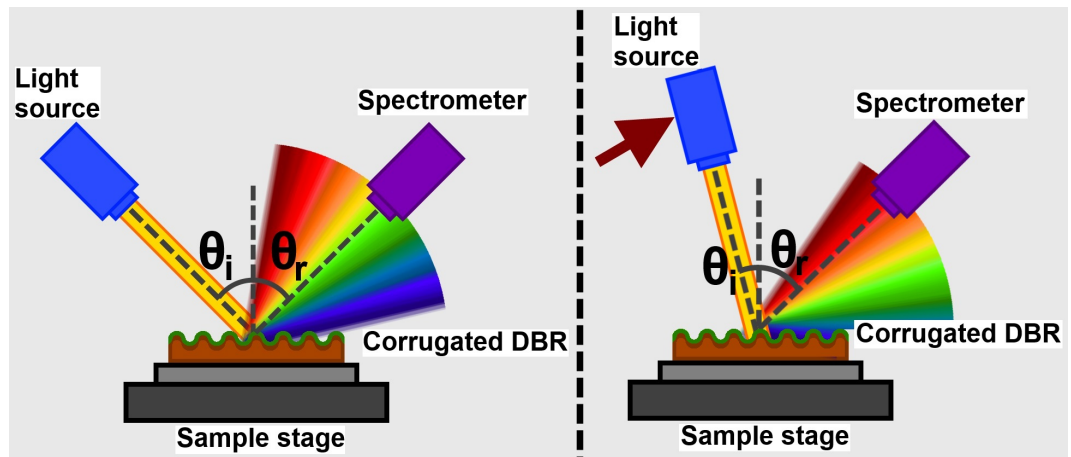


Figure 10.19: [Left panel] A corrugated DBR reflecting incident light into a broad range of angles and wavelengths. [Right panel] The measured reflection peak is red-shifted when the incident beam θ_i is moved toward the angle of the detector θ_r .

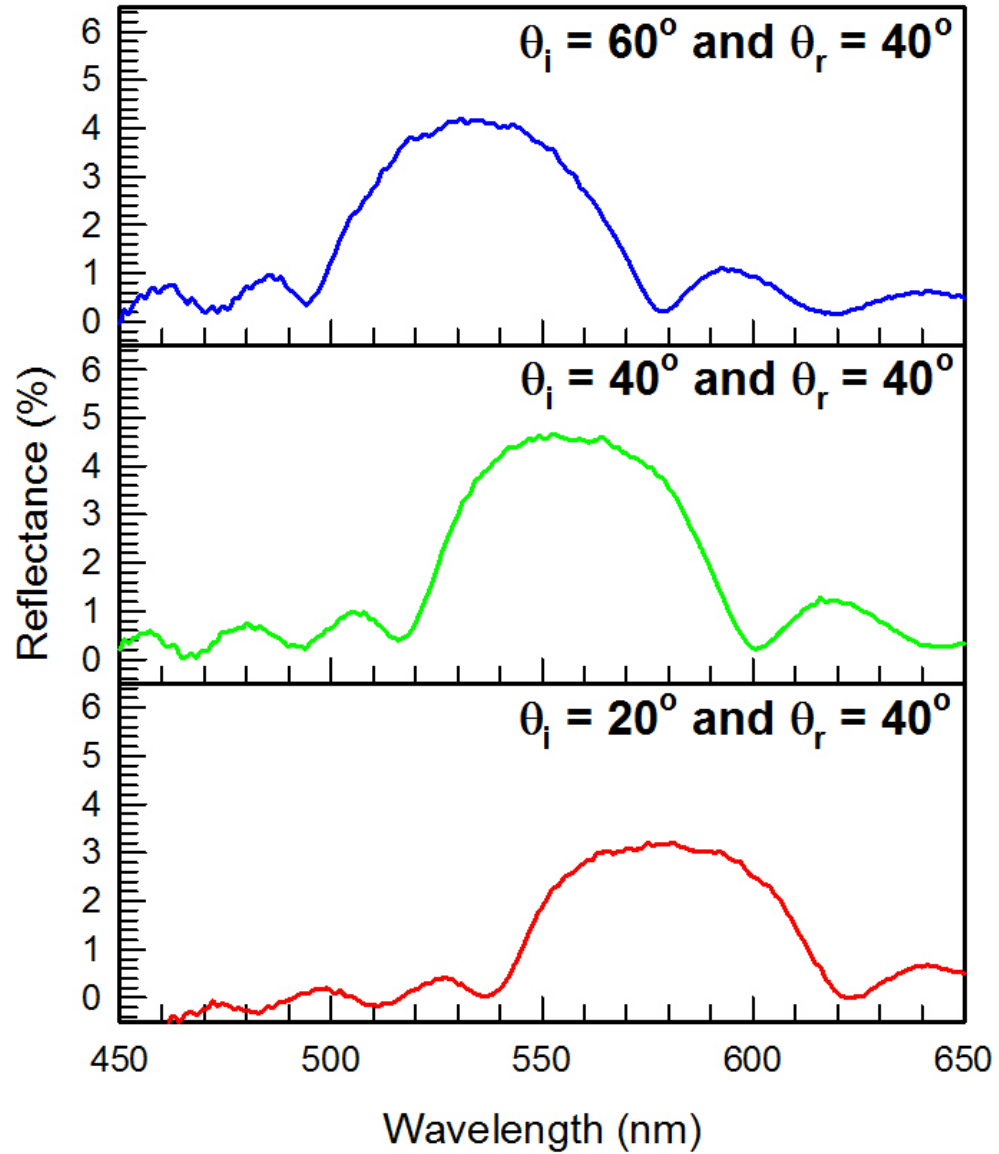


Figure 10.20: The measured reflection spectrum from a corrugated DBR when the angle of reflection was kept constant ($\theta_r = 40 \pm 1^\circ$), while different angles of incidence θ_i were tested. The top, middle and bottom captions are plots of reflection spectrum which were measured at 60° , 40° and 20° angles of incidence respectively. Moving the angle of incidence θ_i closer to the angle of reflection θ_r red-shifted the wavelength of the reflection peak.

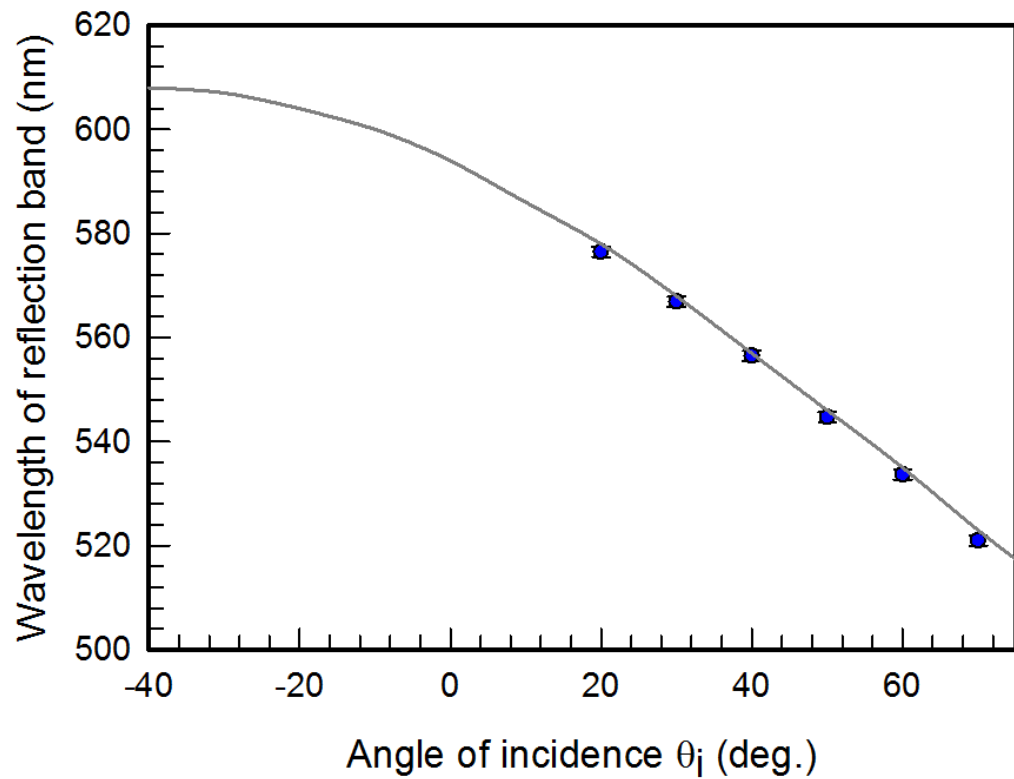


Figure 10.21: The wavelength of the reflection peak from the corrugated DBR was plotted with respect to the angle of incidence θ_i . Measurements are represented by the blue data-points. Error bars were determined by the resolution of the spectrometer. The angular dependence was modelled by the modified optical transfer matrix method (represented by the grey curve). Moving the angle of incidence θ_i closer to the angle of reflection θ_r red-shifted the wavelength of the reflection peak. This was due to the corrugated DBR offering a wide range of surfaces to reflect the incident light. The wavelength is its longest when the two beams are parallel ($\theta_i + \theta_r = 0$).

(because θ_r is constant in this experiment). Section 10.5.2 showed the wavelength of the reflection peak blue-shift when the angle between θ_i and θ_r was greater. The experiment in this section tested the optical properties of the corrugated DBR sample when angle of incidence θ_i varied and the angle of reflection was kept fixed $\theta_r = 40^\circ$. Both θ_i and θ_r are with respect to the surface normal of the substrate (not the curvature of the corrugations).

Figure 10.20 shows the reflection spectrum of the corrugated DBR when the angle of incidence was 60° (top caption), 40° (middle caption) and 20° (bottom caption). Moving the angle of incidence θ_i closer to the angle of reflection θ_r red-shifted the wavelength of the reflection peak. This is also shown in figure 10.21, which is a plot of the wavelength of the reflection peak with respect to angle of incidence θ_i . Reflection measurements of the corrugated DBR are represented by the blue data-points. The angle between θ_i and θ_r ($\Delta\theta = |\theta_i + \theta_r|$) was used to extract the wavelength of the reflection peak from the modified optical transfer matrix model (represented by the grey curve in figure 10.21).

Unlike the flat DBR, the reflection spectrum from the corrugated DBR can still be measured during off specular measurements (when $\theta_i \neq \theta_r$). However, the wavelength of the reflection peak changed with respect to θ_i . This experiment confirmed that increasing angle between θ_i and θ_r ($\Delta\theta = |\theta_i + \theta_r|$) changes the wavelength of the measured reflection peak. Hence, the wavelength of the reflection peak from a corrugated DBR is angular dependent when changing θ_i .

10.5.4 Rotating the corrugated sample

Figure 10.22 is a diagram of a flat DBR which is being measured as the sample is being rotated. The angle of incidence θ_i and the measured angle of reflection θ_r are with respect to the surface normal of the substrate. Sample rotation θ_s was measured with respect to the original position of the substrate surface plain. This was when $\theta_i = \theta_r$ with respect to the surface normal of the substrate. Rotating the sample changes the angles of both θ_i and θ_r . Rotating the sample away from its original position (when $\theta_i = \theta_r$) misaligns the beam path ($\theta_i \neq \theta_r$). The reflected beam diverges away from the spectrometer and the reflection spectrum is not measured.

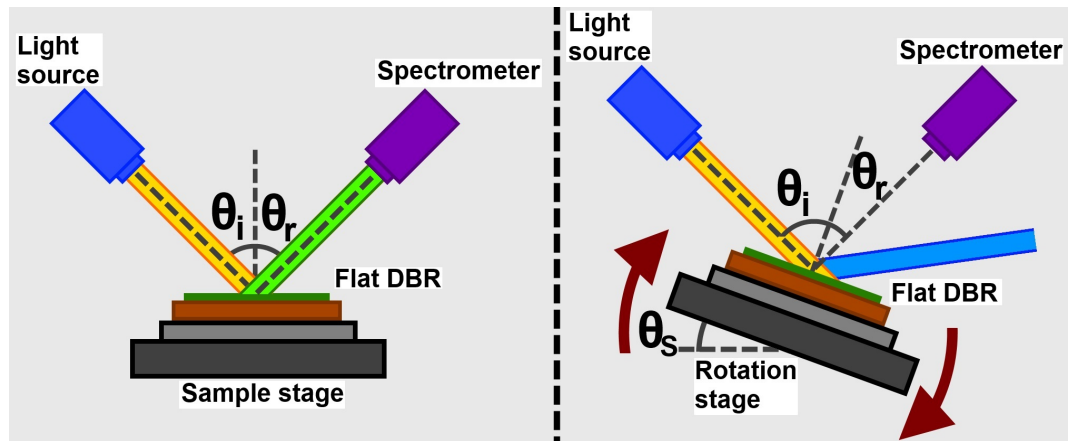


Figure 10.22: [Left panel] A flat DBR reflecting a beam of light. [Right panel] The flat DBR is rotated, which changes the angle of incidence and reflection. Changing the angle of incidence also changes the wavelength of the reflected beam, which cannot be detected since the set-up is misaligned.

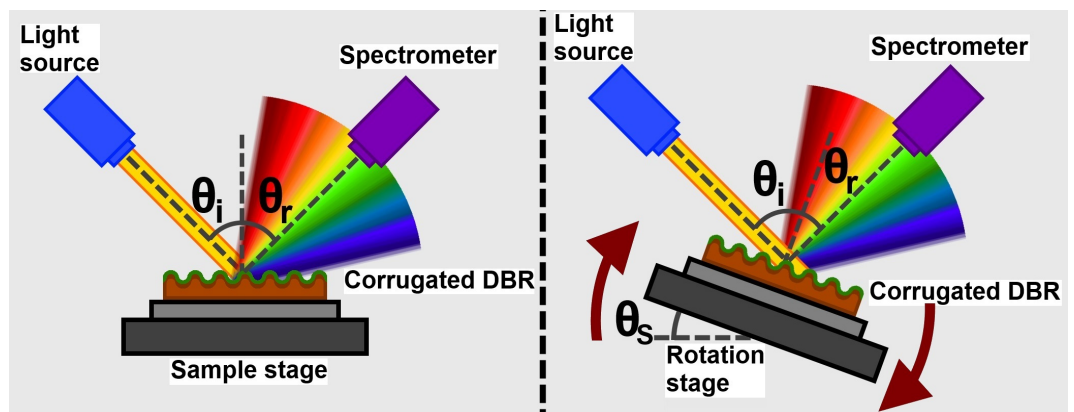


Figure 10.23: [Left panel] A corrugated DBR reflecting light over a broad range of angles and wavelengths. [Right panel] The distribution of the reflected wavelengths remains unchanged. Therefore, changing the orientation of the sample does change the wavelength of the reflection band measured at θ_r .

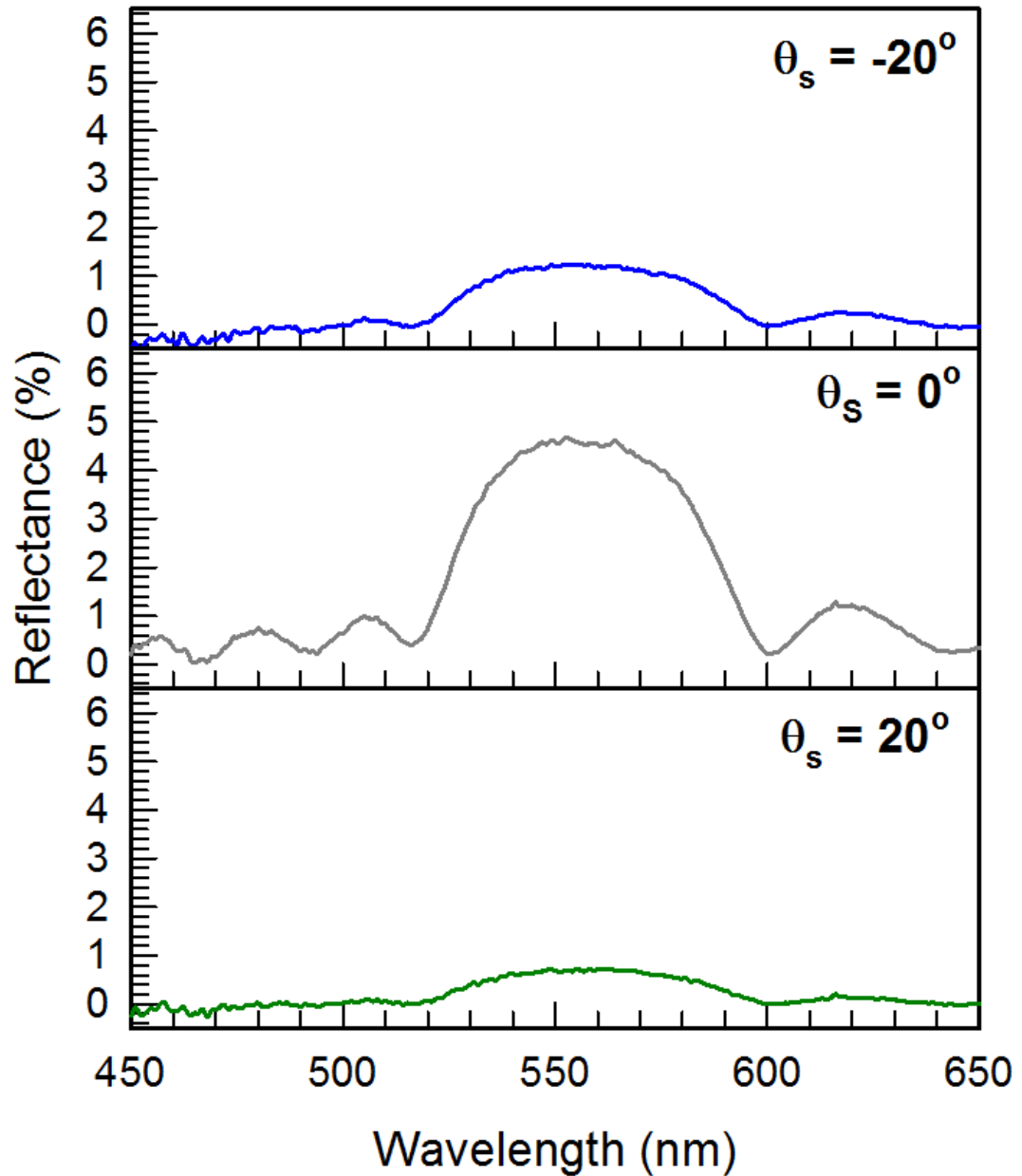


Figure 10.24: The measured spectra when the sample was rotated. The orientation of the sample θ_s is with respect to its original position when $\theta_i = \theta_r = 40^\circ$. Rotating the sample changes the magnitude of θ_i and θ_r with respect to the surface normal of the substrate. However, the angle between θ_i and θ_r remained constant at $\Delta\theta = 80^\circ$. Reflection spectrum was measured when the sample was rotated -20° (top caption), 0° (middle caption) and 20° (bottom caption) from its original position. The wavelength of the reflection band did not change when the sample was rotated. Angular dependence of the corrugated DBR was removed during this experiment.

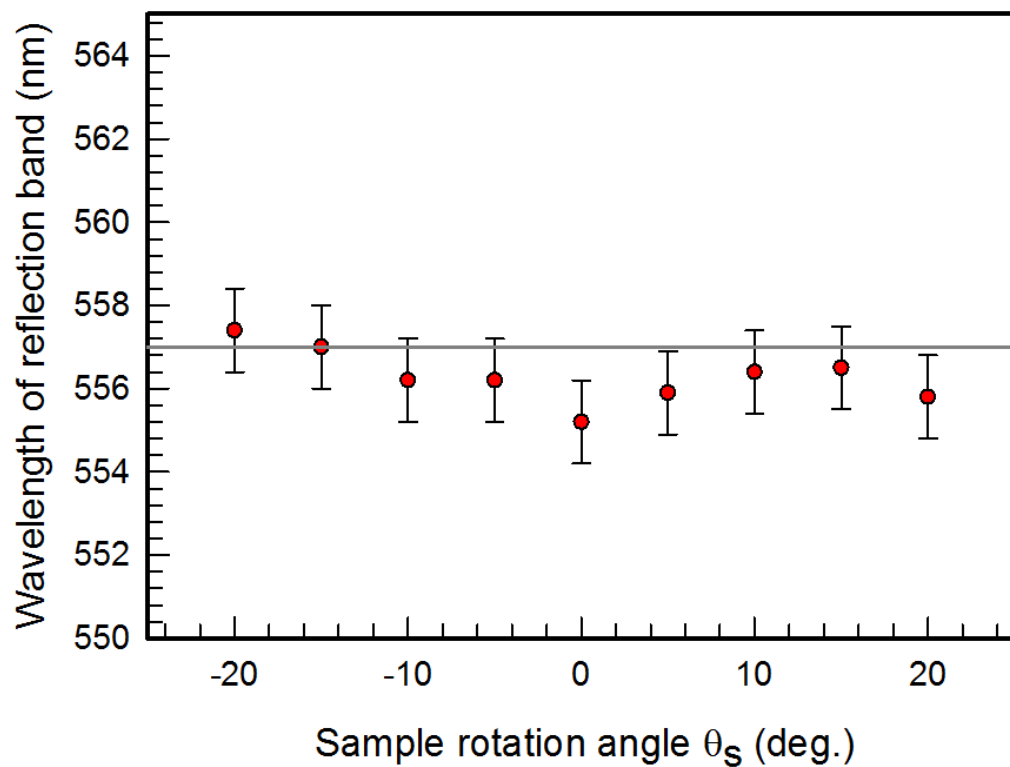


Figure 10.25: Wavelength of the reflection peak with respect to the sample rotation angle θ_s . The angle between the incident and the reflected light was kept constant at $\Delta\theta = 80^\circ$. The sample was at its original position when $\theta_i = \theta_r = 20^\circ$. Measurements are represented by the red data-points. Errors were determined by the resolution of the UV/visible spectrometer. The grey line represents the modelled data. Rotating the sample did not significantly change the wavelength of reflection peak. This demonstrates that the wavelength of the reflection peak from a corrugated DBR is not angular dependent when it is rotated.

Figure 10.23 is a diagram of a corrugated being measured as it is being rotated. Unlike the flat DBR, reflection spectra from the corrugated DBR can still be measured when the sample is rotated. This is due to the broad range of reflections from the curvature of the corrugations. Previous experiments (see sections 10.5.2 and 10.5.3) showed that the wavelength of the reflection peaks had blue-shifted when θ_r deviated away from θ_i and vice versa. However, the angle between the incident and reflected light is constant when only the orientation/angle of the sample is rotated ($\Delta\theta = |\theta_r - \theta_i| = \text{constant}$). Although, the angles of both θ_i and θ_r are changed with respect to the surface normal of the substrate when the sample is rotated (see figure 10.23).

Figure 10.24 shows three plots of the measured reflection spectrum from the corrugated DBR when it was being rotated. The angle between the incident and reflected light were $\Delta\theta = |\theta_r - \theta_i| = 80^\circ$ during these measurements. The reflection spectrum was measured when the sample was rotated -20° (top panel), 0° (middle panel) and 20° (bottom panel). The wavelength of the reflection peak stayed constant $\lambda = 557 \pm 2nm$ during this experiment. Figure 10.25 showed the same result for more measurements (red data-points) of the same experiment. The grey curve is the modelled wavelength with respect to the orientation of the sample. All of the modelled data remained constant as the angle between θ_i and θ_r was constant.

The beam path from a flat DBR is misaligned when it is rotated, where as the curvature of the DBR reduces misalignment. A corrugated DBR has a broad distribution of angled reflection surfaces due to its curvature. This curvature is not lost when the sample is rotated. There are surfaces which reflect incident light θ_i at a reflection angle of θ_r , even when the sample is rotated. Furthermore, the wavelength of the reflection band from a corrugated DBR remains constant when the sample is rotated. The angular dependence of the reflection band wavelength was reduced when rotating a corrugated DBR.

10.6 Reflectance of the corrugated DBR

The reflectance of the corrugated DBRs were significantly less than the flat DBRs. Both the flat and the corrugated DBRs were made from 30 alternating layers of CA/PVK. Reflectance of the the reflection peaks from the flat

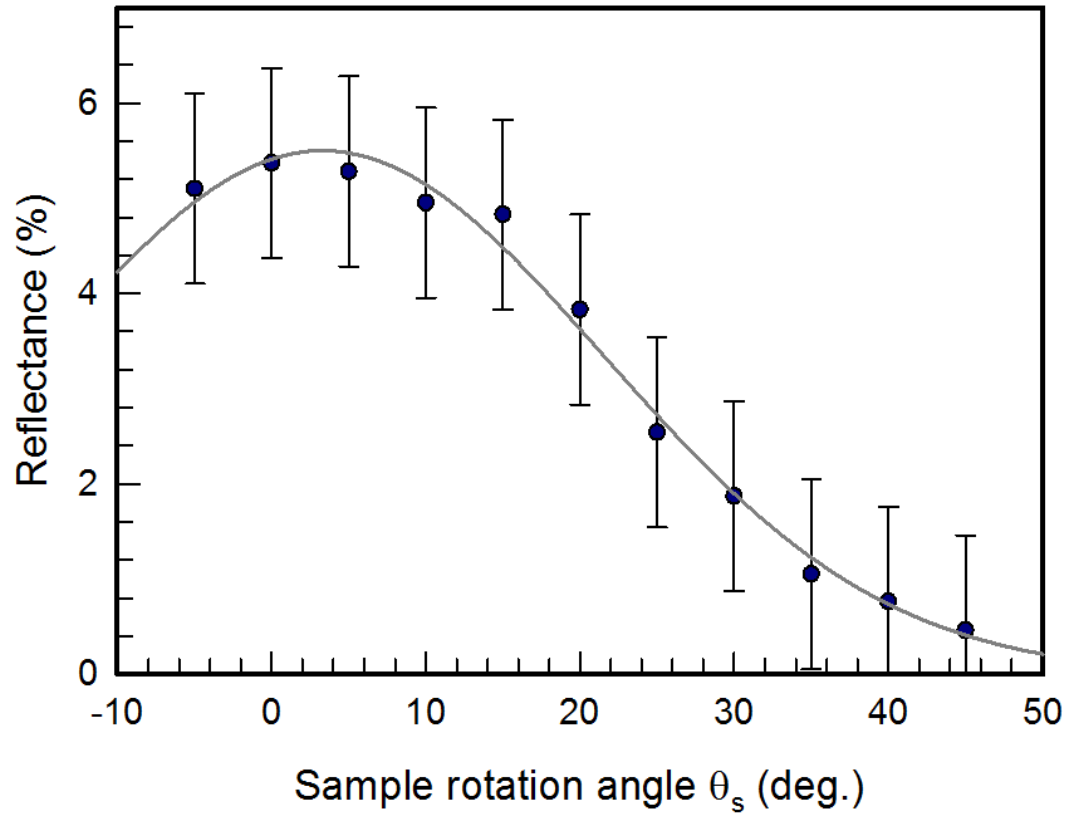


Figure 10.26: Change in the reflectance of a corrugated DBR when it is rotated. The angle between the incident and reflected light was kept constant during this experiment ($\Delta\theta = 40^\circ$). The sample was in its ‘original position’ ($\theta_s = 0$) when the angle of incidence and reflection were both $\theta_i = \theta_r = 20^\circ$ with respect to the surface normal of the substrate. Measurements are represented by the data-points and the errors were determined by the resolution of the spectrometer. The grey curve is a quadratic polynomial fit. Rotating the corrugated DBR away from its original position $\theta_s \neq 0$ reduced the reflectance of the measured reflection peak.

DBR (when deposited onto an elastomer substrate) were approximately $\sim 80\%$. However, the reflectance of the reflection peaks from the corrugated DBR were approximately $\sim 5.5\%$ for similar experiments. Furthermore, the reflectance of the corrugated DBR's reflection peak decreased when off specular reflections were being measured.

Figure 10.26 is a plot of the measured reflectance from the corrugated DBR with respect to the sample rotation angle θ_s . The angular separation between the angle of incidence and reflection was constant ($\Delta\theta = 40^\circ$) during this experiment. However, the angle of incidence and reflection were not equal $\theta_i \neq \theta_r$ (with respect to the surface normal of the substrate) when the sample was rotated ($\theta_s \neq 0$). The measurements were off-specular and the reflectance reduced when $\theta_s \neq 0$.

A corrugated DBR is approximately flat when the amplitude of the corrugations approach zero ($A_c \rightarrow 0$) and the wavelength tends to infinity ($\ell_c \rightarrow \infty$). All of the incident light remains collimated when it is reflected. Whereas a corrugated DBR reflects light over a wider area. The intensity (power per unit area) is reduced as the light is measured further away from the sample (so energy is conserved [10]).

The reflectance in figure 10.26 was its largest when the measured reflection was specular. This was due to the DBR being relatively shallow ($A_c \ll \ell_c$), which keeps specular reflection intensity high and scattered intensity low. Increasing the curvature in the sample ($A_c \approx \ell_c$) would most likely reduce/increase the intensity of the specular/non-specular reflections respectively. However, this was not tested and more experiments would be needed to make a thorough conclusion.

10.7 Summary

The reflection from a flat DBR is specular and can only be measured when $\theta_i = \theta_r$. A corrugated DBR reflects incident light over a wide distribution of angles. However, angular dependence was still present in the corrugated DBR when $\Delta\theta = |\theta_r + \theta_i|$ had changed. Although, these optical properties are unique to the corrugated DBR as there are no off-specular reflections from a flat DBR.

The angular dependence when rotating a DBR was reduced by corrugating the multi-layer film. Wavelength of the reflection peak remained constant when the sample was being rotated. This was due to the curvature of the corrugated surface, offering a broad range of angles of incidence and reflection. Rotating the sample does not change this property of the corrugated DBR surface. Measuring the reflection spectrum from a flat DBR is only possible when $\theta_i = \theta_r$. Rotating a flat DBR would misalign the beam path ($\theta_i \neq \theta_r$) and no reflectance would be measured.

The corrugated DBR could be useful in optical devices such as light emitting displays [4] and solar cells [8]. Although, placing the corrugated DBR on top of a flat device may not be very useful. This is discussed by using an LED as an example. The angular dependence of the corrugated DBR would only be removed when the angle between LED (light source) and the observer (detector) is constant. This is not practical as someone may not want to be directly in front of the display. However, corrugating a flexible organic LED with the DBR may be a better solution. The LED would be encapsulated within a resonant cavity over a wide range of angles. A more thorough investigation would be needed to test if this technique would work.

Chapter 11

Conclusion and future work

Distributed Bragg reflectors were made by routinely spin-coating alternating polymer layers. Reflection bands were measured in both the UV/visible [84] and the infra-red [91] wavelengths. The wavelength positions of the reflection bands were easily changed by controlling the rotation speed of the spin-coater during sample preparation. Reflectance of the reflection bands was controlled by the number of layers deposited. Broadening of the reflection band was also possible by periodically increasing the thickness of layers (chirping) during sample preparation. All of these variables were controlled when preparing samples with a self-built automated spin-coater [84]. Furthermore, the polymers and solvents used to prepare samples are commonly available and cheap.

The benefits of this system are that the optical properties of the samples can be readily changed. Preparation of other polymer photonic structures, such as using block-copolymers or colloids [19, 37, 38], do not have the high level of control for all of the variables discussed throughout this thesis. This is due to the specific properties of the block-copolymers or colloids restricting the variation possible when preparing samples. It is difficult to change the bandwidth of the reflection peak, for example, since all of the units making the photonic structure are of a fixed size.

There are already pre-existing all-polymer Bragg reflectors, such as the CA/PVK DBRs [20, 103]. However, the PVP/PS DBR samples in this thesis are cheap and require less harmful solvents for sample preparation (toluene is less harmful to the environment than chlorobenzene [104, 105]). The PVP/PS DBRs were also shown to have controllable reflection bands in the infra-red [91],

which could be useful for applications such as telecommunications [10, 22].

Neutron reflectivity and the remeasured UV/visible spectra from old samples, had shown that there was trapped solvent the PVP/PS DBR samples from their preparation. This was also determined when modelling the optical properties of the DBR, using a modified optical transfer matrix method. The modelled reflection spectrum was compared to the measurements and improved by lowering the refractive index contrast between the polymer layers. However, it was not possible to measure the quantity of solvent lingering in the multi-layer. I would suggest focusing on improving sample preparation, rather than researching techniques to improve the model. Spending time modelling the optical properties of defective samples wouldn't lead to results which would progress this research further. The residual solvent was an unwanted problem which should have been removed. Annealing the DBRs above the glass transition temperature of PVP ($T_g = 170^\circ C$) burned the samples. Other techniques should be investigated further (like periodically annealing the sample).

Sample quality was improved by annealing the DBR periodically during its preparation (approximately after every 20 layers were deposited). More layers which contributed to the total reflectance could be added to the sample. The exact reasons for why more layers could be added to the sample are not yet thoroughly understood. Testing the limits of large multi-layered structures may be useful for other applications such as polymer electronics, sensors, organic LEDs and organic solar cells are currently being prepared using multi-layered structures [5, 27, 106]. These devices could be integrated on top of one another to save space [50]. Understanding the limits of stacked multi-layer polymer structures may help make more complex all polymer integrated devices.

Other sample preparation techniques may be more useful for large scale multi-layer production than spin-coating. For example, melt processing [44], roll to roll processing [64] and screen printing [107] are alternative techniques which can produce thin film structures over a large scale. Any mass production of these DBR should be tested using these manufacturing techniques to reduce costs further. However, sample quality should be maintained and tested by using techniques such as ellipsometry, AFM, TOF-SIMS and neutron reflectivity.

Corrugating the Bragg reflectors did improve their angular dependence. However, this was only the case when rotating the sample. Angular dependence

was still measured when changing the separation between the angle of incidence and/or reflection. More experiments would be needed to see if corrugated DBRs would be useful for applications such as displays and solar cells.

TOF-SIMS measurements showed that the thickness of the layers in the PVP/PS multi-layer were reproducible and could be controlled. The resolution of the TOF-SIMS set-up did have errors as large as $\sim 20nm$. However, the Ar_{2000}^+ etching beam was shown to be far superior than other systems. Especially since the beam was etching through a ‘challenging polymer’ which is susceptible to cross-linking [78]. The PVP/PS DBRs could be used to test the Ar_{2000}^+ sputter beam further. For example, do you get a better resolution when the ion beam is fired with less energy?

The multi-layer PVP/PS samples could also be used to calibrate other sputtering analysis techniques, such as Plasma Assisted Desorption Ionisation (PADI) [108]. This technique functions by etching the surface of a sample with plasma (which is created in ambient atmosphere). Ionised particles are sputtered off the sample and measured using a mass spectrometer.

The multi-layer structure of polymer DBRs could also be used as gigahertz acoustic devices. Changes in the density of the polymer layers would create an interface. The multi-layer structure would reflect phonon, which is comparable to when the Bragg reflector reflects photons. These acoustic multi-layer structures could be used as gigahertz acoustic mirrors [109, 110].

Further development of the DBR samples could be investigated by integrating them into optical devices. This includes creating photonic cavities to improve the efficiency of displays [4, 5], lasers [6, 7] and solar cells [8, 9]. It also includes etching all-polymer optical devices into 2D photonic structures to improve their efficiency [16]. However, the reflectance of the Bragg reflectors would need to be greater than 99% [43]. This would be achieved by improving sample preparation further, or replacing one of the polymers with an alternative. The replacement polymer should increase the refractive index contrast of the polymer layers. Another alternative may be preparing samples with layers of thickness $\lambda/4$, which may require a different polymer system or preparation technique. Switching to a different polymer system, like the CA/PVK DBRs, may be a better solution when integrating polymer DBRs into devices.

Bibliography

- [1] Mitsuteru Kimura et. al. Tunable multilayer-film distributed-bragg-reflector filter. *Journal of Applied Physics*, 50(3):1222–1225, 1976.
- [2] Richard Lytel et. al. Narrowband electrooptic tunable notch filter. *Applied Optics*, 25(21):3889–3895, 1986.
- [3] V. Mullonia et. al. Porous silicon microcavities as optical chemical sensors. *Applied Physics Letters*, 76(18):2523, 2525 2000.
- [4] Ali M. Adawi et. al. Improving the light extraction efficiency of red-emitting conjugated polymer light emitting diodes. *Journal of Applied Physics*, 99, 2006.
- [5] Franky So, editor. *Organic Electronics: Materials, Processing, Devices and Applications*. CRC Press, 2010.
- [6] H. Takeuchi et. al. Single mode lasing in polymeric distributed-feedback structure formed on inorganic distributed bragg reflector. *Laser Physics Letters*, 5(1):41–44, 2007.
- [7] Simon Hooker and Colin Webb. *Laser Physics*. Oxford master series in atomic, optical, and laser physics. Oxford University Press, 2010.
- [8] Silvia Colodrero et. al. Porous one-dimensional photonic crystals improve the power-conversion efficiency of dye-sensitized solar cells. *Advanced Materials*, 21:764–770, 2009.
- [9] Frederik C. Krebs. Fabrication and processing of polymer solar cells: A review of printing and coating techniques. *Solar Energy Materials and Solar Cells*, 93:394–412, 2009.
- [10] Eugene Hecht. *Optics*. Addison Wesley, 4th (international) edition, 2002.

- [11] Terry A. King F. Graham Smith and Dan Wilkins. *Optics and Photonics An Introduction*. Wiley & Sons, 2007.
- [12] S Kinoshita et. al. Physics of structural colors. *Rep. Prog. Phys.*, (71), 2008.
- [13] Geoffrey Brooker. *Modern Classical Optics*. Oxford University Press, 2002.
- [14] Lukas Novokny and Bert Hecht. *Principles of nano-optics*. Cambridge University Press, 2006.
- [15] A.L. Álvarez et. al. Polymeric multilayers for integration into photonic devices. *Thin Solid Films*, 443:277–280, 2003.
- [16] Thomas F. Krauss et. al. Photonic crystals in the optical regime * past, present and future. *Progress in Quantum Electronics*, 23:51–96, 1999.
- [17] Richard A. L. Jones. *Soft Machines - Nanotechnology and life*. 1. Oxford University Press, 2007.
- [18] Richard A. L. Jones. *Soft Condensed Matter*. Oxford Master Series in Condensed Matter Physics. Oxford University Press, 1 edition, 2002.
- [19] Andrew J. Parnell et. al. Continuously tuneable optical filters from self-assembled block copolymer blends. *Soft Matter*, 9:3721–3725, 2011.
- [20] Toshiyuki Komikado et. al. Surface-emitting distributed-feedback dye laser of a polymeric multilayer fabricated by spin coating. *Applied Physics Letters*, 89(061123), 2006.
- [21] Mathias Kolle et. al. Bio-inspired band-gap tunable elastic optical multilayer fibers. *Adv. Mater*, 25:2239–2245, 2013.
- [22] Hamid Esmaeilzadeh et. al. A broadband optical fiber based inline polarizer for telecom wavelength range. *Sensors and Actuators A*, 185:59–65, 2012.
- [23] Anna M. Belu et. al. Tof-sims characterization and imaging of controlled-release drug delivery systems. *Analytical Chemistry*, 72(22):5625–5638, 2000.

- [24] Gregory L. Fisher et. al. Three-dimensional time-of-flight secondary ion mass spectrometry imaging of a pharmaceutical in a coronary stent coating as a function of elution time. *Analytical Chemistry*, 81(24):9930–9940, 2009.
- [25] Basudam Adhikari et. al. Polymers in sensor applications. *Progress in Polymer Science*, 29:699–766, 2004.
- [26] Jeroen K. J. van Duren et. al. Relating the morphology of poly(p-phenylene vinylene)/methanofullerene blends of solar-cell performance. *Advanced Functional Materials*, 14(5):425–434, 2004.
- [27] Mark Geoghegan and Georges Hadziioannou. *Polymer Electronics*. Oxford Mater Series in Condensed Matter Physics. Oxford University Press, 2013.
- [28] Greg Haugstad. *Atomic Force Microscopy : Understanding Basic Modes and Advanced Applications*. Wiley, 2012.
- [29] J. R. Hook & H. E. Hall. *Solid State Physics*. Wiley & Sons, 2nd edition edition, 2006.
- [30] Pete Vukusic et. al. Photonic structures in biology. *Nature*, 424:852–655, 2003.
- [31] Andrew Richard Parker. 515 million years of structural colour. *Journal of Optics A*, 2:R15–R28, 2000.
- [32] P. Vukusic et. al. Quantified interference and diffraction in single morpho butterfly scales. *Proceedings of the Royal Society B*, 266:1403–1411, 1999.
- [33] P. Vukusic et. al. Physical methods for investigating structural colours in biological systems. *Journal of the Royal Society Interface*, 6:S133–S148, 2009.
- [34] Chinkyoo Kim et. al. Critical thickness of gan thin films on sapphire (0001). *Applied Physics Letters*, 69(16):2358–2360, 1996.
- [35] Jongseung Yoon. Defect-mode mirrorless lasing in dye-doped organic/inorganic hybrid one-dimensional photonic crystal. *Applied Physics Letters*, 88(091102), 2006.

- [36] Thomas Krauss et. al. Two dimensional photonic-bandgap structures operating in near-infrared wavelengths. *Nature*, 383:699–702, 1996.
- [37] Alvaro Blanco et. al. Large-scale synthesis of a silicon photonic crystal with a complete three-dimensional bandgap near 1.5 micrometres. *Nature*, 405:437–440, 2000.
- [38] Toshimitsu Kanai et. al. New route to produce dry colloidal crystals without cracks. *Langmuir*, 25(23):13315–13317, 2009.
- [39] Mark G. Scullion et. al. Slotted photonic crystal sensors. *Sensors*, 13:3675–3710, 2013.
- [40] E. Yablonovitch et. al. Photonic band structure: The face-centered-cubic case employing nonspherical atoms. *Physical review letters*, 67(17):2295–2298, 1991.
- [41] Kanna Aoki et. al. Three-dimensional photonic crystals for optical wavelengths assembled by micromanipulation. *Applied Physics Letters*, 81(17):3122–3124, 2002.
- [42] Pater Bermel et. al. Improving thin-film crystalline silicon solar cell efficiencies with photonic crystals. *Optics express*, 15(25), 2007.
- [43] H. Sakata et. al. Green-emitting organic vertical-cavity laser pumped by in-gan-based laser diode. *Electronics Letters*, 43(25), December 2007.
- [44] Kenneth D. Singer. Melt-processed all-polymer distributed bragg reflector laser. *Optics Express*, 19(16), 2011.
- [45] Y S Zhao et. al. Efficiency enhancement of in-gan/gan light-emitting diodes with a back-surface distributed bragg reflector. *Journal of Electronic Materials*, 32(12), 2003.
- [46] Ali M. Adawi et. al. Spontaneous emission control in micropillar cavities containing a fluorescent molecular dye. *Advanced Materials*, 18:742–747, 2006.
- [47] Gert Strobl. *The Physics of Polymers*. Springer, 3rd edition, 2007.
- [48] F. Haaf et. al. Polymers of n-vinylpyrrolidone: Synthesis, characterization and uses. *Polymer Journal*, 17(1):143–152, 1985.

- [49] Michael Clugston and Rosalind Flemming. *Advanced Chemistry*. Oxford University Press, 2000.
- [50] David Voss. Cheap and cheerful circuits. *Nature*, 407:442–444, Sept 2000.
- [51] R.M.A. Azzam and N.M. Bashara. *Ellipsometry and polarized light*. Elsevier Science, 3rd edition, 1996.
- [52] Charalambos C. Katsidis et. al. General transfer-matrix method for optical multilayer systems with coherent, partially coherent, and incoherent interference. *Applied Optics*, 41(19):3978–3987, 2002.
- [53] Klaus Halbach. Matrix representation of gaussian optics. *American Journal of Physics*, 32(90), 1964.
- [54] H.E. Bennett et. al. Relation between surface roughness and specular reflectance at normal incidence. *Journal of the Optical Society of America*, 1961.
- [55] Michihiro Furusaka & Naoya Torikai Toyoko Imae, Toshiji Kanaya, editor. *Neutrons in Soft Matter*. Wiley & Sons, 1 edition, 2001.
- [56] *Multilayer Thin Films*. Wiley-VCH, 1 edition, 2003.
- [57] K. Norrman et. al. 6 studies of spin-coated polymer films. *Annu. Rep. Prog. Chem., Sect. C*,, 101:174–201, 2005.
- [58] Jinhan Cho et. al. Fabrication of highly ordered multilayer films using a spin self-assembly method. *Advanced Materials*, 13(14):1706–1708, July 2001.
- [59] D. E. Bomside et. al. Spin coating: One-dimensional model. *Journal of Applied Physics*, 66(11):8158–5193, 1989.
- [60] Andreas M'unch et. al. Spin coating of an evaporating polymer solution. *Physics of Fluids*, 23(102101), 2011.
- [61] Marco Maccarini. *Surface and Interface Properties of Industrially Relevant Polymers*. PhD thesis, University of Sheffield, Department of Physics and Astronomy, 2002.

- [62] Kenneth E. Strawhecker et. al. The critical role of solvent evaporation on the roughness of spin-cast polymer films. *Macromolecules*, 34(14):4669–4672, 2001.
- [63] Alexander A. Zakhidov et. al. Hydrofluoroethers as orthogonal solvents for the chemical processing of organic electronic materials. *Advanced Materials*, 20:3481–3484, 2008.
- [64] Roar Sondergaard et. al. Roll-to-roll fabrication of polymer solar cells. *Materials Today*, 15(1-2):36–49, 2012.
- [65] E.A. Grulke J. Brandrup, E.H. Immergut, editor. *Polymer Handbook*. Wiley Press, 1999.
- [66] Soney C. George et. al. Transport phenomena through polymeric systems. *Progress in Polymer Science*, 26:1985–1017, 2001.
- [67] Harland G. Tompkins and William A. McGahan. *Spectroscopic Ellipsometry and Reflectometry*. Wiley-Interscience, 1999.
- [68] C. M. Herzinger et. al. Ellipsometric determination of optical constants for silicon and thermally grown silicon dioxide via a multi-sample, multi-wavelength, multi-angle investigation. *Journal of applied physics*, 83(6):3323–3336, March 1998.
- [69] Peter R. Griffiths & James A. de Haseth. *Fourier transform infrared spectrometry*, volume 83. Wiley interscience, 1986.
- [70] Barbara Stuart. *Infrared Spectroscopy : Fundamentals and Application*. Wiley, 1 edition, 2004.
- [71] B. T. M. Willis & C. J. Carlile. *Experimental neutron scattering*. Oxford University press, 1 edition, 2009.
- [72] J Penfold et. al. The application of the specular reflection of neutrons to the study of surfaces and interfaces. *J. Phys., Condens. Matter*, 2:1369–1412, 1990.
- [73] Arfken Weber. *Mathematical Methods for Physicists*. Elsevier Academic Press, 6 edition, 2005.

- [74] Andrew Nelson. Co-refinement of multiple-contrast neutron/X-ray reflectivity data using *MOTOFIT*. *Journal of Applied Crystallography*, 39(2):273–276, April 2006.
- [75] John C. Vickerman. *Surface Analysis: The principal techniques*. John Wiley & Sons, 2003.
- [76] Kakan Nygren et. al. Bioimaging tof-sims: High resolution 3d imaging of single cells. *Microscopy Research and Technique*, 70:969–974, 2007.
- [77] Christine M. Mahoney et. al. Temperature-controlled depth profiling in polymeric materials using cluster secondary ion mass spectrometry (sims). *Applied Surface Science*, 252:6502–6505, 2006.
- [78] Rasmus Havelund et. al. Improving secondary ion mass spectrometry c60 n+ sputter depth profiling of challenging polymers with nitric oxide gas dosing. *American Chemical Society*, 2013.
- [79] Ian S. Gilmore. Sims of organics: advances in 2d and 3d imaging and future outlook. *Journal of Vacuum Science and Technology: A*, 31(5), 2013.
- [80] J. L. S. Lee et. al. Organic depth profiling of a nanostructured delta layer reference material using large argon cluster ions. *Analytical Chemistry*, 82(1):98–105, 2010.
- [81] Alexander G. Shard et. al. Argon cluster ion beams for organic depth profiling: Results from a vamas interlaboratory study. *Analytical Chemistry*, 84:7865–7873, 2012.
- [82] John C. Vickerman and David Briggs. *TOF-SIMS Surface Analysis By Mass Spectrometry*. IM Publications, 2001.
- [83] V. T. Cherepin. *Secondary Ion Mass Spectroscopy of Solid Surfaces*. VNU Science Press BV, 1987.
- [84] James Bailey et. al. Thin film polymer photonics: Spin cast distributed bragg reflectors and chirped polymer structures. *European Physical Journal E*, 33:41–49, 2010.

- [85] David Ennis et. al. Direct spincasting of polystyrene thin films onto poly(methyl methacrylate). *J Polym Sci Part B: Polym Phys*, 44:3234–3244, August 2006.
- [86] Richard A. L. Jones. *Polymers at surfaces and interfaces*. Cambridge University Press, 1999.
- [87] J.M.H.M. Scheutjens T. Cosgrove G. J. Fleer, M. A. Cohen Stuart and B. Vincent. *Polymers at Interfaces*. Chapman and Hall, 1st edition, 1993.
- [88] Rita Mehra. Application of refractive index mixing rules in binary systems of hexadecane and heptadecane with n-alkanols at different temperatures. *Proc. Indian Acad. Sci. (Chem. Sci.)*, 115(2):147154, April 2003.
- [89] J Perlich et. al. Solvent content in thin spin-coated polystyrene homopolymer films. *Macromolecules*, 42(1):337–344, 2009.
- [90] Andrii Buvailo et. al. Thin polymer film based rapid surface acoustic wave humidity sensors. *Sensors and Actuators B: Chemical*, (156):444–449, 2011.
- [91] James Bailey et. al. Infrared dielectric mirrors based on thin film multilayers of polystyrene and polyvinylpyrrolidone. *Journal of Polymer Science Part B: Polymer Physics*, 49:732–739, 2011.
- [92] Yuri Borodko et. al. Probing the interaction of poly(vinylpyrrolidone) with platinum nanocrystals by uv-raman and ftir. *Journal of Physical Chemistry B*, 110:23052–23059, 2006.
- [93] Gerald Oster et. al. Ultraviolet and infrared spectral studies of polyvinylpyrrolidone. *Journal of American Chemical Society*, 76(5):1393–1396, 1954.
- [94] Sarah E. Caudill et. al. Interferometric measurements of refractive index dispersion in polymers over the visible and near-infrared spectral range. *Journal of Applied Polymer Science*, 100:65–72, 2006.
- [95] Olivier Félix et. al. Are sprayed lbl-films stratified? a first assessment of the nanostructure of spray-assembled multilayers by neutron reflectometry. *C. R. Chimie*, 12:225–234, 2009.

- [96] R. N. S. Sodhi et. al. Analysis of ink/coating penetration on paper surfaces by time-of-flight secondary ion mass spectrometry (tof-sims) in conjunction with principal component analysis (pca). *The Journal of Adhesion*, 84(3):277–292, 2008.
- [97] James Sharp et. al. Mechanically driven wrinkling instability in thin film polymer bilayers. *Physical review E*, 75(011601), 2007.
- [98] N. Gibbons et. al. Corrugated metallodielectric superlattices via release-rollup assembly. *Optical Society of America*, 19(16), 2011.
- [99] Gen Kamita et. al. Multilayer mirrored bubbles with spatially-chirped and elastically-tuneable optical bandgaps. *Optics express*, 20(6):4430–4434, 2012.
- [100] Chi-Mon Chen et. al. Wrinkling instabilities in polymer films and their applications. *Society of Chemical Industry*, 61:1041–1047, March 2012.
- [101] Kevin R. Langley et. al. Microtextured surfaces with gradient wetting properties. *Langmuir*, 26(23):18349–18356, 2010.
- [102] J. Song et. al. International journal of solids and structures. *Buckling of a stiff thin film on a compliant substrate in large deformation*, 45:3107–3121, 2008.
- [103] Multi layered mirrors fabricated by spin-coating organic polymers. Toshiyuki komikado. *Thin Solid Films*, 2007.
- [104] Sigma Alrich Materials Safety Data Sheet. Toluene (hplc grade). Revision date: 04.02.2013.
- [105] Sigma Alrich Materials Safety Data Sheet. Chlorobenzene (hplc grade). Revision date: 04.12.2012.
- [106] Stephen R. Forrest. The path to ubiquitous and low-cost organic electronic appliances on plastic. *Nature*, 428:911–918, 2004.
- [107] Anke Teichler et. al. Inkjet printing of organic electronics comparison of deposition techniques and state-of-the-art developments. *Journal of Materials Chemistry C*, 1:19101925, 2013.

- [108] A. Boweld et. al. Surface analysis using a new plasma assisted desorption/ionisation source for mass spectrometry in ambient air. *Review of scientific instruments*, 2012.
- [109] David J. Farmer et. al. Quantized phonon modes in loaded polymer films. *Journal of applied physics*, 113(033516), 2013.
- [110] P. M. Walker et. al. Coherent elastic waves in a one-dimensional polymer hypersonic crystal. *Applied Physics letters*, 97(073106), 2011.